

School of Electrical Engineering, Computing and
Mathematical Sciences

**Wave-Packet Convergent Close-Coupling Approach to
Ion-Atom Collisions**

Shukhrat Alladustov

This thesis is presented for the Degree of
Doctor of Philosophy
of
Curtin University

August 2019

Declaration

To the best of my knowledge and belief this thesis contains no material previously published by any other person except where due acknowledgment has been made.

This thesis contains no material which has been accepted for the award of any other degree or diploma in any university.



Shukhrat Alladustov

4th August, 2019

Contents

Summary	vi
List of publications	x
1 Introduction	1
2 Overview of existing theories	6
2.1 Classical-trajectory Monte Carlo model	7
2.2 Perturbative methods	8
2.2.1 Born approximation	9
2.2.2 Distorted-wave Born approximation	10
2.2.3 Continuum-distorted-wave approaches	11
2.3 Non-perturbative methods	12
2.3.1 Close-coupling approach	12
2.3.2 Impact-parameter Faddeev approach	14
2.3.3 Methods based on direct numerical solution	15
2.3.4 Convergent close-coupling approach	17

3	Convergent close-coupling approach to collisions of multiply-charged ions with hydrogen	20
3.1	Introduction	20
3.2	The Schrödinger equation for scattering of multiply-charged ions on hydrogen	22
3.3	Hydrogenic wave functions	28
3.4	Matrix elements	30
3.4.1	Evaluation of matrix elements	34
3.5	Chapter summary	41
4	Wave-packet convergent close-coupling approach to proton collisions with helium	42
4.1	Introduction	42
4.2	The Schrödinger equation for proton collisions with helium	44
4.3	Matrix elements	53
4.4	Evaluation of matrix elements	59
4.5	Chapter summary	62
5	Experimental Observables	63
5.1	Total cross sections	63
5.2	Differential ionisation cross section	65
5.3	Chapter summary	69

6	Proton scattering on excited states of hydrogen	70
6.1	Convergence studies	71
6.2	Final results for proton scattering on excited states of hydrogen	73
6.2.1	Proton scattering on the $2s$ state of hydrogen	74
6.2.2	Proton scattering on the $2p_0$ and $2p_1$ states of hydrogen .	78
6.2.3	The density matrix	82
6.3	Chapter summary	82
7	C^{6+}-H collisions	84
7.1	Convergence studies	85
7.2	Final results for C^{6+} ion scattering on hydrogen	90
7.2.1	Total cross sections	90
7.2.2	Differential cross sections	94
7.3	Chapter summary	102
8	He^{2+}-H and p-He^+ collisions	104
8.1	Convergence studies	104
8.1.1	Convergence of the total cross sections	105
8.1.2	Convergence of the differential cross sections	106
8.2	Final results for the total cross sections in He^{2+} -H and p - He^+ collisions	111
8.3	Chapter summary	122

9 Proton-helium collisions	123
9.1 Convergence studies	124
9.2 Total cross sections	126
9.2.1 Electron capture and excitation	127
9.2.2 Ionisation	130
9.3 Chapter summary	133
10 Conclusion and Outlook	135
A Momentum-transfer vectors	141
B Momentum-transfer vectors for proton-helium system	146
C Signed Statement of Coauthors	149
Abbreviations	155
List of Figures	156
Bibliography	163

Summary

The present thesis is devoted to the application of the wave-packet convergent-close coupling (WP-CCC) method to ion-atom collisions. We apply the method to three- and four-body problems and compare the obtained results with experimental and other theoretical results, where available. We study proton scattering on excited states of hydrogen, collisions of bare ions (He^{2+} and C^{6+}) with hydrogen, and proton collisions with the helium atom and He^+ ion.

In our approach, the collisional system is described by the total scattering wave function, which satisfies the time-independent Schrödinger equation (TISE). Interactions between the particles are given by the long-range Coulomb potential. The scattering wave function is expanded within the two-centre approach in terms of the basis made of target- and projectile-centred eigenstates and pseudostates. To describe positive-energy states we employ the wave-packet approach. The continuum of all involved atoms are discretised sufficiently dense using bin states. Depending on the considered collisional system the basis consists of the wave functions for the hydrogen-like atom of charge Z and the helium atom. The helium wave functions are found by numerically solving the Schrödinger equation for helium. Then, inserting the expansion into the TISE using a semiclassical approximation, where the projectile motion relative to the target is treated classically and target is treated fully quantum-mechanically, leads to a set of coupled differential equations for the expansion coefficients.

The obtained system of equations is solved to find transition amplitudes, which are used to calculate cross sections for elastic scattering, target excitation, electron capture and ionisation, as well as differential ionisation cross sections.

Main results

- The WP-CCC method is applied to the three-body problem of proton scattering on the excited ($2s$, $2p_0$, $2p_1$) states of hydrogen:
 - The total cross sections are calculated for elastic scattering, excitation, ionisation and electron capture.
 - The density matrix elements for excitation of 2-shell states of hydrogen are also provided.
- The method is also applied to C^{6+} -H($1s$) collisions:
 - The total cross sections are calculated for electron capture and ionisation.
 - Singly differential cross section is provided for 1 and 2.5 MeV/amu C^{6+} -impact ionisation of atomic hydrogen.
 - Doubly differential cross sections in the ejected-electron energy at certain fixed ejection angles, and in ejected-electron angle for fixed ejection energies are calculated for 1 and 2.5 MeV/amu C^{6+} -impact ionisation of atomic hydrogen.
- He^{2+} -H and p - He^+ collisions are studied using the WP-CCC approach:
 - Total cross sections are calculated for electron capture and ionisation for both collisional systems in the range from 10 keV/amu to 1 MeV/amu.

- Fully differential cross section for He^{2+} -impact ionisation of atomic hydrogen is provided as a function of the electron ejection angle.
 - Doubly differential cross section for He^{2+} -impact ionisation of atomic hydrogen is provided in the energy and the angle of the ejected electron.
 - Singly differential cross section for He^{2+} -impact ionisation of atomic hydrogen is calculated in the angle of the ejected electron.
 - Balmer- α emission cross section is calculated in He^{2+} -H collisions.
- The WP-CCC approach is extended to a four-body problem of proton-helium collisions:
 - The helium atom is treated using the frozen-core approximation where electron-electron correlation is fully taken into account.
 - Total cross sections are calculated for electron capture and single ionisation in the range from 15 keV to 1 MeV.
 - Total double-ionisation cross sections are calculated by using the independent event model.
 - Partial cross sections for electron capture into $2s$ and $2p$ states of hydrogen, and excitation of the $2s$ and $2p$ states of the target are calculated.

The thesis is organised in the following way:

In Chapter 1 we describe the motivation and background of ion-atom collisions. Existing theories and their applications to the considered collisional systems are briefly discussed in Chapter 2. Chapter 3 is devoted to the description of the WP-CCC approach to collisions of protons and bare ions with

excited atomic hydrogen. Application of the method to a four-body problem of proton-helium collisions is described in Chapter 4. Analytical formulas for calculating probabilities, total and differential cross sections, as well as density matrices using the transition amplitudes are presented in Chapter 5. In Chapter 6 we provide the results of the single- and two-center WP-CCC methods in proton scattering on excited states of atomic hydrogen and make comparisons with experimental data and other calculations, where available. The total and differential cross sections for collisions of fully-stripped carbon ion with hydrogen are given in Chapter 7. Chapter 8 is devoted to the description the present WP-CCC results for He^{2+} -H and p - He^+ collisions. In Chapter 9 we present our results for the total electron-capture and ionisation cross sections for p -He collisions and compare with experimental and other theoretical results. Finally, in Chapter 10 we draw conclusions and give some possible outlook for further research.

List of publications

During my studies I have coauthored 5 peer-reviewed papers. They are listed below in reverse-chronological order.

1. J. Faulkner, I. B. Abdurakhmanov, Sh. U. Alladustov, A. S. Kadyrov, and I. Bray, "Electron capture, excitation and ionization in He^{2+} -H and H^+ - He^+ collisions", [Plasma Phys. Control. Fusion](#) **61**, 095005 (2019).
2. Sh. U. Alladustov, I. B. Abdurakhmanov, A. S. Kadyrov, I. Bray, and K. Bartschat, "Wave-packet continuum-discretization approach to proton collisions with helium", [Phys. Rev. A](#) **99**, 052706 (2019).
3. A. S. Kadyrov, I. B. Abdurakhmanov, Sh. U. Alladustov, J. J. Bailey, and I. Bray, "Development of convergent close-coupling approach to hadron interactions with matter", [J. Phys. Conf. Ser.](#) **1154**, 012013 (2019).
4. I. B. Abdurakhmanov, K. Massen-Hane, Sh. U. Alladustov, J. J. Bailey, A. S. Kadyrov, and I. Bray, "Ionization and electron capture in collisions of bare carbon ions with hydrogen", [Phys. Rev. A](#) **98**, 062710 (2018).
5. I. B. Abdurakhmanov, Sh. U. Alladustov, J. J. Bailey, A. S. Kadyrov, and I. Bray, "Proton scattering from excited states of atomic hydrogen", [Plasma Phys. Control. Fusion](#) **60**, 095009 (2018).

Copyright acknowledgment: This thesis contains material originally published in these papers.

Statement of Contribution of Others

This thesis is based on the materials of several joint publications. I contributed to developing theoretical methods, data collection and analysis, developing the computer code and performing calculations, as well as preparing the manuscript for these publications. Below, the contributions of the other coauthors are briefly specified for each paper.

Description of the WP-CCC approach to four-body problems in Chapters 3 and 4, and the results given in Chapter 9 are based on the paper by Sh. U. Alladustov, I. B. Abdurakhmanov, A. S. Kadyrov, I. Bray, and K. Bartschat, "Wave-packet continuum-discretization approach to proton collisions with helium", *Phys. Rev. A* 99, 052706 (2019). All the coauthors contributed to the development of the underlying theory and preparation of the manuscript for the paper.

The content of Chapter 6 is based on the paper by I. B. Abdurakhmanov, Sh. U. Alladustov, J. J. Bailey, A. S. Kadyrov, and I. Bray, "Proton scattering from excited states of atomic hydrogen", *Plasma Phys. Control. Fusion* 60, 095009 (2018). Coauthors I. B. Abdurakhmanov and J. J. Bailey contributed to developing the computer code and performing calculations. All the coauthors contributed to the development of the underlying theory and preparation of the manuscript for the paper.

The content of Chapter 7 is based on the paper by I. B. Abdurakhmanov, K. Massen-Hane, Sh. U. Alladustov, J. J. Bailey, A. S. Kadyrov, and I. Bray, "Ionization and electron capture in collisions of bare carbon ions with hydrogen", Phys. Rev. A 98, 062710 (2018). Coauthors I. B. Abdurakhmanov and K. Massen-Hane contributed to developing the computer code and performing calculations. All the coauthors contributed to the development of the underlying theory and preparation of the manuscript for the paper.

The content of Chapter 8 is based on the paper J. Faulkner, I. B. Abdurakhmanov, Sh. U. Alladustov, A. S. Kadyrov, and I. Bray, "Electron capture, excitation and ionization in $\text{He}^{2+}\text{-H}$ and $\text{H}^+\text{-He}^+$ collisions", Plasma Phys. Control. Fusion 61, 095005 (2019). Coauthors J. Faulkner and I. B. Abdurakhmanov contributed to performing calculations. All the coauthors contributed to the development of the research methods and preparation of the manuscript for the paper.

Signature of Candidate



Signature of Supervisor



Acknowledgments

I would like to start the acknowledgment by thanking my supervisor Professor Alisher Kadyrov, who was the main initiator of this project. His guidance, discussions and lectures on Quantum Physics helped me to gain knowledge in ion-atom collisions and to develop programming skills, which were crucial factors for completing this thesis. I am thankful for his active involvement during the whole course and his indispensable support. It would not be possible to complete this thesis without his dedication and commitment.

Also, I express my gratitude to my co-supervisor Dr. Ilkhom Abdurakhmanov who was always willing to offer his assistance with any issues I faced. Especially, I thank him for his guidance in developing the computer code for the obtained results. I am also grateful to my co-supervisor Professor Igor Bray. His advice and recommendations greatly helped to improve the quality of this thesis.

I thank all members of the Theoretical Physics group for a friendly research environment. Specifically, I would like to mention Professor Dmitry Fursa and research fellow Dr. Ravshan Utamuratov for their useful discussions. I also acknowledge PhD students Jackson, Charlie and Liam for sharing their experience and for being just friends.

I acknowledge Curtin University for creating an opportunity to obtain the PhD course and providing the financial support.

Finally, I am deeply thankful to my parents and the other members of my family for their understanding and continuous encouragement.

Chapter 1

Introduction

The study of ion-atom collisions is one of the intensive research areas in atomic physics. These collisions create an opportunity to enlarge our knowledge of the structure of atoms, the few-body dynamics and driving mechanisms through the experiments and theoretical calculations. A thorough understanding of the underlying processes including ionisation, excitation and charge-exchange is essential for applications in a wide range of fundamental and practical sciences. Collisions of hydrogen and helium atoms are of particular importance due to their abundance in nature and involvement in fundamental physical processes. Examples of the application of these scattering studies include the sciences such as astrophysics, astrophysical modelling and plasma physics. Ion-atom collisions lie behind many occurring astrophysical processes. In particular, modelling astrophysical shocks rely on accurate cross sections for proton-hydrogen collisions [1]. They play an important role in fusion research, where collisions data are needed for plasma heating methods to produce the hot plasma and investigating the physical properties of the fusion plasma [2]. In this process, the confined plasma is known to create excited hydrogen atoms, therefore proton scattering on excited states of hydrogen has also practical importance, for example in the ITER project (see Fig. 1.1 for a projected ITER tokamak). Also

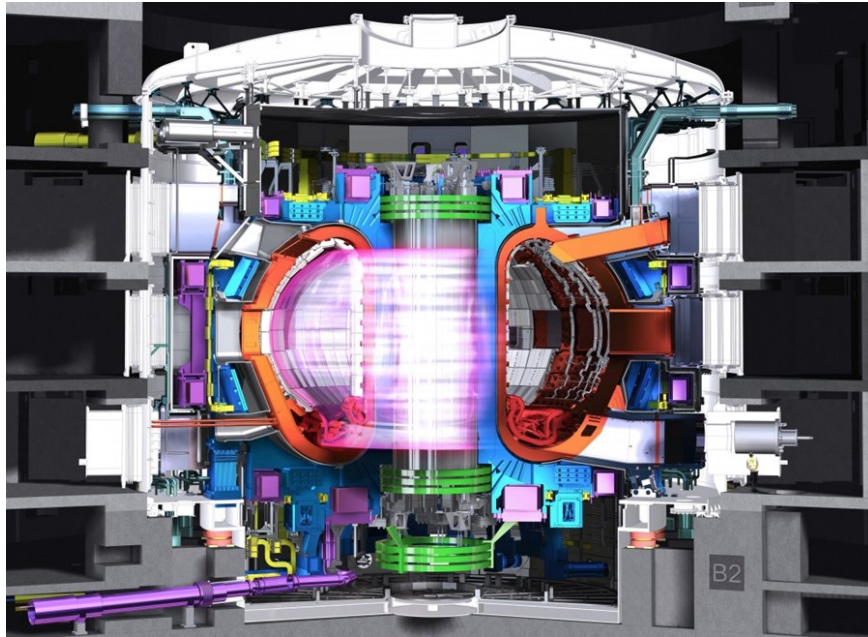


Figure 1.1: Tokamak. Image courtesy of ITER.

in plasma modelling, applications of the diagnostic methods such as charge-exchange recombination spectroscopy, beam emission spectroscopy and motional Stark effect spectroscopy require accurate data on charge-exchange, ionisation and excitation cross sections [3, 4].

In terms of the practical application, scattering studies of atoms by proton and bare ions are relevant to hadron therapy of cancer [5, 6]. Hadron therapy has considerable advantages over conventional X-ray therapy as illustrated in Fig. 1.2. In proton beam therapy, high doses of radiation can be delivered precisely to tumours without significantly harming surrounding tissue. This leads to a more efficient treatment and fewer side effects. Using carbon ions as projectiles is considered to be even more efficient than protons because of a sharper Bragg peak in the radiation dose distribution curve, which reduces the damage to healthy tissue. Latest advancements in technology, medical imaging and computing allowed implementing proton and carbon therapies in medicine.

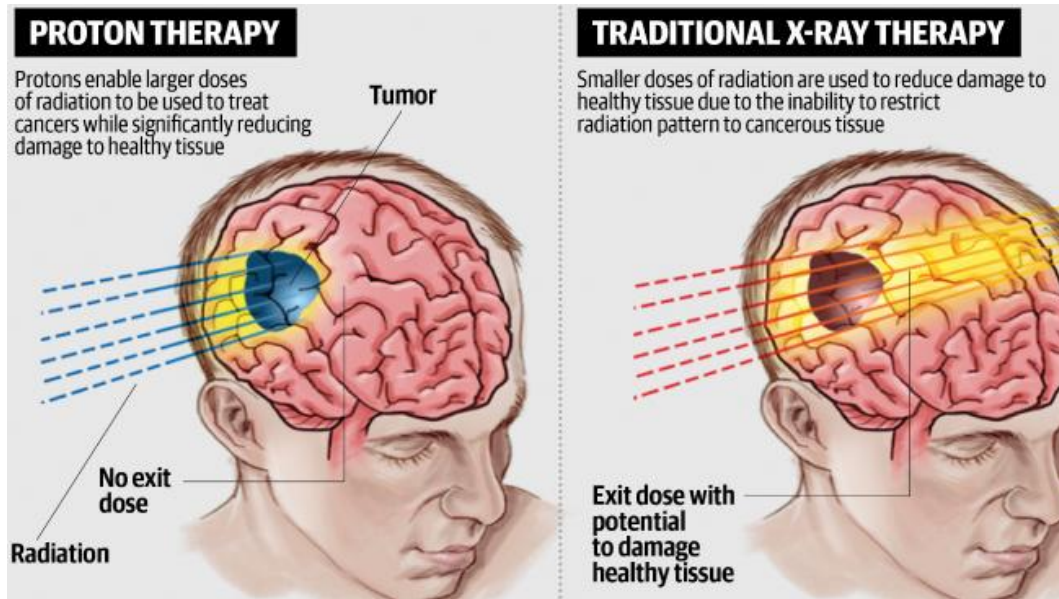


Figure 1.2: Comparison of proton and traditional x-ray therapies [7].

However, establishing influence of radiation to living organisms has always been an important issue. Therefore, accurate cross-section data for carbon and proton collisions with relevant targets is crucial in improving our understanding of the radiation damage. The helium and hydrogen targets are not of the primary importance in the collisional processes applicable to hadron therapy, but studying simplest targets and testing theoretical models are considered to be the first necessary steps towards studying more complex targets such as the water molecule.

Ion-atom collisions have been very attractive both theoretically and experimentally for several decades. The pioneering studies for simple processes taking place in ion-atom collisions date back to the first half of the last century [8, 9] and more advanced works appeared in 1950s [10–14]. Due to progress in experimental and computing technologies, various experimental techniques and theoretical approaches were developed to study scattering of the targets from simple hydrogen atom to more complex many-electron atoms by singly- and

multiply-charged ions (see [15–18] for detailed description of the field). In particular, many theoretical works were devoted to study a three-body problem of proton and multiply-charged ion collisions with atomic hydrogen [19–37]. From a theoretical point of view, studying atomic hydrogen and hydrogen-like targets is much simpler than other many-electron systems because of the analytically known hydrogenic wave functions and the absence of the electron-electron correlations. Therefore, these three-body problems are convenient for applying various approaches and approximations.

The helium atom is a good starting point of studying many-electron targets because it is the simplest multi-electron atom and is easily available for experimental studies. Collisions of helium with ions allow us to study the dynamic-correlation effects between the target electrons in the underlying processes including charge exchange. However, describing the helium atom as a two-electron system is rather challenging. Therefore, in some theoretical methods the electron-electron correlations are simply ignored. Another challenge in studying the helium target is related with the wave functions and the corresponding energy levels. Since, the Schrödinger equation for helium has no analytical solutions, their accuracy depends on applied approximations and numerical approaches. Therefore, collisions involving helium provide a sensitive test for employed theoretical methods. For these reasons, collisions of helium with various ions, particularly proton-helium collisions, have been investigated to a great extent both theoretically [38–58] and experimentally [59–69].

The breakup processes provide detailed, often more complete, information about dynamics of ion-atom collisions. Studying geometries of the scattered particles helps to understand the interaction effects between the projectile and recoil-target ion and ejected electrons. Post-collisional behavior of the particles can be explained by the total cross sections to a certain extent, but impor-

tant information is lost due to integration over the momenta of the particles in the final channels. Differential studies of ejected electrons in the ionisation process are rather challenging, but can describe the driving mechanisms in the collisions in more detail. Experimental differential studies of the ionisation processes involve determining momentum vectors of all collision particles. The first experimental techniques for such studies became available about six decades ago. Ehrhardt *et al.* [70] provided differential ionisation cross sections for electron-helium collisions by measuring momenta of the outgoing electrons. Perturbative methods [71] at high, and non-perturbative methods [72] at low, projectile energies were quite successful in reproducing the experimental data. However, unlike for light projectiles, the ionisation processes in scattering of atoms by heavy particles are not yet fully understood. Kinematically complete experimental study of differential ionisation in ion-atom collisions is very challenging, as it requires measuring the momenta of scattered ions in addition to the momenta of ejected electrons. The problem remained unsolved for a long time even after the experimental techniques became available for electron momentum. Complete experiments became possible with the introduction of such experimental techniques as COLTRIMS (cold-target recoil-ion momentum spectroscopy) [73]. Since the advancement of these techniques, differential studies of the breakup processes in ion-atom collisions, particularly single ionisation of helium by proton impact, attracted an increasing interest [74–85]. However, a wide range of unexplained discrepancies between theory and experiment emphasise the need for more studies on these collisional systems both theoretically and experimentally.

Chapter 2

Overview of existing theories

Together with the progress in experimental techniques for investigating ion-atom collisions, various theoretical approaches have been developed and successfully applied to model them. One of the well-known and widely used theoretical methods is the classical-trajectory Monte Carlo (CTMC) model. Semiclassical and quantum-mechanical methods can be classified as perturbative and non-perturbative approaches. Perturbative treatment is applicable for systems with a relatively small interaction time between the projectile and the atomic electron. The latter is the case when the speed of the projectile significantly exceeds that of the atomic electron. For collision systems where perturbative approaches are not applicable, non-perturbative methods are used. It should be noted that most of the theories are based on solving the Schrödinger equation corresponding to a many-body system, which cannot be solved analytically. Below we describe typical approaches that were applied to ion-atom collisions and give examples of their application.

2.1 Classical-trajectory Monte Carlo model

The first rather simple form of the classical-trajectory Monte Carlo method was developed to analyse hydrogen-deuterium reactions by Hirschfelder *et al.* [86]. However, only one trajectory was included in the study because of the calculation difficulties, as the classical trajectories had to be calculated using a mechanical calculator. With the advancement of super-computers, the classical-trajectory method became an active tool in investigating electron-capture and ionisation processes in ion-atom collisions [22, 25]. The CTMC approach to three-body problems is based on numerically solving a set of first-order differential equations obtained from the classical Hamiltonian of a collision system. The interactions between the projectile, the target nucleus and the electron are described by the Coulomb forces. The orientation and momentum of the target electron as well as the impact parameter within the interaction range are selected randomly using a Monte Carlo method. Then high-order Runge-Kutta method is employed to integrate the equations of motion, and an occurred collision process is established. Calculated trajectories are used to obtain charge-transfer and ionisation cross sections. They can also be used to generate differential cross sections. Accuracy of calculations depends on the number of evaluated trajectories. Accordingly, a sufficient number of trajectories needs to be calculated to avoid errors. The method is applicable for a wide range of scattering problems including collisions of multiply-charged ions with atomic hydrogen and is most effective in the intermediate energy range. Examples of successful applications include the calculations of ionisation and electron-capture cross sections in multiply-charged ion-hydrogen collisions by Olson and Schultz [27], Fiol and Olson [30] and Jorge *et al.* [37].

The CTMC method is also applicable to multi-electron targets. The effec-

tiveness and validity of the method was studied in collisions of highly-charged ions with Ne by Olson *et al.* [87]. All interaction forces between the projectile, the target nucleus and electrons were taken into account. In this approach, the existence of more electrons increases the number of coupled differential equations multiple times in comparison with three-body problems. However, computing time did not change significantly because of the use of vector-processors to solve the system of equations. In another work, the method was used to investigate bare-ion collisions with helium by Zajfman and Maor [88], where the He atom was stabilised using the Heisenberg uncertainty principle on the classical system. Schultz and Olson [89] also employed this approach to study proton and antiproton scattering on helium. The target was treated as one electron system neglecting the electron-electron correlation. Then, the well-known three-body CTMC method was applied to calculate the cross sections for ionisation and charge transfer. The obtained results agreed with the available experimental data reasonably well at the incident projectile energies from 25 keV to 500 keV. As we mentioned above, the accuracy of the results are dependent on the statistics. Therefore, a large number of trajectories need to be evaluated that might be quite time consuming even with abilities of modern computers.

2.2 Perturbative methods

Perturbative methods are proven to be very efficient for fast collisions, where interaction time between the incident projectile and the target electron is relatively short. We describe several perturbative approaches that were successfully applied to the systems considered in this work.

2.2.1 Born approximation

At very high energies, perturbation by the projectile is not very strong, therefore the scattering wave function can be expanded in fast convergent series. This procedure is known as the Born approximation. Simplest form of this approximation, the first Born approximation (FBA) involves replacing the total scattering wave function with the incident-channel wave function. The FBA approach is especially practical in treating hydrogen-like targets, where scattering amplitudes can be evaluated analytically making calculations fairly easy. However, because of the absence of coupling between channels, charge effects are lost in obtaining the scattering amplitudes. Therefore, projectiles with the same mass but opposite charges give the same result. The first application of the Born approximation to ion-atom collisions was performed by Brinkman and Kramers [9] without including the Coulomb interaction between the nuclei. Later, Bates and Dalgarno [11], Bates and Griffing [12] and Jackson and Schiff [14] employed this method to describe the charge-exchange processes in proton-hydrogen collisions including the heavy-particle interaction. In all these works, the Born calculations agreed well with experiment at impact energies above 25 keV. This approach was also applied to study differential ionisation of hydrogen by proton impact by Kuyatt and Jorgensen [90], where the calculations for double differential cross section and angular dependence of the ejected electrons were provided based on the Born approximation. Belkic *et al.* [26] reviewed the validity of the approach in a number of scattering problems. Outcomes of the work showed effectiveness of the method at high energies.

The application of the Born approximations in multi-electron systems is not straightforward. The charge-exchange processes in proton-helium collisions were studied by Belkić [39], where the FBA was corrected for the boundary condi-

tions. The helium atom was treated as a one-electron system and described by the Roothaan-Hartree-Fock and hydrogen-like wave functions. Good agreement with the experiment was obtained at energies from 50 keV to 50 MeV with the Roothaan-Hartree-Fock wave functions. Also, validity of the first Born approximation was studied by Popov *et al.* [91] for differential charge-transfer processes for the same system. The differential cross sections for transfer excitation and transfer ionisation were calculated and electron-electron correlations were found to be important in the initial helium state. Overall, it was concluded that the FBA is applicable for the collisions at incident proton energies above 500 keV and for sufficiently small scattering angles.

2.2.2 Distorted-wave Born approximation

Another commonly-used perturbative method based on the ideas of the Born approximation is the distorted-wave Born approximation (DWBA), where the unperturbed plane wave is replaced by a distorted wave. The purpose of the method is to include part of the interaction between the target nucleus and the electron in the wave functions, so-called distorted waves, describing initial or final channels. This also enables to achieve faster convergence of the perturbation series because of the weaker remaining perturbation. This method was applied to various many-body scattering problems including proton-helium collisions. A number of distorted-wave theories were discussed by Toshima *et al.* [92] and the DWBA results for electron capture in p -He collisions are compared with the existing experiments and other theoretical calculations. The four-body DWBA method was employed by Mancev *et al.* [93] and Jana *et al.* [44]. In the recent work of Rahmanian *et al.* [94] the three-body DWBA was applied. These works demonstrated that DWBA method is quite effective in describing the three-body and four-body systems at high energies.

2.2.3 Continuum-distorted-wave approaches

The perturbative models described above are valid at sufficiently high energies. At energies close to the intermediate energy region, distortion of the target wave functions by the projectile becomes important. One of the models that take this distortion into account successfully is the continuum-distorted-wave (CDW) approach. The approach was first developed by Cheshire [95] to study fast proton collisions with atomic hydrogen. Belkic and Gayet [96] employed this method to calculate the electron-capture cross sections for proton and alpha particle collisions with hydrogen. Later, it was extended to the ionisation problem [97]. A detailed review of the CDW approach including the description of its validity was reported by Belkic *et al.* [26] for electron-capture processes in various ion-atom collisions. After some developments, the CDW method was applied also to a multi-electron target by Belkić *et al.* [98], where proton-helium collisions were considered.

One of the widely used forms of the CDW method is the continuum-distorted-wave eikonal-initial-state (CDW-EIS) approach, where the distortion in the initial and final states are treated using the eikonal approximation and the continuum-distorted-wave approximation, respectively. This approach was developed by Crothers and McCann [99] to calculate the total cross section for ionisation of hydrogen by multiply-charged ions, a significant improvement was achieved in comparison with the existing theoretical models. Later, the method was applied to describe proton impact ionisation of the excited hydrogen atom by Fainstein *et al.* [100]. The CDW-EIS method was also applied to multi-electron targets including the helium atom. Fainstein *et al.* [101] presented the CDW-EIS calculations for collisions of bare ions with helium. Helium atom was treated as a one electron system. They observed some deviations in comparison

with the experiment, which was suggested to be because of neglecting the residual target and the projectile fields. A generalisation of the CDW-EIS approach to collisions of bare ions with multi-electron targets (He, Ne, Ar) was presented by Abufager *et al.* [102] employing the independent event model (IEM). The results of this generalised approach provided better agreement with the experiment in comparison with the previous CDW-EIS calculations. The fully differential cross section for single ionisation of helium by 75-keV protons was calculated by Ciappina *et al.* [81] within the CDW-EIS approach. The importance of the post-collisional interactions between the projectile and the residual target ion and the electron were also analysed.

2.3 Non-perturbative methods

When relative speed of the projectile is smaller or comparable with the classical speed of the orbiting target electron the perturbative models are not valid. At these energies, different non-perturbative methods are more suitable. Most of the non-perturbative approaches are based on solving the differential Schrödinger equation for the collisional system, either directly or using basis-expansion (close-coupling) methods.

2.3.1 Close-coupling approach

The close-coupling method is a sophisticated approach to studying ion-atom collisions. In this approach the total scattering wave function is expanded in terms of suitably chosen basis functions. The expansion is inserted into the Schrödinger equation to obtain a set of coupled equations for time-dependent coefficients. In solving the coupled equations, initial conditions should be taken into account. The coefficients are used to calculate the probabilities and cross

sections for transitions into included channels. Effectiveness of the close-coupling method depends on the choice of the basis functions and the completeness of the basis. The basis functions approximate both negative- and positive-energy eigenstates of the participating atoms. The negative-energy eigenfunctions can directly be used to approximate bound states, but to incorporate the continuum it needs to be discretised. Convergence of the final results depends on density of discretisation. One of the ways of discretising the continuum states is to superpose the continuum eigenfunctions in a given energy range, first suggested by Bethe and Salpeter [103]. The negative-energy states (unless they are taken to be the eigenstates) are not necessarily orthogonal to the continuum states and together are called *pseudostates*. However, using eigenstates is not a unique way of forming a basis. In order to increase convergence of the results, different basis sets were used. Examples of such bases include the Sturmian functions, the Gaussian functions, the Slater-type orbitals and others.

A number of close-coupling models with different basis functions and size of the basis were tested on proton-hydrogen collisions. The pioneering close-coupling approach was introduced by Bates [20]. Later, a two-state approximation was applied to calculate the electron-capture cross section into the ground state of hydrogen by McCarroll and Bates [21]. Good agreement was obtained in comparison with the available experiments. Following the success of these works the problem was studied actively by applying the close-coupling approach with more basis functions [23, 24]. This enabled to study excitation and capture cross sections into excited states. Cheshire *et al.* [23], Gallaher and Wilets [104], Shakeshaft [105] extended the close-coupling method by including positive-energy pseudostates to study the ionisation process too. Results of all these calculations agreed fairly well with the experimental data, however convergence of the results was not established because of the incompleteness of the employed

bases. There were more featured works with larger bases: 10-molecular-state calculations by Kimura and Thorson [106], one-centre calculations with a basis made of the Slater-orbitals by Ford *et al.* [107], calculations with 394-Gaussian pseudostates by Toshima [28] and calculations with the Sturmian pseudostates by Winter [34]. More complete bases with positive-energy eigenstates allowed to investigate all involved processes in proton-hydrogen collisions including ionisation, excitation and electron capture.

The close-coupling method was successfully applied to study many-electron systems too. The first rather simple two-state close-coupling calculations were performed by Green *et al.* [43] for electron capture into the ground state of hydrogen in proton-helium collisions. After more than two decades, more sophisticated calculations with a larger basis were performed by Winter [48]. He calculated the electron-capture and single-ionisation cross sections employing 50 Sturmian-basis functions, but electron exchange in the final transfer channels was neglected. Slim *et al.* [47] presented 51-state calculations with Gaussian basis functions, where electron exchange in the H-He⁺ channel was taken into account. Both calculations failed to achieve a sufficient level of convergence, however fairly good agreement with the experimental data was observed in both of the works.

2.3.2 Impact-parameter Faddeev approach

As we have seen above and will see later, most of the theoretical approaches are based on solving the Schrödinger equation for the scattering problem of interest. However, this is not a unique way of describing the collisions. An alternative approach to the system of three particles is based on the Faddeev integral equations, which include all interactions in a quantum-mechanical formulation. There are several methods of solving the Faddeev equations. One of them was

proposed by Avakov *et al.* [108, 109], where the three-particle equations were reduced to the two-particle Lippmann-Schwinger type equations using the Alt-Grassberger-Sandhas method. Further, the partial-wave expansion was used to bring them into one-dimensional integral equations. The integral equations were solved in the K-matrix Born approximation within the impact-parameter representation. The approach was applied to study electron-transfer processes in ion-atom collisions. Particularly, calculations were performed for the partial and total charge-exchange cross sections in hydrogen and helium collisions with fully stripped ions. Also, this method was successfully extended to proton collisions with alkali atoms [110]. Later, it was shown that the used charge-exchange amplitudes can be written as a product of two terms, the first of which is explicitly written by the internuclear Coulomb potential and the second one is independent of this interaction. This modification significantly simplified the numerical calculations. Collisions of fully stripped ions (H^+ , He^{2+} and Li^{3+}) with helium were studied with this new approach by Alt *et al.* [111]. Later, the Coulomb potentials used within the method were replaced by the full two-particle off-shell Coulomb T-matrices [112] and the method was applied to calculate the total and differential electron-transfer cross sections. For both processes, calculations were in very good agreement with the available experimental data.

2.3.3 Methods based on direct numerical solution

Direct solution of the time-dependent Schrödinger equation (TDSE) or the Hartree-Fock equation on a numerical lattice is another theoretical approach. This method was successfully applied by Maruhn-Rezwani *et al.* [113] to calculate charge-transfer probabilities in proton-hydrogen collisions. The TDSE was solved numerically in cylindrical coordinates and the calculated wave functions were used to obtain the probabilities for corresponding processes. The results

were in good agreement with the experimental data. Another successful attempt in solving the TDSE directly was presented by Bottcher [114]. They were able to calculate the total-charge cross sections for H^+ -H and C^{6+} -H collisions.

Kořakowska *et al.* [115] also used the direct solution method to study the excitation and charge-transfer processes in proton-hydrogen collisions, where the TDSE was solved on a three-dimensional Cartesian lattice. The results of the calculations agreed with the available experiments and other close-coupling calculations. Advantages of these kinds of lattice methods are in their application in wide range of projectile energy and possibility of visually observing collision dynamics in the three-dimensional lattice. However, direct solution of the equation of motion can be very time-consuming depending on the considered processes; therefore, a limited success was achieved to study collisions beyond simpler three-body systems.

Another direct method, which is based on solving the Lippman-Schwinger equations, was developed by Kadyrov *et al.* [116]. These three-dimensional equations can be solved using the partial-wave expansion in momentum-space, but employing the expansion method for some collisional systems requires including a large number of partial waves. This may complicate calculations or make them not feasible at all. For such scattering problems, the direct solution method was found to be very efficient and demonstrated in electron-hydrogen collisions. The calculations reproduced the partial-wave-expansion results showing the validity of the approach. Later this method was extended to ion-atom collisions [32]. The calculated electron-capture cross section for proton collisions with hydrogen was in good agreement with experiment on a wide range of impact energy. The method was also applied to calculate the total and differential cross sections for charge transfer in proton-hydrogen collisions and elastic scattering in antiproton-hydrogen collisions by Kadyrov *et al.* [35].

2.3.4 Convergent close-coupling approach

The convergent close-coupling (CCC) approach is one of the most powerful basis-expansion methods that allows studying all underlying processes in light- and heavy-ion collisions with atoms. It was first developed for electron-hydrogen collisions by Bray and Stelbovics [117, 118]. The method is based on solving the Lippmann-Schwinger equation in momentum space. The target Hamiltonian is diagonalised in a complete basis of the Laguerre functions. With increasing basis size the negative- and positive-energy pseudostates of the target respectively converge to eigenstates and provide sufficiently dense continuum discretisation. The advantage of the method is that convergence of the results is established by simply increasing number of the Laguerre functions. The method was extended to two-electron targets by Fursa and Bray [119], who reported differential and integrated cross section calculations for processes taking place in electron-helium scattering. Results for both the hydrogen and helium targets were in good agreement with the available experimental data. It was also successfully applied to electron collisions with targets such as hydrogen-like atoms [120], helium-like atoms [121] and the hydrogen molecule [122]. The method is considered to be one of the most successful approaches to studying electron-atom collisions.

Another significant achievement of the CCC approach came with the application to positron collisions with hydrogen by Kadyrov and Bray [29]. Studying positively-charged projectiles is more challenging than electrons because of the existence of capture channels (positronium-formation channels in the case of positron-atom collisions) that requires a two-centre treatment. Convergence of the two-centre expansion was studied within the s-wave model. Later, the problem of convergence was re-addressed using the full CCC formalism [31]. It was found that a two-centre expansion leads to a convergent result when complete set

of pseudostates are included on both centres. Ionisation of the atomic hydrogen by positron impact near threshold was studied by Kadyrov *et al.* [33] using the s-wave and full CCC methods. The two-centre CCC method was also applied to antiproton-positronium collisions. A significant enhancement between the anti-hydrogen formation in antiproton scattering on an excited and the ground states of positronium was found by Kadyrov *et al.* [123]. This was especially large at low energies, which have not been observed in previous experimental studies. The developed method was applied to calculate (anti)hydrogen formation in positronium collisions with (anti)protons at near threshold energies by Rawlins *et al.* [124]. Later, an overview of the theories applied to describe positron scattering on atoms and molecules in recent years, including the CCC method was presented by Kadyrov and Bray [125]. Recently Kadyrov *et al.* [126] reported the results of comprehensive quantum calculations for antihydrogen formation in antiproton-positronium collisions using the CCC method.

Heavy-particle collisions with atoms is another application area of the approach. The single-centre convergent close-coupling method was developed by Abdurakhmanov *et al.* [127] for antiproton-hydrogen collisions and later was extended to calculate differential ionisation cross section for the same system [128]. The results of both integrated and differential cross section calculations were in agreement with the experimental data. The method was extended to more complex targets too, such as noble gases and molecules. Abdurakhmanov *et al.* [129] developed a time-dependent CCC method to antiproton collisions with the hydrogen molecule (H_2). These single-centre approaches were developed for negatively-charged projectiles, which were not applicable to proton scattering problems unless energy of the protons is sufficiently high. The first two-centre fully quantum-mechanical (QM) CCC approach was developed by Abdurakhmanov *et al.* [130] to calculate electron-capture and ionisation cross

sections in proton-hydrogen collisions at lower and intermediate energies.

A new approach to ion-atom collisions within the CCC method based on constructing continuum states using wave-packets was developed by Abdurakhmanov *et al.* [131]. It was also applied to study differential ionisation in proton-hydrogen scattering [132]. The main idea of the wave-packet convergent close-coupling (WP-CCC) approach is discretising the continuum and constructing square-integrable continuum states by subdividing the continuum into bins and then integrating the continuum eigenfunction within each bin. This method will be explained in detail in Chapter 3. The wave-packet CCC approach was proven to be very advantageous to study differential cross sections, as it allows discretising the continuum as dense as needed and investigating ejected electrons with arbitrary energy in the breakup processes. The WP-CCC method was also applied to study proton scattering from excited states of hydrogen [133]. Recently, we applied this method to bare-ion scattering on hydrogen [134].

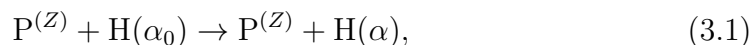
The applications of the CCC approach cover collisions of many-electron atoms with heavy particles too. Abdurakhmanov *et al.* [135] studied single-ionisation processes in antiproton-helium collisions using the QM-CCC method. Generally good agreement between calculations and experiments was observed. Also, the single-centre CCC approach was employed for energetic C^{6+} scattering on helium by Abdurakhmanov *et al.* [136]. The results were in reasonable agreement with the experiments since the single-centre approach is valid for positively charged projectiles at high energies. Later, the wave-packet continuum-discretisation treatment of helium was developed by Abdurakhmanov *et al.* [137]. It was applied to study single ionisation of helium by antiprotons and energetic protons. Quite recently, we have extended this approach to calculate total cross sections for electron capture and ionisation in proton-helium collisions at impact energies where the single-centre approach is not applicable [138].

Chapter 3

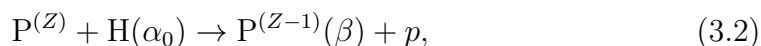
Convergent close-coupling approach to collisions of multiply-charged ions with hydrogen

3.1 Introduction

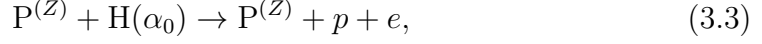
This chapter describes the wave-packet convergent close-coupling (WP-CCC) approach to scattering of singly- and multiply-charged ions on the ground and excited states of hydrogen. The method is developed for a fully-stripped projectile of charge Z , with $Z = 1$ corresponding to proton. We assume that the electron of the target is initially in the α_0 channel of the atom. With a sufficiently large basis, constructed from bound and continuum states, and taking into account coupling between channels we investigate all underlying processes including excitation



electron capture



and ionisation



where $P^{(Z)}$ is a fully-stripped projectile ion of nuclear charge Z , $P^{(Z-1)}$ is a hydrogen-like ion of charge $(Z - 1)$. For protons we use the symbol p . Indices α and β denote the full set of quantum numbers representing states in the $P^{(Z)}$ -H and $P^{(Z-1)}$ - p channels, respectively.

In our approach, a semiclassical treatment of the three-body system (the projectile, the target nucleus and the electron) is employed, where the projectile motion relative to the target is treated classically and target electron is treated fully quantum-mechanically. The target nucleus is located at the origin and we assume that the projectile is moving along a classical trajectory $\mathbf{R} \equiv \mathbf{R}(t) = \mathbf{b} + \mathbf{v}t$, where \mathbf{b} is the impact parameter vector and \mathbf{v} is the initial velocity of the projectile relative to the target. The vector \mathbf{b} is defined to be perpendicular to the direction of the moving projectile, that is $\mathbf{b} \cdot \mathbf{v} = 0$ (see Fig. 3.1).

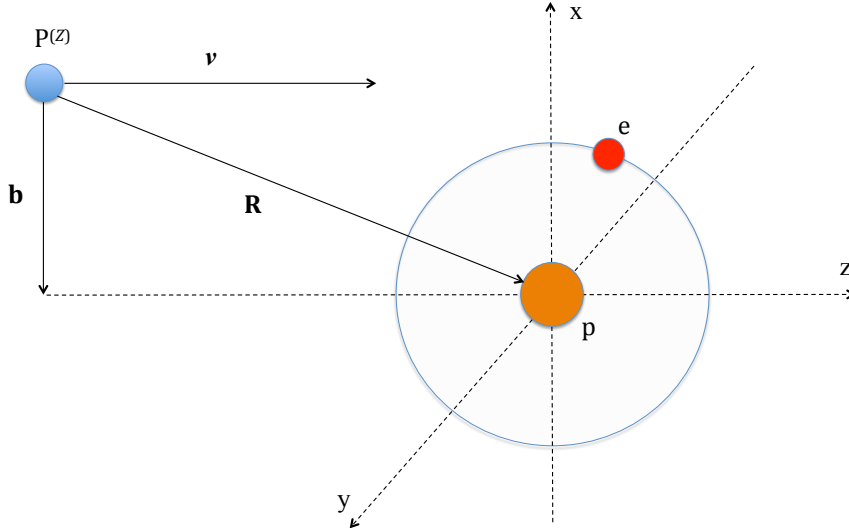


Figure 3.1: An illustration of collisions of multiply-charged ions with hydrogen in the coordinate system, with the origin set at the target nucleus.

In the stationary formulation, this three-body system is described by the

total scattering wave function, which satisfies the three-body time-independent Schrödinger equation (SE). Interactions between the particles are given by the long-range Coulomb potential. The scattering wave function is expanded within the two-centre approach in terms of the basis made of target- and projectile-centred eigenstates and pseudostates. Then, inserting this expansion into the SE leads to a set of coupled differential equations for the expansion coefficients. The obtained system of equations is solved to find transition amplitudes, which are used to calculate cross sections for elastic scattering, electron capture and ionisation, as well as differential ionisation cross sections.

Throughout the work, the indices P and T denote the projectile and the target, respectively. Unless otherwise specified, hereafter we use atomic units. In this chapter, the projectile is a multiply-charged ion and the target is hydrogen.

3.2 The Schrödinger equation for scattering of multiply-charged ions on hydrogen

The total scattering wave function Ψ , describing collisions of multiply-charged ions with atomic hydrogen, satisfies the exact three-body time-independent Schrödinger equation

$$(H - E)\Psi = 0, \quad (3.4)$$

where H is the 3-body Hamiltonian, E is the total energy of the system

$$E = \frac{k_\alpha^2}{2\mu_1} + \epsilon_\alpha = \frac{k_\beta^2}{2\mu_2} + \epsilon_\beta \quad (3.5)$$

where, \mathbf{k}_α is the momentum of the projectile relative to the hydrogen atom in the α channel, $\mu_1 = m_P m_T / (m_P + m_T)$ is the reduced mass of this system with m_P and m_T being masses of the projectile and the target and ϵ_α is the eigenenergy of the state α , \mathbf{k}_β is the momentum of the formed hydrogen-like atom relative

to the residual proton in the β channel, $\mu_2 = (m_P + 1)(m_T - 1)/(m_P + m_T)$ is the reduced mass and ϵ_β is the eigenenergy of the state β of the hydrogen-like atom.

The total Hamiltonian H of the scattering system can be represented in two equivalent forms as

$$H = K_\sigma + H_T + V_P, \quad (3.6)$$

$$H = K_\rho + H_P + V_T, \quad (3.7)$$

where

$$K_\sigma = -\frac{\nabla_\sigma^2}{2\mu_1} \quad \text{and} \quad K_\rho = -\frac{\nabla_\rho^2}{2\mu_2} \quad (3.8)$$

are the kinetic energy operators,

$$H_T = -\frac{\nabla_{\mathbf{r}_1}^2}{2} - \frac{1}{r_1} \quad \text{and} \quad H_P = -\frac{\nabla_{\mathbf{r}_2}^2}{2} - \frac{Z}{r_2} \quad (3.9)$$

are the target and projectile Hamiltonians,

$$V_P = \frac{Z}{R} - \frac{Z}{r_2} \quad \text{and} \quad V_T = \frac{Z}{R} - \frac{1}{r_1} \quad (3.10)$$

are the interactions between the projectile and the target and between the hydrogenlike ion and the target nucleus, respectively.

Here \mathbf{R} is the position vector of the incident projectile, \mathbf{r}_1 , \mathbf{r}_2 and \mathbf{r} are the position vectors of the electron relative to the target nucleus, the projectile and the midpoint of the nuclei respectively, $\boldsymbol{\sigma}$ is the position vector of the projectile relative to centre of mass of the hydrogen atom and $\boldsymbol{\rho}$ is the position vector of the formed hydrogen-like atom relative to the residual proton (see Fig. 3.2).

There are various ways of expanding the total scattering wave function. In our approach, it is expanded in terms of N target-centred and M projectile-

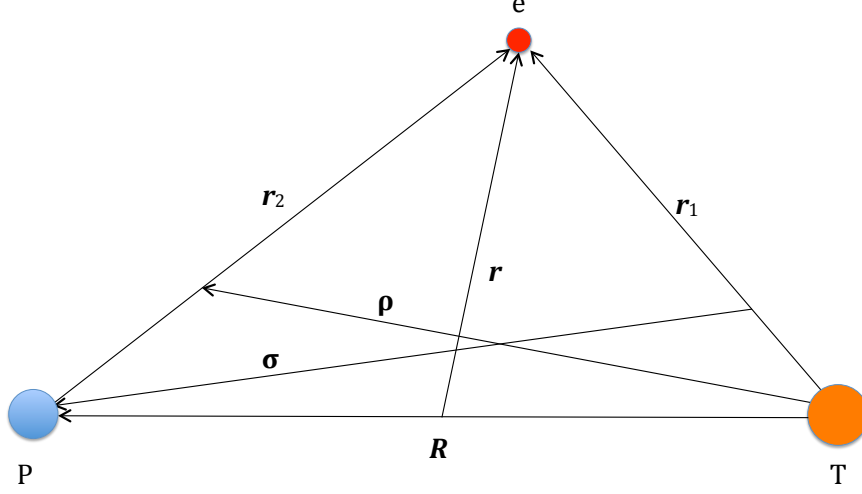


Figure 3.2: The Jacobi coordinates for the scattering system.

centred states as

$$\Psi = \sum_{\alpha=1}^N a_{\alpha}(t, \mathbf{b}) \psi_{\alpha}^{\text{H}}(\mathbf{r}_1) e^{i\mathbf{k}_{\alpha}\sigma} + \sum_{\beta=1}^M b_{\beta}(t, \mathbf{b}) \psi_{\beta}^{(Z)}(\mathbf{r}_2) e^{i\mathbf{k}_{\beta}\rho}, \quad (3.11)$$

where ψ_{α}^{H} and $\psi_{\beta}^{(Z)}$ are the corresponding wave functions for the atomic hydrogen and the hydrogen-like atom of nuclear charge Z , respectively. Their detailed definitions will be given later. The exponential argument consists of a dot product of two vectors. Separation of the electronic and nuclear motions is explained by the Born-Oppenheimer approximation [15]. The expansion coefficients $a_{\alpha}(t, \mathbf{b})$ and $b_{\alpha}(t, \mathbf{b})$ at $t \rightarrow +\infty$ represent the transition amplitudes into the corresponding target and projectile states.

We insert this expansion of the scattering wave function into the Schrödinger equation (3.4), and taking two equivalent forms of the total Hamiltonian in

Eqs. (3.6) and (3.7) into account, obtain

$$\begin{aligned}
 & \sum_{\alpha=1}^N (K_{\sigma} + H_T + V_P) a_{\alpha}(t, \mathbf{b}) \psi_{\alpha}^{\text{H}}(\mathbf{r}_1) e^{i\mathbf{k}_{\alpha}\boldsymbol{\sigma}} \\
 & + \sum_{\beta=1}^M (K_{\rho} + H_P + V_T) b_{\beta}(t, \mathbf{b}) \psi_{\beta}^{(Z)}(\mathbf{r}_2) e^{i\mathbf{k}_{\beta}\boldsymbol{\rho}} \\
 & = E \left(\sum_{\alpha=1}^N a_{\alpha}(t, \mathbf{b}) \psi_{\alpha}^{\text{H}}(\mathbf{r}_1) e^{i\mathbf{k}_{\alpha}\boldsymbol{\sigma}} + \sum_{\beta=1}^M b_{\beta}(t, \mathbf{b}) \psi_{\beta}^{(Z)}(\mathbf{r}_2) e^{i\mathbf{k}_{\beta}\boldsymbol{\rho}} \right). \quad (3.12)
 \end{aligned}$$

The action of the operator K_{σ} (K_{ρ}) is independent of the position vector \mathbf{r}_1 (\mathbf{r}_2) therefore we have

$$K_{\sigma} (a_{\alpha}(t, \mathbf{b}) \psi_{\alpha}^{\text{H}}(\mathbf{r}_1) e^{i\mathbf{k}_{\alpha}\boldsymbol{\sigma}}) = -\frac{\nabla_{\boldsymbol{\sigma}}^2}{2\mu_1} (a_{\alpha}(t, \mathbf{b}) e^{i\mathbf{k}_{\alpha}\boldsymbol{\sigma}}) \psi_{\alpha}^{\text{H}}(\mathbf{r}_1), \quad (3.13)$$

$$K_{\rho} (b_{\beta}(t, \mathbf{b}) \psi_{\beta}^{(Z)}(\mathbf{r}_2) e^{i\mathbf{k}_{\beta}\boldsymbol{\rho}}) = -\frac{\nabla_{\boldsymbol{\rho}}^2}{2\mu_2} (b_{\beta}(t, \mathbf{b}) e^{i\mathbf{k}_{\beta}\boldsymbol{\rho}}) \psi_{\beta}^{(Z)}(\mathbf{r}_2), \quad (3.14)$$

where the Laplacians of the products can be expanded as

$$\begin{aligned}
 \nabla_{\boldsymbol{\sigma}}^2 (a_{\alpha}(t, \mathbf{b}) e^{i\mathbf{k}_{\alpha}\boldsymbol{\sigma}}) & = \nabla_{\boldsymbol{\sigma}}^2 (a_{\alpha}(t, \mathbf{b})) e^{i\mathbf{k}_{\alpha}\boldsymbol{\sigma}} + 2\nabla_{\boldsymbol{\sigma}} (a_{\alpha}(t, \mathbf{b})) \nabla_{\boldsymbol{\sigma}} e^{i\mathbf{k}_{\alpha}\boldsymbol{\sigma}} \\
 & + a_{\alpha}(t, \mathbf{b}) \nabla_{\boldsymbol{\sigma}}^2 e^{i\mathbf{k}_{\alpha}\boldsymbol{\sigma}}, \quad (3.15)
 \end{aligned}$$

$$\begin{aligned}
 \nabla_{\boldsymbol{\rho}}^2 (b_{\beta}(t, \mathbf{b}) e^{i\mathbf{k}_{\beta}\boldsymbol{\rho}}) & = \nabla_{\boldsymbol{\rho}}^2 (b_{\beta}(t, \mathbf{b})) e^{i\mathbf{k}_{\beta}\boldsymbol{\rho}} + 2\nabla_{\boldsymbol{\rho}} (b_{\beta}(t, \mathbf{b})) \nabla_{\boldsymbol{\rho}} e^{i\mathbf{k}_{\beta}\boldsymbol{\rho}} \\
 & + b_{\beta}(t, \mathbf{b}) \nabla_{\boldsymbol{\rho}}^2 e^{i\mathbf{k}_{\beta}\boldsymbol{\rho}}. \quad (3.16)
 \end{aligned}$$

Functions $a_{\alpha}(t, \mathbf{b})$ and $b_{\beta}(t, \mathbf{b})$ vary slowly with $\boldsymbol{\sigma}$ and $\boldsymbol{\rho}$, therefore terms containing $\nabla_{\boldsymbol{\sigma}}^2 a_{\alpha}$ and $\nabla_{\boldsymbol{\rho}}^2 a_{\beta}$ can be neglected (see [16]) in the last two equations. We take into account the actions of the gradient and Laplacian operators on the plane waves

$$\nabla_{\boldsymbol{\sigma}} e^{i\mathbf{k}_{\alpha}\boldsymbol{\sigma}} = i\mathbf{k}_{\alpha} e^{i\mathbf{k}_{\alpha}\boldsymbol{\sigma}}, \quad \nabla_{\boldsymbol{\sigma}}^2 e^{i\mathbf{k}_{\alpha}\boldsymbol{\sigma}} = -k_{\alpha}^2 e^{i\mathbf{k}_{\alpha}\boldsymbol{\sigma}}, \quad (3.17)$$

$$\nabla_{\boldsymbol{\rho}} e^{i\mathbf{k}_{\beta}\boldsymbol{\rho}} = i\mathbf{k}_{\beta} e^{i\mathbf{k}_{\beta}\boldsymbol{\rho}}, \quad \nabla_{\boldsymbol{\rho}}^2 e^{i\mathbf{k}_{\beta}\boldsymbol{\rho}} = -k_{\beta}^2 e^{i\mathbf{k}_{\beta}\boldsymbol{\rho}}. \quad (3.18)$$

In addition, we write

$$\frac{\mathbf{k}_{\alpha}}{\mu_1} \nabla_{\boldsymbol{\sigma}} = \frac{\partial}{\partial t}, \quad \frac{\mathbf{k}_{\beta}}{\mu_2} \nabla_{\boldsymbol{\rho}} = \frac{\partial}{\partial t}. \quad (3.19)$$

With these, after simple algebra Eq. (3.12) is rewritten in the following form

$$\begin{aligned}
 & \sum_{\alpha=1}^N \left(\left(-\frac{\partial}{\partial t} + \frac{k_{\alpha}^2}{2\mu_1} \right) a_{\alpha}(t, \mathbf{b}) \right) \psi_{\alpha}^{\text{H}}(\mathbf{r}_1) e^{i\mathbf{k}_{\alpha}\boldsymbol{\sigma}} \\
 & + \sum_{\beta=1}^M \left(\left(-\frac{\partial}{\partial t} + \frac{k_{\beta}^2}{2\mu_2} \right) b_{\beta}(t, \mathbf{b}) \right) \psi_{\beta}^{(Z)}(\mathbf{r}_2) e^{i\mathbf{k}_{\beta}\boldsymbol{\rho}} \\
 & + \sum_{\alpha=1}^N (H_T + V_P) a_{\alpha}(t, \mathbf{b}) \psi_{\alpha}^{\text{H}}(\mathbf{r}_1) e^{i\mathbf{k}_{\alpha}\boldsymbol{\sigma}} + \sum_{\beta=1}^M (H_P + V_T) b_{\beta}(t, \mathbf{b}) \psi_{\beta}^{(Z)}(\mathbf{r}_2) e^{i\mathbf{k}_{\beta}\boldsymbol{\rho}} \\
 & = \sum_{\alpha=1}^N \left(\frac{k_{\alpha}^2}{2\mu_1} + \epsilon_{\alpha} \right) a_{\alpha}(t, \mathbf{b}) \psi_{\alpha}^{\text{H}}(\mathbf{r}_1) e^{i\mathbf{k}_{\alpha}\boldsymbol{\sigma}} + \sum_{\beta=1}^M \left(\frac{k_{\beta}^2}{2\mu_2} + \epsilon_{\beta} \right) b_{\beta}(t, \mathbf{b}) \psi_{\beta}^{(Z)}(\mathbf{r}_2) e^{i\mathbf{k}_{\beta}\boldsymbol{\rho}},
 \end{aligned} \tag{3.20}$$

where on the right-hand side we replaced the total energy E with the explicit forms given in Eq. (3.5).

After deleting similar terms from both sides, the equation is reduced to

$$\begin{aligned}
 & \sum_{\alpha=1}^N \dot{a}_{\alpha}(t, \mathbf{b}) \psi_{\alpha}^{\text{H}}(\mathbf{r}_1) e^{i\mathbf{k}_{\alpha}\boldsymbol{\sigma}} + \sum_{\beta=1}^M \dot{b}_{\beta}(t, \mathbf{b}) \psi_{\beta}^{(Z)}(\mathbf{r}_2) e^{i\mathbf{k}_{\beta}\boldsymbol{\rho}} \\
 & = \sum_{\alpha=1}^N (H_T - \epsilon_{\alpha} + V_P) a_{\alpha}(t, \mathbf{b}) \psi_{\alpha}^{\text{H}}(\mathbf{r}_1) e^{i\mathbf{k}_{\alpha}\boldsymbol{\sigma}} \\
 & \quad + \sum_{\beta=1}^M (H_P - \epsilon_{\beta} + V_T) b_{\beta}(t, \mathbf{b}) \psi_{\beta}^{(Z)}(\mathbf{r}_2) e^{i\mathbf{k}_{\beta}\boldsymbol{\rho}},
 \end{aligned} \tag{3.21}$$

where a dot over the coefficients stands for the derivative with respect to time. Now we successively multiply all terms of the resulting equation by $\psi_{\alpha'}^{\text{H}*}(\mathbf{r}_1) e^{-i\mathbf{k}_{\alpha'}\boldsymbol{\sigma}}$ for $\alpha' = 1, \dots, N$ and $\psi_{\beta'}^{(Z)*}(\mathbf{r}_2) e^{-i\mathbf{k}_{\beta'}\boldsymbol{\rho}}$ for $\beta' = 1, \dots, M$. Then, by integrating over the variables \mathbf{r}_1 and \mathbf{r}_2 we obtain a set of coupled first-order differential equations for the time-dependent coefficients:

$$\left\{ \begin{aligned}
 & i\dot{a}_{\alpha'} + i \sum_{\beta=1}^M \dot{b}_{\beta} K_{\alpha'\beta}^T = \sum_{\alpha=1}^N a_{\alpha} D_{\alpha'\alpha}^T + \sum_{\beta=1}^M b_{\beta} Q_{\alpha'\beta}^T, \\
 & i \sum_{\alpha=1}^N \dot{a}_{\alpha} K_{\beta'\alpha}^P + i\dot{b}_{\beta'} = \sum_{\alpha=1}^N a_{\alpha} Q_{\beta'\alpha}^P + \sum_{\beta=1}^M b_{\beta} D_{\beta'\beta}^P, \\
 & \alpha' = 1, 2, \dots, N, \quad \beta' = 1, 2, \dots, M.
 \end{aligned} \right. \tag{3.22}$$

Here, $D_{\alpha'\alpha}^T$ and $D_{\beta'\beta}^P$ are the direct matrix elements of the forms

$$D_{\alpha'\alpha}^T = \int d\mathbf{r}_1 \psi_{\alpha'}^{\text{H}*}(\mathbf{r}_1) e^{i(\mathbf{k}_\alpha - \mathbf{k}_{\alpha'})\boldsymbol{\sigma}} (H_T - \epsilon_\alpha + V_P) \psi_\alpha^{\text{H}}(\mathbf{r}_1), \quad (3.23)$$

$$D_{\beta'\beta}^P = \int d\mathbf{r}_2 \psi_{\beta'}^{(Z)*}(\mathbf{r}_2) e^{i(\mathbf{k}_\beta - \mathbf{k}_{\beta'})\boldsymbol{\rho}} (H_P - \epsilon_\beta + V_T) \psi_\beta^{(Z)}(\mathbf{r}_2) \quad (3.24)$$

and for the rearrangement matrix elements we have

$$K_{\beta'\alpha}^P = \int d\mathbf{r}_1 \psi_{\beta'}^{(Z)*}(\mathbf{r}_1 - \mathbf{R}) e^{i(\mathbf{k}_\alpha \boldsymbol{\sigma} - \mathbf{k}_{\beta'} \boldsymbol{\rho})} \psi_\alpha^{\text{H}}(\mathbf{r}_1), \quad (3.25)$$

$$K_{\alpha'\beta}^T = \int d\mathbf{r}_1 \psi_{\alpha'}^{\text{H}*}(\mathbf{r}_1) e^{i(\mathbf{k}_\beta \boldsymbol{\rho} - \mathbf{k}_{\alpha'} \boldsymbol{\sigma})} \psi_\beta^{(Z)}(\mathbf{r}_1 - \mathbf{R}), \quad (3.26)$$

$$Q_{\beta'\alpha}^P = \int d\mathbf{r}_1 \psi_{\beta'}^{(Z)*}(\mathbf{r}_1 - \mathbf{R}) e^{i(\mathbf{k}_\alpha \boldsymbol{\sigma} - \mathbf{k}_{\beta'} \boldsymbol{\rho})} (H_T - \epsilon_\alpha + V_P) \psi_\alpha^{\text{H}}(\mathbf{r}_1), \quad (3.27)$$

$$Q_{\alpha'\beta}^T = \int d\mathbf{r}_1 \psi_{\alpha'}^{\text{H}*}(\mathbf{r}_1) e^{i(\mathbf{k}_\beta \boldsymbol{\rho} - \mathbf{k}_{\alpha'} \boldsymbol{\sigma})} (H_P - \epsilon_\beta + V_T) \psi_\beta^{(Z)}(\mathbf{r}_1 - \mathbf{R}). \quad (3.28)$$

In the definition of the matrix elements we used the relation between the position vectors $\mathbf{r}_2 = \mathbf{r}_1 - \mathbf{R}$.

The system of equations (3.22) is solved subject to the following initial boundary condition

$$\begin{aligned} a_\alpha(-\infty, \mathbf{b}) &= \delta_{\alpha, \alpha_0}, \quad \alpha = 1, \dots, N, \\ b_\beta(-\infty, \mathbf{b}) &= 0, \quad \beta = 1, \dots, M, \end{aligned} \quad (3.29)$$

which assumes that the electron of the target atom is initially in the α_0 state that can be the ground or an excited state of hydrogen.

In the single-centre approach, the total scattering wave function in Eq. (3.11) is written simpler as

$$\Psi = \sum_{\alpha=1}^N a_\alpha(t, \mathbf{b}) \psi_\alpha^{\text{H}}(\mathbf{r}_1) e^{i\mathbf{k}_\alpha \boldsymbol{\sigma}}, \quad (3.30)$$

and the system of differential equations (3.22) reduces to

$$i\dot{a}_{\alpha'} = \sum_{\alpha=1}^N a_\alpha D_{\alpha'\alpha}^T, \quad \alpha' = 1, 2, \dots, N, \quad (3.31)$$

with the initial boundary condition

$$a_\alpha(-\infty, \mathbf{b}) = \delta_{\alpha, \alpha_0}, \quad \alpha = 1, \dots, N. \quad (3.32)$$

3.3 Hydrogenic wave functions

Here we describe the wave functions of a hydrogen-like atom of arbitrary nuclear charge Z used in the expansion of the total scattering wave function (3.11). There are two ways of generating the continuum states within the CCC approach: Laguerre-basis [117] and wave-packet [131] methods. In this work, the continuum states are constructed using the wave-packet continuum-discretisation method.

Each state β of the hydrogen-like atom is described by three quantum numbers $\{n, l, m\}$, the principal, orbital and magnetic quantum numbers, respectively. For negative-energy states (bound states), the wave functions are separated into radial and angular parts as

$$\psi_{\beta}^{(Z)}(\mathbf{r}) = \phi_{nl}^{(Z)}(r)Y_{lm}(\hat{\mathbf{r}}) \quad (3.33)$$

and for positive-energy states (continuum states) as

$$\psi_{\beta}^{(Z)}(\mathbf{r}) = \sqrt{\frac{2}{\pi}} \sum_{lm} i^l \exp(-i\eta_l) R_{\kappa l}^{(Z)}(r) Y_{lm}^*(\hat{\mathbf{\kappa}}) Y_{lm}(\hat{\mathbf{r}}), \quad (3.34)$$

where Y_{lm} are the spherical harmonics, $\kappa = \sqrt{2\varepsilon}$ is the momentum of the continuum state, with ε being the energy of the state and η_l is the Coulomb phase shift.

For bound states, the orthonormal radial wave functions can be written analytically as

$$\phi_{nl}^{(Z)}(r) = \sqrt{Z \frac{(n-l-1)!}{(n+l)!}} e^{-Zr/n} \frac{(2Zr)^{l+1}}{n^{2+l}} L_{n-l-1}^{2l+1} \left(\frac{2Zr}{n} \right), \quad (3.35)$$

where L_{n-l-1}^{2l+1} denotes an associated Laguerre polynomial. Corresponding energies of the bound states for each principal number n are found as

$$\epsilon_n = -\frac{Z^2}{2n^2}, \quad n = 1, 2, \dots \quad (3.36)$$

For a positive energy $\varepsilon = \kappa^2/2$, the corresponding continuum radial wave function is given as

$$R_{\kappa l}^{(Z)}(r) = \frac{1}{\sqrt{2\pi}} (2\kappa r)^{l+1} \exp\left(\frac{Z\pi}{2\kappa}\right) \frac{|\Gamma(l+1 - iZ/\kappa)|}{(2l+1)!} \times e^{-i\kappa r} {}_1F_1\left(\frac{iZ}{\kappa} + l + 1, 2l + 2, 2irk\right), \quad (3.37)$$

where ${}_1F_1$ is a confluent hypergeometric function. These continuum functions are not square-integrable, and therefore not suitable for the close-coupling approach. To overcome this problem we construct wave packets to generate continuum states as

$$\phi_{il}^{(Z)}(r) = \frac{1}{\sqrt{w_i}} \int_{\kappa_{i-1}}^{\kappa_i} d\kappa R_{\kappa l}^{(Z)}(r), \quad (3.38)$$

where

$$w_i = \kappa_i - \kappa_{i-1}, \quad (3.39)$$

and $\kappa_i = \sqrt{2\mathcal{E}_i}$. Non-overlapping intervals $[\mathcal{E}_{i-1}, \mathcal{E}_i]_{i=1}^{N_c}$ divide the interval $[0, E_{\max}]$ into N_c subintervals, where E_{\max} is the maximum allowed energy of the ejected electron. The intervals $[\mathcal{E}_{i-1}, \mathcal{E}_i]_{i=1}^{N_c}$ are called discretisation bins, with N_c as the number of bins.

The wave packets constructed in this way are orthonormal

$$\langle \phi_{il}^{(Z)} | \phi_{jl}^{(Z)} \rangle = \delta_{ij}, \quad (3.40)$$

and satisfy the following relation

$$\langle \phi_{il}^{(Z)} | H_T | \phi_{jl}^{(Z)} \rangle = \epsilon_i \delta_{ij}, \quad (3.41)$$

where ϵ_i is the corresponding energy of the bin state defined as

$$\epsilon_i = \frac{\mathcal{E}_{i-1} + \sqrt{\mathcal{E}_{i-1}\mathcal{E}_i} + \mathcal{E}_i}{3}. \quad (3.42)$$

Then, continuum pseudostates are obtained as

$$\psi_{ilm}^{(Z)}(\mathbf{r}) = \phi_{il}^{(Z)}(r)Y_{lm}(\hat{\mathbf{r}}). \quad (3.43)$$

These continuum pseudostates together with the eigenstates form a basis to describe the hydrogen-like atom of charge Z . For the wave functions of hydrogen (i.e., when $Z = 1$) we use the notation ψ^{H} instead of $\psi^{(1)}$.

3.4 Matrix elements

Next, using the definitions of the wave functions we simplify the matrix elements (3.23)-(3.28) to the form convenient for calculations. As described in Appendix A, the exponential factors entering in the direct matrix elements in Eqs. (3.23) and (3.24) can be written as

$$(\mathbf{k}_\alpha - \mathbf{k}_{\alpha'})\boldsymbol{\sigma} = \mathbf{q}_\perp \mathbf{b} + (\varepsilon_{\alpha'} - \varepsilon_\alpha)t, \quad (3.44)$$

$$(\mathbf{k}_\beta - \mathbf{k}_{\beta'})\boldsymbol{\rho} = \mathbf{q}_\perp \mathbf{b} + (\varepsilon_{\beta'} - \varepsilon_\beta)t. \quad (3.45)$$

The same in the rearrangement matrix elements (3.25)-(3.28) are written as

$$\mathbf{k}_\alpha \boldsymbol{\sigma} - \mathbf{k}_{\beta'} \boldsymbol{\rho} = \mathbf{q}_\perp \mathbf{b} + \mathbf{q}_{\alpha,\beta'\parallel} vt - \mathbf{v} \mathbf{r}_1, \quad (3.46)$$

$$\mathbf{k}_\beta \boldsymbol{\rho} - \mathbf{k}_{\alpha'} \boldsymbol{\sigma} = \mathbf{q}_\perp \mathbf{b} + \mathbf{q}_{\beta,\alpha'\parallel} vt + \mathbf{v} \mathbf{r}_1, \quad (3.47)$$

where \mathbf{q}_\perp is the perpendicular component of the momentum transfer which is the same in all transitions. Parallel components $\mathbf{q}_{\alpha,\beta'\parallel}$ and $\mathbf{q}_{\beta,\alpha'\parallel}$ depend on transition states and given as

$$\mathbf{q}_{\alpha,\beta'\parallel} = \frac{v}{2} + \frac{\varepsilon_{\beta'} - \varepsilon_\alpha}{v}, \quad \mathbf{q}_{\beta,\alpha'\parallel} = -\frac{v}{2} + \frac{\varepsilon_{\alpha'} - \varepsilon_\beta}{v}. \quad (3.48)$$

As $e^{\mathbf{q}_\perp \mathbf{b}}$ is the same in all matrix elements, it can be factored out and canceled when the matrix elements are inserted into Eq. (3.22). Therefore, we omit them

but keep the original notations. However, in calculating differential cross sections we take these factors into account. With these relations, the matrix elements can be rewritten in the following forms

$$D_{\alpha'\alpha}^T = e^{i(\epsilon_{\alpha'} - \epsilon_{\alpha})t} \tilde{D}_{\alpha'\alpha}^T, \quad (3.49)$$

$$D_{\beta'\beta}^P = e^{i(\epsilon_{\beta'} - \epsilon_{\beta})t} \tilde{D}_{\beta'\beta}^P, \quad (3.50)$$

$$K_{\beta'\alpha}^P = e^{i(\epsilon_{\beta'} - \epsilon_{\alpha})t} e^{iv^2 t/2} \tilde{K}_{\beta'\alpha}^P, \quad (3.51)$$

$$K_{\alpha'\beta}^T = e^{i(\epsilon_{\alpha'} - \epsilon_{\beta})t} e^{-iv^2 t/2} \tilde{K}_{\alpha'\beta}^T, \quad (3.52)$$

$$Q_{\beta'\alpha}^P = e^{i(\epsilon_{\beta'} - \epsilon_{\alpha})t} e^{iv^2 t/2} \tilde{Q}_{\beta'\alpha}^P, \quad (3.53)$$

$$Q_{\alpha'\beta}^T = e^{i(\epsilon_{\alpha'} - \epsilon_{\beta})t} e^{-iv^2 t/2} \tilde{Q}_{\alpha'\beta}^T, \quad (3.54)$$

where

$$\tilde{D}_{\alpha'\alpha}^T = \int d\mathbf{r}_1 \psi_{\alpha'}^{\text{H}*}(\mathbf{r}_1) (H_T - \epsilon_{\alpha} + V_P) \psi_{\alpha}^{\text{H}}(\mathbf{r}_1), \quad (3.55)$$

$$\tilde{D}_{\beta'\beta}^P = \int d\mathbf{r}_2 \psi_{\beta'}^{(Z)*}(\mathbf{r}_2) (H_P - \epsilon_{\beta} + V_T) \psi_{\beta}^{(Z)}(\mathbf{r}_2), \quad (3.56)$$

$$\tilde{K}_{\beta'\alpha}^P = \int d\mathbf{r}_1 \psi_{\beta'}^{(Z)*}(\mathbf{r}_1 - \mathbf{R}) e^{-iv\mathbf{r}_1} \psi_{\alpha}^{\text{H}}(\mathbf{r}_1), \quad (3.57)$$

$$\tilde{K}_{\alpha'\beta}^T = \int d\mathbf{r}_1 \psi_{\alpha'}^{\text{H}*}(\mathbf{r}_1) e^{iv\mathbf{r}_1} \psi_{\beta}^{(Z)}(\mathbf{r}_1 - \mathbf{R}), \quad (3.58)$$

$$\tilde{Q}_{\beta'\alpha}^P = \int d\mathbf{r}_1 \psi_{\beta'}^{(Z)*}(\mathbf{r}_1 - \mathbf{R}) e^{-iv\mathbf{r}_1} (H_T - \epsilon_{\alpha} + V_P) \psi_{\alpha}^{\text{H}}(\mathbf{r}_1), \quad (3.59)$$

$$\tilde{Q}_{\alpha'\beta}^T = \int d\mathbf{r}_1 \psi_{\alpha'}^{\text{H}*}(\mathbf{r}_1) e^{iv\mathbf{r}_1} (H_P - \epsilon_{\beta} + V_T) \psi_{\beta}^{(Z)}(\mathbf{r}_1 - \mathbf{R}). \quad (3.60)$$

According to the definition of the wave functions both for eigenstates and continuum states, we have

$$\langle \psi_{\alpha'}^{\text{H}} | H_T - \epsilon_{\alpha} | \psi_{\alpha}^{\text{H}} \rangle = 0, \quad \alpha, \alpha' = 1, \dots, N, \quad (3.61)$$

$$\langle \psi_{\beta'}^{(Z)} | H_P - \epsilon_{\beta} | \psi_{\beta}^{(Z)} \rangle = 0, \quad \beta, \beta' = 1, \dots, M. \quad (3.62)$$

Therefore, the direct matrix elements can be further simplified as

$$\tilde{D}_{\alpha'\alpha}^T = \int d\mathbf{r}_1 \psi_{\alpha'}^{\text{H}*}(\mathbf{r}_1) V_P \psi_{\alpha}^{\text{H}}(\mathbf{r}_1), \quad (3.63)$$

$$\tilde{D}_{\beta'\beta}^P = \int d\mathbf{r}_2 \psi_{\beta'}^{(\text{Z})*}(\mathbf{r}_2) V_T \psi_{\beta}^{(\text{Z})}(\mathbf{r}_2). \quad (3.64)$$

However, in the rearrangement matrix elements \tilde{Q}^P and \tilde{Q}^T , the terms containing $(H_T - \epsilon_{\alpha})\psi_{\alpha}^{\text{H}}$ and $(H_P - \epsilon_{\beta})\psi_{\beta}^{(\text{Z})}$ remain for the continuum states (wave packets representing the continuum). For a function

$$f(\mathbf{r}) = \frac{1}{\sqrt{w}} \int_{\kappa_1}^{\kappa_2} d\kappa g_{\kappa}(\mathbf{r}), \quad (3.65)$$

where g_{κ} is an eigenfunction of an operator h , i.e.,

$$h g_{\kappa}(\mathbf{r}) = \epsilon_{\kappa} g_{\kappa}(\mathbf{r}) = \frac{\kappa^2}{2} g_{\kappa}(\mathbf{r}), \quad (3.66)$$

we have

$$(h - \varepsilon) f(\mathbf{r}) = \frac{1}{\sqrt{w}} \int_{\kappa_{i-1}}^{\kappa_i} d\kappa \left(\frac{\kappa^2}{2} - \varepsilon \right) g_{\kappa}(\mathbf{r}). \quad (3.67)$$

Applying this to the positive-energy states of hydrogen and the hydrogen-like atom, we introduce

$$\chi_{\alpha}^{\text{H}}(\mathbf{r}) = (H_T - \epsilon_{\alpha})\psi_{\alpha}^{\text{H}} = \chi_{\alpha}^{\text{H}}(r) Y_{l_{\alpha} m_{\alpha}}(\hat{\mathbf{r}}), \quad (3.68)$$

with

$$\chi_{\alpha}^{\text{H}}(r) = \frac{1}{\sqrt{w_{n_{\alpha}}}} \int_{\kappa_{n_{\alpha}-1}}^{\kappa_{n_{\alpha}}} d\kappa \left(\frac{\kappa^2}{2} - \varepsilon_{\alpha} \right) \phi_{\kappa l_{\alpha}}^{\text{H}}(r), \quad (3.69)$$

where ε_{α} is the energy of the target electron in channel α . Similarly, we introduce

$$\chi_{\beta}^{(\text{Z})}(\mathbf{r}) = (H_P - \epsilon_{\beta})\psi_{\beta}^{(\text{Z})} = \chi_{\beta}^{(\text{Z})}(r) Y_{l_{\beta} m_{\beta}}(\hat{\mathbf{r}}), \quad (3.70)$$

with

$$\chi_{\beta}^{(\text{Z})}(r) = \frac{1}{\sqrt{w_{n_{\beta}}}} \int_{\kappa_{n_{\beta}-1}}^{\kappa_{n_{\beta}}} d\kappa \left(\frac{\kappa^2}{2} - \varepsilon_{\beta} \right) \phi_{\kappa l_{\beta}}^{\text{Z}}(r), \quad (3.71)$$

where ϵ_β is the energy of the β state of the hydrogen-like atom. For eigenfunctions $\psi_\beta^{(Z)}$ and ψ_α^H , we have $\chi_\beta^{(Z)} = 0$ and $\chi_\alpha^H = 0$.

Taking into account these definitions and the analytical forms of the potentials V_P and V_T given in Eq. (3.10), the direct matrix elements can be written as

$$\tilde{D}_{\alpha'\alpha}^T = \frac{Z}{R} \delta_{\alpha,\alpha'} - Z \int d\mathbf{r}_1 \psi_{\alpha'}^{H*}(\mathbf{r}_1) \frac{1}{|\mathbf{r}_1 - \mathbf{R}|} \psi_\alpha^H(\mathbf{r}_1), \quad (3.72)$$

$$\tilde{D}_{\beta'\beta}^P = \frac{Z}{R} \delta_{\beta,\beta'} - \int d\mathbf{r}_2 \psi_{\beta'}^{(Z)*}(\mathbf{r}_2) \frac{1}{|\mathbf{r}_2 + \mathbf{R}|} \psi_\beta^{(Z)}(\mathbf{r}_2) \quad (3.73)$$

and the rearrangements matrix elements as

$$\tilde{K}_{\beta'\alpha}^P = \int d\mathbf{r}_1 \psi_{\beta'}^{(Z)*}(\mathbf{r}_1 - \mathbf{R}) e^{-iv\mathbf{r}_1} \psi_\alpha^H(\mathbf{r}_1), \quad (3.74)$$

$$\tilde{K}_{\alpha'\beta}^T = \int d\mathbf{r}_1 \psi_{\alpha'}^{H*}(\mathbf{r}_1) e^{iv\mathbf{r}_1} \psi_\beta^{(Z)}(\mathbf{r}_1 - \mathbf{R}), \quad (3.75)$$

$$\begin{aligned} \tilde{Q}_{\beta'\alpha}^P &= \frac{Z}{R} \int d\mathbf{r}_1 \psi_{\beta'}^{(Z)*}(\mathbf{r}_1 - \mathbf{R}) e^{-iv\mathbf{r}_1} \psi_\alpha^H(\mathbf{r}_1) \\ &\quad - Z \int d\mathbf{r}_1 \frac{\psi_{\beta'}^{(Z)*}(\mathbf{r}_1 - \mathbf{R})}{|\mathbf{r}_1 - \mathbf{R}|} e^{-iv\mathbf{r}_1} \psi_\alpha^H(\mathbf{r}_1) \\ &\quad + \int d\mathbf{r}_1 \psi_{\beta'}^{(Z)*}(\mathbf{r}_1 - \mathbf{R}) e^{-iv\mathbf{r}_1} \chi_\alpha^H(\mathbf{r}_1), \end{aligned} \quad (3.76)$$

$$\begin{aligned} \tilde{Q}_{\alpha'\beta}^T &= \frac{Z}{R} \int d\mathbf{r}_1 \psi_{\alpha'}^{H*}(\mathbf{r}_1) e^{iv\mathbf{r}_1} \psi_\beta^{(Z)}(\mathbf{r}_1 - \mathbf{R}) - \int d\mathbf{r}_1 \frac{\psi_{\alpha'}^{H*}(\mathbf{r}_1)}{r_1} e^{iv\mathbf{r}_1} \psi_\beta^{(Z)}(\mathbf{r}_1 - \mathbf{R}) \\ &\quad + \int d\mathbf{r}_1 \psi_{\alpha'}^{H*}(\mathbf{r}_1) e^{iv\mathbf{r}_1} \chi_\beta^{(Z)}(\mathbf{r}_1 - \mathbf{R}). \end{aligned} \quad (3.77)$$

Now let us define the following operators for arbitrary wave functions f and g

$$D[f, g] = \int d\mathbf{r} f^*(\mathbf{r}) \frac{1}{|\mathbf{R} - \mathbf{r}|} g(\mathbf{r}), \quad (3.78)$$

$$A[f, g] = \int d\mathbf{r} f^*(\mathbf{r} - \mathbf{R}) e^{-iv\mathbf{r}} g(\mathbf{r}), \quad (3.79)$$

$$B[f, g] = \int d\mathbf{r} \frac{f^*(\mathbf{r} - \mathbf{R})}{|\mathbf{r} - \mathbf{R}|} e^{-iv\mathbf{r}} g(\mathbf{r}). \quad (3.80)$$

Dependence of the operators on \mathbf{R} is omitted for brevity. With these definitions

we can express the matrix elements in the final forms used in calculations

$$\tilde{D}_{\alpha'\alpha}^T = Z \left(\frac{1}{R} \delta_{\alpha,\alpha'} - D[\psi_{\alpha'}^H, \psi_{\alpha}^H] \right), \quad (3.81)$$

$$\tilde{D}_{\beta'\beta}^P = \frac{Z}{R} \delta_{\beta,\beta'} - (-1)^{\ell_{\beta} + \ell_{\beta'}} D[\psi_{\beta'}^{(Z)}, \psi_{\beta}^{(Z)}], \quad (3.82)$$

$$\tilde{K}_{\beta'\alpha}^P = A[\psi_{\beta'}^{(Z)}, \psi_{\alpha}^H], \quad (3.83)$$

$$\tilde{K}_{\alpha'\beta}^T = A^*[\psi_{\beta}^{(Z)}, \psi_{\alpha'}^H], \quad (3.84)$$

$$\tilde{Q}_{\beta'\alpha}^P = Z \left(\frac{1}{R} A[\psi_{\beta'}^{(Z)}, \psi_{\alpha}^H] - B[\psi_{\beta'}^{(Z)}, \psi_{\alpha}^H] \right) + A[\psi_{\beta'}^{(Z)}, \chi_{\alpha}^H], \quad (3.85)$$

$$\tilde{Q}_{\alpha'\beta}^T = \frac{Z}{R} A^*[\psi_{\beta}^{(Z)}, \psi_{\alpha'}^H] - (-1)^{\ell_{\beta} + \ell_{\alpha'}} e^{i\nu^2 t} B[\psi_{\alpha'}^H, \psi_{\beta}^{(Z)}] + A^*[\psi_{\beta}^{(Z)}, \chi_{\alpha'}^H], \quad (3.86)$$

where the symbol $*$ stands for the complex conjugation. In obtaining the final forms of the matrix elements we used a change of variable whenever needed and the relation $\psi_{nlm}(-\mathbf{r}) = (-1)^l \psi_{nlm}(\mathbf{r})$. Also, we substituted the variable \mathbf{r}_2 with the equivalent form of $(\mathbf{r}_1 - \mathbf{R})$. From the equations (3.81)-(3.86) we can see that calculating three types of integrals enables to derive all the matrix elements needed in solving the set of differential equations (3.22).

3.4.1 Evaluation of matrix elements

In this subsection, we provide the calculation details for integrals $D[\psi_{\beta'}, \psi_{\beta}]$ needed for the direct matrix elements as well as $A[\psi_{\beta'}, \psi_{\alpha}]$ and $B[\psi_{\beta'}, \psi_{\alpha}]$ needed for the rearrangement matrix elements. The first integral is calculated in spherical and the latter two in spheroidal coordinates.

Direct matrix elements

First, we deal with the integral operator D for the wave functions $\psi_{\beta'}$ and ψ_{β} (which can be the wave functions of either hydrogen or the hydrogen-like atom)

given as

$$D[\psi_{\beta'}, \psi_{\beta}] = \int d\mathbf{r} \psi_{\beta'}^*(\mathbf{r}) \frac{1}{|\mathbf{r} - \mathbf{R}|} \psi_{\beta}(\mathbf{r}). \quad (3.87)$$

Radial and angular parts of the wave functions $\psi_{\beta'}$ and ψ_{β} can be separated as

$$\psi_{\beta'}^*(\mathbf{r}) = \phi_{n_{\beta'} m_{\beta'}}(r) Y_{l_{\beta'} m_{\beta'}}^*(\hat{\mathbf{r}}), \quad \psi_{\beta}(\mathbf{r}) = \phi_{n_{\beta} m_{\beta}}(r) Y_{l_{\beta} m_{\beta}}(\hat{\mathbf{r}}). \quad (3.88)$$

We also use the following expansion

$$\frac{1}{|\mathbf{r} - \mathbf{R}|} = 4\pi \sum_{\lambda\mu} \frac{1}{2\lambda + 1} U_{\lambda}(R, r) Y_{\lambda\mu}^*(\hat{\mathbf{R}}) Y_{\lambda\mu}(\hat{\mathbf{r}}), \quad (3.89)$$

with

$$U_{\lambda}(R, r) = \begin{cases} R^{\lambda}/r^{\lambda+1} & \text{for } r \geq R, \\ r^{\lambda}/R^{\lambda+1} & \text{for } r < R. \end{cases} \quad (3.90)$$

Inserting these into Eq. (3.87) we obtain

$$\begin{aligned} D[\psi_{\beta'}, \psi_{\beta}] &= 4\pi \sum_{\lambda\mu} \frac{Y_{\lambda\mu}^*(\hat{\mathbf{R}})}{2\lambda + 1} \int dr r^2 \phi_{n_{\beta'} m_{\beta'}}(r) U_{\lambda}(R, r) \phi_{n_{\beta} m_{\beta}}(r) \\ &\quad \times \int d\hat{\mathbf{r}} Y_{l_{\beta} m_{\beta}}(\hat{\mathbf{r}}) Y_{\lambda\mu}(\hat{\mathbf{r}}) Y_{l_{\beta'} m_{\beta'}}^*(\hat{\mathbf{r}}). \end{aligned} \quad (3.91)$$

The spherical harmonics and Clebsch-Gordan coefficients satisfy the following relation

$$\int d\hat{\mathbf{r}} Y_{l_{\beta} m_{\beta}}(\hat{\mathbf{r}}) Y_{\lambda\mu}(\hat{\mathbf{r}}) Y_{l_{\beta'} m_{\beta'}}^*(\hat{\mathbf{r}}) = \sqrt{\frac{[\lambda][l_{\beta}]}{4\pi[l_{\beta}]}} C_{l_{\beta} 0 \lambda 0}^{l_{\beta'} 0} C_{l_{\beta} m_{\beta} \lambda\mu}^{l_{\beta'} m_{\beta'}}, \quad (3.92)$$

where $[l] = 2l + 1$. This yields the final expression for the integral

$$\begin{aligned} D[\psi_{\beta'}, \psi_{\beta}] &= \sqrt{\frac{4\pi[l_{\beta}]}{[l_{\beta}]}} \sum_{\lambda\mu} \frac{Y_{\lambda\mu}^*(\hat{\mathbf{R}})}{\sqrt{[\lambda]}} C_{l_{\beta} 0 \lambda 0}^{l_{\beta'} 0} C_{l_{\beta} m_{\beta} \lambda\mu}^{l_{\beta'} m_{\beta'}} \\ &\quad \times \int dr r^2 \phi_{n_{\beta'} m_{\beta'}}(r) U_{\lambda}(R, r) \phi_{n_{\beta} m_{\beta}}(r) \\ &= \sqrt{\frac{4\pi[l_{\beta}]}{[l_{\beta}]}} \sum_{\lambda=|q|}^{\infty} \frac{Y_{\lambda\mu}^*(\hat{\mathbf{R}})}{\sqrt{[\lambda]}} C_{l_{\beta} 0 \lambda 0}^{l_{\beta'} 0} C_{l_{\beta} m_{\beta} \lambda q}^{l_{\beta'} m_{\beta'}} \int dr r^2 \phi_{n_{\beta'} m_{\beta'}}(r) U_{\lambda}(R, r) \phi_{n_{\beta} m_{\beta}}(r), \end{aligned} \quad (3.93)$$

where $q = m_{\beta'} - m_{\beta}$. In the second line of the equation we used well-known properties of the Clebsch-Gordan coefficients to simplify the sums. The remaining radial integrals are calculated numerically.

Rearrangement matrix elements

Here we present our calculation method for the integrals A and B for arbitrary wave functions $\psi_{\beta'}$ and ψ_{α} . Specifically, we have

$$A[\psi_{\beta'}, \psi_{\alpha}] = \int d\mathbf{r}_1 \psi_{\beta'}^*(\mathbf{r}_1 - \mathbf{R}) e^{-i\mathbf{v}\mathbf{r}_1} \psi_{\alpha}(\mathbf{r}_1), \quad (3.94)$$

$$B[\psi_{\beta'}, \psi_{\alpha}] = \int d\mathbf{r}_1 \frac{\psi_{\beta'}^*(\mathbf{r}_1 - \mathbf{R})}{|\mathbf{r}_1 - \mathbf{R}|} e^{-i\mathbf{v}\mathbf{r}_1} \psi_{\alpha}(\mathbf{r}_1). \quad (3.95)$$

These are calculated using a molecular frame. First, the integrals are written in a more convenient form for application of the method. The vector \mathbf{r}_1 and \mathbf{r}_2 are expressed in terms of \mathbf{r} (see Fig. 3.2) as

$$\mathbf{r}_1 = \mathbf{r} + \mathbf{R}/2 \quad (3.96)$$

and

$$\mathbf{r}_2 = \mathbf{r} - \mathbf{R}/2. \quad (3.97)$$

Therefore, the integral A can be written as

$$A[\psi_{\beta'}, \psi_{\alpha}] = e^{-i\mathbf{v}^2 t/2} \int d\mathbf{r} \psi_{\beta'}^*(\mathbf{r} - \mathbf{R}/2) e^{-i\mathbf{v}\mathbf{r}} \psi_{\alpha}(\mathbf{r} + \mathbf{R}/2). \quad (3.98)$$

Next, we express the wave functions in a molecular frame and use spheroidal coordinates. In this frame, the origin of a coordinate system is set in the midpoint of the two centres (the projectile and the target nucleus) and z' axis is directed along the vector \mathbf{R} as in Fig. 3.3.

In the molecular frame, absolute values of the vectors remain unchanged and angular parts are rotated using the Wigner d -matrix $d_{mq}^l(\Theta)$ [139]. Accordingly, the spherical harmonics can be expanded as

$$Y_{lm}(\hat{\mathbf{r}}) = \sum_q Y_{lq}(\hat{\mathbf{r}}') d_{mq}^l(\Theta), \quad (3.99)$$

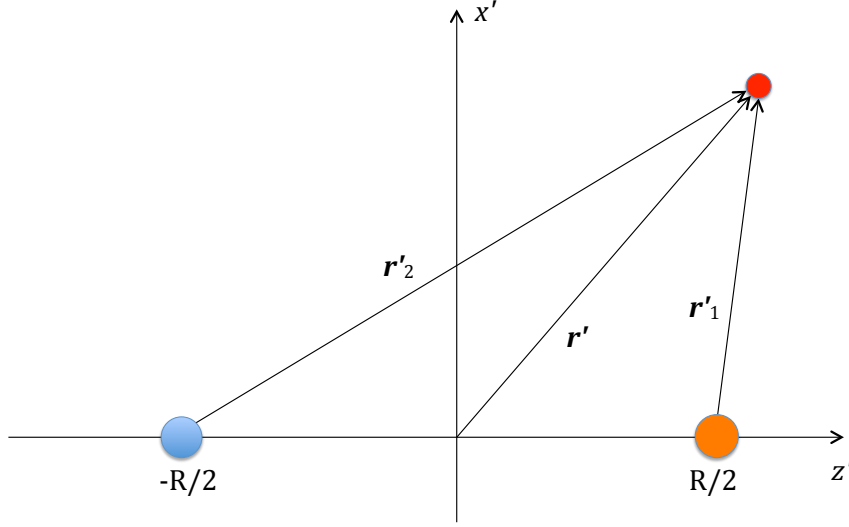


Figure 3.3: The Jacobi coordinates for the scattering system. The origin is set at the midpoint of the nuclei.

where Θ is the polar angle of \mathbf{R} , the position vector of the projectile relative to the target nucleus, and given as

$$\Theta = \arcsin\left(\frac{b}{R}\right). \quad (3.100)$$

Then, Eq. (3.98) is written as

$$A[\psi_{\beta'}, \psi_{\alpha}] = e^{-iv^2t/2} \sum_{q, q'} d_{m_{\beta'} q'}^{l_{\beta'}}(\Theta) d_{m_{\alpha} q}^{l_{\alpha}}(\Theta) \int d\mathbf{r}' \psi_{\beta'}^*(\mathbf{r}'_2) e^{-i\mathbf{v}' \cdot \mathbf{r}'} \psi_{\alpha}(\mathbf{r}'_1). \quad (3.101)$$

The absolute values and polar angles of the vectors \mathbf{r}'_1 , \mathbf{r}'_2 and \mathbf{r}' can be expressed in the new cartesian coordinates (x', y', z') as

$$r_1 = \sqrt{(z' - R/2)^2 + x'^2}, \quad (3.102)$$

$$r_2 = \sqrt{(z' + R/2)^2 + x'^2}, \quad (3.103)$$

$$r = \sqrt{z'^2 + x'^2} \quad (3.104)$$

and

$$\cos \theta'_{r_1} = \frac{z' - R/2}{r_1}, \quad (3.105)$$

$$\cos \theta'_{r_2} = \frac{z' + R/2}{r_2}, \quad (3.106)$$

$$\cos \theta'_r = \frac{z'}{r}. \quad (3.107)$$

As the absolute values of the vectors \mathbf{r}' and \mathbf{r} are the same, we kept the notation r for the absolute value of the vector \mathbf{r}' too (the same for \mathbf{r}'_1 and \mathbf{r}'_2). Now we introduce spheroidal coordinates (η, τ, φ) , where coordinates of the electron (x', y', z') are described as

$$\begin{aligned} x' &= \frac{R}{2} \sqrt{(\eta^2 - 1)(1 - \tau^2)} \cos \varphi, \\ y' &= \frac{R}{2} \sqrt{(\eta^2 - 1)(1 - \tau^2)} \sin \varphi, \\ z' &= \frac{R}{2} \eta \tau, \end{aligned} \quad (3.108)$$

with $1 \leq \eta < \infty$, $-1 \leq \tau \leq 1$ and $0 \leq \varphi \leq 2\pi$. In this new coordinates, expressions (3.102)-(3.107) take the following forms

$$r_1 = \frac{R}{2}(\eta - \tau), \quad (3.109)$$

$$r_2 = \frac{R}{2}(\eta + \tau), \quad (3.110)$$

$$r = \frac{R}{2} \sqrt{\eta^2 + \tau^2 - 1} \quad (3.111)$$

and

$$\cos \theta'_{r_1} = \frac{\eta \tau - 1}{\eta - \tau}, \quad (3.112)$$

$$\cos \theta'_{r_2} = \frac{\eta \tau + 1}{\eta + \tau}, \quad (3.113)$$

$$\cos \theta'_r = \frac{\eta \tau}{\sqrt{\eta^2 + \tau^2 - 1}}. \quad (3.114)$$

In Eqs. (3.109)-(3.111) we set $\varphi = 0$ in x' , because r_1 , r_2 and r are independent of φ . Direction of the vector \mathbf{R} was defined by \mathbf{v} , therefore

$$\cos \theta'_v = \cos \theta'_R = \frac{vt}{R}, \quad \sin \theta'_v = \sin \theta'_R = \frac{b}{R}. \quad (3.115)$$

Now we calculate the dot product of the vectors \mathbf{v}' and \mathbf{r}' , which is used in Eq. (4.88), as

$$\mathbf{v}' \cdot \mathbf{r}' = vr (\sin \theta'_v \sin \theta'_r \cos \varphi + \cos \theta'_v \cos \theta'_r). \quad (3.116)$$

Taking into account Eqs. (3.114), (3.115) and

$$\sin \theta'_r = \frac{\sqrt{(\eta^2 - 1)(1 - \tau^2)}}{\sqrt{\eta^2 + \tau^2 - 1}}, \quad (3.117)$$

we obtain the expression for the dot product in terms of spheroidal coordinates

$$\mathbf{v}' \cdot \mathbf{r}' = \frac{vb}{2} \sqrt{(\eta^2 - 1)(1 - \tau^2)} \cos \varphi + \frac{vt^2}{2} \eta \tau. \quad (3.118)$$

The spherical harmonics are written as

$$Y_{lm}(\theta, \phi) = \sqrt{\frac{(2l+1)(l-m)!}{4\pi(l+m)!}} P_l^m(\cos \theta) e^{im\phi}, \quad (3.119)$$

where P_l^m are the associated Legendre polynomials. Using these we can write Eq. (4.88) as

$$\begin{aligned} A[\psi_{\beta'}, \psi_{\alpha}] &= e^{-iv^2t/2} \frac{R^3}{32\pi^2} \sqrt{(2l_{\beta'} + 1)(2l_{\alpha} + 1)} \\ &\times \sum_{q, q'} d_{m_{\beta'} q'}^{l_{\beta'}}(\Theta) d_{m_{\alpha} q}^{l_{\alpha}}(\Theta) \sqrt{\frac{(l_{\beta'} - q')!(l_{\alpha} - q)!}{(l_{\beta'} + q')!(l_{\alpha} + q)!}} \\ &\times \int_1^\infty d\eta \int_{-1}^1 d\tau (\eta^2 - \tau^2) e^{-i\frac{vt^2}{2}\eta\tau} \phi_{n_{\beta'} l_{\beta'}} \left(\frac{R(\eta + \tau)}{2} \right) \phi_{n_{\alpha} l_{\alpha}} \left(\frac{R(\eta - \tau)}{2} \right) \\ &\times P_{l_{\beta'}}^{q'} \left(\frac{\eta\tau + 1}{\eta + \tau} \right) P_{l_{\alpha}}^q \left(\frac{\eta\tau - 1}{\eta - \tau} \right) \int_0^{2\pi} d\varphi e^{i\frac{vb}{2}\sqrt{(\eta^2-1)(1-\tau^2)}\cos\varphi} e^{i(m_{\alpha} - m_{\beta'})\varphi}. \end{aligned} \quad (3.120)$$

We note that

$$\int_0^{2\pi} e^{ix \cos \varphi} e^{im\varphi} d\varphi = 2\pi i^m J_m(x), \quad (3.121)$$

where J_m are the Bessel functions, which have the following property

$$J_m(-x) = (-1)^m J_m(x). \quad (3.122)$$

By taking this fact into account Eq. (3.120) can be further simplified as

$$\begin{aligned} A[\psi_{\beta'}, \psi_{\alpha}] &= e^{-iv^2t/2} \frac{R^3}{16\pi} \sqrt{(2l_{\beta'} + 1)(2l_{\alpha} + 1)} \\ &\times \sum_{q, q'} (-i)^{q-q'} d_{m_{\beta'} q'}^{l_{\beta'}}(\Theta) d_{m_{\alpha} q}^{l_{\alpha}}(\Theta) \sqrt{\frac{(l_{\beta'} - q')!(l_{\alpha} - q)!}{(l_{\beta'} + q')!(l_{\alpha} + q)!}} \\ &\times \int_1^{\infty} d\eta \int_{-1}^1 d\tau (\eta^2 - \tau^2) e^{-i\frac{vt^2}{2}\eta\tau} \phi_{n_{\beta'} l_{\beta'}} \left(\frac{R(\eta + \tau)}{2} \right) \phi_{n_{\alpha} l_{\alpha}} \left(\frac{R(\eta - \tau)}{2} \right) \\ &\times P_{l_{\beta'}}^{q'} \left(\frac{\eta\tau + 1}{\eta + \tau} \right) P_{l_{\alpha}}^q \left(\frac{\eta\tau - 1}{\eta - \tau} \right) J_{q-q'} \left(\frac{vb}{2} \sqrt{(\eta^2 - 1)(1 - \tau^2)} \right). \end{aligned} \quad (3.123)$$

It can be seen that the integrand in the equation

$$B[\psi_{\beta'}, \psi_{\alpha}] = \int d\mathbf{r}_1 \frac{\psi_{\beta'}^*(\mathbf{r}_1 - \mathbf{R})}{|\mathbf{r}_1 - \mathbf{R}|} e^{-iv\mathbf{r}_1} \psi_{\alpha}(\mathbf{r}_1) \quad (3.124)$$

differs from the integrand in $A[\psi_{\beta'}, \psi_{\alpha}]$ only by the factor $|\mathbf{r}_1 - \mathbf{R}|$ divided in the first wave function, therefore $B[\psi_{\beta'}, \psi_{\alpha}]$ can be found by replacing $\phi_{n_{\beta'} l_{\beta'}}(R(\eta + \tau)/2)$ with $\phi_{n_{\beta'} l_{\beta'}}(R(\eta + \tau)/2) / (R(\eta + \tau)/2)$ in the final expression Eq. (3.123), that is

$$\begin{aligned} B[\psi_{\beta'}, \psi_{\alpha}] &= e^{-iv^2t/2} \frac{R^2}{8\pi} \sqrt{(2l_{\beta'} + 1)(2l_{\alpha} + 1)} \\ &\times \sum_{q, q'} (-i)^{q-q'} d_{m_{\beta'} q'}^{l_{\beta'}}(\Theta) d_{m_{\alpha} q}^{l_{\alpha}}(\Theta) \sqrt{\frac{(l_{\beta'} - q')!(l_{\alpha} - q)!}{(l_{\beta'} + q')!(l_{\alpha} + q)!}} \\ &\times \int_1^{\infty} d\eta \int_{-1}^1 d\tau (\eta - \tau) e^{-i\frac{vt^2}{2}\eta\tau} \phi_{n_{\beta'} l_{\beta'}} \left(\frac{R(\eta + \tau)}{2} \right) \phi_{n_{\alpha} l_{\alpha}} \left(\frac{R(\eta - \tau)}{2} \right) \\ &\times P_{l_{\beta'}}^{q'} \left(\frac{\eta\tau + 1}{\eta + \tau} \right) P_{l_{\alpha}}^q \left(\frac{\eta\tau - 1}{\eta - \tau} \right) J_{q-q'} \left(\frac{vb}{2} \sqrt{(\eta^2 - 1)(1 - \tau^2)} \right). \end{aligned} \quad (3.125)$$

The remaining integrals entering the final expressions (3.123) and (3.125) are evaluated numerically.

3.5 Chapter summary

We presented details of the theoretical approach based on the convergent close-coupling method for a three-body problem of fully-stripped projectiles scattering on the ground and excited states of hydrogen. We applied the wave-packet approach to discretise the continuum for both target and projectile, and obtained the pseudostates to describe the positive-energy states. The eigenstates and pseudostates of both target and projectile (only target in the single-centre approach) were used to expand the total scattering wave function. This expansion was inserted into the exact three-body Schrödinger equation to obtain a system of differential equations for the time-dependent transition amplitudes. The coefficients present in the system of equations, consist of direct and rearrangement matrix elements. The matrices were simplified using spherical and spheroidal coordinates and brought to the forms ready for numerical calculations. Our theoretical approach for the four-body proton-helium system will be described in the next chapter.

Chapter 4

Wave-packet convergent close-coupling approach to proton collisions with helium

4.1 Introduction

In this chapter we develop a semiclassical wave-packet convergent close-coupling (WP-CCC) method for proton scattering on helium. We treat the latter as a four-body system of the projectile, the target nucleus and two electrons, where the electron-electron correlation effects are fully taken into account. A frozen-core approximation is employed, where one of the electrons remains in the ground state of He^+ throughout the collision. Under this assumption the helium wave functions and corresponding energy levels are obtained numerically by solving the Schrödinger equation for the helium atom. The positive-energy states of the target and the hydrogen atom formed after electron capture by the projectile are constructed using the wave-packet approach.

The projectile motion relative to the target nucleus is treated classically as in the previous chapter. We assume that the projectile moves along the straight-line trajectory $\mathbf{R} \equiv \mathbf{R}(t) = \mathbf{b} + \mathbf{v}t$, where \mathbf{b} is an impact parameter and \mathbf{v} is the

initial velocity of the projectile relative to the target (see Fig. 4.1). Vectors \mathbf{b} and \mathbf{v} are perpendicular to each other.

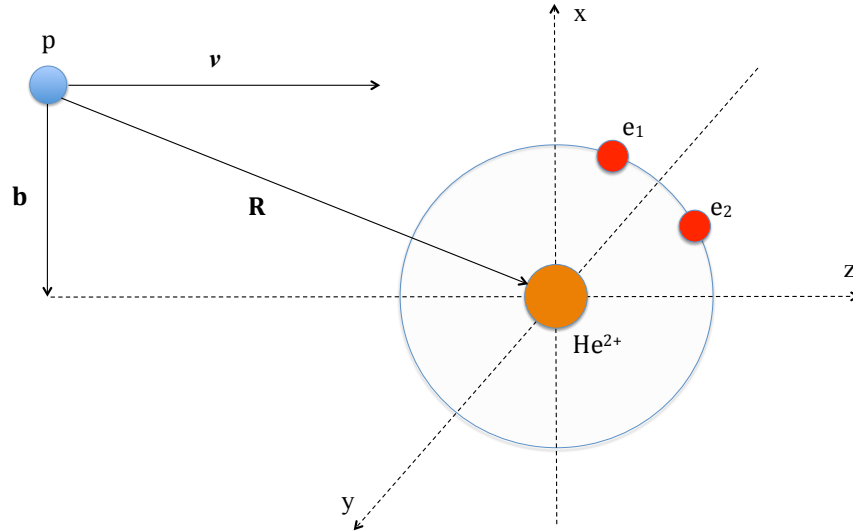


Figure 4.1: An illustration of the coordinate system, with the origin set at the target nucleus.

The total scattering wave function is expanded in a basis made of target- and projectile-centred functions. The projectile-centred functions are written as products of the He^+ and H wave functions. In the single-centre approach only target-centred functions are used. We follow the same procedure described in Chapter 3 to obtain a set of coupled differential equations for the transition amplitudes. The obtained transition amplitudes are used to calculate various cross sections.

The indices P and T denote the projectile and the target, respectively. In this chapter, the projectile is proton and the target is helium.

4.2 The Schrödinger equation for proton collisions with helium

In the stationary formalism, the total scattering wave function Ψ of the proton-helium system satisfies the exact four-body time-independent Schrödinger equation

$$(H - E)\Psi = 0, \quad (4.1)$$

where H is the full 4-body Hamiltonian and E is the total energy. The latter can be written in the following alternative forms

$$\begin{aligned} E &= \frac{k_\alpha^2}{2\mu_1} + E_\alpha^{\text{He}} \\ &= E_0 + \frac{k_{1\beta}^2}{2\mu_2} + \epsilon_{1\beta} \\ &= E_0 + \frac{k_{2\beta}^2}{2\mu_2} + \epsilon_{2\beta}, \end{aligned} \quad (4.2)$$

where E_0 is the ground state energy of the He^+ ion. Index α denotes the full set of quantum numbers representing a state in the direct p -He channel. Index β denotes the same but in the rearrangement channel H- He^+ , formed after the projectile captures the active electron of the target. Furthermore, \mathbf{k}_α is the momentum of the projectile relative to the helium atom in the α channel, $\mu_1 = m_P m_T / (m_P + m_T)$ is the reduced mass of this system with m_P and m_T being masses of the projectile and the target, and E_α^{He} is the energy of helium with the active electron being in the α channel, $\mathbf{k}_{1\beta}$ (and $\mathbf{k}_{2\beta}$) is the momentum of the formed hydrogen atom relative to the residual helium ion in the 1β (2β) channel, $\mu_2 = (m_P + 1)(m_T - 1) / (m_P + m_T)$ is the reduced mass, and $\epsilon_{1\beta}$ ($\epsilon_{2\beta}$) is the energy of the electron of the hydrogen atom in the 1β (2β) channel. Channel 1β is the same as channel 2β but with the electron of the residual target and that of the hydrogen atom exchanged. In the work we refer to channels of the active

electron as helium channels for simplicity, e.g., α channel of helium means that the active electron of helium is in the α channel.

The total Hamiltonian H of this scattering system can be represented in the following equivalent forms

$$H = K_\sigma + H_{T_1} + H_{T_2} + V_P + V_{12}, \quad (4.3)$$

$$H = K_{\rho_1} + H_{P_1} + H_{T_2} + V_1, \quad (4.4)$$

$$H = K_{\rho_2} + H_{P_2} + H_{T_1} + V_2, \quad (4.5)$$

where

$$K_\sigma = -\frac{\nabla_\sigma^2}{2\mu_1}, \quad K_{\rho_i} = -\frac{\nabla_{\rho_i}^2}{2\mu_2}, \quad i = 1, 2 \quad (4.6)$$

are kinetic-energy operators,

$$V_P = \frac{2}{R} - \frac{1}{x_1} - \frac{1}{x_2} \quad (4.7)$$

is the interaction between the projectile and the target,

$$V_1 = \frac{2}{R} - \frac{2}{r_2} - \frac{1}{x_1} + \frac{1}{|\mathbf{r}_1 - \mathbf{r}_2|} \quad (4.8)$$

is the interaction between the hydrogen atom, formed after one of the electrons captured by the projectile, and the remaining helium ion,

$$V_2 = \frac{2}{R} - \frac{2}{r_1} - \frac{1}{x_2} + \frac{1}{|\mathbf{r}_1 - \mathbf{r}_2|} \quad (4.9)$$

is the same as the latter one but for another electron captured by the projectile,

$$V_{12} = \frac{1}{|\mathbf{r}_1 - \mathbf{r}_2|}. \quad (4.10)$$

is the interaction between two electrons of the target. The Hamiltonians of the hydrogen atom and the He^+ ion formed by each of the target electrons are written as

$$H_{P_i} = -\frac{\nabla_{\mathbf{x}_i}^2}{2} - \frac{1}{x_i}, \quad i = 1, 2, \quad (4.11)$$

$$H_{T_i} = -\frac{\nabla_{\mathbf{r}_i}^2}{2} - \frac{2}{r_i}, \quad i = 1, 2, \quad (4.12)$$

respectively. Here \mathbf{R} , \mathbf{r}_1 , and \mathbf{r}_2 are the position vectors of the incident proton and the two electrons relative to the helium nucleus, \mathbf{x}_1 and \mathbf{x}_2 are the position vectors of the electrons relative to the incident proton, $\boldsymbol{\sigma}$ is the position vector of the proton relative to centre of mass of the helium atom, and $\boldsymbol{\rho}_1$ ($\boldsymbol{\rho}_2$) is the position of the proton and the first (second) electron system relative to the helium ion (see Fig. 4.2).

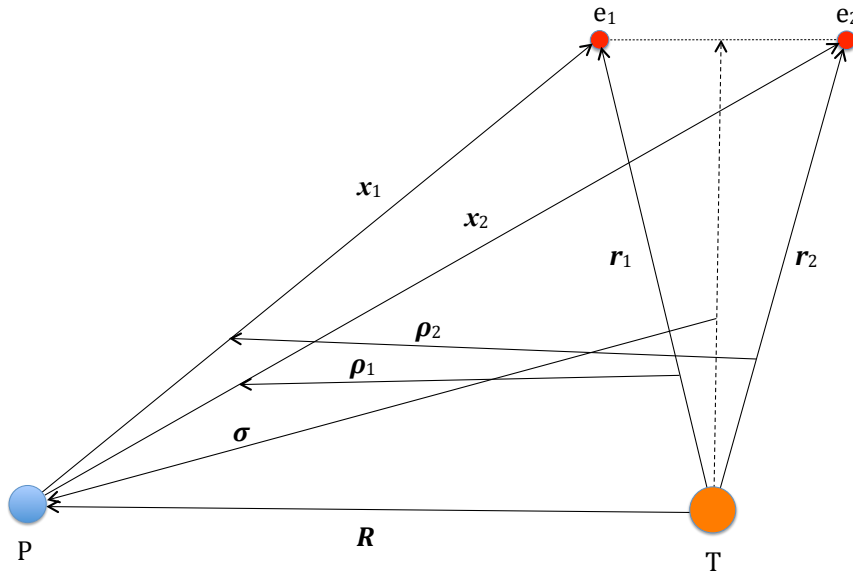


Figure 4.2: The Jacobi coordinates for the proton-helium system.

With these definitions the Hamiltonian of the helium atom is written as

$$H_T = H_{T_1} + H_{T_2} + V_{12}. \quad (4.13)$$

We assume that the total electronic spin is conserved in the collision process and neglect spin effects. Then the total scattering wave function is expanded in

terms of N target-centred and M projectile-centred pseudostates as

$$\begin{aligned} \Psi = & \sum_{\alpha=1}^N a_{\alpha}(t, \mathbf{b}) \psi_{\alpha}^{\text{He}}(\mathbf{r}_1, \mathbf{r}_2) e^{i\mathbf{k}_{\alpha}\sigma} \\ & + \frac{1}{\sqrt{2}} \sum_{\beta=1}^M b_{\beta}(t, \mathbf{b}) \left[\psi_{\beta}^{\text{H}}(\mathbf{x}_1) \psi_{1s}^{\text{He}^+}(\mathbf{r}_2) e^{i\mathbf{k}_{1\beta}\rho_1} + \psi_{\beta}^{\text{H}}(\mathbf{x}_2) \psi_{1s}^{\text{He}^+}(\mathbf{r}_1) e^{i\mathbf{k}_{2\beta}\rho_2} \right], \end{aligned} \quad (4.14)$$

where $\psi_{\alpha}^{\text{He}}$ is the wave function for helium, which will be described below, ψ_{β}^{H} and $\psi_{1s}^{\text{He}^+}$ are the wave function of hydrogen and the ground-state wave function of He^+ , respectively, defined in Chapter 3. The exponential argument consists of a dot product of two vectors. The expansion coefficients $a_{\alpha}(t, \mathbf{b})$ and $b_{\alpha}(t, \mathbf{b})$ at $t \rightarrow +\infty$ represent the transition amplitudes into the various target and projectile states.

We substitute the expansion (4.14) into Eq. (4.1) taking into account three equivalent forms of the total Hamiltonian (4.3)-(4.5):

$$\begin{aligned} & \sum_{\alpha=1}^N (K_{\sigma} + H_{T_1} + H_{T_2} + V_P + V_{12} - E) a_{\alpha}(t, \mathbf{b}) \psi_{\alpha}^{\text{He}}(\mathbf{r}_1, \mathbf{r}_2) e^{i\mathbf{k}_{\alpha}\sigma} \\ & + \frac{1}{\sqrt{2}} \sum_{\beta=1}^M \left[(K_{\rho_1} + H_{P_1} + H_{T_2} + V_1 - E) b_{\beta}(t, \mathbf{b}) \psi_{\beta}^{\text{H}}(\mathbf{x}_1) \psi_{1s}^{\text{He}^+}(\mathbf{r}_2) e^{i\mathbf{k}_{1\beta}\rho_1} \right. \\ & \left. + (K_{\rho_2} + H_{P_2} + H_{T_1} + V_2 - E) b_{\beta}(t, \mathbf{b}) \psi_{\beta}^{\text{H}}(\mathbf{x}_2) \psi_{1s}^{\text{He}^+}(\mathbf{r}_1) e^{i\mathbf{k}_{2\beta}\rho_2} \right] = 0. \end{aligned} \quad (4.15)$$

First, we note that for the ground-state wave function of the He^+ we have

$$(H_{T_i} - E_0) \psi_{1s}^{\text{He}^+}(\mathbf{r}_i) = 0, \quad i = 1, 2 \quad (4.16)$$

and therefore the terms containing these operators cancel out in the sums. With this and taking into account the the actions of the gradient and Laplacian operators on the plane waves

$$\nabla_{\sigma} e^{i\mathbf{k}_{\alpha}\sigma} = i\mathbf{k}_{\alpha} e^{i\mathbf{k}_{\alpha}\sigma}, \quad \nabla_{\rho_1} e^{i\mathbf{k}_{1\beta}\rho_1} = i\mathbf{k}_{1\beta} e^{i\mathbf{k}_{1\beta}\rho_1}, \quad \nabla_{\rho_2} e^{i\mathbf{k}_{2\beta}\rho_2} = i\mathbf{k}_{2\beta} e^{i\mathbf{k}_{2\beta}\rho_2}, \quad (4.17)$$

$$\nabla_{\sigma}^2 e^{i\mathbf{k}_{\alpha}\sigma} = -k_{\alpha}^2 e^{i\mathbf{k}_{\alpha}\sigma}, \quad \nabla_{\rho_1}^2 e^{i\mathbf{k}_{1\beta}\rho_1} = -k_{\beta}^2 e^{i\mathbf{k}_{1\beta}\rho_1}, \quad \nabla_{\rho_2}^2 e^{i\mathbf{k}_{2\beta}\rho_2} = -k_{\beta}^2 e^{i\mathbf{k}_{2\beta}\rho_2}, \quad (4.18)$$

and the relations

$$\frac{\mathbf{k}_\alpha}{\mu_1} \nabla_\sigma = \frac{\partial}{\partial t}, \quad \frac{\mathbf{k}_{1\beta}}{\mu_2} \nabla_{\rho_1} = \frac{\partial}{\partial t}, \quad \frac{\mathbf{k}_{2\beta}}{\mu_2} \nabla_{\rho_2} = \frac{\partial}{\partial t}, \quad (4.19)$$

Eq. (4.15) can be rewritten as

$$\begin{aligned} & \sum_{\alpha=1}^N \dot{a}_\alpha(t, \mathbf{b}) \psi_\alpha^{\text{He}}(\mathbf{r}_1, \mathbf{r}_2) e^{i\mathbf{k}_\alpha \sigma} \\ & + \frac{1}{\sqrt{2}} \sum_{\beta=1}^M \dot{b}_\beta(t, \mathbf{b}) \left[\psi_\beta^{\text{H}}(\mathbf{x}_1) \psi_{1s}^{\text{He}^+}(\mathbf{r}_2) e^{i\mathbf{k}_{1\beta} \rho_1} + \psi_\beta^{\text{H}}(\mathbf{x}_2) \psi_{1s}^{\text{He}^+}(\mathbf{r}_1) e^{i\mathbf{k}_{2\beta} \rho_2} \right] \\ & = \sum_{\alpha=1}^N (H_T + V_P - E_\alpha^{\text{He}}) a_\alpha(t, \mathbf{b}) \psi_\alpha^{\text{He}}(\mathbf{r}_1, \mathbf{r}_2) e^{i\mathbf{k}_\alpha \sigma} \\ & + \frac{1}{\sqrt{2}} \sum_{\beta=1}^M \left[(H_{P_1} + V_1 + V_{12} - \varepsilon_\beta^{\text{H}}) b_\beta(t, \mathbf{b}) \psi_\beta^{\text{H}}(\mathbf{x}_1) \psi_{1s}^{\text{He}^+}(\mathbf{r}_2) e^{i\mathbf{k}_{1\beta} \rho_1} \right. \\ & \left. + (H_{P_2} + V_2 + V_{12} - \varepsilon_\beta^{\text{H}}) b_\beta(t, \mathbf{b}) \psi_\beta^{\text{H}}(\mathbf{x}_2) \psi_{1s}^{\text{He}^+}(\mathbf{r}_1) e^{i\mathbf{k}_{2\beta} \rho_2} \right] = 0. \quad (4.20) \end{aligned}$$

In obtaining the last expression we used the definitions of the total energies and neglected the terms $\nabla_\sigma^2 a_\alpha$, $\nabla_{\rho_1}^2 b_\beta$ and $\nabla_{\rho_2}^2 b_\beta$, because coefficients a_α and b_β vary slowly with t and are very small.

Next we successively multiply all terms of Eq. (4.20) by $\psi_{\alpha'}^{\text{He}^*}(\mathbf{r}_1, \mathbf{r}_2) e^{-i\mathbf{k}_{\alpha'} \sigma}$ for $\alpha' = 1, \dots, N$ and $\psi_{\beta'}^{\text{H}^*}(\mathbf{x}_1) \psi_{1s}^{\text{He}^+}(\mathbf{r}_2) e^{-i\mathbf{k}_{1\beta'} \rho_1} + \psi_{\beta'}^{\text{H}^*}(\mathbf{x}_2) \psi_{1s}^{\text{He}^+}(\mathbf{r}_1) e^{-i\mathbf{k}_{2\beta'} \rho_2}$ for $\beta' = 1, \dots, M$ from both sides. After integrating over all variables except for σ , ρ_1 and ρ_2 , we obtain a set of coupled first-order differential equations for the time-dependent coefficients:

$$\begin{cases} i\dot{a}_{\alpha'} + i \sum_{\beta=1}^M \dot{b}_\beta K_{\alpha'\beta}^T = \sum_{\alpha=1}^N a_\alpha D_{\alpha'\alpha}^T + \sum_{\beta=1}^M b_\beta Q_{\alpha'\beta}^T, \\ i \sum_{\alpha=1}^N \dot{a}_\alpha K_{\beta'\alpha}^P + i \sum_{\beta=1}^M \dot{b}_\beta L_{\beta'\beta}^P = \sum_{\alpha=1}^N a_\alpha Q_{\beta'\alpha}^P + \sum_{\beta=1}^M b_\beta D_{\beta'\beta}^P, \\ \alpha' = 1, 2, \dots, N, \quad \beta' = 1, 2, \dots, M. \end{cases} \quad (4.21)$$

Here the direct matrix elements have the forms

$$D_{\alpha'\alpha}^T = \langle \mathbf{k}_{\alpha'}, \psi_{\alpha'}^{\text{He}} | H_T - E_{\alpha}^{\text{He}} + V_P | \psi_{\alpha}^{\text{He}}, \mathbf{k}_{\alpha} \rangle, \quad (4.22)$$

$$L_{\beta'\beta}^P = \frac{1}{2} \sum_{i,j=1,2} \langle \mathbf{k}_{i\beta'}, \psi_{\beta'}^{\text{H}}, \psi_{1s}^{\text{He}^+} | \psi_{\beta}^{\text{H}}, \psi_{1s}^{\text{He}^+}, \mathbf{k}_{j\beta} \rangle, \quad (4.23)$$

$$D_{\beta'\beta}^P = \frac{1}{2} \sum_{i,j=1,2} \langle \mathbf{k}_{i\beta'}, \psi_{\beta'}^{\text{H}}, \psi_{1s}^{\text{He}^+} | H_{Pi} - \varepsilon_{\beta}^{\text{H}} | \psi_{\beta}^{\text{H}}, \psi_{1s}^{\text{He}^+}, \mathbf{k}_{j\beta} \rangle \\ + \frac{1}{2} \sum_{i,j=1,2} \langle \mathbf{k}_{i\beta'}, \psi_{\beta'}^{\text{H}}, \psi_{1s}^{\text{He}^+} | V_i | \psi_{\beta}^{\text{H}}, \psi_{1s}^{\text{He}^+}, \mathbf{k}_{j\beta} \rangle. \quad (4.24)$$

For the rearrangement matrix elements we have

$$K_{\beta'\alpha}^P = \frac{1}{\sqrt{2}} \sum_{i=1,2} \langle \mathbf{k}_{i\beta'}, \psi_{\beta'}^{\text{H}}, \psi_{1s}^{\text{He}^+} | \psi_{\alpha}^{\text{He}}, \mathbf{k}_{\alpha} \rangle, \quad (4.25)$$

$$K_{\alpha'\beta}^T = \frac{1}{\sqrt{2}} \sum_{i=1,2} \langle \mathbf{k}_{\alpha'}, \psi_{\alpha'}^{\text{He}} | \psi_{\beta}^{\text{H}}, \psi_{1s}^{\text{He}^+}, \mathbf{k}_{i\beta} \rangle, \quad (4.26)$$

$$Q_{\beta'\alpha}^P = \frac{1}{\sqrt{2}} \sum_{i=1,2} \langle \mathbf{k}_{i\beta'}, \psi_{\beta'}^{\text{H}}, \psi_{1s}^{\text{He}^+} | H_T - E_{\alpha}^{\text{He}} + V_P | \psi_{\alpha}^{\text{He}}, \mathbf{k}_{\alpha} \rangle, \quad (4.27)$$

$$Q_{\alpha'\beta}^T = \frac{1}{\sqrt{2}} \sum_{i=1,2} \langle \mathbf{k}_{\alpha'}, \psi_{\alpha'}^{\text{He}} | H_{Pi} - \varepsilon_{\beta}^{\text{H}} + V_i | \psi_{\beta}^{\text{H}}, \psi_{1s}^{\text{He}^+}, \mathbf{k}_{i\beta} \rangle. \quad (4.28)$$

We will return to the explicit calculations of the matrix elements after defining the wave functions for the helium pseudostates.

The above system of equations is solved subject to the initial boundary condition

$$a_{\alpha}(-\infty, \mathbf{b}) = \delta_{\alpha,1s}, \quad \alpha = 1, \dots, N, \\ b_{\beta}(-\infty, \mathbf{b}) = 0, \quad \beta = 1, \dots, M, \quad (4.29)$$

which assumes that the active target electron is initially in the $1s$ orbital.

The single-centre approach to proton-helium collisions is much simpler in comparison with the two-centre one, due to the absence of capture channels. In this case, the total scattering wave function is expanded using only target-centred functions as

$$\Psi = \sum_{\alpha=1}^N a_{\alpha}(t, \mathbf{b}) \psi_{\alpha}^{\text{He}}(\mathbf{r}_1, \mathbf{r}_2) e^{i\mathbf{k}_{\alpha}\sigma}. \quad (4.30)$$

As a result the set of differential equations (4.21) for the time-dependent coefficients simplifies to

$$i\dot{a}_{\alpha'} = \sum_{\alpha=1}^N a_{\alpha} D_{\alpha'\alpha}^T, \quad \alpha' = 1, 2, \dots, N, \quad (4.31)$$

where $D_{\alpha'\alpha}^T$ is given by Eq. (4.22).

Helium wave functions

The target description is more complicated in this case, since we have a two-electron system and electron-electron correlation as well as electron-exchange effects must be incorporated. The Schrödinger equation for this system cannot be solved analytically. Therefore, a numerical approach needs to be developed to find the solutions. Various existing theoretical works revealed that a careful choice of the helium wave functions is important in dealing with collisions of ions with the helium atom. Especially in the close-coupling approach they should be defined very accurately to obtain good convergence. In the present work we use the wave-packet-based description of the helium atom in the frozen-core approximation developed in [140]. Assuming that the total electronic spin of He in the ground state, $S = 0$, is conserved during the collision, we write the spatial part of the wave function in the symmetric form

$$\psi_{\alpha}^{\text{He}}(\mathbf{r}_1, \mathbf{r}_2) = \psi_{\alpha}(\mathbf{r}_1)\psi_{1s}^{(Z)}(\mathbf{r}_2) + \psi_{\alpha}(\mathbf{r}_2)\psi_{1s}^{(Z)}(\mathbf{r}_1), \quad (4.32)$$

where $\psi_{1s}^{(Z)}$ is the $1s$ orbital of the hydrogen-like atom of nuclear charge Z given in (3.35). This is a generalisation of the wave function used by Abdurakhmanov *et al.* [140], where it was set $Z = 2$ to correspond to the ground-state wave functions of He^+ .

To obtain the functions ψ_{α} for each state α , we numerically solve the Schrödinger

equation for helium

$$H_T \psi_\alpha^{\text{He}}(\mathbf{r}_1, \mathbf{r}_2) = E_\alpha \psi_\alpha^{\text{He}}(\mathbf{r}_1, \mathbf{r}_2), \quad (4.33)$$

where E_α is the total energy of the state α . Solutions of this equation depend on the parameter Z . We slightly vary Z so that the total ground-state energy of the helium atom is equal to the experimental value of -2.904 a.u. [141]. Substituting the expansion (4.32) of the helium wave functions into Eq. (4.33), then projecting the result onto $\psi_{1s}^{(Z)}$, and taking into account $\langle \psi_{1s}^{(Z)} | \psi_{1s}^{(Z)} \rangle = 1$, we obtain the following integro-differential equation for ψ_α :

$$\begin{aligned} & [\nabla_{\mathbf{r}_1}^2 - 2V_1(r_1) + 2\varepsilon_\alpha + 2(2-z)V_2] \psi_\alpha(\mathbf{r}_1) \\ & + \left(2\varepsilon_\alpha + \frac{2(2-z)}{r_1} \right) \langle \psi_{1s}^{(Z)} | \psi_\alpha \rangle \psi_{1s}^{(Z)}(\mathbf{r}_1) + \left\langle \psi_{1s}^{(Z)} \left| \nabla_{\mathbf{r}_2}^2 + \frac{4}{r_2} \right| \psi_\alpha \right\rangle_{\mathbf{r}_1} \psi_{1s}^{(Z)}(\mathbf{r}_1) \\ & - 2 \left\langle \psi_{1s}^{(Z)} \left| \frac{1}{|\mathbf{r}_1 - \mathbf{r}_2|} \right| \psi_\alpha \right\rangle_{\mathbf{r}_1} \psi_{1s}^{(Z)}(\mathbf{r}_1) = 0, \end{aligned} \quad (4.34)$$

where

$$V_1(r_1) = -2/r_1 + \left\langle \psi_{1s}^{(Z)} \left| \frac{1}{|\mathbf{r}_1 - \mathbf{r}_2|} \right| \psi_{1s}^{(Z)} \right\rangle_{\mathbf{r}_1} \quad (4.35)$$

is the Hartree potential for the electron of the hydrogen-like ion of charge Z , and

$$V_2 = \left\langle \psi_{1s}^{(Z)} \left| \frac{1}{r_2} \right| \psi_{1s}^{(Z)} \right\rangle = \int_0^\infty \psi_{1s}^{(Z)}(r_2) \frac{1}{r_2} \psi_{1s}^{(Z)}(r_2) dr_2. \quad (4.36)$$

Separating the radial and angular parts of the wave functions for both bound and continuum states, we obtain from Eq. (4.34) the following equation for the radial function $R_\alpha(r)$:

$$\begin{aligned} & \frac{d^2 R_\alpha(r)}{dr^2} - \left[\frac{l(l+1)}{r^2} - \frac{4}{r} + 2W_0[\psi_{1s}^{(Z)}, \psi_{1s}^{(Z)}] - 2\varepsilon_\alpha - 2(2-z)V_2 \right] R_\alpha(r) \\ & = \left[\frac{2}{2l+1} W_l[\psi_{1s}^{(Z)}, R_\alpha] - 2 \int_0^\infty \psi_{1s}^{(Z)}(t) W_0[\psi_{1s}^{(Z)}, \psi_{1s}^{(Z)}] R_\alpha(t) dt \right. \\ & \quad \left. - \left(2\varepsilon_\alpha + \frac{2(2-z)}{r} \right) \int_0^\infty \psi_{1s}^{(Z)}(t) R_\alpha(t) dt \right] \psi_{1s}^{(Z)}(r), \end{aligned} \quad (4.37)$$

where

$$W_l[f, g] = \frac{1}{r^{l+1}} \int_0^r f(t)g(t)t^l dt + r^l \int_r^\infty \frac{f(t)g(t)}{t^{l+1}} dt. \quad (4.38)$$

We use an iterative approach to solve Eq. (4.37), where the Numerov method is applied in each iteration to find solutions of the linear inhomogeneous second-order differential equation for $R_\alpha^{(i)}(r)$, where i is the index of iteration. $R_\alpha^{(0)}(r)$ is found by replacing the right-hand side of Eq. (4.37) with zero. To ensure sufficient accuracy of the solution, the number of iterations N_{it} was set to be large enough so that for all values of r there is at least four digit agreement between $R_\alpha^{(N_{\text{it}}-1)}(r)$ and $R_\alpha^{(N_{\text{it}})}(r)$.

Equation (4.37) was solved several times by slowly varying the parameter Z until the corresponding ground-state total energy of helium best matches to the experimental value. The specific value of Z was found to be 1.99. Table 4.1 presents the total energies of the helium atom, where one electron is frozen in the $1s$ orbital while the other one is active. The calculated total energies of various states of helium are compared with the theoretical results of Abdurakhmanov *et al.* [140] and Slim *et al.* [47], and also with the measured values of Bashkin and Stoner [141]. Except for the ground state, all energies agree up to three digits in all of the aforementioned works.

For negative energies this system has a discrete set of solutions. For positive energies the equation has a continuous solution with a non-normalisable radial wave function. Therefore, as in the case of hydrogen, we construct wave packets using the helium continuum-state wave functions. We define

$$\phi_{il}(r) = \nu_{il} \int_{\kappa_{i-1}}^{\kappa_i} d\kappa R_{\kappa l}(r), \quad (4.39)$$

where ν_{il} is the normalisation coefficient. Discretisation points $\kappa_i, i = 1, \dots, N_c$ and E_{max} are defined in a similar way as for hydrogen. Then the wave packets

Table 4.1: Total binding energy (in a.u.) of the helium atom in a specific state. Only the active orbitals in the $(1snl)$ singlet states are listed in the first column.

state	present	Ref. [140]	Ref. [47]	Expt. [141]
$1s$	-2.9040	-2.8725	-2.8655	-2.9036
$2s$	-2.1432	-2.1434	-2.1430	-2.1459
$3s$	-2.0605	-2.0606	-2.0604	-2.0613
$4s$	-2.0332	-2.0333	-2.0309	-2.0336
$2p$	-2.1223	-2.1224	-2.1224	-2.1239
$3p$	-2.0546	-2.0547	-2.0547	-2.0552
$4p$	-2.0308	-2.0309	-2.0307	-2.0311
$3d$	-2.0555	-2.0556	-2.0555	-2.0556

based on the two-electron helium wave functions are written as

$$\psi_{\alpha}^{\text{He}}(\mathbf{r}_1, \mathbf{r}_2) = \psi_{1s}^{(Z)}(\mathbf{r}_2) \phi_{n_{\alpha}l_{\alpha}}(r_1) Y_{l_{\alpha}m_{\alpha}}(\hat{\mathbf{r}}_1) + \psi_{1s}^{(Z)}(\mathbf{r}_1) \phi_{n_{\alpha}l_{\alpha}}(r_2) Y_{l_{\alpha}m_{\alpha}}(\hat{\mathbf{r}}_2), \quad (4.40)$$

where the normalisation coefficients are given as

$$\nu_{n_{\alpha}l_{\alpha}} = \left[2 \left(\langle \phi_{n_{\alpha}l_{\alpha}} | \phi_{n_{\alpha}l_{\alpha}} \rangle + \delta_{l_{\alpha}0} \delta_{m_{\alpha}0} \langle \phi_{n_{\alpha}l_{\alpha}} | \phi_{1s}^{(Z)} \rangle \right) \right]^{-1/2} \quad (4.41)$$

and $\phi_{1s}^{(Z)}$ is the radial part of the function $\psi_{1s}^{(Z)}$.

Both hydrogen and helium wave packets are referred to as bin states. Together with the eigenstates, they form the bases for the hydrogen and helium atoms. We note that the basis parameters E_{max} and N_c must be sufficiently large to obtain accurate cross sections. Their choice will be discussed in the results chapter.

4.3 Matrix elements

Matrix elements (4.23)–(4.28) are written in integral forms as

$$D_{\alpha'\alpha}^T = \int d\mathbf{r}_1 d\mathbf{r}_2 \psi_{\alpha'}^{\text{He}*}(\mathbf{r}_1, \mathbf{r}_2) e^{i(\mathbf{k}_{\alpha}\sigma - \mathbf{k}_{\alpha'}\sigma)} (H_T - E_{\alpha}^{\text{He}} + V_P) \psi_{\alpha}^{\text{He}}(\mathbf{r}_1, \mathbf{r}_2), \quad (4.42)$$

$$\begin{aligned}
L_{\beta'\beta}^P = & \frac{1}{2} \left[\int d\mathbf{r}_1 d\mathbf{r}_2 \psi_{\beta'}^{H*}(\mathbf{x}_1) \psi_{1s}^{He^+}(\mathbf{r}_2) e^{i(\mathbf{k}_{1\beta} - \mathbf{k}_{1\beta'}) \cdot \boldsymbol{\rho}_1} \psi_{\beta}^H(\mathbf{x}_1) \psi_{1s}^{He^+}(\mathbf{r}_2) \right. \\
& + \int d\mathbf{r}_1 d\mathbf{r}_2 \psi_{\beta'}^{H*}(\mathbf{x}_1) \psi_{1s}^{He^+}(\mathbf{r}_2) e^{i(\mathbf{k}_{2\beta} \boldsymbol{\rho}_2 - \mathbf{k}_{1\beta'} \boldsymbol{\rho}_1)} \psi_{\beta}^H(\mathbf{x}_2) \psi_{1s}^{He^+}(\mathbf{r}_1) \\
& + \int d\mathbf{r}_1 d\mathbf{r}_2 \psi_{\beta'}^{H*}(\mathbf{x}_2) \psi_{1s}^{He^+}(\mathbf{r}_1) e^{i(\mathbf{k}_{1\beta} \boldsymbol{\rho}_1 - \mathbf{k}_{2\beta'} \boldsymbol{\rho}_2)} \psi_{\beta}^H(\mathbf{x}_1) \psi_{1s}^{He^+}(\mathbf{r}_2) \\
& \left. + \int d\mathbf{r}_1 d\mathbf{r}_2 \psi_{\beta'}^{H*}(\mathbf{x}_2) \psi_{1s}^{He^+}(\mathbf{r}_1) e^{i(\mathbf{k}_{2\beta} - \mathbf{k}_{2\beta'}) \cdot \boldsymbol{\rho}_2} \psi_{\beta}^H(\mathbf{x}_2) \psi_{1s}^{He^+}(\mathbf{r}_1) \right], \quad (4.43)
\end{aligned}$$

$$\begin{aligned}
D_{\beta'\beta}^P = & \frac{1}{2} \left[\int d\mathbf{r}_1 d\mathbf{r}_2 \psi_{\beta'}^{H*}(\mathbf{x}_1) \psi_{1s}^{He^+}(\mathbf{r}_2) e^{i(\mathbf{k}_{1\beta} - \mathbf{k}_{1\beta'}) \cdot \boldsymbol{\rho}_1} (H_{P1} - \varepsilon_{\beta}^H + V_1) \psi_{\beta}^H(\mathbf{x}_1) \psi_{1s}^{He^+}(\mathbf{r}_2) \right. \\
& + \int d\mathbf{r}_1 d\mathbf{r}_2 \psi_{\beta'}^{H*}(\mathbf{x}_1) \psi_{1s}^{He^+}(\mathbf{r}_2) e^{i(\mathbf{k}_{2\beta} \boldsymbol{\rho}_2 - \mathbf{k}_{1\beta'} \boldsymbol{\rho}_1)} (H_{P2} - \varepsilon_{\beta}^H + V_2) \psi_{\beta}^H(\mathbf{x}_2) \psi_{1s}^{He^+}(\mathbf{r}_1) \\
& + \int d\mathbf{r}_1 d\mathbf{r}_2 \psi_{\beta'}^{H*}(\mathbf{x}_2) \psi_{1s}^{He^+}(\mathbf{r}_1) e^{i(\mathbf{k}_{1\beta} \boldsymbol{\rho}_1 - \mathbf{k}_{2\beta'} \boldsymbol{\rho}_2)} (H_{P2} - \varepsilon_{\beta}^H + V_1) \psi_{\beta}^H(\mathbf{x}_1) \psi_{1s}^{He^+}(\mathbf{r}_2) \\
& \left. + \int d\mathbf{r}_1 d\mathbf{r}_2 \psi_{\beta'}^{H*}(\mathbf{x}_2) \psi_{1s}^{He^+}(\mathbf{r}_1) e^{i(\mathbf{k}_{2\beta} - \mathbf{k}_{2\beta'}) \cdot \boldsymbol{\rho}_2} (H_{P1} - \varepsilon_{\beta}^H + V_2) \psi_{\beta}^H(\mathbf{x}_2) \psi_{1s}^{He^+}(\mathbf{r}_1) \right]. \quad (4.44)
\end{aligned}$$

For the rearrangement matrix elements we have

$$\begin{aligned}
K_{\beta'\alpha}^P = & \frac{1}{\sqrt{2}} \left[\int d\mathbf{r}_1 d\mathbf{r}_2 \psi_{\beta'}^{H*}(\mathbf{x}_1) \psi_{1s}^{He^+}(\mathbf{r}_2) e^{i(\mathbf{k}_{\alpha} \boldsymbol{\sigma} - \mathbf{k}_{1\beta'} \boldsymbol{\rho}_1)} \psi_{\alpha}^{He}(\mathbf{r}_1, \mathbf{r}_2) \right. \\
& \left. + \int d\mathbf{r}_1 d\mathbf{r}_2 \psi_{\beta'}^{H*}(\mathbf{x}_2) \psi_{1s}^{He^+}(\mathbf{r}_2) e^{i(\mathbf{k}_{\alpha} \boldsymbol{\sigma} - \mathbf{k}_{2\beta'} \boldsymbol{\rho}_2)} \psi_{\alpha}^{He}(\mathbf{r}_1, \mathbf{r}_2) \right], \quad (4.45)
\end{aligned}$$

$$\begin{aligned}
K_{\alpha'\beta}^T = & \frac{1}{\sqrt{2}} \left[\int d\mathbf{r}_1 d\mathbf{r}_2 \psi_{\alpha'}^{He*}(\mathbf{r}_1, \mathbf{r}_2) e^{i(\mathbf{k}_{1\beta} \boldsymbol{\rho}_1 - \mathbf{k}_{\alpha'} \boldsymbol{\sigma})} \psi_{\beta}^H(\mathbf{x}_1) \psi_{1s}^{He^+}(\mathbf{r}_2) \right. \\
& \left. + \int d\mathbf{r}_1 d\mathbf{r}_2 \psi_{\alpha'}^{He*}(\mathbf{r}_1, \mathbf{r}_2) e^{i(\mathbf{k}_{2\beta} \boldsymbol{\rho}_2 - \mathbf{k}_{\alpha'} \boldsymbol{\sigma})} \psi_{\beta}^H(\mathbf{x}_2) \psi_{1s}^{He^+}(\mathbf{r}_2) \right], \quad (4.46)
\end{aligned}$$

$$\begin{aligned}
Q_{\beta'\alpha}^P = & \frac{1}{\sqrt{2}} \left[\int d\mathbf{r}_1 d\mathbf{r}_2 \psi_{\beta'}^{H*}(\mathbf{x}_1) \psi_{1s}^{He^+}(\mathbf{r}_2) e^{i(\mathbf{k}_{\alpha} \boldsymbol{\sigma} - \mathbf{k}_{1\beta'} \boldsymbol{\rho}_1)} (H_T - E_{\alpha}^{He} + V_P) \psi_{\alpha}^{He}(\mathbf{r}_1, \mathbf{r}_2) \right. \\
& \left. + \int d\mathbf{r}_1 d\mathbf{r}_2 \psi_{\beta'}^{H*}(\mathbf{x}_2) \psi_{1s}^{He^+}(\mathbf{r}_2) e^{i(\mathbf{k}_{\alpha} \boldsymbol{\sigma} - \mathbf{k}_{2\beta'} \boldsymbol{\rho}_2)} (H_T - E_{\alpha}^{He} + V_P) \psi_{\alpha}^{He}(\mathbf{r}_1, \mathbf{r}_2) \right], \quad (4.47)
\end{aligned}$$

$$\begin{aligned}
Q_{\alpha'\beta}^T = & \frac{1}{\sqrt{2}} \left[\int d\mathbf{r}_1 d\mathbf{r}_2 \psi_{\alpha'}^{He*}(\mathbf{r}_1, \mathbf{r}_2) e^{i(\mathbf{k}_{1\beta} \boldsymbol{\rho}_1 - \mathbf{k}_{\alpha'} \boldsymbol{\sigma})} (H_{P1} - \varepsilon_{\beta}^H + V_1) \psi_{\beta}^H(\mathbf{x}_1) \psi_{1s}^{He^+}(\mathbf{r}_2) \right. \\
& \left. + \int d\mathbf{r}_1 d\mathbf{r}_2 \psi_{\alpha'}^{He*}(\mathbf{r}_1, \mathbf{r}_2) e^{i(\mathbf{k}_{2\beta} \boldsymbol{\rho}_2 - \mathbf{k}_{\alpha'} \boldsymbol{\sigma})} (H_{P2} - \varepsilon_{\beta}^H + V_2) \psi_{\beta}^H(\mathbf{x}_2) \psi_{1s}^{He^+}(\mathbf{r}_2) \right]. \quad (4.48)
\end{aligned}$$

In this section we reduce the matrix elements (4.42)–(4.48) into forms that are suitable for numerical evaluation by taking into account the definitions of the wave functions. As described in Appendix B, exponential factors entering the direct matrix elements can be written as follows:

$$(\mathbf{k}_\alpha - \mathbf{k}_{\alpha'})\boldsymbol{\sigma} = \mathbf{q}_\perp \mathbf{b} + (\varepsilon_{\alpha'} - \varepsilon_\alpha)t, \quad (4.49)$$

$$(\mathbf{k}_{1\beta} - \mathbf{k}_{1\beta'})\boldsymbol{\rho}_1 = \mathbf{q}_\perp \mathbf{b} + (\varepsilon_{\beta'} - \varepsilon_\beta)t, \quad (4.50)$$

$$(\mathbf{k}_{2\beta} - \mathbf{k}_{2\beta'})\boldsymbol{\rho}_1 = \mathbf{q}_\perp \mathbf{b} + (\varepsilon_{\beta'} - \varepsilon_\beta)t, \quad (4.51)$$

$$\mathbf{k}_{1\beta}\boldsymbol{\rho}_1 - \mathbf{k}_{2\beta'}\boldsymbol{\rho}_2 = \mathbf{q}_\perp \mathbf{b} + (\varepsilon_{\beta'} - \varepsilon_\beta)t, \quad (4.52)$$

$$\mathbf{k}_{2\beta}\boldsymbol{\rho}_1 - \mathbf{k}_{1\beta'}\boldsymbol{\rho}_2 = \mathbf{q}_\perp \mathbf{b} + (\varepsilon_{\beta'} - \varepsilon_\beta)t \quad (4.53)$$

and the exponential terms in the rearrangement matrix elements as

$$\mathbf{k}_\alpha\boldsymbol{\sigma} - \mathbf{k}_{1\beta'}\boldsymbol{\rho}_1 = \mathbf{k}_\alpha\boldsymbol{\sigma} - \mathbf{k}_{2\beta'}\boldsymbol{\rho}_2 = \mathbf{q}_\perp \mathbf{b} + \mathbf{q}_{\alpha,\beta'\parallel}vt - \mathbf{v}\mathbf{r}_1, \quad (4.54)$$

$$\mathbf{k}_{1\beta}\boldsymbol{\rho}_1 - \mathbf{k}_{\alpha'}\boldsymbol{\sigma} = \mathbf{k}_{2\beta}\boldsymbol{\rho}_1 - \mathbf{k}_{\alpha'}\boldsymbol{\sigma} = \mathbf{q}_\perp \mathbf{b} + \mathbf{q}_{\beta,\alpha'\parallel}vt + \mathbf{v}\mathbf{r}_1, \quad (4.55)$$

where \mathbf{q}_\perp is the perpendicular component of the momentum transfer, which is the same in all transitions. The parallel components $\mathbf{q}_{\alpha,\beta'\parallel}$ and $\mathbf{q}_{\beta,\alpha'\parallel}$ depend on the transition states and are given as

$$\mathbf{q}_{\alpha,\beta'\parallel} = \frac{v}{2} + \frac{\varepsilon_{\beta'} - \varepsilon_\alpha}{v}, \quad \mathbf{q}_{\beta,\alpha'\parallel} = -\frac{v}{2} + \frac{\varepsilon_{\alpha'} - \varepsilon_\beta}{v}. \quad (4.56)$$

As $e^{\mathbf{q}_\perp \mathbf{b}}$ is the same in all matrix elements, it can be factored out and cancels when the matrix elements are inserted into Eq. (4.21). Therefore, we omit them but keep the original notations. Using these results and summing similar terms, the matrix elements (4.42)–(4.48) can be written in the forms

$$D_{\alpha'\alpha}^T = 2e^{i(\varepsilon_{\alpha'} - \varepsilon_\alpha)t} \tilde{D}_{\alpha'\alpha}^T, \quad (4.57)$$

$$L_{\beta'\beta}^P = \delta_{\beta',\beta} + e^{i(\varepsilon_{\beta'} - \varepsilon_\beta)t} \tilde{L}_{\beta'\beta}^P, \quad (4.58)$$

$$D_{\beta'\beta}^P = e^{i(\varepsilon_{\beta'} - \varepsilon_\beta)t} \tilde{D}_{\beta'\beta}^P, \quad (4.59)$$

$$K_{\beta'\alpha}^P = \sqrt{2}e^{i(\epsilon_{\beta'} - \epsilon_\alpha)t} e^{iv^2t/2} \tilde{K}_{\beta'\alpha}^B, \quad (4.60)$$

$$K_{\alpha'\beta}^T = \sqrt{2}e^{i(\epsilon_{\alpha'} - \epsilon_\beta)t} e^{-iv^2t/2} \tilde{K}_{\alpha'\beta}^A, \quad (4.61)$$

$$Q_{\beta'\alpha}^P = \sqrt{2}e^{i(\epsilon_{\beta'} - \epsilon_\alpha)t} e^{iv^2t/2} \tilde{Q}_{\beta'\alpha}^P, \quad (4.62)$$

$$Q_{\alpha'\beta}^T = \sqrt{2}e^{i(\epsilon_{\alpha'} - \epsilon_\beta)t} e^{-iv^2t/2} \tilde{Q}_{\alpha'\beta}^T, \quad (4.63)$$

where

$$\tilde{D}_{\alpha'\alpha}^T = \int d\mathbf{r}_1 d\mathbf{r}_2 \psi_{\alpha'}^{\text{He}^*}(\mathbf{r}_1, \mathbf{r}_2) V_P \psi_\alpha^{\text{He}}(\mathbf{r}_1, \mathbf{r}_2), \quad (4.64)$$

$$\tilde{L}_{\beta'\beta}^P = \int d\mathbf{r}_1 d\mathbf{r}_2 \psi_{\beta'}^{\text{H}^*}(\mathbf{r}_2 - \mathbf{R}) \psi_{1s}^{\text{He}^+}(\mathbf{r}_1) e^{-iv\mathbf{r}_2} \psi_\beta^{\text{H}}(\mathbf{r}_1 - \mathbf{R}) \psi_{1s}^{\text{He}^+}(\mathbf{r}_2) e^{iv\mathbf{r}_1}, \quad (4.65)$$

$$\begin{aligned} \tilde{D}_{\beta'\beta}^P &= \int d\mathbf{r}_1 d\mathbf{r}_2 \psi_{\beta'}^{\text{H}^*}(\mathbf{r}_1 - \mathbf{R}) \psi_{1s}^{\text{He}^+}(\mathbf{r}_2) V_1 \psi_\beta^{\text{H}}(\mathbf{r}_1 - \mathbf{R}) \psi_{1s}^{\text{He}^+}(\mathbf{r}_2) \\ &+ \int d\mathbf{r}_1 d\mathbf{r}_2 \psi_{\beta'}^{\text{H}^*}(\mathbf{r}_2 - \mathbf{R}) \psi_{1s}^{\text{He}^+}(\mathbf{r}_1) e^{iv(\mathbf{r}_1 - \mathbf{r}_2)} [H_{P_1} - \varepsilon_\beta^{\text{H}} + V_1] \psi_\beta^{\text{H}}(\mathbf{r}_1 - \mathbf{R}) \psi_{1s}^{\text{He}^+}(\mathbf{r}_2), \end{aligned} \quad (4.66)$$

and

$$\tilde{K}_{\beta'\alpha}^P = \int d\mathbf{r}_1 d\mathbf{r}_2 \psi_{\beta'}^{\text{H}^*}(\mathbf{r}_1 - \mathbf{R}) \psi_{1s}^{\text{He}^+}(\mathbf{r}_2) e^{-iv\mathbf{r}_1} \psi_\alpha^{\text{He}}(\mathbf{r}_1, \mathbf{r}_2), \quad (4.67)$$

$$\tilde{K}_{\alpha'\beta}^T = \int d\mathbf{r}_1 d\mathbf{r}_2 \psi_{\alpha'}^{\text{He}^*}(\mathbf{r}_1, \mathbf{r}_2) e^{iv\mathbf{r}_1} \psi_\beta^{\text{H}}(\mathbf{r}_1 - \mathbf{R}) \psi_{1s}^{\text{He}^+}(\mathbf{r}_2), \quad (4.68)$$

$$\tilde{Q}_{\beta'\alpha}^P = \int d\mathbf{r}_1 d\mathbf{r}_2 \psi_{\beta'}^{\text{H}^*}(\mathbf{r}_1 - \mathbf{R}) \psi_{1s}^{\text{He}^+}(\mathbf{r}_2) e^{-iv\mathbf{r}_1} [H_T - E_\alpha^{\text{He}} + V_P] \psi_\alpha^{\text{He}}(\mathbf{r}_1, \mathbf{r}_2), \quad (4.69)$$

$$\tilde{Q}_{\alpha'\beta}^T = \int d\mathbf{r}_1 d\mathbf{r}_2 \psi_{\alpha'}^{\text{He}^*}(\mathbf{r}_1, \mathbf{r}_2) e^{-iv\mathbf{r}_1} [H_{P_1} - \varepsilon_\beta^{\text{H}} + V_1] \psi_\beta^{\text{H}}(\mathbf{r}_1 - \mathbf{R}) \psi_{1s}^{\text{He}^+}(\mathbf{r}_2). \quad (4.70)$$

Here the vectors \mathbf{x}_1 and \mathbf{x}_2 were replaced with the equivalent forms of $(\mathbf{r}_1 - \mathbf{R})$ and $(\mathbf{r}_2 - \mathbf{R})$, respectively.

In the direct matrix element \tilde{D}^T and the first term of \tilde{D}^P the terms with $(H_T - E_\alpha^{\text{He}})$ and $(H_P - \varepsilon_\beta^{\text{H}})$ vanish, since for both eigenstates and bin states we have

$$\langle \psi_{\alpha'}^{\text{He}} | H_T - E_\alpha^{\text{He}} | \psi_\alpha^{\text{He}} \rangle = 0, \quad \alpha', \alpha = 1, \dots, N, \quad (4.71)$$

$$\langle \psi_{\beta'}^{\text{H}} | H_P - \varepsilon_\beta^{\text{H}} | \psi_\beta^{\text{H}} \rangle = 0, \quad \beta', \beta = 1, \dots, M. \quad (4.72)$$

However, in the rearrangement matrix elements \tilde{Q}^P , \tilde{Q}^T and in the second term of \tilde{D}^P , the terms containing $[H_T - E_\alpha^{\text{He}}]\psi_\alpha^{\text{He}}$ and $[H_P - \varepsilon_\beta^{\text{H}}]\psi_\beta^{\text{H}}$ remain, because the wave packets representing the continuum are not eigenstates. As in the Chapter 3 we define

$$\chi_\beta^{\text{H}}(\mathbf{r}) = [H_P - \varepsilon_\beta^{\text{H}}]\psi_\beta^{\text{H}}(\mathbf{r}) = \chi_\beta^{\text{H}}(r)Y_{l_\beta m_\beta}(\hat{\mathbf{r}}), \quad (4.73)$$

with

$$\chi_\beta^{\text{H}}(r) = \frac{1}{\sqrt{w_{n_\beta}}} \int_{\kappa_{n_\beta-1}}^{\kappa_{n_\beta}} d\kappa \left(\frac{\kappa^2}{2} - \varepsilon_\beta^{\text{H}} \right) \phi_{\kappa l_\beta}^{\text{H}}(r), \quad (4.74)$$

where $\varepsilon_\beta^{\text{H}}$ is the energy of the β state of hydrogen. Similarly, we introduce

$$\chi_\alpha^{\text{He}}(\mathbf{r}) = \chi_\alpha^{\text{He}}(r)Y_{l_\alpha m_\alpha}(\hat{\mathbf{r}}), \quad (4.75)$$

with

$$\chi_\alpha^{\text{He}}(r) = \frac{1}{\sqrt{w_{n_\alpha}}} \int_{\kappa_{n_\alpha-1}}^{\kappa_{n_\alpha}} d\kappa \left(\frac{\kappa^2}{2} - \varepsilon_\alpha^{\text{He}} \right) \phi_{\kappa l_\alpha}^{\text{He}}(r), \quad (4.76)$$

where $\varepsilon_\alpha^{\text{He}}$ is the energy of the active helium electron in channel α . Consequently, we have

$$\begin{aligned} [H_T - E_\alpha^{\text{He}}]\psi_\alpha^{\text{He}}(\mathbf{r}_1, \mathbf{r}_2) &= [H_T - E_\alpha^{\text{He}}] \left(\psi_\alpha(\mathbf{r}_1)\psi_{1s}^{(Z)}(\mathbf{r}_2) + \psi_\alpha(\mathbf{r}_2)\psi_{1s}^{(Z)}(\mathbf{r}_1) \right) \\ &= \chi_\alpha^{\text{He}}(\mathbf{r}_1)\psi^z(\mathbf{r}_2) + \chi_\alpha^{\text{He}}(\mathbf{r}_2)\psi^z(\mathbf{r}_1). \end{aligned} \quad (4.77)$$

For eigenfunctions ψ_β^{H} and ψ_α^{He} , we have $\chi_\beta^{\text{H}} = 0$ and $\chi_\alpha^{\text{He}} = 0$.

Using the expansion of the helium wave function the matrix elements $\tilde{L}_{\beta'\beta}^P$, $\tilde{K}_{\beta'\alpha}^P$ and $\tilde{K}_{\alpha'\beta}^T$ [Eqs. (4.65), (4.67) and (4.68), respectively] can be written as

$$\tilde{L}_{\beta'\beta}^P = \delta_{\beta,\beta'} + A[\psi_{\beta'}^{\text{H}}, \psi_{1s}^{\text{He}^+}][A[\psi_\beta^{\text{H}}, \psi_{1s}^{\text{He}^+}]]^*, \quad (4.78)$$

$$\tilde{K}_{\beta'\alpha}^P = \langle \psi_{1s}^{\text{He}^+} | \psi_{1s}^{(Z)} \rangle A[\psi_{\beta'}^{\text{H}}, \psi_\alpha] + \langle \psi_{1s}^{\text{He}^+} | \psi_\alpha \rangle A[\psi_{\beta'}^{\text{H}}, \psi_{1s}^{(Z)}], \quad (4.79)$$

$$\tilde{K}_{\alpha'\beta}^T = (\tilde{K}_{\beta,\alpha'}^P)^*, \quad (4.80)$$

and the rearrangement matrix elements (4.69) and (4.70) as

$$\begin{aligned}\tilde{Q}_{\beta'\alpha}^P &= \frac{\tilde{K}_{\beta'\alpha}^P}{R} - \langle \psi_{1s}^{\text{He}^+} | \psi_{1s}^{(Z)} \rangle B[\psi_{\beta'}^{\text{H}}, \psi_{\alpha}] - \langle \psi_{1s}^{\text{He}^+} | \psi_{\alpha} \rangle B[\psi_{\beta'}^{\text{H}}, \psi_{1s}^{(Z)}] \\ &\quad - D[\psi_{1s}^{\text{He}^+}, \psi_{1s}^{(Z)}] A[\psi_{\beta'}^{\text{H}}, \psi_{\alpha}] - D[\psi_{1s}^{\text{He}^+}, \psi_{\alpha}] A[\psi_{\beta'}^{\text{H}}, \psi_{1s}^{(Z)}] \\ &\quad + \langle \psi_{1s}^{\text{He}^+} | \psi_{1s}^{(Z)} \rangle A[\psi_{\beta'}^{\text{H}}, \chi_{\alpha}^{\text{He}}] + \langle \psi_{1s}^{\text{He}^+} | \chi_{\alpha}^{\text{He}} \rangle A[\psi_{\beta'}^{\text{H}}, \psi_{1s}^{(Z)}],\end{aligned}\quad (4.81)$$

$$\begin{aligned}\tilde{Q}_{\alpha'\beta}^T &= \frac{\tilde{K}_{\alpha'\beta}^T}{R} - \left(\langle \psi_{1s}^{\text{He}^+} | \psi_{1s}^{(Z)} \rangle A[\psi_{\beta}^{\text{H}}, \tilde{\psi}_{\alpha'}] + \langle \psi_{1s}^{\text{He}^+} | \psi_{\alpha'} \rangle A[\psi_{\beta}^{\text{H}}, \tilde{\psi}_{1s}^{(Z)}] \right. \\ &\quad + D[\psi_{1s}^{\text{He}^+}, \psi_{1s}^{(Z)}] A[\psi_{\beta}^{\text{H}}, \psi_{\alpha'}] + D[\psi_{1s}^{\text{He}^+}, \psi_{\alpha'}] A[\psi_{\beta}^{\text{H}}, \psi_{1s}^{(Z)}] \\ &\quad - A[\psi_{\beta}^{\text{H}}, \psi_{\alpha'} D[\psi_{1s}^{\text{He}^+}, \psi_{1s}^{(Z)}]] - A[\psi_{\beta}^{\text{H}}, \psi_{1s}^{(Z)}] D[\psi_{1s}^{\text{He}^+}, \psi_{\alpha'}] \\ &\quad \left. - \langle \psi_{1s}^{\text{He}^+} | \psi_{1s}^{(Z)} \rangle A[\chi_{\beta}^{\text{H}}, \psi_{\alpha'}] - \langle \psi_{1s}^{\text{He}^+} | \psi_{\alpha'} \rangle A[\chi_{\beta}^{\text{H}}, \psi_{1s}^{(Z)}] \right)^*,\end{aligned}\quad (4.82)$$

where operators D , A and B are defined in Eqs. (3.78)-(3.80) in Chapter 3. We also introduced short-hand notations $\tilde{\psi}_{\alpha'} = \psi_{\alpha'}/r$ and $\tilde{\psi}_{1s}^{(Z)} = \psi_{1s}^{(Z)}/r$.

For the direct matrix elements we have

$$\begin{aligned}\tilde{D}_{\alpha'\alpha}^T &= D[\psi_{\alpha'}, \psi_{\alpha}] + \langle \psi_{1s}^{(Z)} | \psi_{\alpha} \rangle D[\psi_{\alpha'}, \psi_{1s}^{(Z)}] + \langle \psi_{\alpha'} | \psi_{1s}^{(Z)} \rangle D[\psi_{1s}^{(Z)}, \psi_{\alpha}] \\ &\quad + \langle \psi_{\alpha} | \psi_{\alpha'} \rangle D[\psi_{1s}^{(Z)}, \psi_{1s}^{(Z)}],\end{aligned}\quad (4.83)$$

$$\begin{aligned}\tilde{D}_{\beta'\beta}^P &= \delta_{\beta,\beta'} D[\psi_{1s}^{\text{He}^+}, \psi_{1s}^{\text{He}^+}] + (-1)^{l_{\beta}+l_{\beta'}} D[\psi_{\beta'}, \psi_{\beta}] + E[\psi_{\beta'}^{\text{H}*} \psi_{\beta}^{\text{H}}, D[\psi_{1s}^{\text{He}^+}, \psi_{1s}^{\text{He}^+}]] \\ &\quad + \frac{2}{R} A[\psi_{\beta'}^{\text{H}}, \psi_{1s}^{\text{He}^+}] (A[\psi_{\beta}^{\text{H}}, \psi_{1s}^{\text{He}^+}])^* - B[\psi_{\beta'}^{\text{H}}, \psi_{1s}^{\text{He}^+}] (A[\psi_{\beta}^{\text{H}}, \psi_{1s}^{\text{He}^+}])^* \\ &\quad - A[\psi_{\beta'}^{\text{H}}, \psi_{1s}^{\text{He}^+}] (A[\psi_{\beta}^{\text{H}}, \tilde{\psi}_{1s}^{\text{He}^+}])^* + C_{\beta',\beta} + A[\chi_{\beta'}^{\text{H}}, \psi_{1s}^{\text{He}^+}] (A[\psi_{\beta}^{\text{H}}, \psi_{1s}^{\text{He}^+}])^*,\end{aligned}\quad (4.84)$$

where

$$E(f, g) = \int d\mathbf{r} f(\mathbf{r} - \mathbf{R}) g(\mathbf{r}),\quad (4.85)$$

$$C_{\beta',\beta} = \int d\mathbf{r}_1 d\mathbf{r}_2 \psi_{\beta'}^{\text{H}*}(\mathbf{r}_1 - \mathbf{R}) e^{-i\mathbf{v}\mathbf{r}_1} \psi_{1s}^{\text{He}^+}(\mathbf{r}_1) \psi_{\beta}^{\text{H}}(\mathbf{r}_2 - \mathbf{R}) e^{i\mathbf{v}\mathbf{r}_2} \psi_{1s}^{\text{He}^+}(\mathbf{r}_2) \frac{1}{|\mathbf{r}_1 - \mathbf{r}_2|}.\quad (4.86)$$

4.4 Evaluation of matrix elements

Calculations of the integrals A , B and D were described in details in the previous chapter, here we calculate the remaining integrals E and C . We start with

$$E(\psi_\beta, \psi_\alpha) = \int d\mathbf{r} \psi_\beta(\mathbf{r} - \mathbf{R}) \psi_\alpha(\mathbf{r}) = \int d\mathbf{r} \psi_\beta\left(\mathbf{r} - \frac{\mathbf{R}}{2}\right) \psi_\alpha\left(\mathbf{r} + \frac{\mathbf{R}}{2}\right) \quad (4.87)$$

and follow the same method provided in the previous chapter, changing a coordinate system and using spheroidal coordinates. Thus the integral can be represented as

$$E(\psi_\beta, \psi_\alpha) = \sum_{q, q'} d_{m_\beta q'}^{l_\beta}(\Theta) d_{m_\alpha q}^{l_\alpha}(\Theta) \int d\mathbf{r}' \psi_\beta(\mathbf{r}'_2) \psi_\alpha(\mathbf{r}'_1), \quad (4.88)$$

where

$$r'_1 = \frac{R}{2}(\eta - \tau), \quad r'_2 = \frac{R}{2}(\eta + \tau), \quad (4.89)$$

and

$$\cos \theta'_{r_1} = \frac{\eta\tau - 1}{\eta - \tau}, \quad \cos \theta'_{r_2} = \frac{\eta\tau + 1}{\eta + \tau}. \quad (4.90)$$

This expansion and the relation between spherical harmonics and the associated Legendre polynomials

$$Y_{lm}(\theta, \phi) = \sqrt{\frac{(2l+1)(l-m)!}{4\pi(l+m)!}} P_l^m(\cos \theta) e^{im\phi}, \quad (4.91)$$

allow reducing Eq. (4.87) to

$$\begin{aligned} E(\psi_\beta, \psi_\alpha) &= \frac{R^3}{32\pi^2} \sqrt{(2l_\beta + 1)(2l_\alpha + 1)} \\ &\times \sum_{q, q'} d_{m_\beta q'}^{l_\beta}(\Theta) d_{m_\alpha q}^{l_\alpha}(\Theta) \sqrt{\frac{(l_\beta - q')!(l_\alpha - q)!}{(l_\beta + q')!(l_\alpha + q)!}} \\ &\times \int_1^\infty d\eta \int_{-1}^1 d\tau (\eta^2 - \tau^2) \phi_{n_\beta l_\beta}\left(\frac{R(\eta + \tau)}{2}\right) \phi_{n_\alpha l_\alpha}\left(\frac{R(\eta - \tau)}{2}\right) \\ &\times P_{l_\beta}^{q'}\left(\frac{\eta\tau + 1}{\eta + \tau}\right) P_{l_\alpha}^q\left(\frac{\eta\tau - 1}{\eta - \tau}\right) \int_0^{2\pi} d\varphi e^{i(m_\alpha - m_\beta)\varphi}. \end{aligned} \quad (4.92)$$

By taking into account the fact that

$$\int_0^{2\pi} e^{im\varphi} d\varphi = 2\pi\delta_{m,0}, \quad (4.93)$$

it can further be simplified as

$$\begin{aligned} E(\psi_\beta, \psi_\alpha) &= \delta_{m_\beta, m_\alpha} \frac{R^3}{16\pi} \sqrt{(2l_\beta + 1)(2l_\alpha + 1)} \\ &\times \sum_{q, q'} d_{m_\beta q'}^{l_\beta}(\Theta) d_{m_\alpha q}^{l_\alpha}(\Theta) \sqrt{\frac{(l_\beta - q)!(l_\alpha - q)!}{(l_\beta + q)!(l_\alpha + q)!}} \\ &\times \int_1^\infty d\eta \int_{-1}^1 d\tau (\eta^2 - \tau^2) \phi_{n_\beta l_\beta} \left(\frac{R(\eta + \tau)}{2} \right) \phi_{n_\alpha l_\alpha} \left(\frac{R(\eta - \tau)}{2} \right) \\ &\times P_{l_\beta}^{q'} \left(\frac{\eta\tau + 1}{\eta + \tau} \right) P_{l_\alpha}^q \left(\frac{\eta\tau - 1}{\eta - \tau} \right). \end{aligned} \quad (4.94)$$

Next we describe how to further simplify the most computationally demanding term, $C_{\beta', \beta}$. This term is a part of the matrix element that corresponds to electron exchange between the two possible final transfer channels β' and β containing the hydrogen atom and the He^+ ion. The term $|\mathbf{r}_1 - \mathbf{r}_2|^{-1}$ is expanded as

$$\frac{1}{|\mathbf{r}_1 - \mathbf{r}_2|} = 4\pi \sum_{\lambda\mu} \frac{1}{2\lambda + 1} U_\lambda(r_1, r_2) Y_{\lambda\mu}(\hat{\mathbf{r}}_1) Y_{\lambda\mu}^*(\hat{\mathbf{r}}_2), \quad (4.95)$$

where

$$U_\lambda(r_1, r_2) = \begin{cases} r_1^\lambda / r_2^{\lambda+1} & \text{for } r_2 \geq r_1, \\ r_2^\lambda / r_1^{\lambda+1} & \text{for } r_2 < r_1. \end{cases} \quad (4.96)$$

Then we have

$$\begin{aligned} C_{\beta', \beta} &= \sum_{\lambda\mu} \frac{4\pi}{2\lambda + 1} \left[\int d\mathbf{r}_1 d\mathbf{r}_2 \psi_{\beta'}^{\text{H}*}(\mathbf{r}_1 - \mathbf{R}) e^{-i\mathbf{v}\mathbf{r}_1} \psi_{1s}^{\text{He}^+}(\mathbf{r}_1) \right. \\ &\quad \times \left. \psi_\beta^{\text{H}}(\mathbf{r}_2 - \mathbf{R}) e^{i\mathbf{v}\mathbf{r}_2} \psi_{1s}^{\text{He}^+}(\mathbf{r}_2) U_\lambda(r_1, r_2) Y_{\lambda\mu}^*(\hat{\mathbf{r}}_1) Y_{\lambda\mu}(\hat{\mathbf{r}}_2) \right] \\ &= \sum_{\lambda\mu} \frac{1}{2\lambda + 1} \left[\int d\mathbf{r}_1 \psi_{\beta'}^{\text{H}*}(\mathbf{r}_1 - \mathbf{R}) e^{-i\mathbf{v}\mathbf{r}_1} \phi_0(r_1) Y_{\lambda\mu}(\hat{\mathbf{r}}_1) \right. \\ &\quad \times \left. \int d\mathbf{r}_2 \psi_\beta^{\text{H}}(\mathbf{r}_2 - \mathbf{R}) e^{i\mathbf{v}\mathbf{r}_2} \phi_0(r_2) Y_{\lambda\mu}^*(\hat{\mathbf{r}}_2) U_\lambda(r_1, r_2) \right], \end{aligned} \quad (4.97)$$

where ϕ_0 is the radial part of $\psi_{1s}^{\text{He}^+}$. Each integral entering the sum is calculated as

$$\begin{aligned}
& \int d\mathbf{r}_1 \psi_{\beta'}^{\text{H}*}(\mathbf{r}_1 - \mathbf{R}) e^{-i\mathbf{v}\mathbf{r}_1} \phi_0(r_1) Y_{\lambda\mu}(\hat{\mathbf{r}}_1) \\
& \times \int d\mathbf{r}_2 \psi_{\beta}^{\text{H}}(\mathbf{r}_2 - \mathbf{R}) e^{i\mathbf{v}\mathbf{r}_2} \phi_0(r_2) Y_{\lambda\mu}^*(\hat{\mathbf{r}}_2) U_{\lambda}(r_1, r_2) \\
& = \frac{R^6}{2^8 \pi^2} (2\lambda + 1) \sqrt{(2l_{\beta'} + 1)(2l_{\alpha} + 1)} \\
& \times \sum_{p, p'} \sum_{q, q'} (-i)^{q-q'-p+p'} d_{m_{\beta'} q'}^{l_{\beta'}}(\Theta) d_{\mu q}^{\lambda}(\Theta) d_{m_{\beta} p'}^{l_{\beta}}(\Theta) d_{\mu p}^{\lambda}(\Theta) \\
& \times \sqrt{\frac{(l_{\beta'} - q')!(\lambda - q)!}{(l_{\beta'} + q')!(\lambda + q)!}} \sqrt{\frac{(l_{\beta} - p')!(\lambda - p)!}{(l_{\beta} + p')!(\lambda + p)!}} \\
& \times \int_1^{\infty} d\eta \int_1^{\infty} d\eta' \int_{-1}^1 d\tau (\eta^2 - \tau^2) e^{-i\frac{v\tau^2}{2}\eta\tau} d\eta \int_{-1}^1 d\tau' ((\eta')^2 - (\tau')^2) e^{i\frac{v\tau'^2}{2}\eta'\tau'} \\
& \times \phi_{n_{\beta'} l_{\beta'}} \left(\frac{R(\eta + \tau)}{2} \right) \phi_0 \left(\frac{R(\eta - \tau)}{2} \right) \phi_{n_{\beta} l_{\beta}} \left(\frac{R(\eta' + \tau')}{2} \right) \phi_0 \left(\frac{R(\eta' - \tau')}{2} \right) \\
& \times U \left(\frac{R(\eta - \tau)}{2}, \frac{R(\eta' - \tau')}{2} \right) \\
& \times P_{l_{\beta'}}^{q'} \left(\frac{\eta\tau + 1}{\eta + \tau} \right) P_{\lambda}^q \left(\frac{\eta\tau - 1}{\eta - \tau} \right) P_{l_{\beta}}^{p'} \left(\frac{\eta'\tau' + 1}{\eta' + \tau'} \right) P_{\lambda}^p \left(\frac{\eta'\tau' - 1}{\eta' - \tau'} \right) \\
& \times J_{q-q'} \left(\frac{vb}{2} \sqrt{(\eta^2 - 1)(1 - \tau^2)} \right) J_{p-p'} \left(\frac{vb}{2} \sqrt{((\eta')^2 - 1)(1 - (\tau')^2)} \right). \quad (4.98)
\end{aligned}$$

We can see that the integral is reduced to a 4-dimensional entity. Generally, it can be evaluated for all channels, but the calculations are extremely time consuming. Also, including them in the calculations do not change the results considerably provided the collision energy is not too small. Therefore, we include only the $C_{1s,1s}$ term and neglect all others. This approximation imposes a lower limit on the incident energy below which the results may deteriorate. No further approximations were used in the numerical evaluations of all other direct and rearrangement matrix elements.

4.5 Chapter summary

We presented the semiclassical convergent close-coupling method for the four-body problem of proton collisions with helium. The wave-packet approach was applied to discretise the continuum both for the target and the projectile. The target was treated as a three-body system, where the electron-correlation effects were fully taken into account. We assumed that one of the helium electrons is frozen in the $1s$ orbital of He^+ throughout the collision. The target states were described by parameter-dependent wave functions, with the parameter fixed in such a way that the calculated ground-state energy of the active electron matches the measured value. With this modification, all calculated energy levels of the active electron of helium are in excellent agreement with the corresponding experimental values.

After obtaining positive- and negative-energy states both for the target and the projectile, we expanded the total scattering wave function in terms of the target- and projectile-centred states (only target-centred in the single-centre approach). This expansion was substituted into the Schrödinger equation of the system to obtain the set of coupled differential equations for the time-dependent transition amplitudes for direct and rearrangement scattering. Details of the corresponding matrix elements were provided.

Chapter 5

Experimental Observables

In this chapter we present analytical formulas for calculating total and differential cross sections by using the transition amplitudes defined in Chapters 3 and 4. We use general notations α and β to denote target and projectile channels.

5.1 Total cross sections

When all matrix elements are calculated, we are able to solve the systems of differential equations (3.22) and (4.21). We apply Runge-Kutta method to solve the coupled equations in the region $[-z_{\max}, z_{\max}]$ with sufficiently large z_{\max} . The transition amplitudes $a_{\alpha}(+\infty, \mathbf{b})$ and $b_{\beta}(+\infty, \mathbf{b})$ are obtained for a required range of impact parameters. These amplitudes are used to obtain the probability to find the system in direct-scattering (DS) channel α and electron-capture (EC) channel β for each impact parameter as

$$P_{\alpha}^{\text{DS}}(b) = |a_{\alpha}(+\infty, \mathbf{b}) - \delta_{\alpha, \alpha_0}|^2, \quad P_{\beta}^{\text{EC}}(b) = |b_{\beta}(+\infty, \mathbf{b})|^2, \quad (5.1)$$

where α_0 is the initial channel index. The partial cross sections for the transition into states α and β are calculated by integrating the corresponding weighted

probability functions over the impact parameters in the range $[0, b_{\max}]$ as

$$\sigma_{\alpha}^{\text{DS}} = 2\pi \int_0^{b_{\max}} db b P_{\alpha}^{\text{DS}}(b), \quad \sigma_{\beta}^{\text{EC}} = 2\pi \int_0^{b_{\max}} db b P_{\beta}^{\text{EC}}(b), \quad (5.2)$$

where b_{\max} , the upper limit for the impact parameter, is chosen to be sufficiently large. We used various values for b_{\max} in calculations depending on the considered system and process. The total electron-capture cross section is the sum of the cross sections for transitions into the bound states of the formed atom after electron capture (the hydrogen-like ion in $P^{(Z)}$ -H collisions and hydrogen in p -He collisions):

$$\sigma_{\text{tot}}^{\text{EC}} = \sum_{\beta, \epsilon_{\beta} < 0} \sigma_{\beta}^{\text{EC}}. \quad (5.3)$$

The total ionisation (single-ionisation (SI) for the helium target) cross section is the sum of the partial cross sections for excitation of the positive-energy pseudostates of the target and electron transfer into the continuum of the formed atom after electron capture:

$$\sigma_{\text{tot}}^{\text{SI}} = \sum_{\alpha, \epsilon_{\alpha} > 0} \sigma_{\alpha}^{\text{DS}} + \sum_{\beta, \epsilon_{\beta} > 0} \sigma_{\beta}^{\text{EC}}. \quad (5.4)$$

The total excitation cross section is found as

$$\sigma_{\text{tot}}^{\text{exc}} = \sum_{\alpha \neq \alpha_0, \epsilon_{\alpha} < 0} \sigma_{\alpha}^{\text{DS}}, \quad (5.5)$$

where σ_{α_0} is excluded in the sum, as it corresponds to elastic scattering.

In our work, we also investigate double ionisation of the helium atom. For this purpose, we employ an independent-event model. In this model, double ionisation is modelled as a combination of two independent processes: single ionisation of helium and subsequent ionisation of the helium ion. Accordingly, the double-ionisation probability is the product of the two individual ionisation probabilities. The total probabilities for single ionisation of helium and

ionisation of the helium ion are found as

$$P_{\text{ion}}^{\text{He}}(b) = \sum_{\alpha, \epsilon_{\alpha} > 0} P_{\alpha}^{\text{DS}}(b) + \sum_{\beta, \epsilon_{\beta} > 0} P_{\beta}^{\text{EC}}(b), \quad (5.6)$$

$$P_{\text{ion}}^{\text{He}^+}(b) = \sum_{\gamma, \epsilon_{\gamma} > 0} Q_{\gamma}^{\text{DS}}(b) + \sum_{\xi, \epsilon_{\xi} > 0} Q_{\xi}^{\text{EC}}(b), \quad (5.7)$$

where P_{α}^{DS} (P_{β}^{EC}) is the probability for direct scattering into channel α (for electron capture into channel β) in p -He collisions, and Q_{γ}^{DS} (Q_{ξ}^{EC}) is the probability for direct scattering into channel γ (for electron capture into channel ξ) in p -He⁺ collisions. Finally, the double-ionisation (DI) cross section is calculated as

$$\sigma_{\text{tot}}^{\text{DI}} = 2\pi \int_0^{b_{\text{max}}} db b P_{\text{ion}}^{\text{He}}(b) P_{\text{ion}}^{\text{He}^+}(b). \quad (5.8)$$

5.2 Differential ionisation cross section

To calculate fully and doubly differential cross sections for ionisation of hydrogen by multiply-charged ions and single-ionisation of helium by protons, we first define transition amplitudes. According to Ref. [142] the full direct-scattering amplitude $T^{\text{DS}}(\mathbf{k}_{\alpha'}, \mathbf{k}_{\alpha_0})$ for the projectile momentum transfer from \mathbf{k}_{α_0} to $\mathbf{k}_{\alpha'}$ and electron-capture amplitude $T^{\text{EC}}(\mathbf{k}_{\beta'}, \mathbf{k}_{\alpha_0})$ from \mathbf{k}_{α_0} to $\mathbf{k}_{\beta'}$ are found as

$$T^{\text{DS}}(\mathbf{k}_{\alpha'}, \mathbf{k}_{\alpha_0}) = \langle \Phi_{\alpha'} | \overleftarrow{H} - E | \Psi_{\alpha_0} \rangle, \quad (5.9)$$

and

$$T^{\text{EC}}(\mathbf{k}_{\beta'}, \mathbf{k}_{\alpha_0}) = \langle \Phi_{\beta'} | \overleftarrow{H} - E | \Psi_{\alpha_0} \rangle, \quad (5.10)$$

respectively, where Ψ_{α_0} is the total scattering wave function, H is the total Hamiltonian operator, the arrow over H indicates the direction of its action, E is the total energy of the system, $\Phi_{\alpha'}$ and $\Phi_{\beta'}$ are the asymptotic states corresponding to the final channels α' and β' , respectively. This definition of the

scattering amplitude applicable for all processes taking place in the considered collisional systems. Using the definitions of the asymptotic states we obtain

$$T^{\text{DS}}(\mathbf{k}_{\alpha'}, \mathbf{k}_{\alpha_0}) = \langle \mathbf{k}_{\alpha'} \psi_{\alpha'}^T | \overleftarrow{H} - E | \Psi_{\alpha_0} \rangle, \quad (5.11)$$

$$T^{\text{EC}}(\mathbf{k}_{\beta'}, \mathbf{k}_{\alpha_0}) = \langle \mathbf{k}_{\beta'} \psi_{\beta'}^P | \overleftarrow{H} - E | \Psi_{\alpha_0} \rangle, \quad (5.12)$$

where $\psi_{\alpha'}^T$ and $\psi_{\beta'}^P$ are pseudostates used to describe the target and projectile, respectively. These scattering amplitudes are calculated using the transition-probability amplitudes in the impact-parameter space as

$$\begin{aligned} T^{\text{DS}}(\mathbf{k}_{\alpha'}, \mathbf{k}_{\alpha_0}) &= \frac{1}{2\pi} \int d\mathbf{b} e^{i(\mathbf{p}_{\alpha', \alpha_0})_{\perp} \cdot \mathbf{b}} [a_{\alpha'}(+\infty, \mathbf{b}) - \delta_{\alpha', \alpha_0}] \\ &= e^{im(\varphi_{\alpha'} + \pi/2)} \int_0^{\infty} db b [\tilde{a}_{\alpha'}(+\infty, b) - \delta_{\alpha', \alpha_0}] J_m((\mathbf{p}_{\alpha', \alpha_0})_{\perp} b), \end{aligned} \quad (5.13)$$

$$\begin{aligned} T^{\text{EC}}(\mathbf{k}_{\beta'}, \mathbf{k}_{\alpha_0}) &= \frac{1}{2\pi} \int d\mathbf{b} e^{i(\mathbf{p}_{\beta', \alpha_0})_{\perp} \cdot \mathbf{b}} b_{\beta'}(+\infty, \mathbf{b}) \\ &= e^{im(\varphi_{\beta'} + \pi/2)} \int_0^{\infty} db b [\tilde{b}_{\beta'}(+\infty, b)] J_m((\mathbf{p}_{\beta', \alpha_0})_{\perp} b), \end{aligned} \quad (5.14)$$

where m is the magnetic quantum number of the bound state in the final channel, $\mathbf{p}_{\alpha', \alpha_0} = \mathbf{k}_{\alpha_0} - \mathbf{k}_{\alpha'}$ and $\mathbf{p}_{\beta', \alpha_0} = \mathbf{k}_{\alpha_0} - \mathbf{k}_{\beta'}$, $\varphi_{\alpha'}$ and $\varphi_{\beta'}$ are the azimuthal angles of $\mathbf{k}_{\alpha'}$ and $\mathbf{k}_{\beta'}$, respectively,

$$\tilde{a}_{\alpha'}(t, b) = e^{im\phi_b} a_{\alpha'}(t, \mathbf{b}), \quad \tilde{b}_{\beta'}(+\infty, b) = e^{im\phi_b} b_{\beta'}(+\infty, \mathbf{b}). \quad (5.15)$$

The amplitudes for direct ionisation (DI) is written as

$$T^{\text{DI}}(\boldsymbol{\kappa}, \mathbf{k}_{\alpha'}, \mathbf{k}_{\alpha_0}) = \langle \varphi_{\boldsymbol{\kappa}} | \psi_{\alpha'}^T \rangle T^{\text{DS}}(\mathbf{k}_{\alpha'}, \mathbf{k}_{\alpha_0}) \quad (5.16)$$

and for electron capture into the continuum (ECC) of the atom formed after the target electron captured by the projectile as

$$T^{\text{ECC}}(\boldsymbol{\chi}, \mathbf{k}_{\beta'}, \mathbf{k}_{\alpha_0}) = \langle \varphi_{\boldsymbol{\chi}} | \psi_{\beta'}^P \rangle T^{\text{EC}}(\mathbf{k}_{\beta'}, \mathbf{k}_{\alpha_0}), \quad (5.17)$$

where $\boldsymbol{\kappa}$ ($\boldsymbol{\chi}$) is the momentum of the ejected electron relative to the target nucleus (projectile), $\varphi_{\boldsymbol{\kappa}}$ and $\varphi_{\boldsymbol{\chi}}$ are the corresponding true Coulomb states. In

the single-centre WP-CCC approach, electron capture into the continuum is absent and therefore we set $T^{\text{EC}}(\mathbf{k}_{\beta'}, \mathbf{k}_{\alpha_0}) = 0$.

The DI and ECC amplitudes are used to calculate differential cross sections for ionisation. First, we should note that the amplitudes from the target and the projectile centres with the same projectile momentum should be combined together. However, this is not straightforward as they are given in different frames. To overcome the problem we use the common laboratory frame. The electron momentum relative to the projectile $\boldsymbol{\kappa}$ is written as $\boldsymbol{\kappa} - \mathbf{v}$ in the laboratory frame. When the projectile momentum vectors $\mathbf{k}_{\alpha'}$ and $\mathbf{k}_{\beta'}$ are equal, we use general notation \mathbf{k}_f to denote them. In the laboratory frame, differential cross sections can be formed by the coherent (coh) or incoherent (inc) combinations of the DI and ECC amplitudes. The fully differential cross sections (FDCS) are calculated coherently

$$\frac{d^3\sigma^{\text{coh}}(\boldsymbol{\kappa}, \mathbf{k}_f, \mathbf{k}_{\alpha_0})}{dE_e d\Omega_{\boldsymbol{\kappa}} d\Omega_{\mathbf{k}_f}} = \mu^2 \frac{k_f \kappa}{k_{\alpha_0}} |T^{\text{DI}}(\boldsymbol{\kappa}, \mathbf{k}_{\alpha'}, \mathbf{k}_{\alpha_0}) + T^{\text{ECC}}(\boldsymbol{\kappa} - \mathbf{v}, \mathbf{k}_{\beta'}, \mathbf{k}_{\alpha_0})|^2, \quad (5.18)$$

and incoherently

$$\frac{d^3\sigma^{\text{inc}}(\boldsymbol{\kappa}, \mathbf{k}_f, \mathbf{k}_{\alpha_0})}{dE_e d\Omega_{\boldsymbol{\kappa}} d\Omega_{\mathbf{k}_f}} = \mu^2 \frac{k_f \kappa}{k_{\alpha_0}} (|T^{\text{DI}}(\boldsymbol{\kappa}, \mathbf{k}_{\alpha'}, \mathbf{k}_{\alpha_0})|^2 + |T^{\text{ECC}}(\boldsymbol{\kappa} - \mathbf{v}, \mathbf{k}_{\beta'}, \mathbf{k}_{\alpha_0})|^2), \quad (5.19)$$

where E_e is the energy of the ejected electron, $E_e = \kappa^2/2$. Solid angle $\Omega_{\boldsymbol{\kappa}}$ represents the direction in which the electron is ejected and $\Omega_{\mathbf{k}_f}$ is the solid angle of the scattered projectile. In the laboratory frame, the momentum transfers $\mathbf{p}_{\alpha', \alpha_0}$ and $\mathbf{p}_{\beta', \alpha_0}$ are replaced by $\mathbf{p}_{\alpha', \alpha_0} - \boldsymbol{\kappa}$ and $\mathbf{p}_{\beta', \alpha_0} - \boldsymbol{\kappa}$, respectively. Therefore, perpendicular components of these momentum transfers are substituted with $(\mathbf{p}_{\alpha', \alpha_0} - \boldsymbol{\kappa})_{\perp}$ and $(\mathbf{p}_{\beta', \alpha_0} - \boldsymbol{\kappa})_{\perp}$ in calculating the integrals in Eqs. (5.13) and (5.14), respectively.

The doubly differential cross section (DDCS) in energy of the ejected electron and angle of the scattered projectile is found by integrating the corresponding

FDCS over the solid angle of the ejected electrons as

$$\frac{d^2\sigma(\boldsymbol{\kappa}, \mathbf{k}_f, \mathbf{k}_{\alpha_0})}{dE_e d\Omega_{\mathbf{k}_f}} = \int \frac{d^3\sigma(\boldsymbol{\kappa}, \mathbf{k}_f, \mathbf{k}_{\alpha_0})}{dE_e d\Omega_{\boldsymbol{\kappa}} d\Omega_{\mathbf{k}_f}} d\Omega_{\boldsymbol{\kappa}}. \quad (5.20)$$

The DDCS in angles of the ejected electron and scattered projectile is found by integrating the FDCS over the ejected electron energies as

$$\frac{d^2\sigma(\boldsymbol{\kappa}, \mathbf{k}_f, \mathbf{k}_{\alpha_0})}{d\Omega_{\boldsymbol{\kappa}} d\Omega_{\mathbf{k}_f}} = \int \frac{d^3\sigma(\boldsymbol{\kappa}, \mathbf{k}_f, \mathbf{k}_{\alpha_0})}{dE_e d\Omega_{\boldsymbol{\kappa}} d\Omega_{\mathbf{k}_f}} dE_e. \quad (5.21)$$

The singly differential cross sections (SDCS) in the energy of the ejected electron is obtained by integrating the DDCS of Eq. (5.20) over the solid angle of the scattered projectile as

$$\frac{d\sigma(\boldsymbol{\kappa}, \mathbf{k}_f, \mathbf{k}_{\alpha_0})}{dE_e} = \int \frac{d^2\sigma(\boldsymbol{\kappa}, \mathbf{k}_f, \mathbf{k}_{\alpha_0})}{dE_e d\Omega_{\mathbf{k}_f}} d\Omega_{\mathbf{k}_f}. \quad (5.22)$$

The SDCS in the ejection angle is obtained

$$\frac{d\sigma(\boldsymbol{\kappa}, \mathbf{k}_f, \mathbf{k}_{\alpha_0})}{d\Omega_{\boldsymbol{\kappa}}} = \int \frac{d^2\sigma(\boldsymbol{\kappa}, \mathbf{k}_f, \mathbf{k}_{\alpha_0})}{dE_e d\Omega_{\mathbf{k}_f}} dE_e. \quad (5.23)$$

Total integrated cross section can be obtained by integrating the SDCS. This should lead to the same result as direct summation of cross sections for excitation of the positive-energy pseudostates. This fact is used to test the computer code.

We also state a formula to calculate the density matrix for two arbitrary direct channels. For channels α and α' , this matrix is obtained using the time-dependent direct-transition amplitudes $a_{\alpha\alpha_0}(+\infty, b)$ and $a_{\alpha'\alpha_0}(+\infty, b)$ as follows:

$$\rho_{\alpha'\alpha}^{\alpha_0} = 2\pi \int_0^\infty db b a_{\alpha'\alpha_0}^*(+\infty, b) a_{\alpha\alpha_0}(+\infty, b). \quad (5.24)$$

The matrix $\rho_{\alpha\alpha}^{\alpha_0}$ is real for all channels and coincides with integrated cross sections, that is $\rho_{\alpha\alpha}^{\alpha_0} \equiv \sigma_{\alpha}^{\text{DS}}$. In Chapter 6, we will present density matrices in proton scattering on the excited states of hydrogen.

5.3 Chapter summary

We provided formulas for calculating transition probabilities and total cross sections using the transition amplitudes defined in the previous chapters. Expressions for fully, doubly and singly differential cross sections for ionisation were also presented. Using the theories described in Chapters 3 and 4 and the formulas given in the present chapter, we can calculate the cross sections for elastic scattering, electron capture, excitation and ionisation, as well as the differential ionisation cross sections for both collisional systems ($P^{(Z)}$ -H and p -He). Results of the calculations will be discussed in the next three chapters.

Chapter 6

Proton scattering on excited states of hydrogen

The CCC approach has been successfully applied to proton collisions with the ground state hydrogen [130, 132]. In this chapter, we present results of the two-centre WP-CCC calculations for proton scattering on excited states of hydrogen. We employ two identical bases to describe the target and projectile centres. Our predictions depend on the accuracy of the wave functions and the matrix elements defined in Chapter 3. These were thoroughly checked during calculations. We also investigated the dependence of the resulting cross sections on the number of bins N_c , on the maximum principal quantum number n_{\max} and the maximum angular-momentum quantum number l_{\max} of included states, as well as on the maximum energy of the ejected electron ε_{\max} . The convergence of the cross sections was studied by systematically increasing the number of the basis functions.

For given N_c , n_{\max} and l_{\max} , the total number of states is found as

$$N = \sum_{l=0}^{l_{\max}} (n_{\max} + N_c - l)(2l + 1). \quad (6.1)$$

Our calculations showed that setting $n_{\max} = 10$ and $N_c = 20$ is sufficient to achieve an acceptable level of convergence. The system of differential equations

(3.22) was solved using the Runge-Kutta method for the z component of the projectile position in the range of $[-100, 100]$ at all incident projectile energies. As mentioned in the previous chapter, results also depend on the choice of b_{\max} , the upper limit for the impact parameter. In our calculations we set $b_{\max} = 50$. Increasing this parameter further had no significant effect on the final results.

6.1 Convergence studies

In this section, we describe the results of the convergence study with respect to the maximum orbital-angular momentum number l_{\max} . Fig. 6.1 presents the cross section for electron capture, ionisation and elastic scattering in proton scattering on the excited $2s$ state of atomic hydrogen. The cross sections are given as functions of the projectile energy within the range from 10 keV to 1 MeV. It can be seen that the results are convergent for all processes at all considered energies. In general, reasonable convergence is achieved with $l_{\max} = 6$, while the rates of convergence for elastic scattering and electron capture are faster than that for ionisation. It should be pointed out that at higher energies convergence can be achieved even with smaller l_{\max} .

Similar results for proton scattering on the $2p_0$ and $2p_2$ states of hydrogen are demonstrated in Fig. 6.2. One can see that the ionisation cross section converges a bit slower in comparison with that for electron capture and elastic scattering. A sufficient level of convergence is achieved with $l_{\max} = 6$ for all processes. Therefore, in calculations we set this value for maximum orbital quantum number to produce the final results. As in the case of scattering on the $2s$ state, a faster convergence is observed at higher energies for all the considered channels. At energies above 50 keV, results with $l_{\max} = 2$ approximate the final results perfectly well.

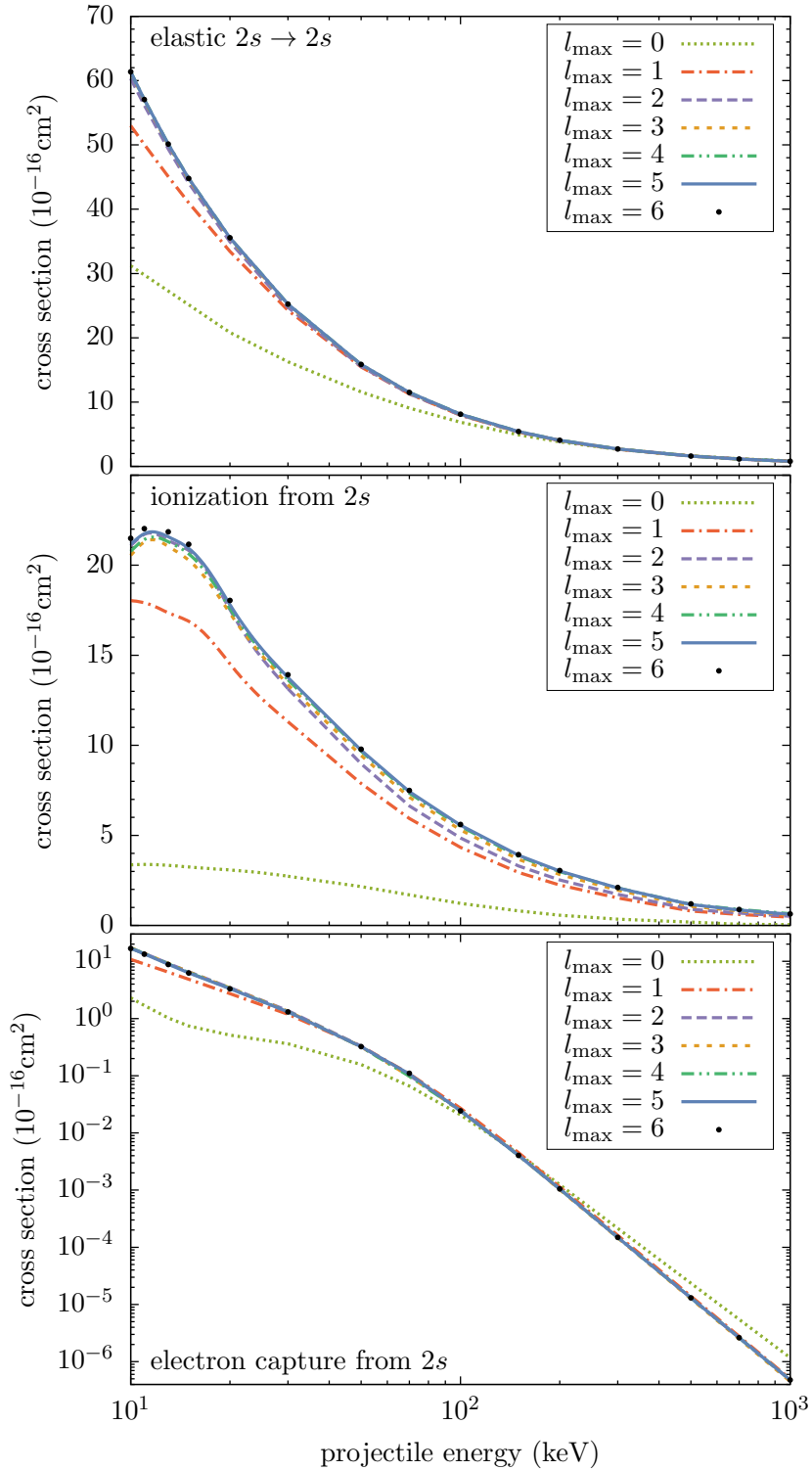


Figure 6.1: Cross sections for elastic scattering, electron capture and ionisation in p -H($2s$) collisions: convergence of the present WP-CCC results with respect to l_{max} .

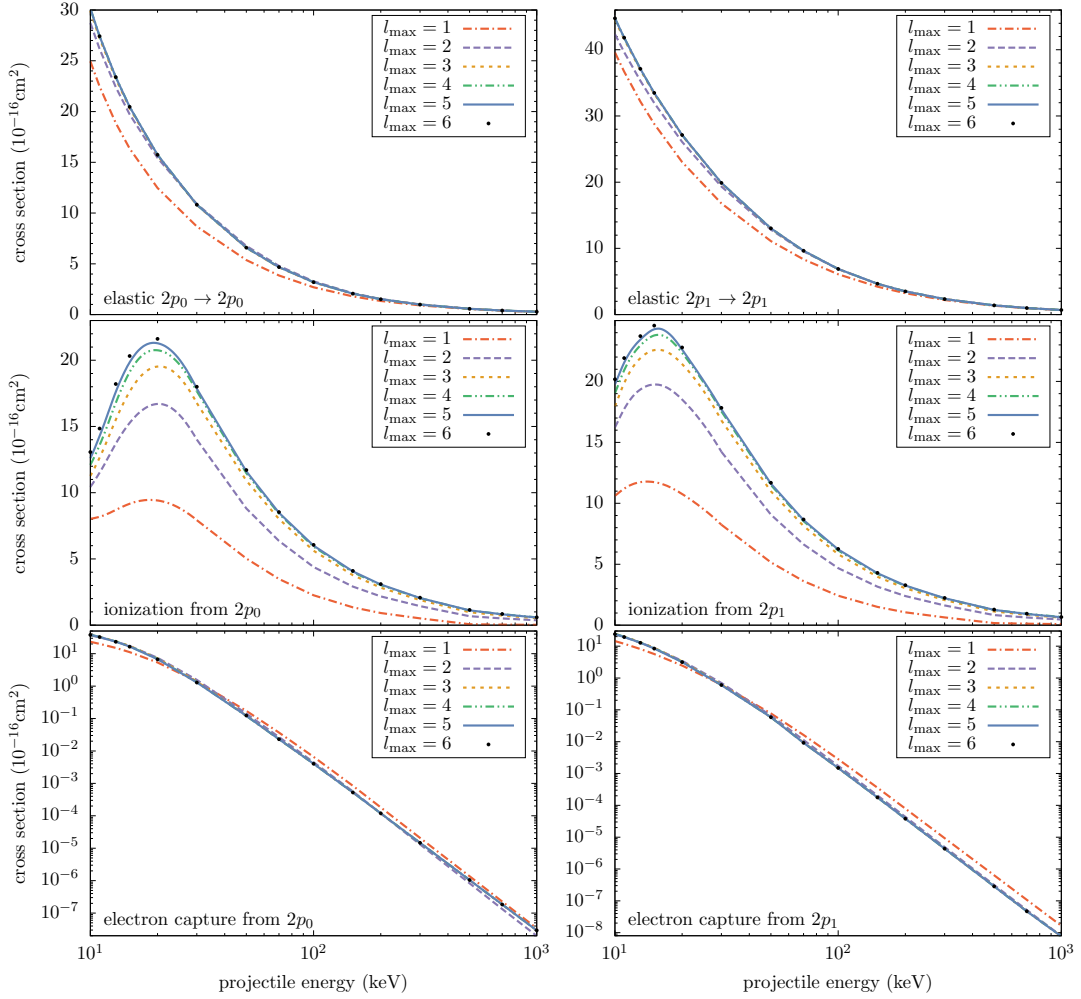


Figure 6.2: Cross sections for elastic scattering, electron capture and ionisation in $p\text{-H}(2p_0)$ and $p\text{-H}(2p_1)$ collisions: convergence of the WP-CCC results with respect to l_{\max} .

6.2 Final results for proton scattering on excited states of hydrogen

As was discussed in the previous section, setting $n_{\max} = 10$, $l_{\max} = 6$ and $N_c = 20$ was sufficient to obtain convergent results for elastic scattering, electron capture and ionisation at all considered energies. The basis with these parameters consists of the 1022 states on each centre. In this section we discuss the final WP-CCC results with the basis of this size, and make comparisons with

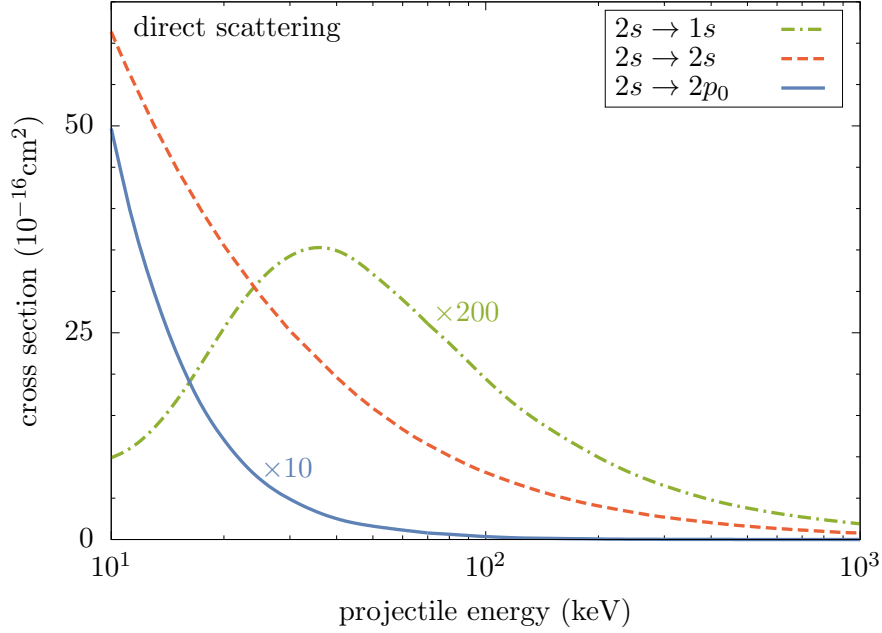


Figure 6.3: Cross sections for super-elastic ($2s \rightarrow 1s$), elastic ($2s \rightarrow 2s$) and quasi-elastic ($2s \rightarrow 2p_0$) scattering in p -H($2s$) collisions as functions of the incident proton energy.

the experiments and other theories whenever available.

6.2.1 Proton scattering on the $2s$ state of hydrogen

The cross sections for elastic scattering as well as for excitation and electron capture up to 3d states were calculated in the energy range from 10 keV to 1 MeV. In figure 6.3 we provide the current results for super-elastic, elastic and quasi-elastic scattering on the excited $2s$ state of atomic hydrogen. It can be seen that elastic scattering ($2s \rightarrow 2s$) is dominant, while super-elastic cross section is significantly smaller. It should also be noted that in the entire energy range, the cross sections for the transitions $2s \rightarrow 2s$ and $2s \rightarrow 2p_0$ decrease exponentially, while the cross section for the $2s \rightarrow 1s$ transition reaches its peak around 40 keV and then decreases steadily as the energy increases.

The cross sections for excitation of the $n = 3$ states of the target are given in Fig. 6.4. The results are aggregated over the magnetic quantum numbers for the final $2p$, $3p$ and $3d$ states. We can see that for the $2s \rightarrow 3s$ and $2s \rightarrow 3d$ transitions, the WP-CCC results and the calculations of Pindzola *et al.* [143] based on the atomic-orbital close-coupling with pseudostates (AOCC-PS) method have similar shapes, however there is a discrepancy in the magnitudes especially in the low-energy region. Reasonably good agreement is obtained for the $2s \rightarrow 3p$ transition below 40 keV, however the AOCC-PS results are systematically lower at higher energies. The CTMC calculations of Pindzola *et al.* [143] are in considerable disagreement with both AOCC-PS and WP-CCC results, nevertheless providing a similar pattern for the $2s \rightarrow 3p$ and $2s \rightarrow 3d$ transitions. For the $2s \rightarrow 3p$ transition, the CTMC calculations are significantly different from the other results both in terms of shape and magnitude. It should also be pointed out that the calculations based on the first Born approximation merge with the present WP-CCC results at high energies, and coincide with the present results at energies above 200 keV.

The cross sections for electron capture into the ground and excited states up to $n = 3$ shell of hydrogen are shown in Fig. 6.5. It can be observed that the cross sections for all considered transitions except for $2s \rightarrow 1s$ fall off very sharply as the energy increases. The current results for electron capture into all the selected states of atomic hydrogen are in overall good agreement with the AOCC-PS calculations [143]. However, there are some noticeable disagreements in comparison with the CTMC results [143]. The CTMC results for the $2s \rightarrow 1s$ transition are higher than other results below 20 keV and lower for the $2s \rightarrow 3d$ transition above 40 keV.

By analysing Figs. 6.4 and 6.5, and comparing the WP-CCC calculations with the AOCC-PS and CTMC results of Pindzola *et al.* [143], one can see that

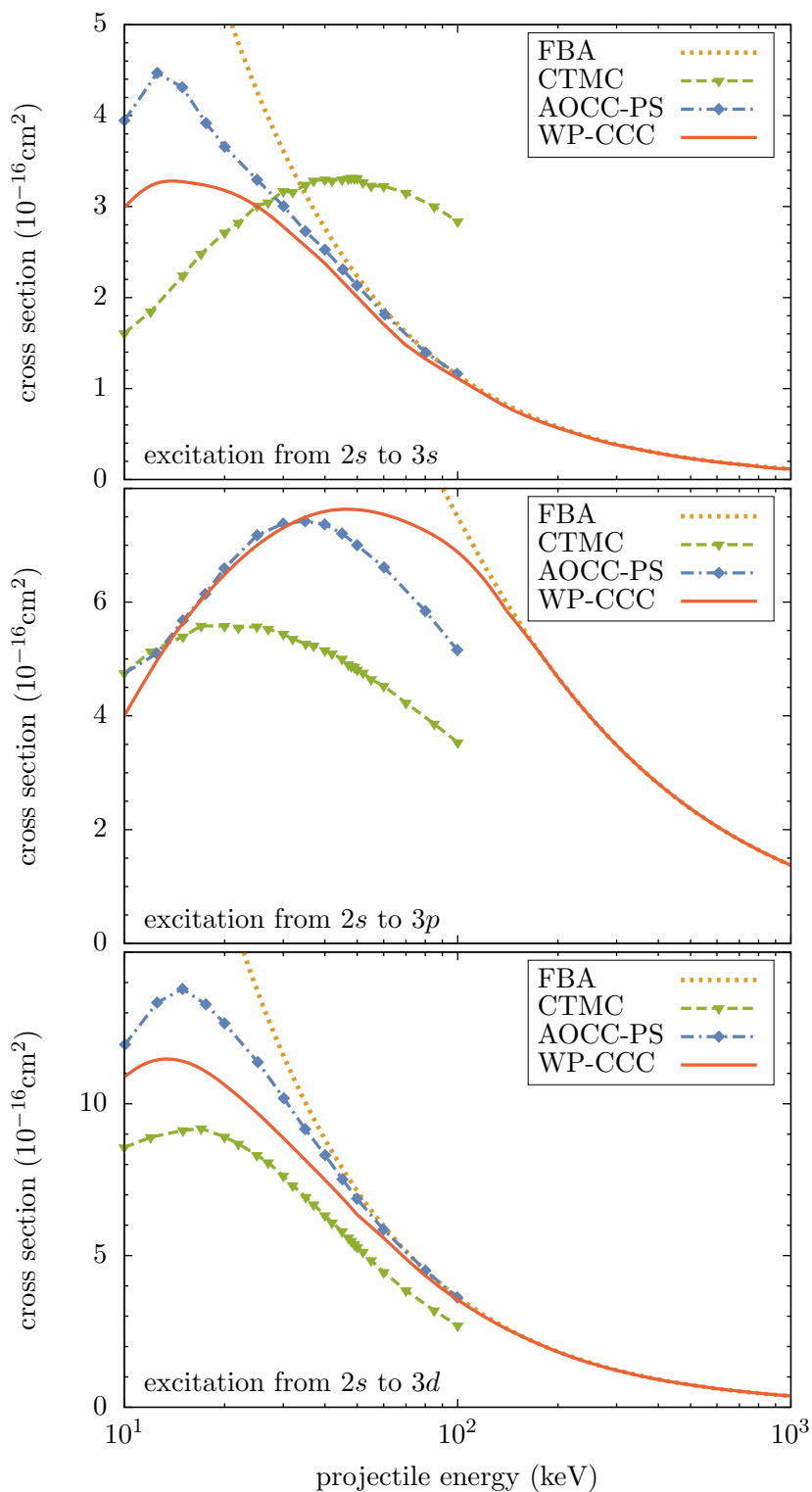


Figure 6.4: Cross sections for excitation of the $n = 3$ shell ($3s$, $3p$, $3d$) states in p - $\text{H}(2s)$ collisions as a function of the incident proton energy. The CTMC and AOCC-PS results are due to Pindzola *et al.* [143]. The FBA results are also shown for comparison.

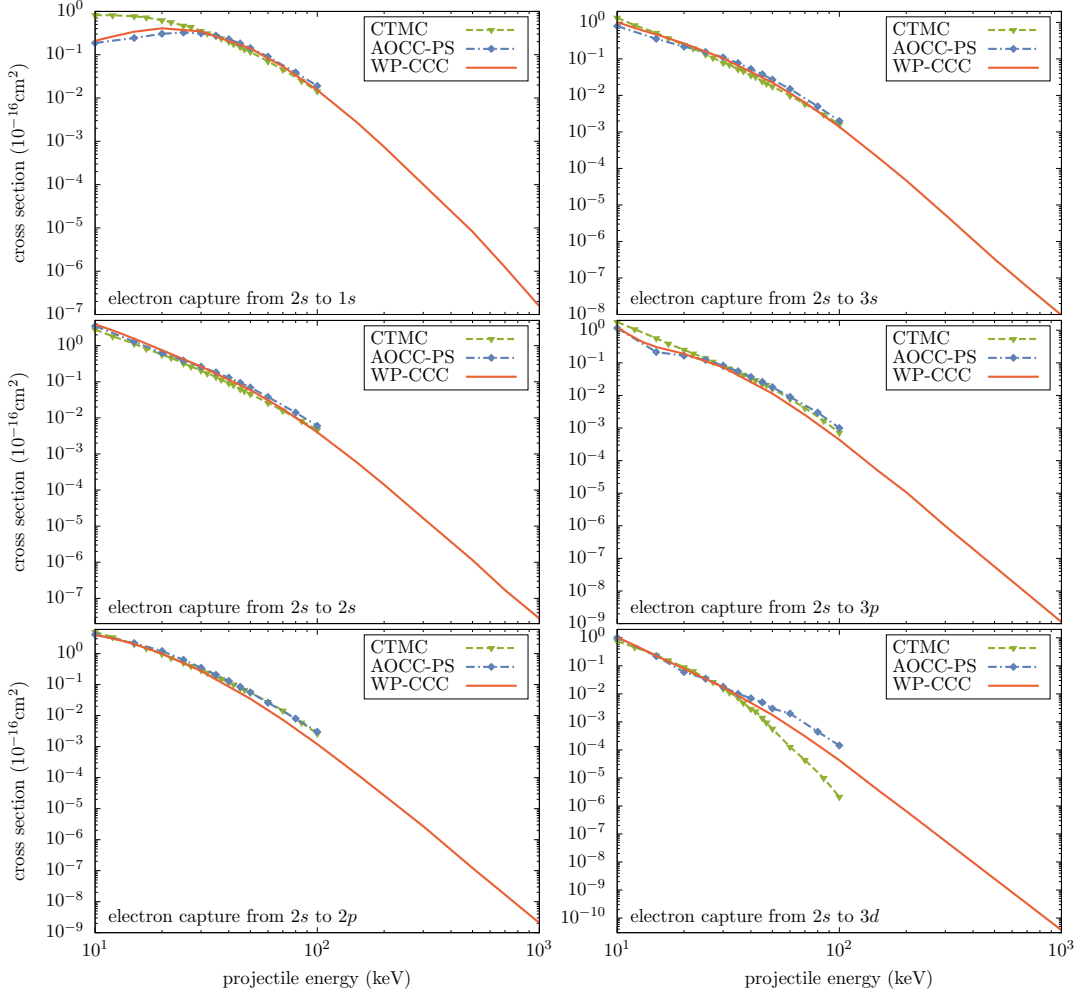


Figure 6.5: Cross sections for electron capture into the $1s$, $2s$, $2p$, $3s$, $3p$ and $3d$ states of hydrogen in $p\text{-H}(2s)$ collisions. The WP-CCC results are represented by the red solid line. The CTMC and AOCC-PS results are due to Pindzola *et al.* [143].

the agreement with AOCC-PS results is much better. However, at some energies there are discrepancies for excitation and electron capture. As described in Chapter 3, in the AOCC-PS calculations, the time-dependent Schrödinger equation of the system is solved by discretising the space on a three-dimensional Cartesian lattice. Pindzola *et al.* [143] employed the same lattice space to describe the electron-capture and excitation processes. However, the WP-CCC calculations have revealed that an accurate description of excitation requires

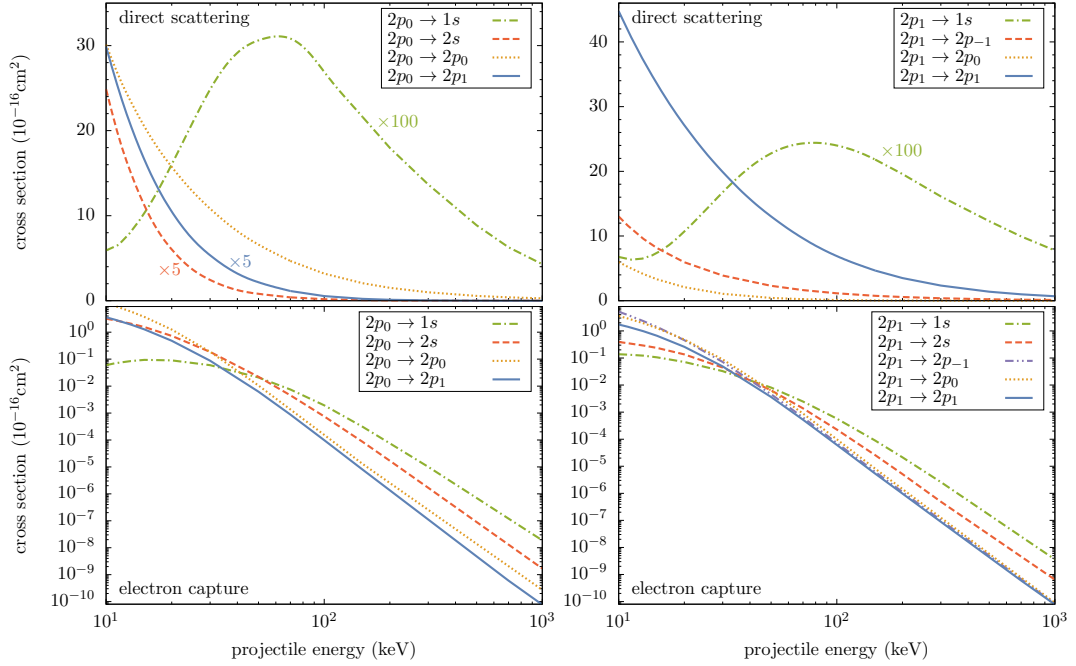


Figure 6.6: Cross sections for super-elastic, elastic and quasi-elastic scattering and electron capture for proton scattering on the excited $2p_0$ and $2p_1$ states of hydrogen as a function of the incident proton energy.

significantly larger space, which is most likely the reason for the observed difference between the results.

6.2.2 Proton scattering on the $2p_0$ and $2p_1$ states of hydrogen

In Fig. 6.6 we provide the energy dependence of the cross sections for elastic scattering and electron capture in proton scattering on the excited $2p_0$ and $2p_1$ states of hydrogen. We can see that the electron-capture cross sections for all transitions decrease monotonically and exhibit exponential fall off above a certain point as the energy increases. Below 30 keV, the cross section for electron capture into the ground state of hydrogen lower than other transition cross sections, while at high energies it is dominant for both $p\text{-H}(2p_0)$ and $p\text{-H}(2p_1)$ collisions.

Table 6.1: Density matrix elements $\rho_{\alpha'\alpha}^{2s}$ (in 10^{-16}cm^2) for excitation of H($2s$) into the final $n=1-4$ shell states of the target by proton impact at 50 keV. Notation: A[-N] implies $A \times 10^{-N}$, the final states α' and α are given in nlm notations.

α'	α	Re	Im	α'	α	Re	Im	α'	α	Re	Im	α'	α	Re	Im
100	100	1.60[-1]	0	210	321	-1.68[-2]	1.63[-1]	310	420	-6.65[-3]	1.64[-2]	400	431	1.73[-1]	3.40[-2]
100	200	-1.21	8.42[-1]	210	322	-2.85[-1]	3.18[-2]	310	421	3.06[-1]	5.64[-2]	400	432	8.43[-2]	1.06[-1]
100	210	-6.68[-2]	1.19[-1]	210	410	1.43[-1]	8.69[-2]	310	422	-3.96[-1]	5.68[-1]	400	433	-7.35[-2]	1.17[-1]
100	211	4.05[-1]	1.74[-1]	210	411	-6.90[-2]	2.30[-2]	310	430	-1.70[-1]	2.19[-1]	410	410	6.39[-1]	0
100	300	2.44[-1]	-1.65[-1]	210	420	8.01[-2]	7.98[-2]	310	431	-3.56[-1]	-2.09[-1]	410	411	2.38[-2]	4.53[-1]
100	310	-5.26[-2]	1.65[-1]	210	421	1.90[-2]	4.76[-2]	310	432	-8.39[-2]	-4.71[-1]	410	420	9.20[-3]	4.57[-2]
100	311	-9.75[-3]	3.46[-2]	210	422	-1.20[-1]	3.35[-2]	310	433	4.55[-1]	-2.37[-1]	410	421	1.49[-1]	4.64[-2]
100	320	-1.63[-1]	1.57[-1]	210	430	-9.16[-2]	-6.34[-3]	311	311	2.27	0	410	422	-2.25[-1]	2.95[-1]
100	321	-6.04[-2]	1.45[-2]	210	431	-4.30[-3]	-8.69[-2]	311	321	7.08[-1]	-8.43[-1]	410	430	-1.10[-1]	7.94[-2]
100	322	-3.92[-2]	-1.14[-1]	210	432	4.60[-2]	-4.15[-2]	311	322	1.33	1.11	410	431	-1.60[-1]	-1.33[-1]
100	400	1.28[-1]	-7.45[-2]	210	433	5.55[-2]	3.06[-2]	311	411	9.19[-1]	7.75[-2]	410	432	-3.02[-2]	-2.27[-1]
100	410	-3.27[-2]	1.03[-1]	211	211	∞	0	311	421	3.67[-2]	-2.08[-1]	410	433	2.19[-1]	-1.15[-1]
100	411	-1.14[-2]	1.11[-2]	211	311	-7.14	2.28[-2]	311	422	3.20[-1]	3.30[-1]	411	411	4.11[-1]	0
100	420	-9.70[-2]	3.53[-2]	211	321	-2.86	3.59	311	431	-9.97[-2]	2.36[-1]	411	421	2.31[-2]	-1.04[-1]
100	421	-1.82[-2]	1.02[-2]	211	322	-5.55	-4.08	311	432	-3.75[-1]	4.71[-2]	411	422	1.90[-1]	1.59[-1]
100	422	-1.95[-2]	-5.94[-2]	211	411	-3.19	-9.03[-2]	311	433	-1.77[-1]	-3.88[-1]	411	431	-6.32[-2]	1.14[-1]
100	430	1.65[-2]	-6.06[-2]	211	421	-1.87[-1]	9.22[-1]	320	320	1.11	0	411	432	-1.76[-1]	2.96[-2]
100	431	4.32[-2]	2.64[-3]	211	422	-1.70	-1.25	320	321	3.80[-1]	5.52[-1]	411	433	-9.70[-2]	-1.73[-1]
100	432	1.78[-2]	1.28[-2]	211	431	6.56[-1]	-1.08	320	322	-7.04[-1]	7.21[-1]	420	420	1.41[-1]	0
100	433	-5.44[-3]	1.98[-2]	211	432	1.45	-2.14[-1]	320	420	2.63[-1]	5.51[-2]	420	421	2.00[-2]	1.65[-3]
200	200	15.9	0	211	433	6.60[-1]	1.39	320	421	1.82[-1]	6.68[-2]	420	422	2.16[-2]	4.28[-2]
200	210	1.25	-8.08[-1]	300	300	2.01	0	320	422	-1.85[-1]	3.41[-1]	420	430	-6.47[-2]	6.04[-2]
200	211	-2.41	-10.3	300	310	-1.40	1.11	320	430	-2.56[-1]	1.71[-1]	420	431	-4.44[-2]	-2.34[-2]
200	300	-4.14	-9.67[-1]	300	311	-6.19[-1]	-5.95[-1]	320	431	-2.30[-1]	-1.99[-1]	420	432	8.11[-3]	-6.53[-3]
200	310	3.39	-9.38[-1]	300	320	-1.17	5.90[-1]	320	432	1.98[-2]	-2.28[-1]	420	433	7.29[-3]	1.37[-2]
200	311	1.79[-1]	1.28	300	321	-9.23[-1]	-7.51[-2]	320	433	2.24[-1]	-4.71[-2]	421	421	4.74[-2]	0
200	320	3.24	-5.09[-1]	300	322	-1.42[-1]	-1.51	321	321	7.31[-1]	0	421	422	-2.10[-2]	1.01[-1]
200	321	1.39	9.51[-1]	300	400	8.89[-1]	-6.43[-3]	321	322	1.30[-1]	1.14	421	431	-6.24[-2]	-2.39[-2]
200	322	-1.28	2.58	300	410	-6.92[-1]	6.41[-1]	321	421	1.51[-1]	-8.48[-2]	421	432	-2.33[-2]	-5.71[-2]
200	400	-2.01	-4.63[-1]	300	411	-3.44[-1]	-3.24[-1]	321	422	6.63[-2]	3.71[-1]	421	433	4.70[-2]	-4.27[-2]
200	410	1.79	-6.57[-1]	300	420	-3.16[-1]	-8.19[-2]	321	431	-2.31[-1]	3.93[-2]	422	422	2.61[-1]	0
200	411	1.04[-1]	6.89[-1]	300	421	-2.53[-1]	8.76[-2]	321	432	-1.93[-1]	-1.61[-1]	422	432	-1.04[-1]	9.12[-2]
200	420	1.03	2.58[-1]	300	422	-1.07[-1]	-6.14[-1]	321	433	9.44[-2]	-2.47[-1]	422	433	-1.30[-1]	-6.27[-2]
200	421	4.82[-1]	8.74[-2]	300	430	2.03[-1]	-2.98[-1]	322	322	1.90	0	430	430	9.18[-2]	0
200	422	-4.53[-1]	1.12	300	431	3.97[-1]	4.74[-2]	322	422	6.53[-1]	4.41[-3]	430	431	2.34[-2]	7.90[-2]
200	430	-6.77[-1]	5.75[-1]	300	432	2.26[-1]	2.27[-1]	322	432	-2.99[-1]	2.80[-1]	430	432	-3.72[-2]	4.04[-2]
200	431	-6.66[-1]	-4.74[-1]	300	433	-1.37[-1]	2.90[-1]	322	433	-3.96[-1]	-1.97[-1]	430	433	-4.80[-2]	-2.67[-2]
200	432	-1.23[-1]	-5.84[-1]	310	310	3.08	0	400	400	4.06[-1]	0	431	431	9.82[-2]	0
200	433	5.20[-1]	-3.09[-1]	310	311	1.54[-1]	2.38	400	410	-3.11[-1]	2.58[-1]	431	432	5.48[-2]	6.19[-2]
210	210	1.62[-1]	0	310	320	1.15	-3.42[-1]	400	411	-1.15[-1]	-1.43[-1]	431	433	-4.11[-2]	7.30[-2]
210	211	6.20[-1]	-6.35[-1]	310	321	1.14	8.75[-1]	400	420	-1.61[-1]	-2.61[-2]	432	432	9.02[-2]	0
210	310	2.22[-1]	1.87[-1]	310	322	-1.27	1.84	400	421	-1.11[-1]	2.78[-2]	432	433	3.34[-2]	9.13[-2]
210	311	-1.29[-1]	2.68[-2]	310	410	1.31	7.09[-3]	400	422	-2.16[-2]	-2.65[-1]	433	433	1.08[-1]	0
210	320	2.70[-1]	1.98[-1]	310	411	2.19[-2]	1.02	400	430	9.79[-2]	-1.37[-1]				

Table 6.2: Density matrix elements $\rho_{\alpha'\alpha}^{2p_0}$ (in 10^{-16}cm^2) for excitation of $\text{H}(2p_0)$ into the final $n=1-4$ shell states of the target by proton impact at 50 keV. Notation: $A[-N]$ implies $A \times 10^{-N}$, the final states α' and α are given in nlm notations.

α'	α	Re	Im	α'	α	Re	Im	α'	α	Re	Im	α'	α	Re	Im
100	100	3.06[-1]	0	210	321	1.57[-1]	2.40	310	420	-5.49[-1]	6.56[-1]	400	431	-1.03[-1]	-2.26[-2]
100	200	1.88[-1]	-4.57[-2]	210	322	1.58[-1]	-1.44[-1]	310	421	-6.55[-1]	-5.12[-1]	400	432	4.33[-3]	-6.79[-2]
100	210	-1.14	-2.81[-1]	210	410	-8.09[-1]	-4.61[-1]	310	422	3.89[-2]	9.78[-2]	400	433	-8.00[-3]	3.13[-3]
100	211	-2.01[-1]	-2.00[-1]	210	411	3.40[-1]	2.51[-1]	310	430	3.38[-1]	-4.77[-1]	410	410	2.77[-1]	0
100	300	-3.95[-2]	-3.94[-2]	210	420	1.05	-1.63[-1]	310	431	4.25[-1]	-5.50[-2]	410	411	-1.02[-1]	4.13[-2]
100	310	3.78[-1]	3.41[-1]	210	421	7.00[-2]	1.09	310	432	7.40[-2]	2.58[-1]	410	420	-2.18[-1]	3.44[-1]
100	311	-1.36[-1]	-1.16[-1]	210	422	8.92[-2]	-1.39[-1]	310	433	2.59[-2]	-2.20[-2]	410	421	-3.41[-1]	-1.95[-1]
100	320	-6.96[-1]	2.71[-1]	210	430	-9.82[-1]	2.44[-1]	311	311	2.19[-1]	0	410	422	2.56[-2]	4.46[-2]
100	321	-1.90[-1]	-7.21[-1]	210	431	-3.57[-1]	-3.95[-1]	311	321	4.42[-1]	8.91[-1]	410	430	1.51[-1]	-2.52[-1]
100	322	-4.25[-2]	5.29[-2]	210	432	2.26[-1]	-2.44[-1]	311	322	2.53[-2]	-6.58[-2]	410	431	1.91[-1]	-5.15[-2]
100	400	-2.61[-2]	-5.47[-2]	210	433	-4.00[-2]	-1.42[-2]	311	411	1.13[-1]	-1.13[-2]	410	432	5.04[-2]	1.11[-1]
100	410	1.71[-1]	2.05[-1]	211	211	4.30[-1]	0	311	421	1.69[-1]	3.49[-1]	410	433	9.84[-3]	-1.16[-2]
100	411	-8.26[-2]	-6.95[-2]	211	311	2.94[-1]	-5.36[-2]	311	422	-3.13[-3]	-5.09[-2]	411	411	6.23[-2]	0
100	420	-3.38[-1]	4.02[-2]	211	321	9.45[-1]	1.03	311	431	-2.01[-1]	-7.76[-2]	411	421	7.93[-2]	1.78[-1]
100	421	-4.87[-2]	-3.39[-1]	211	322	9.90[-3]	-1.06[-1]	311	432	3.11[-2]	-1.34[-1]	411	422	1.72[-4]	-2.76[-2]
100	422	-2.36[-2]	4.27[-2]	211	411	1.53[-1]	-3.92[-2]	311	433	-1.71[-2]	3.42[-3]	411	431	-9.61[-2]	-4.37[-2]
100	430	2.64[-1]	-7.23[-3]	211	421	3.64[-1]	4.32[-1]	320	320	6.80	0	411	432	1.93[-2]	-6.48[-2]
100	431	1.28[-1]	9.65[-2]	211	422	-1.96[-2]	-7.32[-2]	320	321	-2.58[-1]	6.13	411	433	-8.57[-3]	1.22[-3]
100	432	-4.49[-2]	8.78[-2]	211	431	-3.03[-1]	-2.95[-2]	320	322	3.41[-1]	-2.11[-1]	420	420	8.28[-1]	0
100	433	1.24[-2]	8.57[-5]	211	432	-1.29[-2]	-1.94[-1]	320	420	2.22	3.34[-1]	420	421	2.61[-2]	8.07[-1]
200	200	1.61[-1]	0	211	433	-2.14[-2]	1.22[-2]	320	421	-2.90[-1]	2.22	420	422	3.85[-2]	-8.90[-2]
200	210	-8.30[-1]	-4.26[-1]	300	300	3.05[-1]	0	320	422	1.31[-1]	-2.08[-1]	420	430	-4.92[-1]	1.19[-1]
200	211	-3.81[-2]	-1.88[-1]	300	310	-2.48[-1]	-1.55[-1]	320	430	-1.26	2.52[-1]	420	431	-3.31[-1]	-2.96[-1]
200	300	3.17[-2]	-9.28[-2]	300	311	2.12[-1]	-1.81[-2]	320	431	-8.23[-1]	-9.62[-1]	420	432	1.55[-1]	-2.38[-1]
200	310	1.37[-1]	2.67[-1]	300	320	1.23	-3.70[-1]	320	432	5.34[-1]	-6.11[-1]	420	433	-3.58[-2]	-5.42[-3]
200	311	-3.95[-2]	-1.34[-1]	300	321	3.36[-1]	1.10	320	433	-9.78[-2]	-3.11[-2]	421	421	8.18[-1]	0
200	320	-3.50[-1]	-2.32[-1]	300	322	3.64[-2]	-5.59[-2]	321	321	5.71	0	421	422	-9.02[-2]	-4.49[-2]
200	321	2.83[-1]	-3.58[-1]	300	400	1.19[-1]	1.22[-2]	321	322	-2.26[-1]	-3.20[-1]	421	431	-3.07[-1]	3.28[-1]
200	322	-4.12[-2]	3.24[-3]	300	410	-9.84[-2]	-6.78[-2]	321	421	2.10	1.86[-1]	421	432	-2.42[-1]	-1.62[-1]
200	400	1.76[-2]	-5.85[-2]	300	411	9.45[-2]	-2.51[-2]	321	422	-2.11[-1]	-1.24[-1]	421	433	-5.49[-3]	3.70[-2]
200	410	6.19[-2]	1.45[-1]	300	420	3.85[-1]	-9.46[-2]	321	431	-8.77[-1]	8.03[-1]	422	422	1.42[-2]	0
200	411	-3.15[-2]	-7.66[-2]	300	421	1.07[-1]	3.79[-1]	321	432	-6.01[-1]	-4.84[-1]	422	432	3.52[-2]	5.00[-3]
200	420	-1.64[-1]	-1.08[-1]	300	422	-1.88[-3]	-4.39[-2]	321	433	-2.46[-2]	9.60[-2]	422	433	-1.55[-3]	-4.37[-3]
200	421	1.19[-1]	-1.63[-1]	300	430	-1.68[-1]	1.79[-1]	322	322	3.20[-2]	0	430	430	3.88[-1]	0
200	422	-3.05[-2]	1.22[-2]	300	431	-2.12[-1]	-1.12[-1]	322	422	1.93[-2]	-6.22[-3]	430	431	1.33[-1]	2.28[-1]
200	430	1.72[-1]	7.52[-2]	300	432	5.16[-2]	-1.46[-1]	322	432	5.48[-2]	-1.49[-2]	430	432	-1.29[-1]	1.02[-1]
200	431	6.26[-4]	1.04[-1]	300	433	-1.93[-2]	1.42[-3]	322	433	-5.11[-3]	-5.68[-3]	430	433	1.81[-2]	9.50[-3]
200	432	-6.77[-2]	6.63[-3]	310	310	1.07	0	400	400	5.77[-2]	0	431	431	2.54[-1]	0
200	433	4.48[-3]	7.80[-3]	310	311	-3.94[-1]	1.18[-1]	400	410	-7.34[-2]	-1.51[-2]	431	432	2.64[-2]	1.64[-1]
210	210	6.60	0	310	320	-1.05	1.88	400	411	4.97[-2]	-2.09[-2]	431	433	1.77[-2]	-1.22[-2]
210	211	7.24[-1]	7.03[-1]	310	321	-1.69	-1.11	400	420	1.59[-1]	-9.28[-2]	432	432	1.10[-1]	0
210	310	-1.59	-7.48[-1]	310	322	9.74[-3]	1.54[-1]	400	421	1.03[-1]	1.50[-1]	432	433	-6.36[-3]	-1.32[-2]
210	311	5.42[-1]	4.56[-1]	310	410	5.35[-1]	7.28[-2]	400	422	-7.47[-3]	-2.34[-2]	433	433	2.02[-3]	0
210	320	2.18	-4.75[-1]	310	411	-2.13[-1]	6.50[-2]	400	430	-7.43[-2]	1.02[-1]				

Table 6.3: Density matrix elements $\rho_{\alpha'\alpha}^{2p_1}$ (in 10^{-16}cm^2) for excitation of $\text{H}(2p_1)$ into the final $n=1-4$ shell states of the target by proton impact at 50 keV. Notation: $A[-N]$ implies $A \times 10^{-N}$, the final states α' and α are given in nlm notations.

α'	α	Re	Im	α'	α	Re	Im	α'	α	Re	Im	α'	α	Re	Im
100	100	2.28[-1]	0	210	321	-8.87[-1]	7.04[-1]	310	420	-1.69[-1]	-3.33[-2]	400	431	1.29[-2]	8.12[-4]
100	200	-1.23	2.32[-1]	210	322	-1.17	-1.28	310	421	2.58[-2]	-2.82[-1]	400	432	-2.96[-2]	2.05[-2]
100	210	-1.84[-1]	1.60[-1]	210	410	-4.66[-2]	-4.82[-2]	310	422	4.19[-1]	1.95[-2]	400	433	-3.68[-2]	-2.76[-2]
100	211	6.69[-1]	-1.29	210	411	3.79[-1]	-7.70[-2]	310	430	8.06[-2]	-2.76[-2]	410	410	2.08[-2]	0
100	300	-1.75[-1]	-6.42[-2]	210	420	1.36[-1]	2.12[-1]	310	431	2.90[-2]	1.55[-1]	410	411	-1.12[-2]	5.09[-2]
100	310	6.68[-2]	2.27[-2]	210	421	-3.80[-1]	3.27[-1]	310	432	-1.55[-1]	9.14[-2]	410	420	-5.62[-2]	-2.81[-2]
100	311	-3.80[-1]	5.19[-1]	210	422	-5.28[-1]	-5.43[-1]	310	433	-1.27[-1]	-1.26[-1]	410	421	3.11[-2]	-8.77[-2]
100	320	-1.57[-1]	5.04[-3]	210	430	-9.08[-2]	-3.96[-2]	311	311	2.28	0	410	422	1.29[-1]	4.29[-2]
100	321	-1.40[-1]	-4.39[-1]	210	431	1.74[-1]	-2.06[-1]	311	321	-1.77	1.15	410	430	3.31[-2]	-1.30[-3]
100	322	6.86[-1]	-2.16[-1]	210	432	2.79[-1]	6.56[-2]	311	322	-1.89	-2.61	410	431	-1.20[-3]	5.12[-2]
100	400	-6.72[-2]	-3.14[-2]	210	433	1.03[-2]	2.76[-1]	311	411	1.00	4.02[-2]	410	432	-5.92[-2]	1.56[-2]
100	410	1.35[-2]	1.03[-2]	211	211	13.0	0	311	421	-8.49[-1]	5.82[-1]	410	433	-3.16[-2]	-5.67[-2]
100	411	-1.93[-1]	2.27[-1]	211	311	-3.90	-6.00[-1]	311	422	-9.26[-1]	-1.17	411	411	4.58[-1]	0
100	420	-7.26[-2]	3.79[-3]	211	321	2.64	-5.18[-1]	311	431	4.40[-1]	-3.59[-1]	411	421	-3.29[-1]	2.35[-1]
100	421	-4.16[-2]	-2.40[-1]	211	322	7.40[-1]	4.54	311	432	4.97[-1]	1.95[-1]	411	422	-3.62[-1]	-4.54[-1]
100	422	3.59[-1]	-8.02[-2]	211	411	-1.90	-3.09[-1]	311	433	-5.87[-2]	4.94[-1]	411	431	1.78[-1]	-1.43[-1]
100	430	8.67[-4]	-1.58[-2]	211	421	1.36	-3.70[-1]	320	320	1.45	0	411	432	1.85[-1]	7.88[-2]
100	431	1.69[-2]	1.25[-1]	211	422	4.78[-1]	2.14	320	321	3.04[-1]	2.50	411	433	-3.26[-2]	1.85[-1]
100	432	-7.69[-2]	8.26[-2]	211	431	-7.77[-1]	2.87[-1]	320	322	-3.68	5.99[-1]	420	420	2.28[-1]	0
100	433	-9.22[-2]	-4.25[-2]	211	432	-4.91[-1]	-5.82[-1]	320	420	5.52[-1]	-6.96[-2]	420	421	6.10[-3]	3.72[-1]
200	200	∞	0	211	433	4.48[-1]	-5.79[-1]	320	421	1.20[-1]	9.04[-1]	420	422	-5.60[-1]	2.98[-2]
200	210	1.88	-2.30	300	300	3.29[-1]	0	320	422	-1.33	2.13[-1]	420	430	-9.32[-2]	6.68[-2]
200	211	-9.21[-1]	8.17	300	310	2.97[-2]	-4.93[-2]	320	430	-2.14[-1]	2.04[-1]	420	431	-5.89[-2]	-1.78[-1]
200	300	-7.02[-1]	2.88[-1]	300	311	2.23[-1]	-3.51[-1]	320	431	-2.17[-1]	-4.04[-1]	420	432	1.80[-1]	-1.52[-1]
200	310	-1.80	3.56[-1]	300	320	-2.78[-1]	-7.09[-2]	320	432	3.94[-1]	-4.33[-1]	420	433	1.99[-1]	1.38[-1]
200	311	2.85	-4.58	300	321	1.80[-1]	-3.44[-1]	320	433	5.22[-1]	2.83[-1]	421	421	7.03[-1]	0
200	320	6.02	1.14	300	322	4.64[-1]	3.25[-1]	321	321	4.69	0	421	422	5.13[-2]	1.04
200	321	-5.57[-1]	12.3	300	400	1.27[-1]	2.16[-2]	321	322	2.36[-1]	6.76	421	431	-3.41[-1]	7.75[-2]
200	322	-16.5	-2.35[-1]	300	410	1.79[-2]	-3.02[-2]	321	421	1.70	3.29[-2]	421	432	-2.61[-1]	-3.17[-1]
200	400	-3.75[-1]	3.92[-2]	300	411	1.28[-1]	-1.66[-1]	321	422	4.40[-2]	2.53	421	433	2.37[-1]	-3.33[-1]
200	410	-5.19[-1]	2.00[-1]	300	420	-8.03[-2]	-1.74[-2]	321	431	-8.08[-1]	2.55[-1]	422	422	1.58	0
200	411	1.14	-1.74	300	421	7.95[-2]	-1.53[-2]	321	432	-6.79[-1]	-8.08[-1]	422	432	-4.92[-1]	3.73[-1]
200	420	2.41	1.74[-1]	300	422	1.80[-2]	1.67[-1]	321	433	6.19[-1]	-8.45[-1]	422	433	-4.94[-1]	-3.68[-1]
200	421	-2.39[-1]	3.99	300	430	7.29[-2]	-4.53[-2]	322	322	1.01	0	430	430	6.57[-2]	0
200	422	-6.41	-1.37[-1]	300	431	2.19[-2]	-1.49[-2]	322	422	3.85	1.23[-1]	430	431	-2.01[-2]	8.44[-2]
200	430	-9.89[-1]	7.05[-1]	300	432	-6.33[-2]	1.13[-2]	322	432	-1.26	9.50[-1]	430	432	-1.16[-1]	6.17[-3]
200	431	-6.30[-1]	-2.05	300	433	-3.95[-2]	-8.20[-2]	322	433	-1.25	-9.92[-1]	430	433	-3.64[-2]	-1.17[-1]
200	432	2.09	-1.63	310	310	1.45[-1]	0	400	400	5.73[-2]	0	431	431	1.92[-1]	0
200	433	2.02	1.61	310	311	-1.47[-1]	3.76[-1]	400	410	7.86[-3]	-1.86[-2]	431	432	8.27[-2]	1.91[-1]
210	210	4.30[-1]	0	310	320	-3.92[-1]	-1.55[-1]	400	411	5.32[-2]	-6.80[-2]	431	433	-1.59[-1]	1.24[-1]
210	211	-1.30	9.50[-1]	310	321	1.55[-1]	-7.04[-1]	400	420	-4.64[-2]	6.32[-3]	432	432	2.54[-1]	0
210	310	-1.25[-1]	-1.74[-1]	310	322	1.06	1.33[-1]	400	421	1.94[-2]	-2.52[-2]	432	433	6.72[-2]	2.46[-1]
210	311	9.02[-1]	-1.75[-1]	310	410	4.94[-2]	-1.21[-2]	400	422	4.62[-2]	4.35[-2]	433	433	2.64[-1]	0
210	320	2.49[-1]	5.33[-1]	310	411	-4.10[-2]	1.54[-1]	400	430	2.87[-2]	-2.79[-2]				

For direct scattering, the super-elastic cross sections for the $2p_0 \rightarrow 1s$ and $2p_1 \rightarrow 1s$ transitions are much smaller than the cross sections for elastic and quasi elastic scattering. The cross sections for super-elastic scattering increase at the beginning for both transitions reaching their peaks around 60 keV and 80 keV, respectively, then decline almost linearly as the energy increases. The cross sections for the remaining transitions show exponential decay on the entire energy range.

6.2.3 The density matrix

With the formula described in Chapter 5 we are able to generate the density matrices for various projectile energies. As an example, in tables 6.1–6.3 we present the results of our calculations for density matrices in 50 keV proton scattering on the excited $2s$, $2p_0$ and $2p_1$ states of atomic hydrogen. The calculations are provided for excitation of these states into the $n = 1-4$ -shell states. The data on the density matrix elements are of great importance in fusion plasma diagnostics, where the density matrix elements are required for modelling the injection of neutral hydrogen beams.

6.3 Chapter summary

We applied the two-centre WP-CCC approach, described in Chapter 3, to calculate the cross sections for excitation, ionisation and electron capture in proton collisions with the $2s$, $2p_0$ and $2p_1$ states of hydrogen. We first demonstrated convergence of the cross sections for all considered processes by increasing the maximum orbital quantum number of included states at all energies. Convergence of the results was slightly slower at lower energies, but at energies above 100 keV the results converged significantly faster. Once the convergence was

achieved, we presented the cross sections for elastic scattering, electron capture and ionisation from all selected excited states of hydrogen at the impact energies from 10 keV to 1 MeV. We observed significant disagreement in comparison with the AOCC and the CTMC calculations for scattering on the 2s state of hydrogen. We emphasise that the reason for the discrepancy with the former might be not sufficient discretisation of the three-dimensional Cartesian lattice employed by Pindzola *et al.* [143]. Overall good agreement was obtained for the other states. We also provided the cross sections data for transitions into particular states for the first time.

Chapter 7

C^{6+} -H collisions

In this chapter, we describe the results of the single- and two-centre WP-CCC calculations for collisions of bare ions with atomic hydrogen. The underlying theory and calculation details were given in Chapter 3. The convergence of the calculated cross sections with respect to the maximum allowed orbital angular momentum number l_{max} is demonstrated for all underlying processes. The final results are compared with the experimental data and other theoretical results.

To obtain the total cross sections, we fixed the maximum principal number at $n_{\text{max}} = 10$ and the number of bins at $N_c = 20$. These values were sufficient for the integrated cross sections, however a denser discretisation of the continuum was required to obtain convergent differential cross sections, which will be specified later. Other parameters, such as the maximum allowed energy ε_{max} of the ejected electron and maximum impact parameter b_{max} were chosen sufficiently large depending on the considered process. The total cross sections for electron capture and ionisation are calculated for impact energies up to 10 MeV/amu. We also provide the singly and doubly differential cross sections for ionisation in terms of the ejected-electron energy and angle at higher projectile energies (1 and 2 MeV/amu).

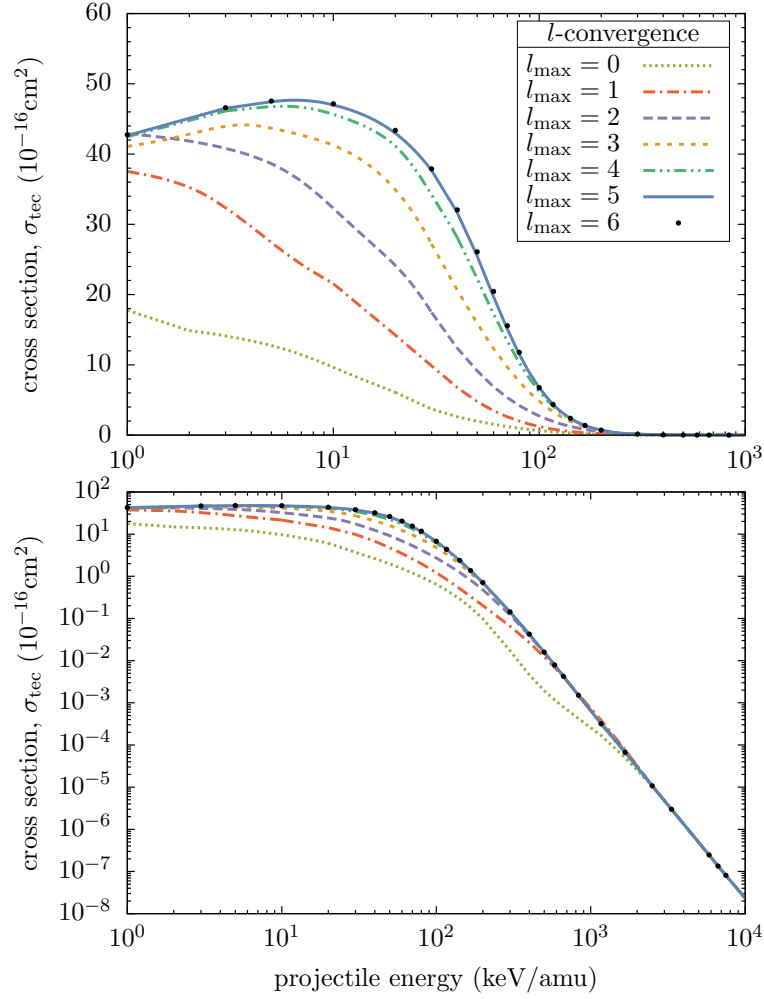


Figure 7.1: Total cross section for electron capture in C^{6+} -H(1s) collisions: convergence of the present WP-CCC results with respect to l_{\max} (top and bottom panels are on linear and logarithmic y scales, respectively).

7.1 Convergence studies

We first investigate the convergence of the total cross section for electron capture in C^{6+} -H(1s) collisions with respect to the maximum orbital quantum number, l_{\max} , of the included states. The results of calculations for different values of l_{\max} up to 6 are represented in Fig. 7.1. The cross sections are provided for the projectile energies ranging from 1 keV/amu to 10 MeV/amu on linear y scale

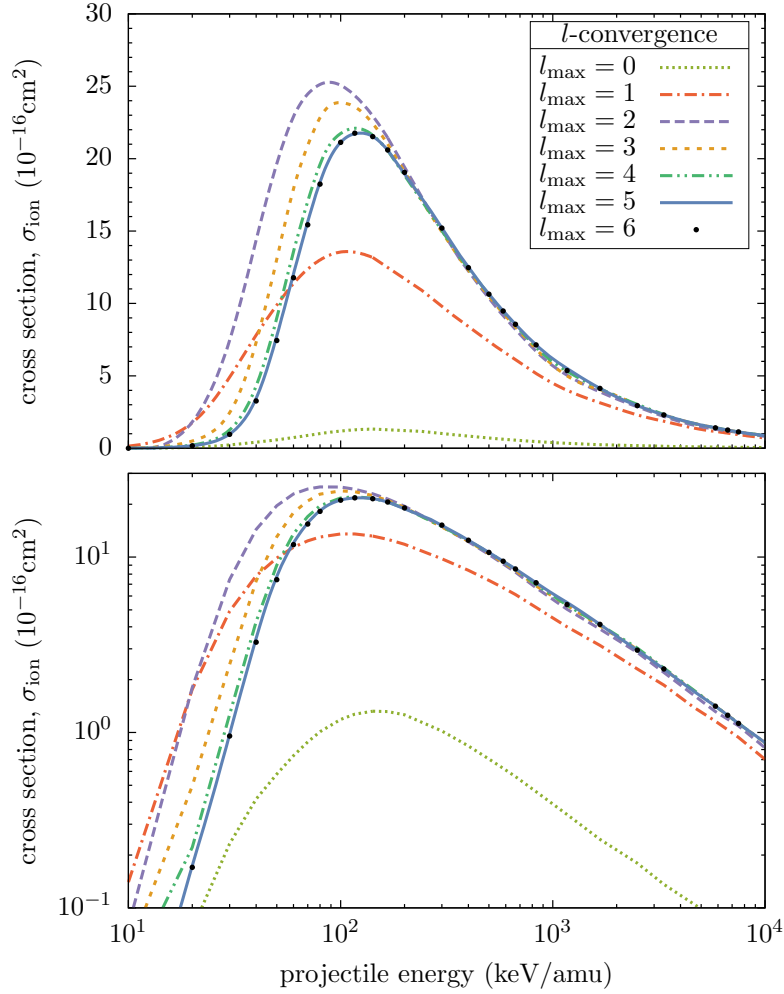


Figure 7.2: Total cross section for ionisation in C^{6+} -H($1s$) collisions: convergence of the present WP-CCC results with respect to l_{\max} (top and bottom panels are on linear and logarithmic y scales, respectively).

(the upper panel), and the same in logarithmic y scale (the lower panel) to highlight the higher energy region. A systematic convergence of the results can be observed with increasing the values of l_{\max} . An acceptable level of convergence is achieved with $l_{\max} = 6$ at all considered energies. However, the rate of convergence is faster at higher energies. The results are sufficiently convergent even with $l_{\max} = 2$ above 500 keV/amu.

In Fig. 7.2, we show the present total cross section for ionisation of hydro-

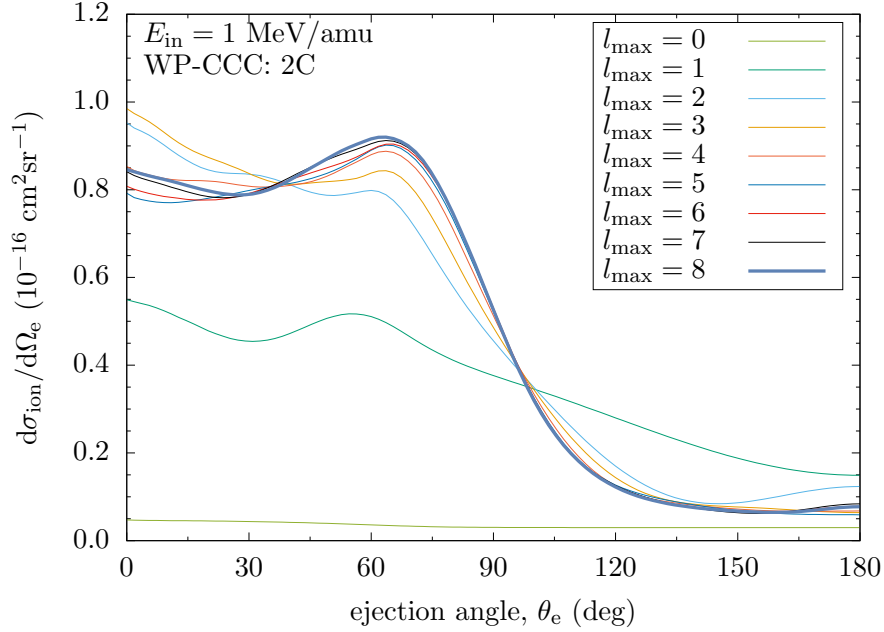


Figure 7.3: Singly differential cross section in the ejected-electron angle for 1 MeV/amu C^{6+} -impact ionisation of atomic hydrogen: convergence of the present two-centre WP-CCC results with respect to l_{max} .

gen by C^{6+} impact with respect to maximum allowed orbital number on linear and logarithmic y scales. As in the case for electron capture, the results for ionisation are also well convergent. One can see that the convergence is not always monotonic with increasing l_{max} . The cross sections go up until $l_{\text{max}} = 2$ and then decrease systematically and converge with $l_{\text{max}} = 6$. Here also, the convergence rate is faster at higher energies. At energies above 200 keV/amu, the cross section with $l_{\text{max}} = 2$ approximates the results with larger l_{max} very well.

The two-centre WP-CCC results for singly differential ionisation cross section with respect to l_{max} at 1 MeV/amu impact energy is presented in Fig. 7.3. We considered the entire range of the electron ejection angle. The continuum was discretised denser to obtain more accurate results and better convergence rate. The number of bins was fixed at $N_c = 30$. In comparison with the inte-

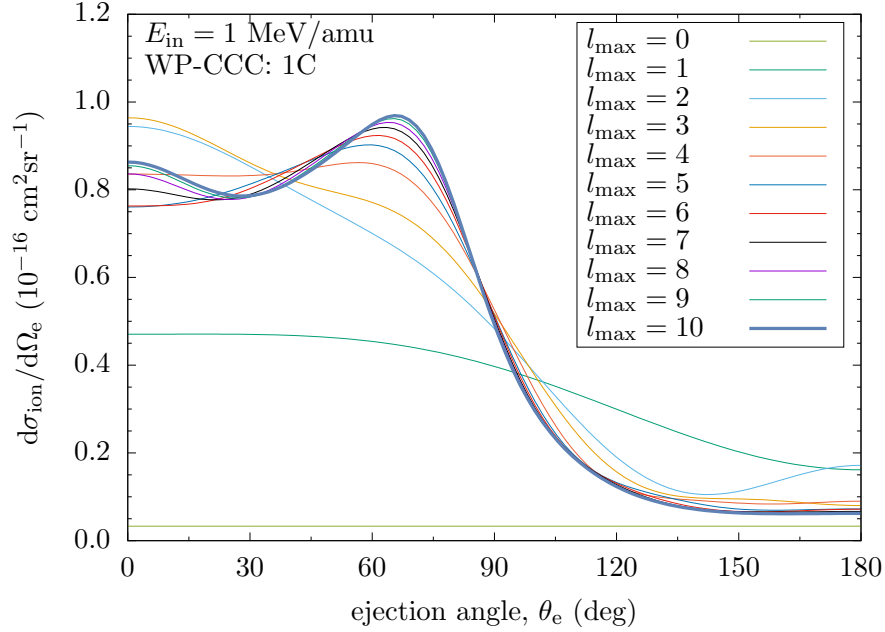


Figure 7.4: The same as in Fig. 7.3, but for the single-centre WP-CCC approach.

grated cross section, convergence of the differential ionisation cross section is not systematic and relatively slower. Nevertheless, fair convergence is achieved by performing calculations up to $l_{\max} = 8$. One can see that the differential ionisation cross section demonstrates clear convergence with increasing l_{\max} at larger ejection angles. However, at smaller ejection angles full convergence appears to require $l_{\max} = 10$.

Together with the two-centre calculations we also performed the single-centre calculations to verify the accuracy of the methods. The single-centre approach is simpler and calculations are easier to perform, though it requires including the states with larger orbital numbers. We will see later that the electron-capture cross section is very small in comparison with the cross section for ionisation at projectile energies around 1 MeV/amu and higher. Therefore, at high energies the single-centre results should reproduce the two-centre calculations reasonably well. Accordingly, the internal consistency of the calculations can be established

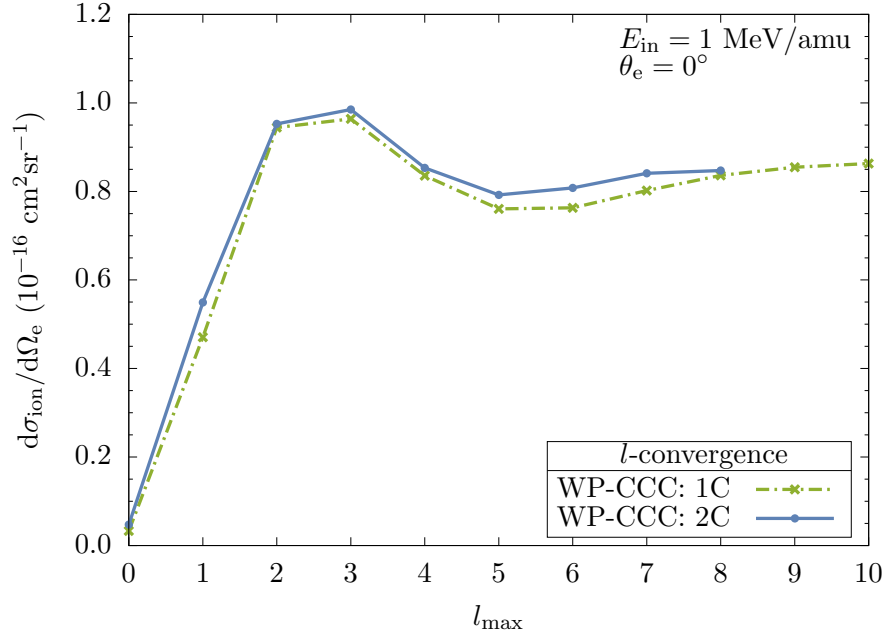


Figure 7.5: Singly differential cross section for 1 MeV/amu C⁶⁺-impact ionisation of atomic hydrogen. Dependence of the present single- and two-centre WP-CCC results on l_{\max} at $\theta = 0^\circ$.

by comparing the two approaches. Convergence of the single-centre WP-CCC results with respect to l_{\max} is shown in Fig. 7.4. In the single-centre calculations we were able to include the states with orbital quantum number up to 10. The figure demonstrates reasonably good convergence. Again, the convergence is slower for small angles as in the two-centre case.

In Fig. 7.5, we demonstrate the convergence of both the single- and the two-centre results for singly differential ionisation cross section for electrons ejected in the direction of the projectile. One can see that the convergence of the two-centre results is somewhat faster than that of the single-centre approach. Also, the figure reveals that the final results of the two approaches agree with each other very well, the difference being only within a few percent. This shows the internal consistency of the employed approach.

7.2 Final results for C^{6+} ion scattering on hydrogen

In this section, we present the final total cross sections for electron capture and ionisation as well as the singly and doubly differential cross sections for ionisation in C^{6+} -H collisions. We start from integrated cross sections.

7.2.1 Total cross sections

As we have seen in the previous section, setting $n_{\max} = 10$, $l_{\max} = 6$ and $N_c = 20$ is sufficient to obtain convergent total cross sections. With these parameters, there are 1267 states included on both centres.

Electron capture

In Fig. 7.6, the WP-CCC results for the total electron-capture cross section are compared with the experimental data of Meyer *et al.* [144] and Goffe *et al.* [145], as well as other theoretical results. The present results are in overall agreement with the experimental data which are available at energies below 10 keV/amu and in the energy range from 100 keV/amu to 200 keV/amu. A good agreement is observed with the calculations based on the molecular-orbital close-coupling (MOCC) method of Harel *et al.* [146] and the CTMC method of Jorge *et al.* [37] in the entire energy range. It should be noted that the WP-CCC results are in excellent agreement with the AOCC calculations of Igenbergs *et al.* [147] at all energies, where the visual discrepancy at very low energies is due to the lack of calculated data by Igenbergs *et al.* [147]. This can be explained by the similarity of the employed methods and basis functions.

Toshima [148] employed the Gaussian-type basis functions within the AOCC

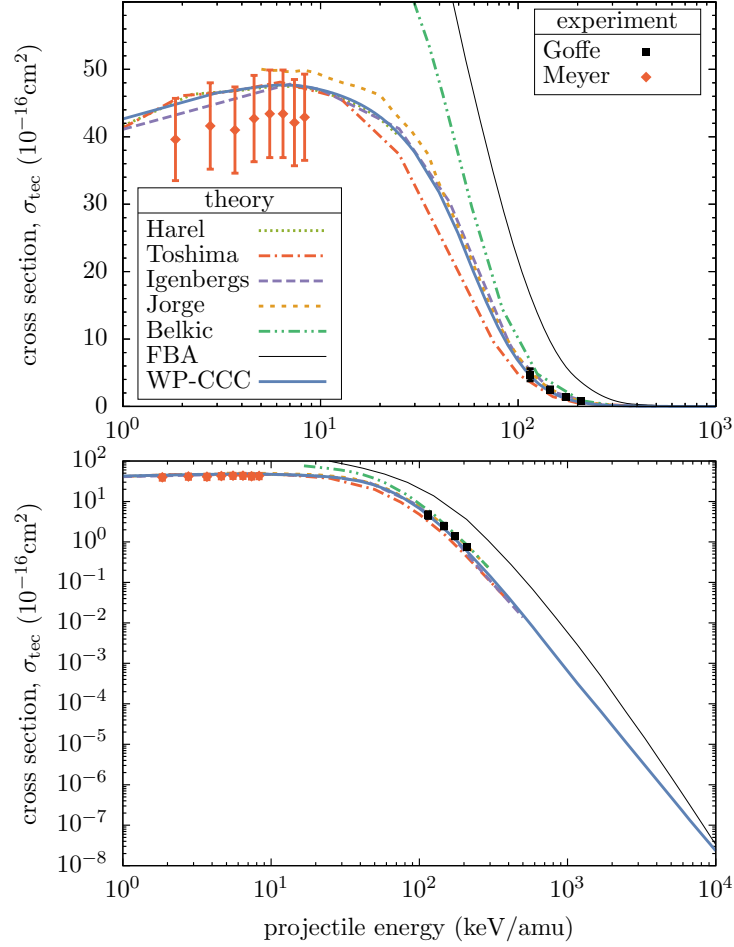


Figure 7.6: Total cross section for electron capture in C^{6+} -H(1s) collisions as a function of incident proton energy (top and bottom panels are on linear and logarithmic y scales, respectively). The present WP-CCC results are represented by the dark blue solid line. The experimental data are due to Goffe *et al.* [145] and Meyer *et al.* [144]. The other theoretical results are from Harel *et al.* [146], Toshima [148], Igenbergs *et al.* [147], Jorge *et al.* [37], and Belkic *et al.* [149]. The FBA results are also given.

approach, their calculations are slightly lower than other results at energies from 20 to 400 keV/amu. Possible reasons for this discrepancy might be the smaller number of included bound states of C^{5+} and the fact that Toshima [148] used a linear combination of the Gauss-type functions to obtain the bound states of the C^{5+} ion. The latter are not true eigenstates. The energies calculated by this method are slightly different from the exact values for some states. Another theoretical result is the B1B method of Belkic *et al.* [149], where distortion

was included in calculating the projectile wavefunction. This fixes incorrect boundary conditions in the FBA approximation. We can see that their results are generally higher at energies below 100 keV/amu and agree with the other results well at higher energies. In addition, the FBA results are also included for comparison. The cross section calculated using this method overestimates the other calculation and the experiment even at very high projectile energies. This shows the importance of higher-order terms in the corresponding perturbation series.

Ionisation

In Fig. 7.7 we present WP-CCC calculations for the total ionisation cross section together with the experimental point of Shah and Gilbody [150] and other theoretical results. The experimental result is available only for one energy of the projectile, where the current WP-CCC results overestimate the experiment by about 10%. It appears to be a common feature of the coupled-channel approaches considered for comparison, as all calculations based on this method overestimate the experiment almost by the same amount. However, it should be noted that the CDW-EIS calculations of Rivarola *et al.* [151] is in better agreement with the experimental data. Their calculated cross section is lower than all other theoretical calculations including the WP-CCC results at energies from 50 keV/amu to 1 MeV/amu.

Igenbergs *et al.* [147] and Toshima [148] also applied the AOCC approach, however the figure reveals some discrepancies between their results and the WP-CCC calculations at energies below 300 keV/amu. This is probably because of the difference in the expansion bases employed in these approaches. Toshima [148] uses Gaussian-type functions. In addition, similarly to the present approach, both the projectile- and target-centred continuum states are included

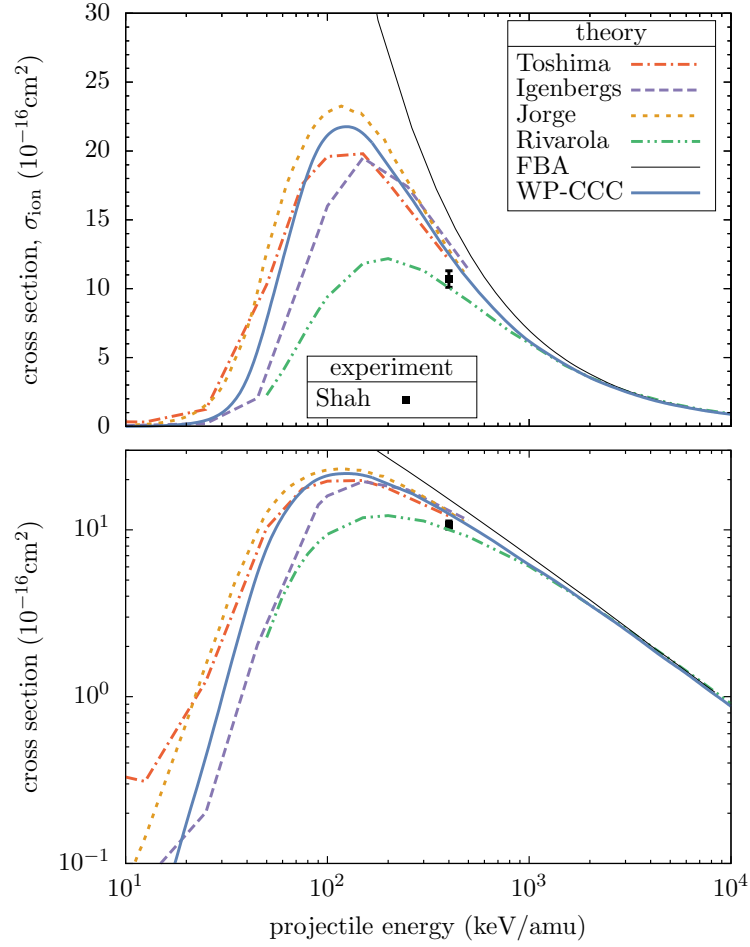


Figure 7.7: Total cross section for ionisation in C^{6+} -H(1s) collisions as a function of incident proton energy (top and bottom panels linear and logarithmic y scales respectively). The present WP-CCC results are represented by the dark blue solid line. The experimental point is due to Shah and Gilbody [150]. The other theoretical results are from Igenbergs *et al.* [147], Toshima [148], Jorge *et al.* [37], and Rivarola *et al.* [151]. The FBA results are also given for comparison.

in the calculations. However, the size of the employed basis, made of Gaussian functions, was comparatively smaller. Igenbergs *et al.* [147] included only the target-centred continuum states. However, if the continuum states are included only on the target centre, the results might be non-convergent unless the projectile energy and l_{\max} are sufficiently high (see [152, 153]).

In comparison with other theoretical approaches, the WP-CCC results significantly overestimate the CDW-EIS calculations of Rivarola *et al.* [151] and

lower than the CTMC calculations of Jorge *et al.* [37] at all considered energies. However, above 1 MeV/amu, all the presented theories agree with each other very well. We can also notice that unlike in the case of electron capture, the FBA calculations merge with the current ionisation cross section above 2 MeV/amu.

7.2.2 Differential cross sections

Obtaining accurate differential cross sections within the employed approach requires denser discretisation of the continuum. This can be achieved simply by increasing the number of bins. Also, the convergence study has revealed the need of inclusion of the continuum states with larger angular momenta. In the two-centre calculations, these parameters were chosen large enough to achieve full convergence. The parameters were set as $n_{\max} = 10$, $l_{\max} = 8$ and $N_c = 30$. This basis consists of 2796 states on each centre. In the single-centre approach we chose parameters as $n_{\max} = 11$, $l_{\max} = 10$ and $N_c = 30$. The basis consists of 4136 states on the target centre.

Singly differential cross section

In Figs. 7.8 and 7.9, we present the calculated singly differential cross sections as functions of electron ejection angle θ_e at projectile energies of 1 MeV/amu and 2.5 MeV/amu, respectively. The results are compared with the experimental data and the CDW-EIS calculations of Tribedi *et al.* [154, 155]. The single-centre WP-CCC calculations are included at 1 MeV/amu for comparison. One can see that the two-centre results are in excellent agreement with the experimental data at 1 MeV/amu except for smaller ejection angles. However, at smaller ejection angles the single- and two-centre approaches agree with each other well and show another peak in the direction of the projectile, which is absent in the

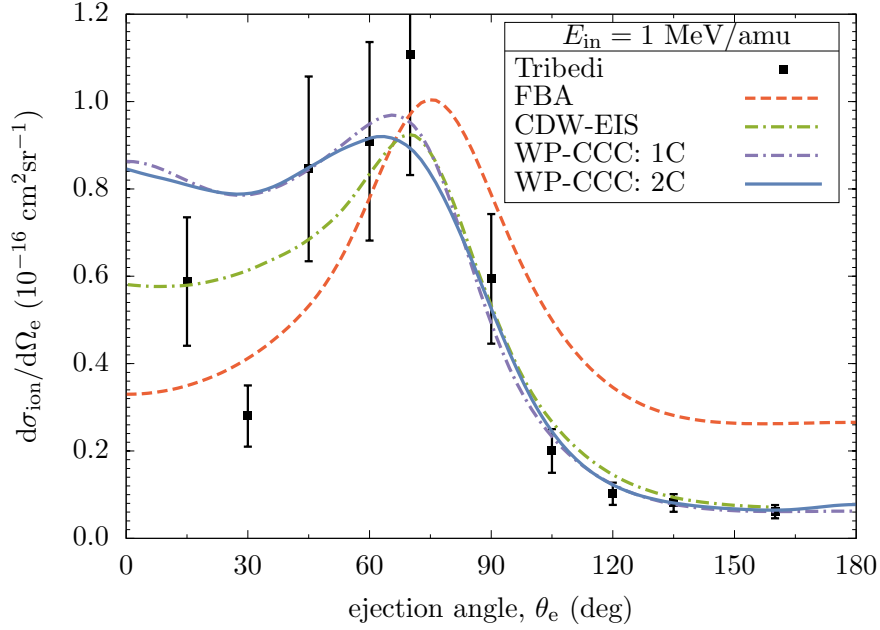


Figure 7.8: Singly differential cross section in the ejected-electron angle for 1 MeV/amu C^{6+} -impact ionisation of atomic hydrogen. The measurements and other calculations are due to Tribedi *et al.* [154, 155]. The FBA results are also shown for comparison.

other results. It should be pointed out that the existence of background noise in the measurements was emphasised by Tribedi *et al.* [154], which might have affected the final results. The single- and two-centre results and the CDW-EIS calculations agree at the ejection angles above 90° . We can also note that the FBA results are not in agreement with other calculations and the experimental data except for some intersection points.

At 2.5 MeV/amu impact energy, the present results agree with the experiment very well except for large electron ejection angles. However, above 90° our calculations are in excellent agreement with the theoretical results of Tribedi *et al.* [154, 155] based on CDW-EIS method. Comparing the discrepancies between the FBA and the two-centre WP-CCC results at 1 MeV/amu and 2.5 MeV/amu one concludes that in the second case, the FBA describes the two-centre calculations considerably better.

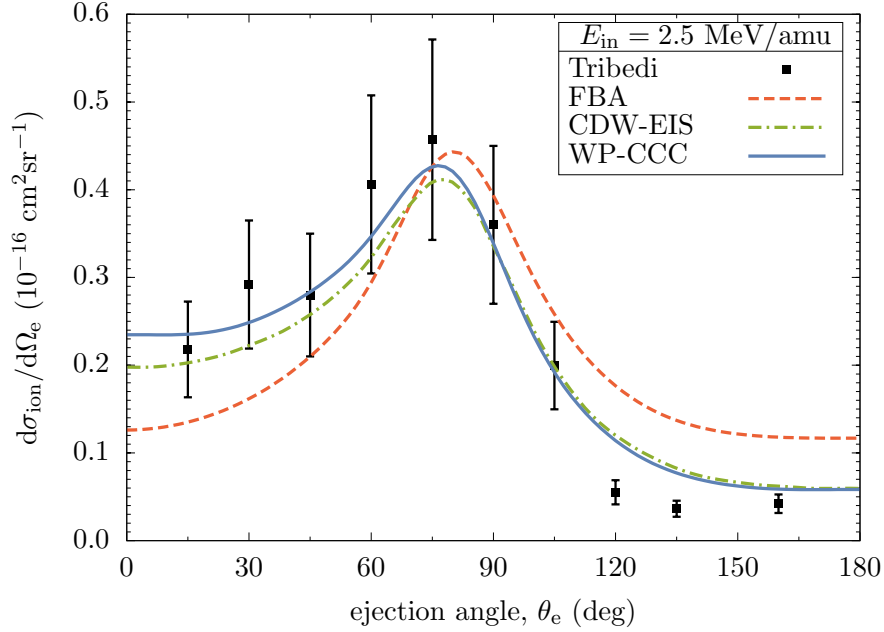


Figure 7.9: The same as in Fig. 7.8 but for 2.5 MeV/amu C⁶⁺-H(1s) collisions.

Doubly differential cross section

In figure 7.10, we present the results of the calculations for doubly differential cross section at 1 MeV/amu impact energy. Electron ejection into angles 15°, 45°, 90° and 120° is considered and dependence of the DDCSs on the ejected electron energy is shown in the energy range from 1 eV to 300 eV. The present results are compared with the experimental data and the CDW-EIS calculations of Tribedi *et al.* [154, 155] and with the FBA results.

The WP-CCC results are in overall fairly good agreement with the experiment. At the smallest considered electron ejection angle, the present calculations slightly overestimate the data at all measured energies except for 40 eV and 100 eV. However, at larger ejection angles the agreement is reasonably good. For 45°, our results are higher than the data at 1 and 3 eV, but are in very good agreement at all remaining energies. The best agreement with the experiment is observed for $\theta_e = 90^\circ$, where the WP-CCC calculations agree with the measure-

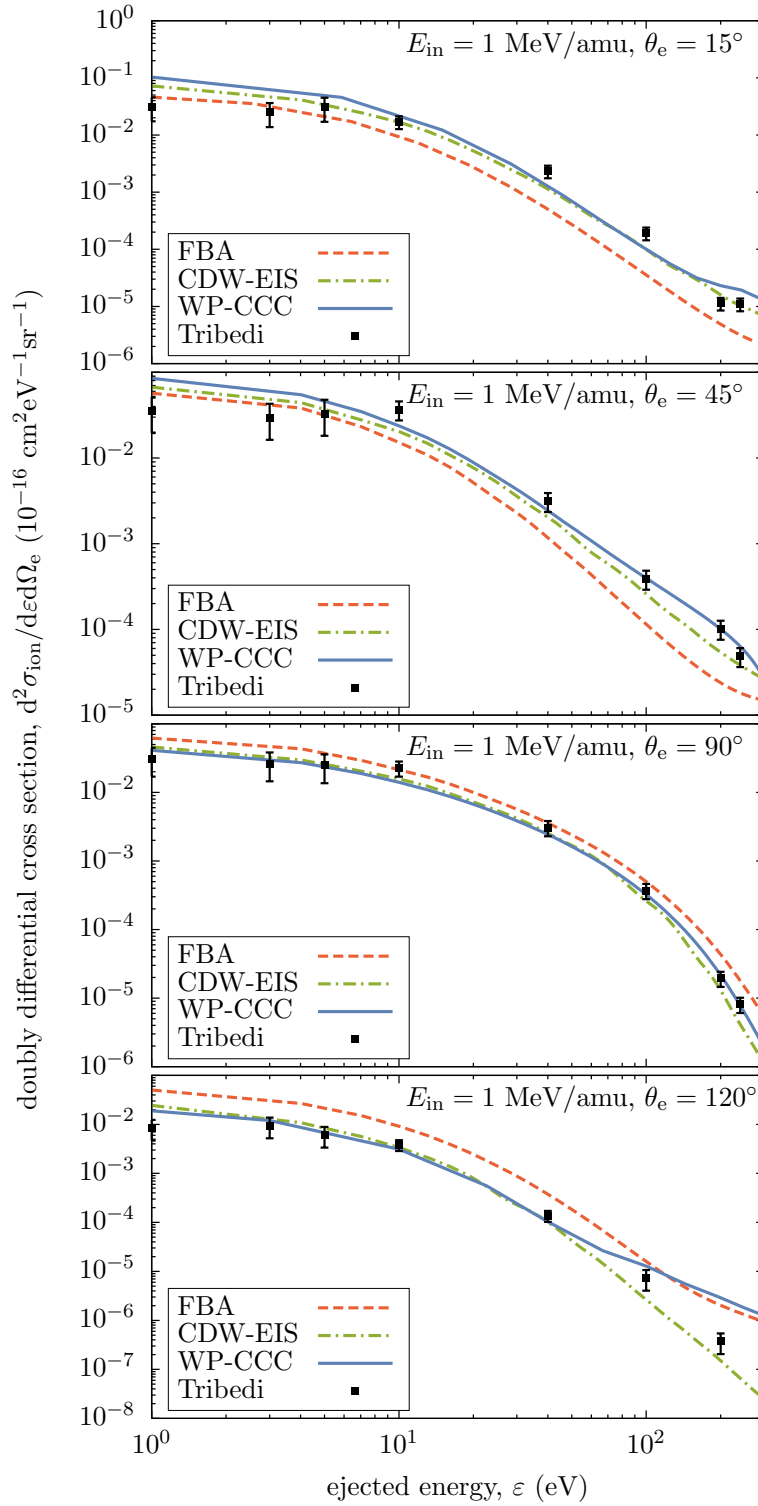


Figure 7.10: Doubly differential cross sections in the ejected-electron energy at certain fixed ejection angles for 1 MeV/amu C^{6+} -impact ionisation of atomic hydrogen. The measurements and the CDW-EIS calculations are due to Tribedi *et al.* [154, 155]. The FBA results are also shown for comparison.

ments very well except for only 10 eV. At the largest considered ejection angle, agreement is observed at energies from 3 to 40 eV. Comparing the current results with the CDW-EIS calculations, one can see overall fairly good agreement at all ejection angles and energies, the difference being within 20%. However, for ejection angles 45° and 120° , we observe clear discrepancies at higher ejection energies. We also notice that the FBA results are systematically lower than the present results for $\theta_e = 15$ and 45° and higher for $\theta_e = 90$ and 120° on the entire energy region considered.

The current results for doubly differential cross section at 2.5 MeV/amu impact energy are given in Fig. 7.11. The results are compared with the measurements and the CDW-EIS calculations of Tribedi *et al.* [154, 155] as well as the FBA results at several electron ejection angles. Generally good agreement can be observed at all considered ejection angles ($\theta_e = 15^\circ, 45^\circ, 90^\circ,$ and 120°) and for all ejection energies except for higher energies. The current results underestimate the data above 50 keV/amu for $\theta_e = 15^\circ$ and 45° and slightly lower for $\theta_e = 120^\circ$. Here also the best agreement for all considered ejection energies is observed for $\theta_e = 90^\circ$. It should be pointed out that for $\theta_e = 90^\circ$ and 120° , the CDW-EIS calculations are also available for comparison and are in excellent agreement with the current results. It is also interesting to compare the two-centre WP-CCC and the FBA results. We can see that the difference between the results is smaller at 2.5 MeV/amu impact energy in comparison with the 1 MeV/amu ones. For 2.5 MeV/amu, the FBA results are slightly lower than the present results for $\theta_e = 15$ and 45° and higher for 120° on the entire considered energy region, however very good agreement is obtained for 90° .

In Figs. 7.12 and 7.13 we show the doubly differential cross sections similar to the previous two figures but as functions of electron ejection angle at several ejection energies for 1 MeV/amu and 2.5 MeV/amu impact energy, respectively.

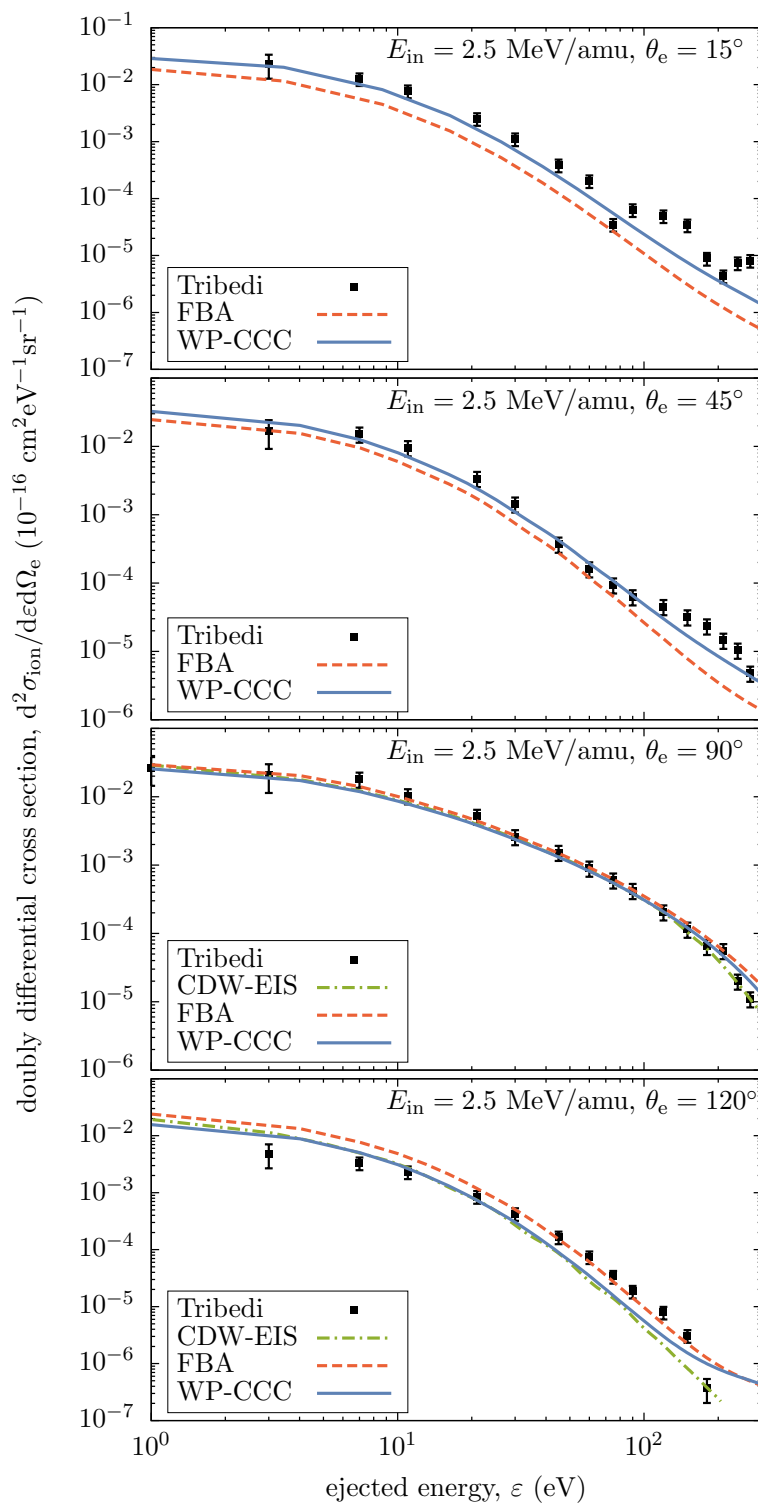


Figure 7.11: The same as in Fig. 7.10, but for 2.5 MeV/amu C^{6+} -H(1s) collisions.

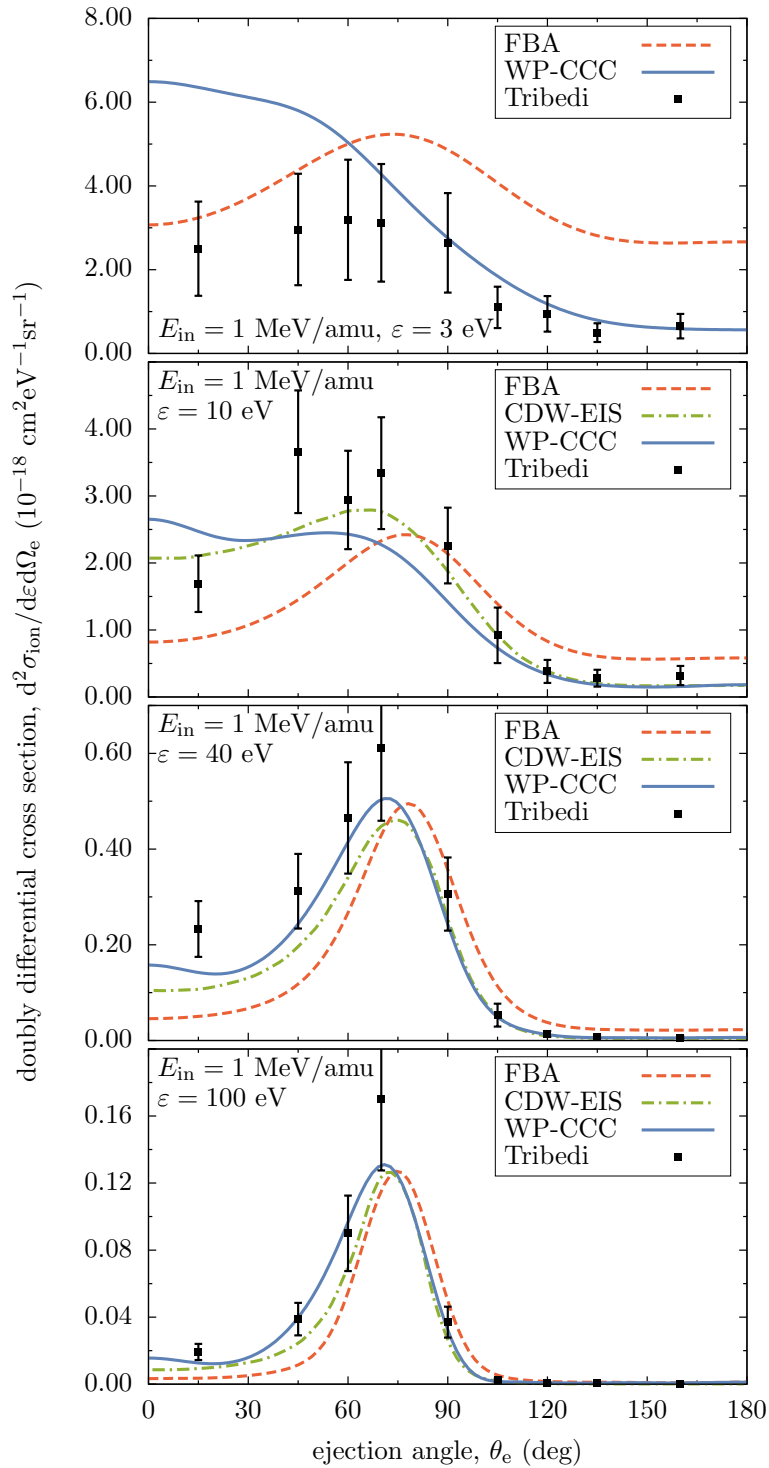


Figure 7.12: Doubly differential cross sections in the ejected-electron angle at certain fixed ejection energies for 1 MeV/amu C^{6+} -impact ionisation of atomic hydrogen. The measurements and the CDW-EIS calculations are due to Tribedi *et al.* [154, 155]. The FBA results are also shown for comparison.

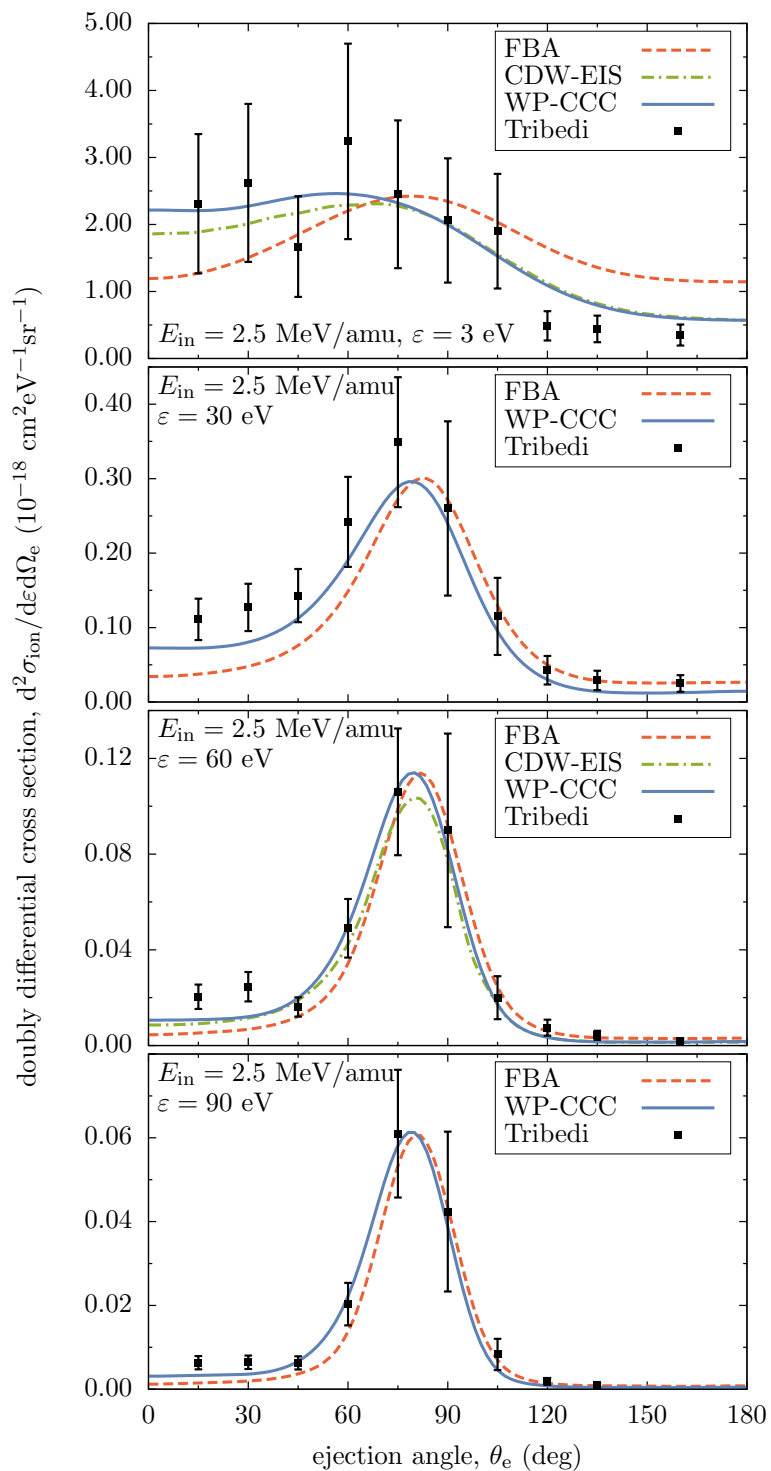


Figure 7.13: The same as in Fig. 7.12, but for 2.5 MeV/amu C^{6+} -H(1s) collisions

For all considered electron ejection energies, the current results agree with the experiments very well for both impact energies. Only some discrepancies are observed for smaller ejection angles for 1 MeV/amu projectiles. It should be pointed out that at 2.5 MeV/amu impact energy the FBA results approach the WP-CCC results closer than at 1 MeV/amu. We recall that at 1 MeV/amu there are large discrepancies between the FBA and WP-CCC results especially at lower ejection energies. The CDW-EIS calculations also in good agreement with the present results at all calculated electron ejection energies.

7.3 Chapter summary

We studied collisions of bare carbon ions with atomic hydrogen using the wave-packet-based convergent close-coupling method. In the two-centre approach described in Chapter 3, the total scattering wave function of the three-body system was expanded in terms of the target- and projectile-centred eigenstates and pseudostates. The pseudostates were constructed using the wave-packet continuum discretisation method. By substituting the expansion in the corresponding three-body time-independent Schrödinger equation, we obtained a set of coupled differential equations for the transition amplitudes into different target- and projectile-centred states. These time-dependent amplitudes were used to obtain the total cross sections for each of the underlying processes as well as the singly and doubly differential cross sections for ionisation.

The convergence of the results was studied in terms of the size of the basis for all calculations. In particular, the convergence was demonstrated with respect to l_{\max} of the included states. The total electron-capture and ionisation cross sections were calculated for impact energies in the range from 1 keV/amu to 10 MeV/amu. For electron capture, excellent agreement with the experiment

was obtained at all considered projectile energies. However, due to the lack of experimental data, the total ionisation cross section results were only compared with a single measured point where the current results were slightly higher. The calculated singly and doubly differential ionisation cross sections were also compared with the available experimental data and very good agreement was observed for 2.5 MeV/amu impact energy. However, for 1 MeV/amu some discrepancies with the experiment still remain, especially at very small electron ejection angles. At these angles, the current calculations for both SDCS and DDCS showed a peak, which has not been observed in the experimental and other theoretical studies.

Chapter 8

He²⁺-H and *p*-He⁺ collisions

Results of the WP-CCC approach applied to He²⁺-H and *p*-He⁺ collisions are described in this chapter. These collisions involve all possible reactions in the system of an α particle, a proton and an electron, but for two different initial states. The theory of the WP-CCC approach to collisions of fully-stripped ions with atomic hydrogen was given in Chapter 3. The described method can be directly applied to the hydrogenlike-ion targets by replacing the hydrogen wave functions with that for hydrogenlike ion. These wave functions were described in the same chapter. First we look at the convergence of the results for all considered processes. Then, the final integrated cross sections for electron capture, excitation and ionisation are presented and compared with experiments and other theories, when available. We also discuss the calculations for the fully, singly and doubly differential cross sections for ionisation in He²⁺-H collisions.

8.1 Convergence studies

As we have discussed in the previous chapters, our calculations depend on several parameters. These parameters need to be chosen to yield accurate results. The calculations showed that the upper limit for the impact parameters should be

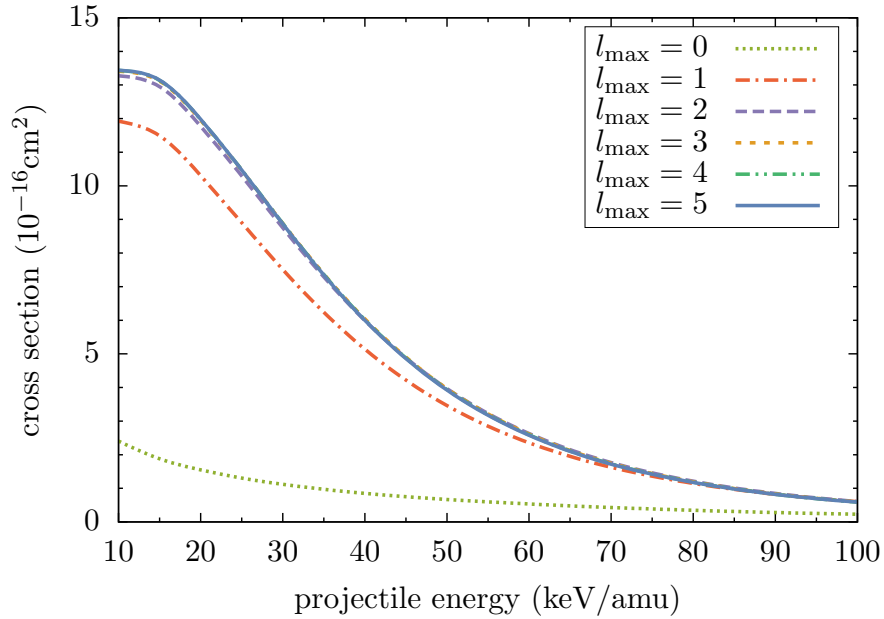


Figure 8.1: Total cross section for electron capture in H^{2+} - $H(1s)$ collisions: convergence of the present WP-CCC results with respect to l_{\max} .

chosen larger with increasing the incident energy. In calculations, b_{\max} was varied up to $b_{\max} = 70$ to achieve convergence. The maximum principal number of the included eigenstates and the number of discretisation bins were set at $n_{\max} = 10$ and $N_c = 20$, respectively. Finally, to find the transition amplitudes, the sets of differential equations, corresponding to two collisional systems, were solved in the range of $z \in [-150, 150]$.

8.1.1 Convergence of the total cross sections

In Figs. 8.1 and 8.2 we demonstrate the convergence of the total cross section for electron capture and ionisation in H^{2+} - $H(1s)$ collisions. We increased the maximum allowed orbital number, l_{\max} , of the included states up to 5. It can be seen that the results systematically converge with increasing l_{\max} , and overall acceptable level of convergence is achieved with $l_{\max} = 4$. For electron capture, the convergence is reached with $l_{\max} = 3$.

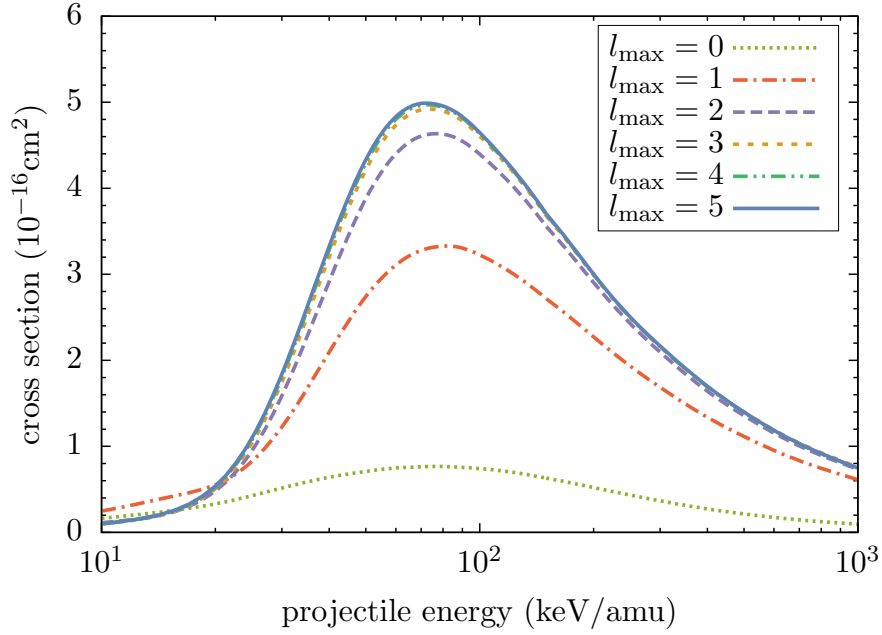


Figure 8.2: Total cross section for ionisation in H^{2+} - $H(1s)$ collisions: convergence of the present WP-CCC results with respect to l_{\max} .

Similar results for p - He^+ collisions are presented in Figs. 8.3 and 8.4. Cross sections demonstrate good convergence for this collisional system too. The convergence rate of the electron-capture cross section is relatively faster, where the difference between the results with $l_{\max} = 2$ and with higher l_{\max} is negligibly small. But for ionisation, the full convergence is achieved only with $l_{\max} = 4$.

8.1.2 Convergence of the differential cross sections

Next, we discuss the convergence of the differential ionisation cross sections in 200 keV/amu He^{2+} -H collisions. In Fig. 8.5 we present the FDCS for ionisation, where the results with various values of l_{\max} are given as functions of the electron ejection angle. We study the electrons with the fixed ejection energy of $\varepsilon_e=20$ eV in the coplanar plane, that is $\varphi_p = 0^\circ$ and $\varphi_e = 0^\circ$. The perpendicular component of the momentum transfer is set at $p_\perp = 0.3$. The FDCS was obtained as an incoherent combination of the DI and ECC components. We can

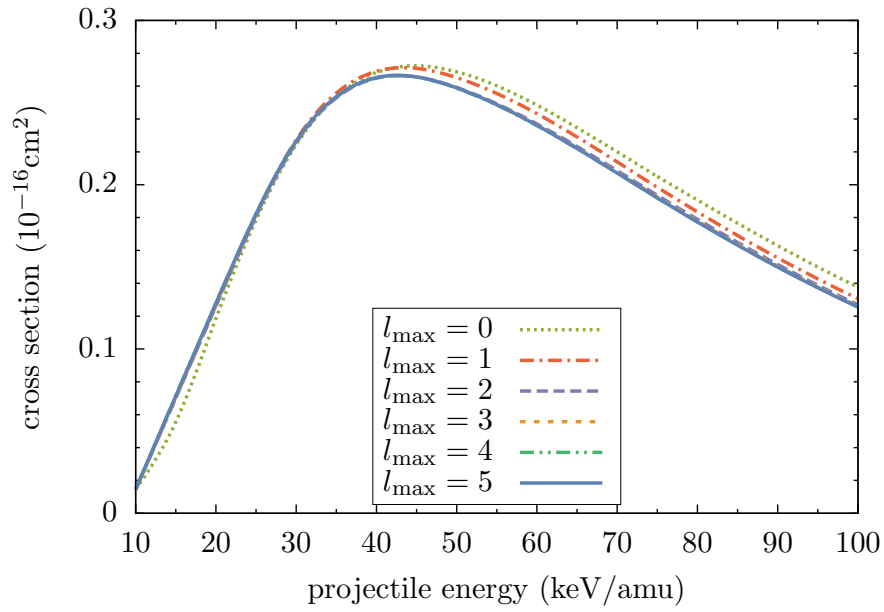


Figure 8.3: Total cross section for electron capture in p - He^+ collisions: convergence of the present WP-CCC results with respect to l_{max} .

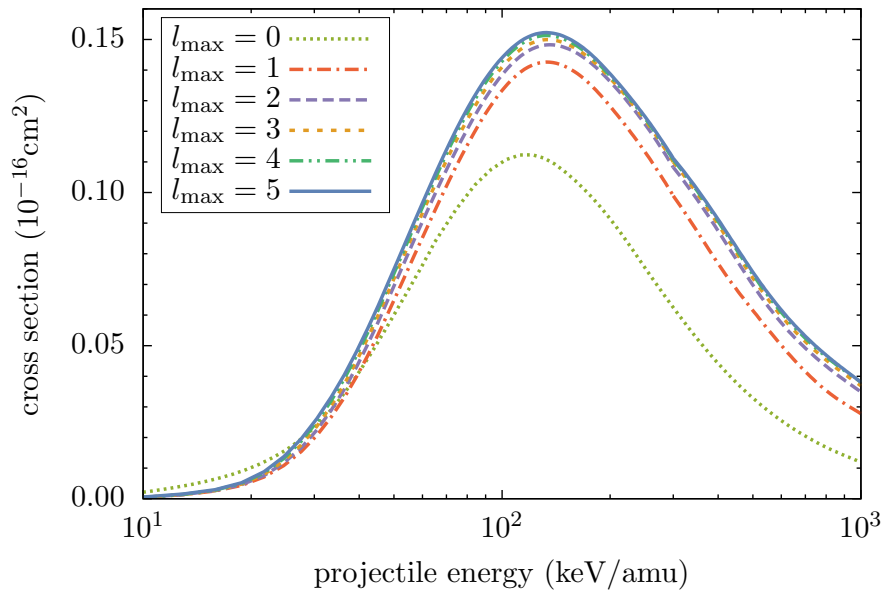


Figure 8.4: Total cross section for ionisation in p - He^+ collisions: convergence of the present WP-CCC results with respect to l_{max} .

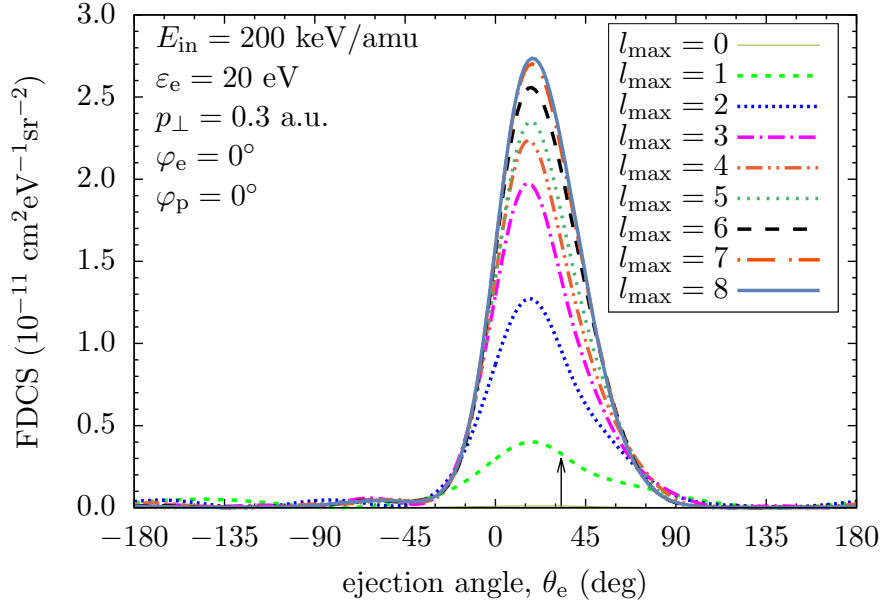


Figure 8.5: Fully differential cross section for He^{2+} -impact ionisation of atomic hydrogen as a function of the electron ejection angle: convergence of the WP-CCC results with respect to l_{\max} . The arrow points in the momentum-transfer direction.

observe that the convergence rate of the differential cross section is comparatively slow, nevertheless the results systematically converge. A sufficient level of convergence is achieved with $l_{\max} = 8$. The arrow near $\varphi_e = 30^\circ$ indicates the momentum-transfer direction. As one can notice that a binary peak appearing in the WP-CCC results and the direction of the momentum transfer slightly differ, however in the FBA calculations they coincide.

Figure 8.6 demonstrates the dependence of the DDCS on the maximum allowed angular momentum number. The DDCS is given as a function of the ejection angle for a fixed value of the electron ejection energy ($\varepsilon_e=20$ eV) in the scattering plane. As discussed in Chapter 5, the DDCS is obtained by integrating the FDCS (shown in Fig. 8.5) over the projectile scattering angle. The DDCS also appears to be convergent with increasing l_{\max} . A fair level of convergence is achieved with $l_{\max} = 8$.

In Fig. 8.7 we show the convergence of the singly differential ionisation cross

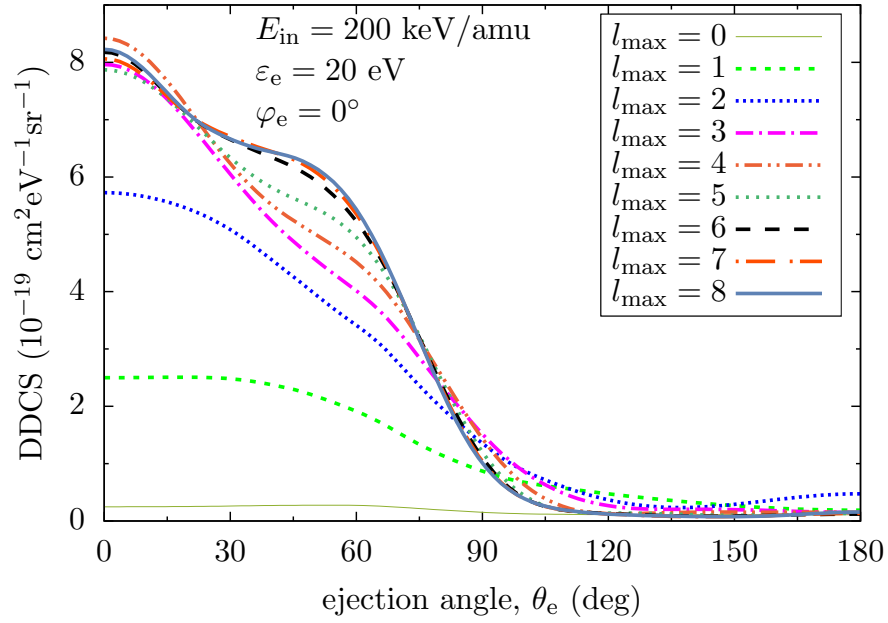


Figure 8.6: Doubly differential cross section for He^{2+} -impact ionisation of atomic hydrogen in the energy and the angle of the ejected electron: convergence of the WP-CCC results with respect to l_{max} .

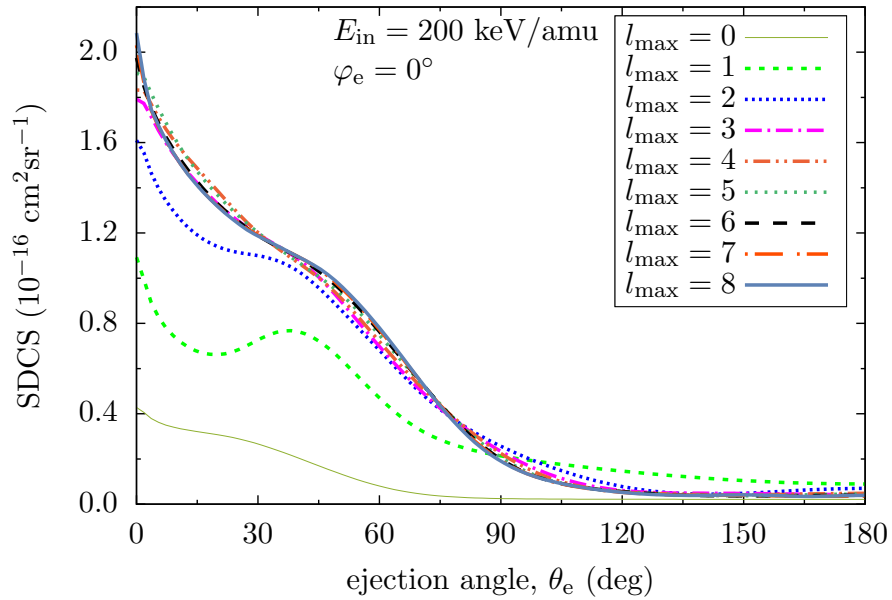


Figure 8.7: Singly differential cross section for He^{2+} -impact ionisation of atomic hydrogen in the angle of the ejected electron: convergence of the WP-CCC results with respect to l_{max} .

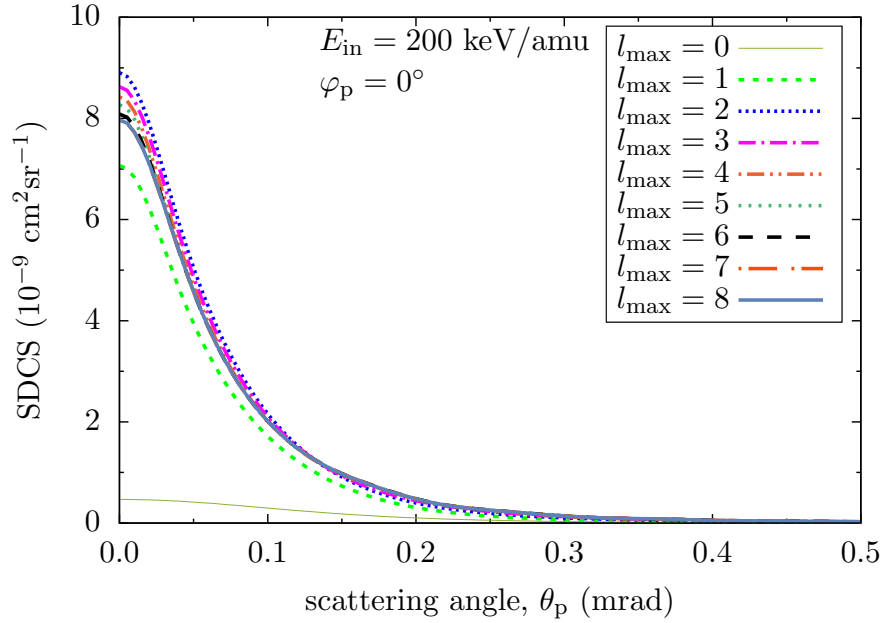


Figure 8.8: Singly differential cross section in the angle of the scattered projectile for He^{2+} -impact ionisation of atomic hydrogen: convergence of the WP-CCC results with respect to l_{max} .

sections for the same collisional system. In the previous figure we demonstrated the DDCS results for a fixed electron ejection energy. Here the SDCS is obtained by integrating the DDCS over all the ejection energies. One can see that this cross section converges relatively faster than the FDCS and the DDCS. Good convergence is obtained with $l_{max} = 8$. The SDCS with the largest l_{max} considered, has a sharp peak at $\theta_e = 0^\circ$ and sharply decreases with increasing ejection angle.

Similar results for the SDCS in the projectile scattering angle and in the electron ejection energy are presented in Figs. 8.8 and 8.9, respectively. Similar to the SDCS in the electron ejection angle, these cross sections are also convergent with $l_{max} = 8$.

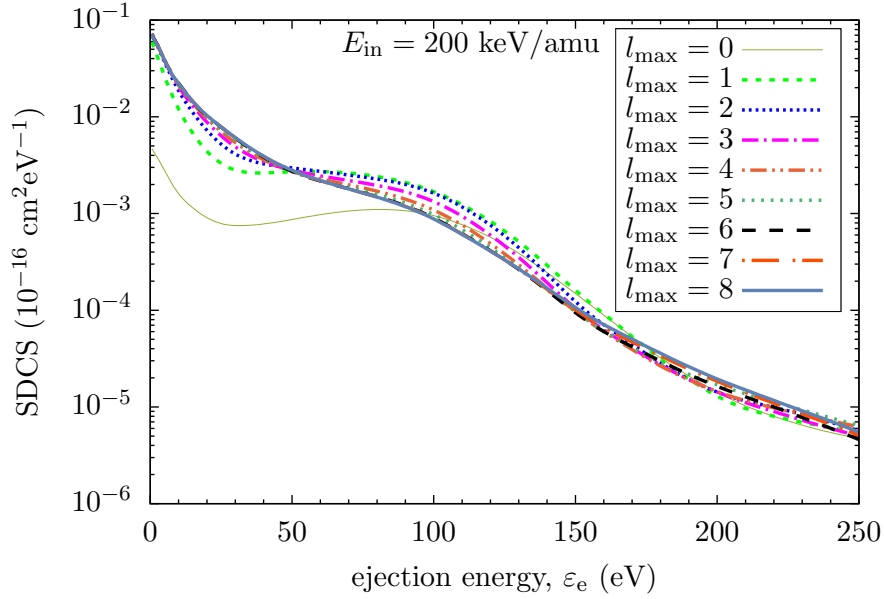


Figure 8.9: Singly differential cross section in the energy of the ejected electron for He^{2+} -impact ionisation of atomic hydrogen: convergence of the WP-CCC results with respect to l_{\max} .

8.2 Final results for the total cross sections in He^{2+} -H and p - He^+ collisions

The convergence study revealed that setting $n_{\max} = 10$, $N_c = 20$ and $l_{\max} = 5$ is sufficient to obtain well-convergent results for the total cross sections. The basis with these parameters consists of 955 states on each centre. Also, the energy dependence of the SDCS, presented in Fig. 8.7, allows us to set the maximum energy, ε_{\max} , of the ejected electrons in constructing the continuum pseudostates. $\varepsilon_e = 250$ eV was shown to be sufficiently large for the SDCS to decrease several orders of magnitude. Therefore, in our calculations we chose $\varepsilon_{\max} = 250$ eV.

In Fig. 8.10 we compare our final total cross section calculations for electron capture with the experimental data [156–159] and other theoretical calculations. The upper and the lower panels are in linear and logarithmic scales, which highlight the lower and the higher energy regions, respectively. One can see

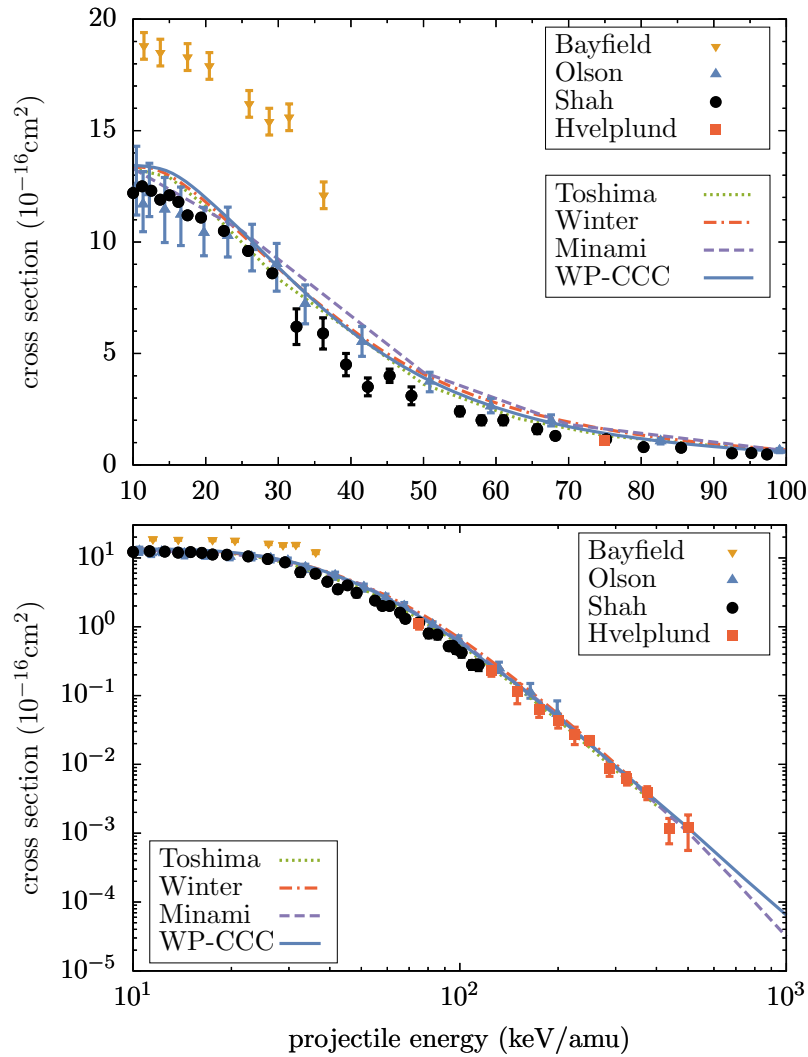


Figure 8.10: Total cross section for electron capture in H^{2+} - $H(1s)$ collisions: the WP-CCC results are compared with the experimental measurements [156–159] and the close-coupling calculations [160, 161]

that the present results are in generally good agreement with the experimental data of Olson *et al.* [157], Shah and Gilbody [158], Hvelplund and Andersen [159]. Also, our results agree with the close-coupling calculations of Toshima [160], Minami *et al.* [162] and Winter [161] very well. It should be pointed out that the data of Bayfield and Khayrallah [156], which are available at lower energies, significantly exceed all other experimental and theoretical results.

The present results for the total ionisation cross section are shown in Fig. 8.11

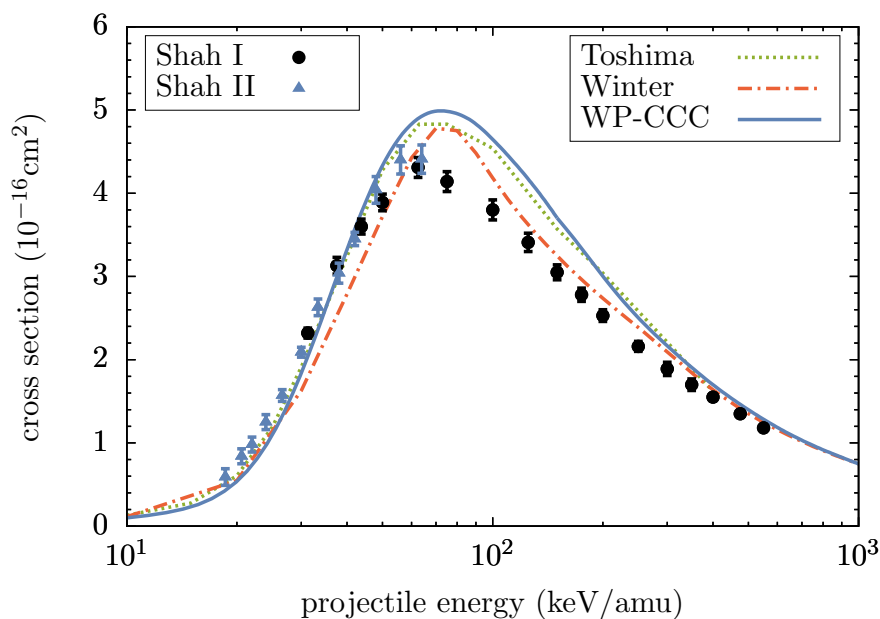


Figure 8.11: Total cross section for ionisation in H^{2+} - $H(1s)$ collisions: the present WP-CCC results are compared with the experimental measurements of Shah and Gilbody [163], Shah *et al.* [164] and the close-coupling calculations of Winter [161] and Toshima [160].

together with the experimental data of Shah and Gilbody [163], Shah *et al.* [164] and the close-coupling calculations of Winter [161] and Toshima [160]. We can see that, the WP-CCC results exceed the measurements in the intermediate energy range, especially at energies where the peak is observed. Above 100 keV/amu, the calculations of Winter [161] agree with experiment better than the other close-coupling results. It should also be noted that above 400 keV/amu, all the theoretical results agree with each other as well as with the experimental data very well. Below 50 keV/amu, the present results are in good agreement with the experimental measurements and the calculations of Toshima [160]. The reason for the disagreement between theory and experiment around the peak cannot be due to the lack of convergence in the employed close-coupling calculations. In Fig. 8.4 we have demonstrated the systematic convergence of the results. As there is very good agreement between the close-coupling calculations in this range, we conclude that it is a common feature of all presented two-centre

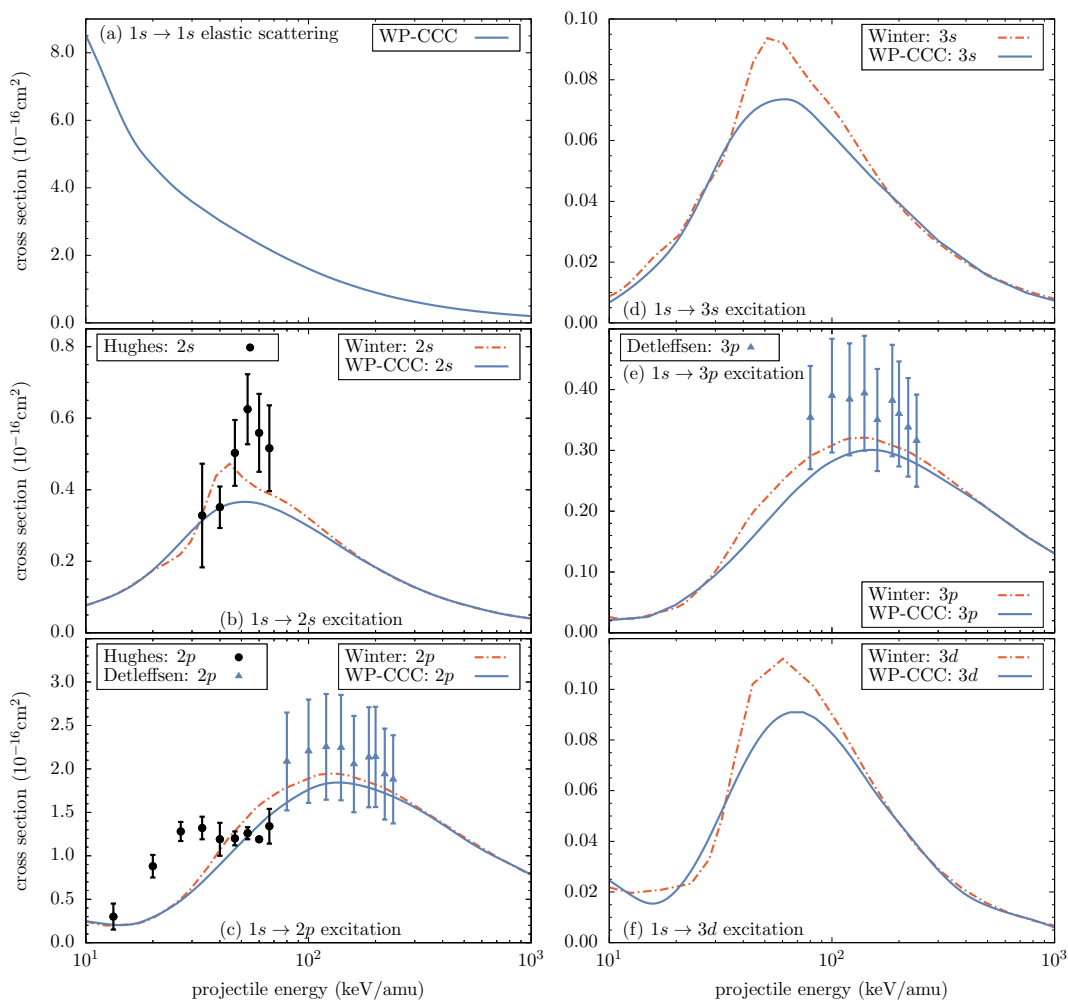


Figure 8.12: Cross sections for excitation of the $n = 1, 2$ and 3 shell states in He^{2+} - $H(1s)$ collisions: the present WP-CCC results are compared with the theoretical calculations of Winter [161]. The experimental data for $2s$, $2p$ and $3p$ excitation are due to Hughes *et al.* [165] and Detleffsen *et al.* [166].

close-coupling calculations. The reason for the observed discrepancy remains unexplained. Therefore, further experimental and theoretical studies, especially in the intermediate energy range, would be of great help for understanding this disagreement.

Figure 8.12 presents the cross sections for excitation of the $n = 1 - 3$ -shell states in He^{2+} - $H(1s)$ collisions. We compare our results with the experimental data of Hughes *et al.* [165] and Detleffsen *et al.* [166] available for excitations

into $2s$, $2p$ and $3p$ states. Also for all these transition, except for the elastic scattering, we make comparison with the close-coupling calculations of Winter [161]. We can see in panel (a) that the elastic scattering cross section declines monotonically with increasing incident energy. The cross sections for excitation into the $n = 2$ and 3 shell states peak at different impact energies, but otherwise have similar shapes. Also, the results reveal that the $2p$ -state excitation cross section is several times larger than that for the other states at the maximum. The present cross section for excitation of the $2s$ state is in good agreement with the experimental data of Hughes *et al.* [165] at the lowest two measured energy points. However, at higher energies (especially around the peak), our results are significantly lower than the experimental measurements. The calculations of Winter [161] also underestimate the data at these energies, and agree well with the WP-CCC results at the high and low end of the energy range.

For excitation of the $2p$ state, the present results and the calculations of Winter [161] are generally in agreement, the latter being slightly higher in the intermediate energy range. In comparison with the experiments of Hughes *et al.* [165] and Detleffsen *et al.* [166], the calculations are within the error bars of the data starting from 50 keV/amu of the incident energy. However, at low energies the measurements of Hughes *et al.* [165] significantly exceed both of the close-coupling calculations and suggest the second peak which is absent in the theoretical predictions. The cross sections for the transition into the $n = 3$ shell target states are presented in panels (d)-(f). Overall, we can see that the WP-CCC results and calculations of Winter [161] agree well with each other at the lowest and highest energies considered. There are some clear disagreements in the intermediate energy range, where the results of Winter [161] are higher than the present results for all these transitions. However, for the $1s \rightarrow 3p$ transition, the discrepancy is relatively smaller. For this transition, results of both

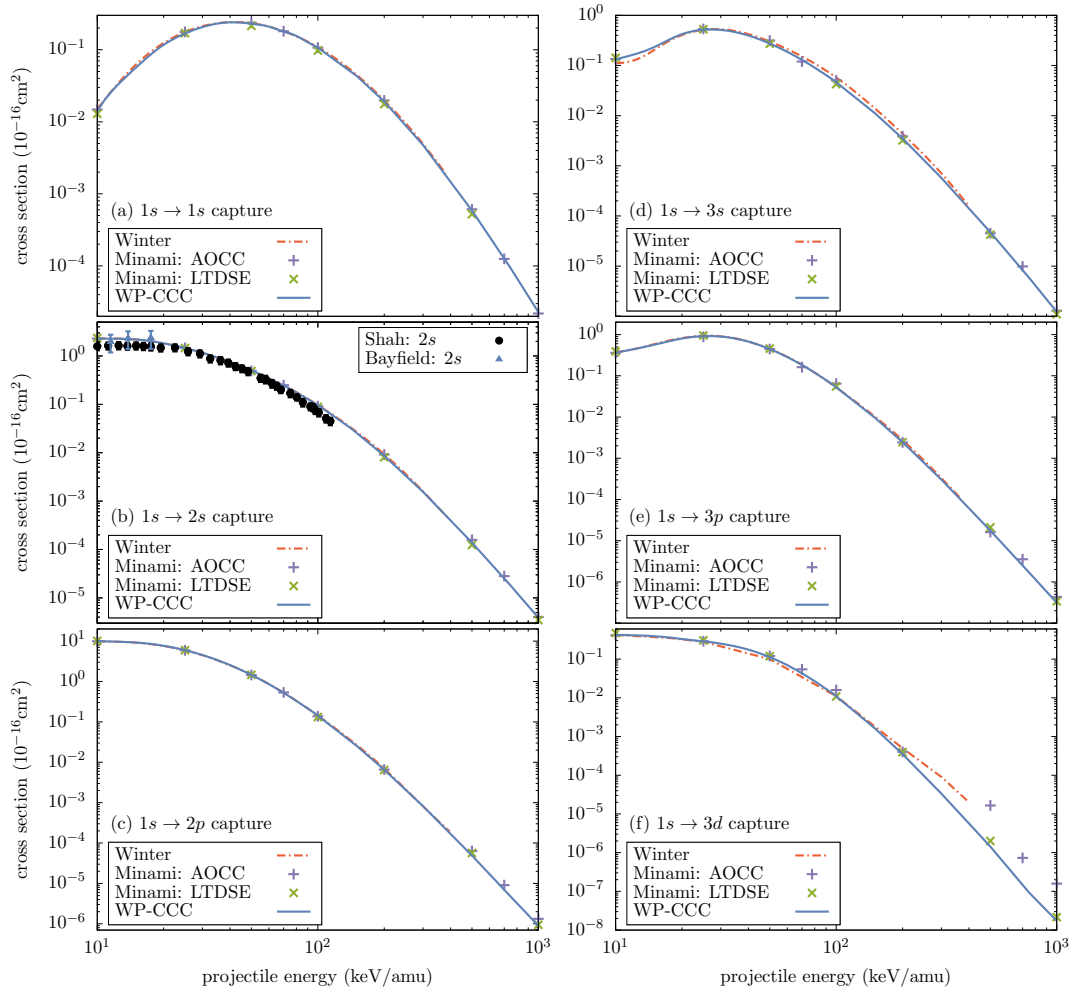


Figure 8.13: Cross sections for electron capture into the $n = 1, 2$ and 3 shell states in $\text{He}^{2+}\text{-H}(1s)$ collisions: the present WP-CCC results are compared with the theoretical calculations of Winter [161] and Minami *et al.* [162]. The experimental data are due to Shah and Gilbody [158] and Bayfield and Khayrallah [156].

calculations are within the error bars of the experimental results of Detleffsen *et al.* [166].

The present cross sections for electron capture into the $n = 1, 2$ and 3 shell states of the He^+ ion are shown in Fig. 8.13. The results are compared with the close-coupling calculations of Winter [161], as well as the calculations of Minami *et al.* [162] based on the AOCC and the lattice time-dependent Schrödinger equation (LTDSE) approaches. Also, we compare with the experimental data

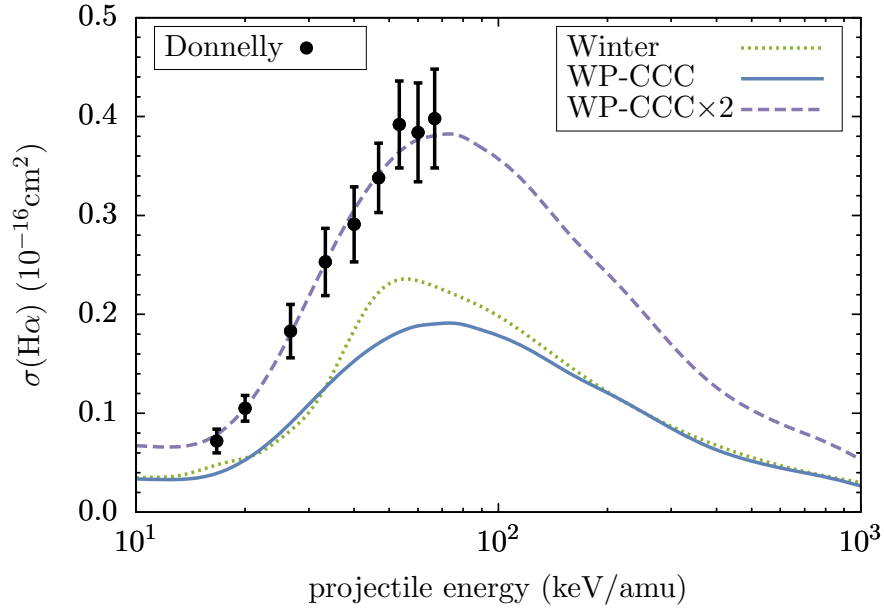


Figure 8.14: Balmer- α emission cross section in $\text{He}^{2+}\text{-H}$ collisions as a function of the impact energy: the present WP-CCC results are compared with the experimental measurements of Donnelly *et al.* [167] and the close-coupling calculations of Winter [161]. The WP-CCC results multiplied by a factor of 2 are also presented for comparison.

of Shah and Gilbody [158] and Bayfield and Khayrallah [156], which are only available for the $1s \rightarrow 2s$ transition. In the entire energy range, the theoretical calculations perfectly agree with each other for all the transitions, except for electron capture into the $3d$ state. For the latter transition, the results are in good agreement below 200 keV/amu, however calculations of Winter [161] and the AOCC calculations Minami *et al.* [162] deviate at higher energies. In comparison with the experiments, we can observe very good agreement which is demonstrated in panel (b).

In Fig. 8.14, we demonstrate the dependence of the cross section on the incident energy for the Balmer- α emission in $\text{He}^{2+}\text{-H}$ collisions. The present results are compared with the experimental data of Donnelly *et al.* [167] and the calculations of Winter [161]. The theoretical results are in overall fair agreement except for the intermediate energy range, where the calculations of Winter [161] exceed

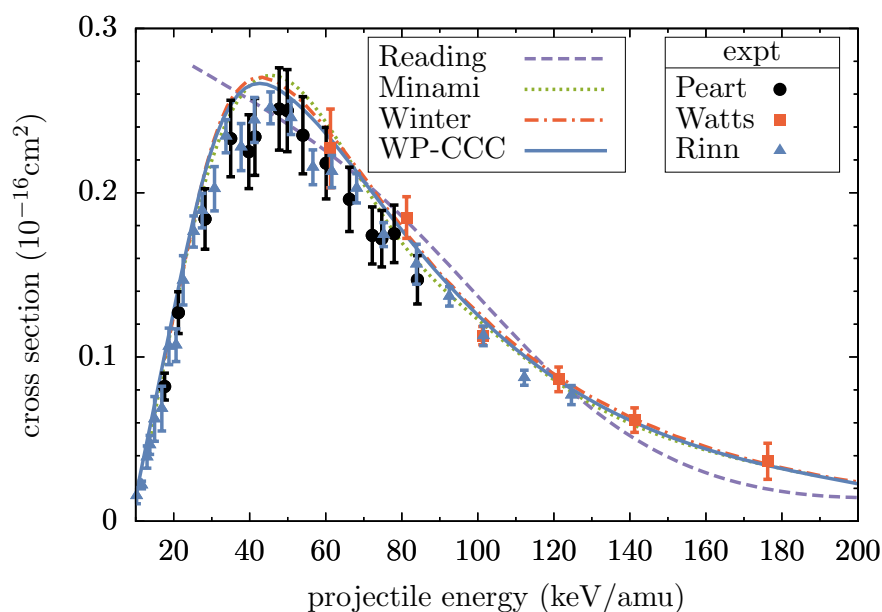


Figure 8.15: Total electron-capture cross section in p - He^+ collisions: the present WP-CCC results are compared with the experimental measurements of Peart *et al.* [169], Watts *et al.* [170] and Rinn *et al.* [171] and the close-coupling calculations of Reading *et al.* [172], Minami *et al.* [173] and Winter [174].

the present results by about 30 %. However, in comparison with the experiment, one can observe significant disagreements. The measurements of Donnelly *et al.* [167] overestimate the WP-CCC results almost two times, which is seen comparing the experimental points and the line obtained by multiplying the present results by the factor of two. It should be pointed out that in the experiment, a contribution of cascades is not taken into account. However, including the cascades even worsens the disagreement. A similar situation was observed for p -H collisions by Abdurakhmanov *et al.* [168]. The calculated Balmer- α emission cross section underestimated the corresponding measurements of Donnelly *et al.* [167] also by approximately a factor of two. However, good agreement was obtained in comparison with the experimental data of Detleffsen *et al.* [166].

Figure 8.15 presents the final total cross section for electron capture in He^{2+} -H collisions. The results are provided for the incident energies up to 200

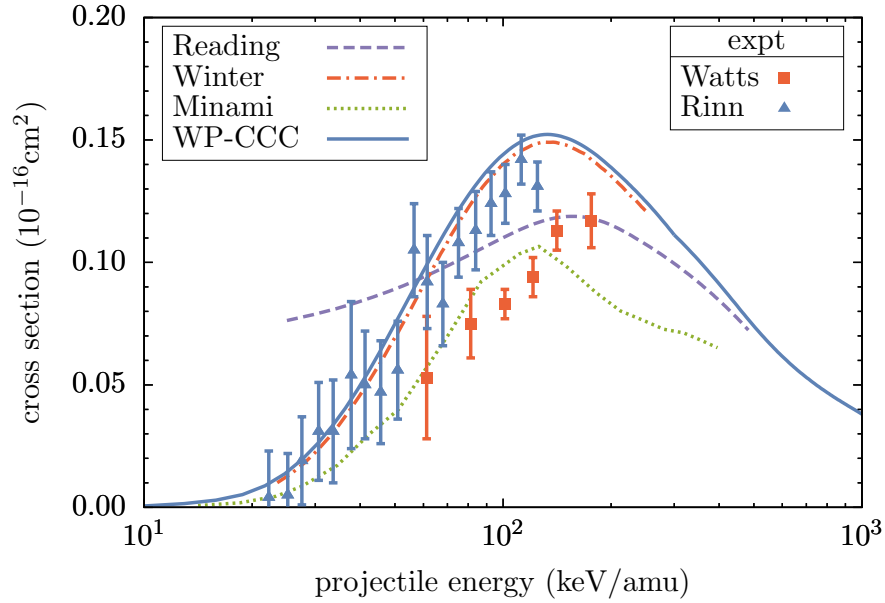


Figure 8.16: Total ionisation cross section in p - He^+ collisions: the present WP-CCC results are compared with the experimental measurements of Watts *et al.* [170] and Rinn *et al.* [175] and the close-coupling calculations of Reading *et al.* [172], Minami *et al.* [173] and Winter [174].

keV/amu and compared with the experimental data of Peart *et al.* [169], Watts *et al.* [170] and Rinn *et al.* [171] as well as the close-coupling calculations of Reading *et al.* [172], Minami *et al.* [173] and Winter [174]. We can see that the present calculations and the experimental results are in overall good agreement. Also, it should be noted that our results are in perfect agreement with the calculations of Winter [174] at all considered energies.

In Fig. 8.16 we show the final WP-CCC results for ionisation in p - He^+ collisions. The results are compared with the experimental data of Watts *et al.* [170] and Rinn *et al.* [175] and the close-coupling calculations of Reading *et al.* [172] and Winter [174]. Again, our calculations are in good agreement with the corresponding calculations of Winter [174]. The small difference between the results is likely to be due to a lack of convergence in calculations of Winter [174], where $l_{\max} = 3$ was used to produce the results. As we have seen in the convergence study above, the ionisation cross section converges only with $l_{\max} = 5$, which was

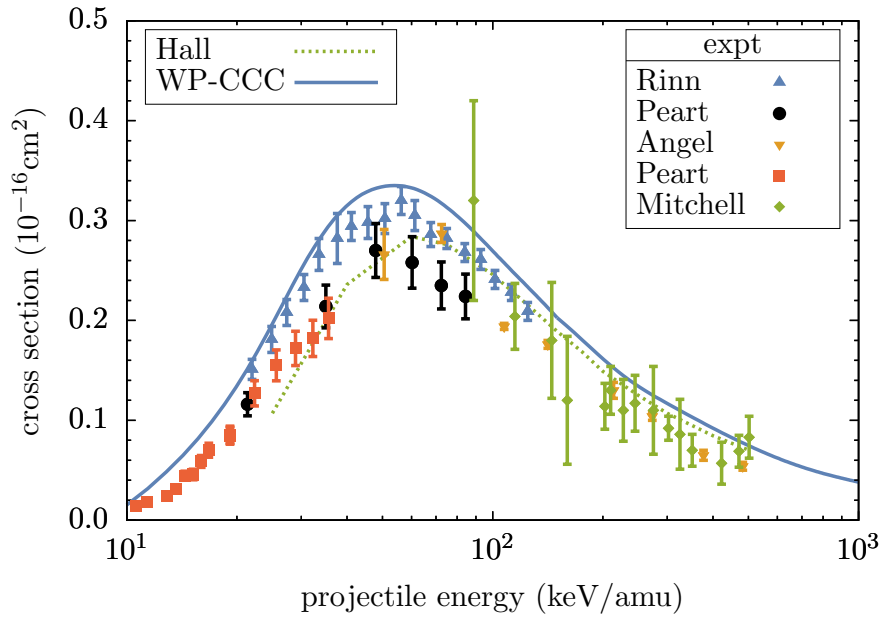


Figure 8.17: Total cross section for electron loss by the target in p - He^+ collisions: the present WP-CCC results are compared with the experimental data of Peart *et al.* [169, 176], Mitchell *et al.* [177], Angel *et al.* [178], Rinn *et al.* [175], Watts *et al.* [170] and the single-centre calculations of Hall *et al.* [179].

taken into account in our calculations. Also, we can see that the present results agree well with the experimental data of Rinn *et al.* [175], which is available on the incident energy range of 20-130 keV/amu. However, there is significant disagreement in comparison with the measurements of Watts *et al.* [170]. In the one and a half centre calculations of Reading *et al.* [172], the AOCC equations were solved using the perturbative approach. They employed only 54 states on the target centre and only the ground state on the projectile centre. We can see that their results are lower than our calculations at the intermediate incident energies but are higher at lower energies, at high energies they tend to merge.

The results for the total electron loss in p - He^+ collisions are provided in Fig. 8.17. The experimental data of Peart *et al.* [169, 176], Mitchell *et al.* [177], Angel *et al.* [178], Rinn *et al.* [175] and the single-centre calculations of Hall *et al.* [179] are also shown for comparison. The figure reveals that there are some

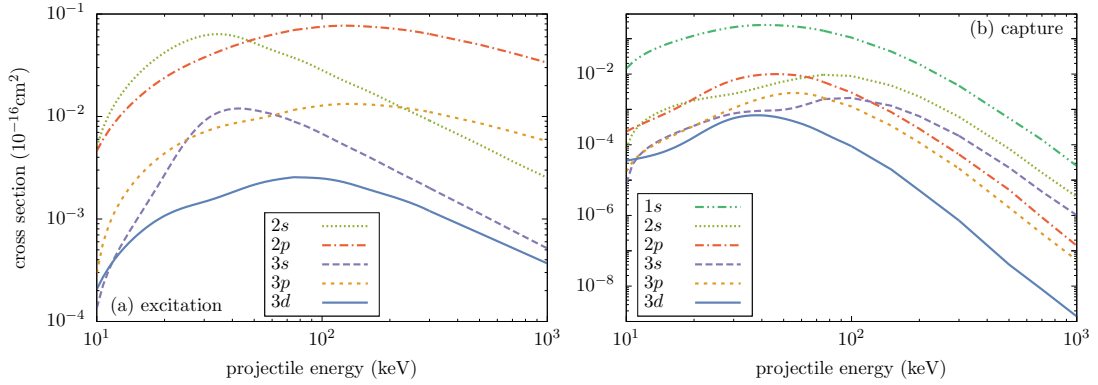


Figure 8.18: Cross sections for excitation and electron capture into the $n = 1, 2$ and 3 shell states in p - He^+ collisions.

discrepancies among the experimental results in the intermediate energy range. At these energies, our calculations only slightly exceed the experimental data of Rinn *et al.* [175] but significantly overestimate the results of Angel *et al.* [178], Peart *et al.* [169, 176]. At high energies, the WP-CCC results somewhat higher than the data of Mitchell *et al.* [177] and agree well at several measured points. Also, it should be pointed out that our results overestimate the single-centre calculations of Hall *et al.* [179] at all considered energies. The difference is more significant at lower energies, and relatively small at higher energies.

Figure 8.18 presents the WP-CCC results for the cross section for excitation [panel (a)] and electron capture [panel (b)] into the $n = 1, 2$ and 3 shell states. One can see that excitation of the $2s$ and $2p$ states of the target is the dominant process at lower and higher energies, respectively. The excitation cross section of the $3d$ state provides the lowest contribution in the entire incident energy range, except for the lowest energies. We can also see in panel (b) that the transfer into the $1s$ state is the dominant process in electron capture.

8.3 Chapter summary

In this chapter we discussed the WP-CCC results applied to He²⁺-H and *p*-He⁺ collisions. We first studied the convergence of the results for each considered process in terms of maximum orbital number of the included states. Having obtained a sufficient level of convergence, we presented the final results and compared with the available experimental data and other theoretical calculations. A level of agreement with other results for the considered processes was mixed. In particular, the present calculations for electron capture into the selected states agreed with the experiment very well, but for excitation we observed some discrepancies. For Balmer- α emission, our results underestimated the experimental data by a factor of 2. For other processes, overall, the WP-CCC results correctly describe the experiment.

Chapter 9

Proton-helium collisions

In this chapter, we discuss the results of the two-centre WP-CCC calculations for underlying processes in proton-helium collisions. The details of the approach was given in Chapter 4. Convergence of the predicted cross sections is studied in terms of the number of the included negative-energy eigenstates and positive-energy pseudostates. After establishing the convergence of the results, we describe the total electron-capture, direct-excitation, single- and double-ionisation cross sections in the energy range from 15 keV to 1 MeV. We also provide the partial cross sections for electron capture and direct excitation into the $n = 2$ shell states of hydrogen and helium, respectively. The results will be compared with experimental data and other theoretical results wherever available.

A number of calculations were performed to check the accuracy of the parameters employed in the approach. Our calculations showed that setting $n_{\max} = 5$ for the maximum principal quantum number of eigenstates is sufficient. As mentioned in Chapter 5, the resulting cross sections are also dependent on the choice of b_{\max} , the upper limit for the impact parameter. In our calculations we set $b_{\max} = 10$. Increasing these parameters further had no significant effect on the final results for total cross sections.

9.1 Convergence studies

We first describe the convergence of the predicted cross sections in terms of the number of target- and projectile-centred states. For simplicity, we used the same number of basis functions on both centres. We systematically increased the basis size by increasing the number of bins and the maximum orbital quantum number of the included states. While increasing the basis size, we carefully checked the accuracy of the employed wave functions for the target and the atom formed by the projectile.

The dependence of the predicted electron-capture and single-ionisation cross sections on the number of bin states is shown in Fig. 9.1. The number of bins N_c was increased up to 20 at projectile energies of 50 keV, 100 keV, 500 keV, and 1 MeV, respectively. In calculations we set $n_{\max} = 5$ and $l_{\max} = 3$. It can be seen that both electron-capture (upper panel) and single-ionisation (lower panel) results appear sufficiently convergent. For both processes, the difference between the cross sections calculated with $N_c = 16$ and $N_c = 20$ is within 0.5% at all considered impact energies. The calculations revealed that including positive-energy pseudostates is not only important to obtain an accurate result for the single-ionisation cross section, but also improves the accuracy of the electron-capture cross section. This can be observed in the upper panel of Fig. 9.1. Similar conclusions were drawn by Slim *et al.* [47]. The ionisation cross section is particularly sensitive to the number of positive-energy pseudostates and the density of the continuum discretisation. To get accurate results and better convergence with respect to the number of positive-energy pseudostates, the maximum energy of the included bin states, E_{\max} , needs to be sufficiently large. Depending on the projectile energy, $k_{\max}(= \sqrt{2E_{\max}})$ ranged from 3.5 for lowest incident energy to 7.5 for highest incident energy. The parameter was checked

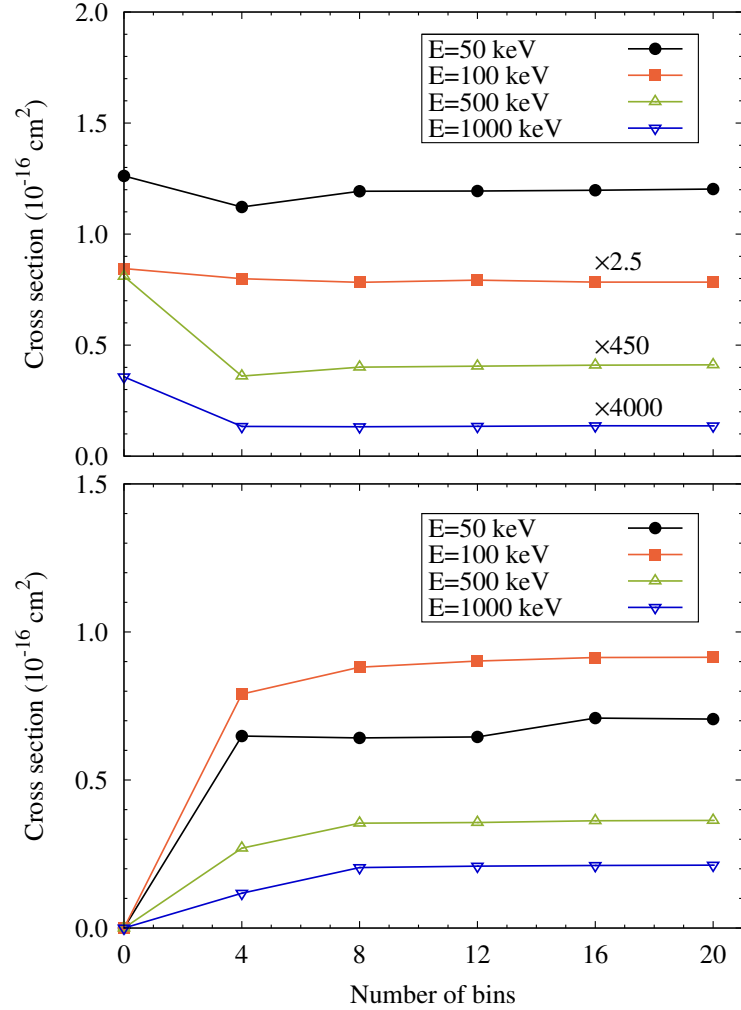


Figure 9.1: Total cross sections for electron capture (upper panel) and single ionisation (lower panel) in *p-He* collisions: convergence of the present WP-CCC results with respect to the number of bin states N_c . The four lines represent the cross sections at the incident proton energies of 50 keV, 100 keV, 500 keV and 1 MeV, respectively.

for each incident energy individually. Note that $N_c = 0$ yields no ionisation cross section due to the lack of positive-energy states.

Next, we investigate the convergence of the electron-capture and ionisation cross sections in terms of the maximum allowed orbital angular momentum quantum number, l_{\max} . The results are presented in Fig. 9.2 for l_{\max} ranging from zero to 4 at impact energies of 50 keV, 100 keV, 500 keV, and 1 MeV. Both electron-capture (upper panel) and ionisation (lower panel) cross sections

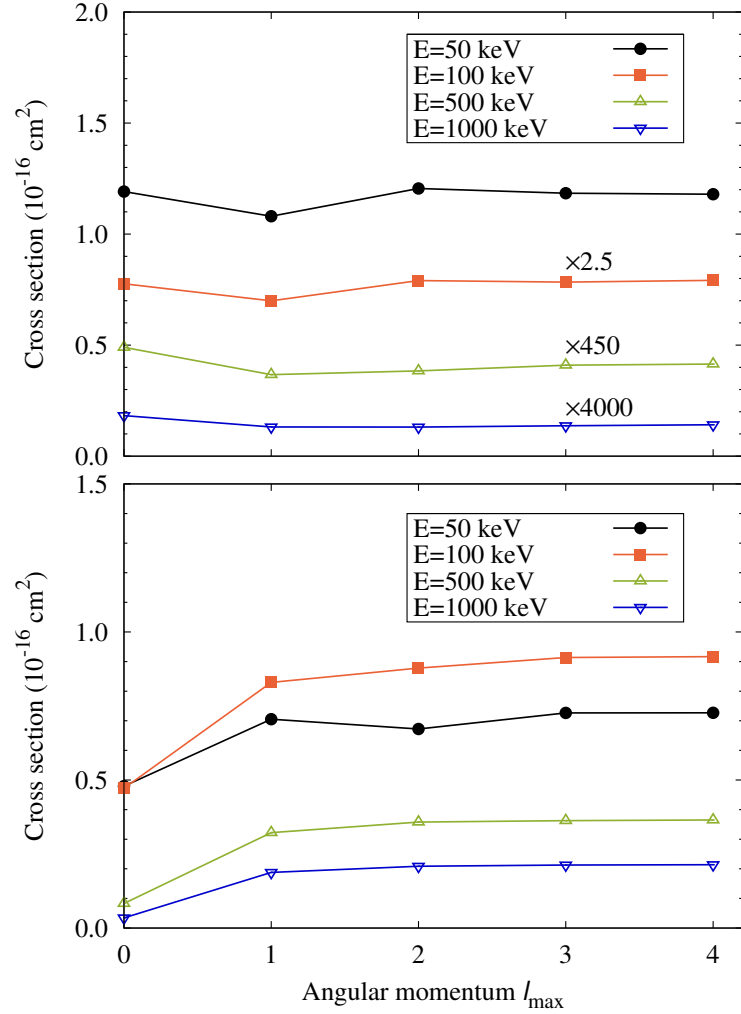


Figure 9.2: The same as in Fig. 9.1, but with respect to l_{\max} . The number of bins was set to $N_c = 20$.

appear convergent in terms of l_{\max} too. In general, convergence was achieved with $l_{\max} = 3$ for all energies considered. It should also be pointed out that as in the case of the number of bins, convergence of the results at higher energies is faster for both electron capture and ionisation.

9.2 Total cross sections

As discussed above, setting $n_{\max} = 5$, $l_{\max} = 3$ and $N_c = 20$ was required to obtain sufficiently accurate results. The basis with these parameters consists of

366 target- and projectile-centred functions. Below we present our main results for the integrated cross sections.

9.2.1 Electron capture and excitation

The present results for the total electron-capture cross section as a function of the incident energy are presented in Fig. 9.3 in comparison with the experimental data and the results of other theoretical works. As described in Chapter 5,

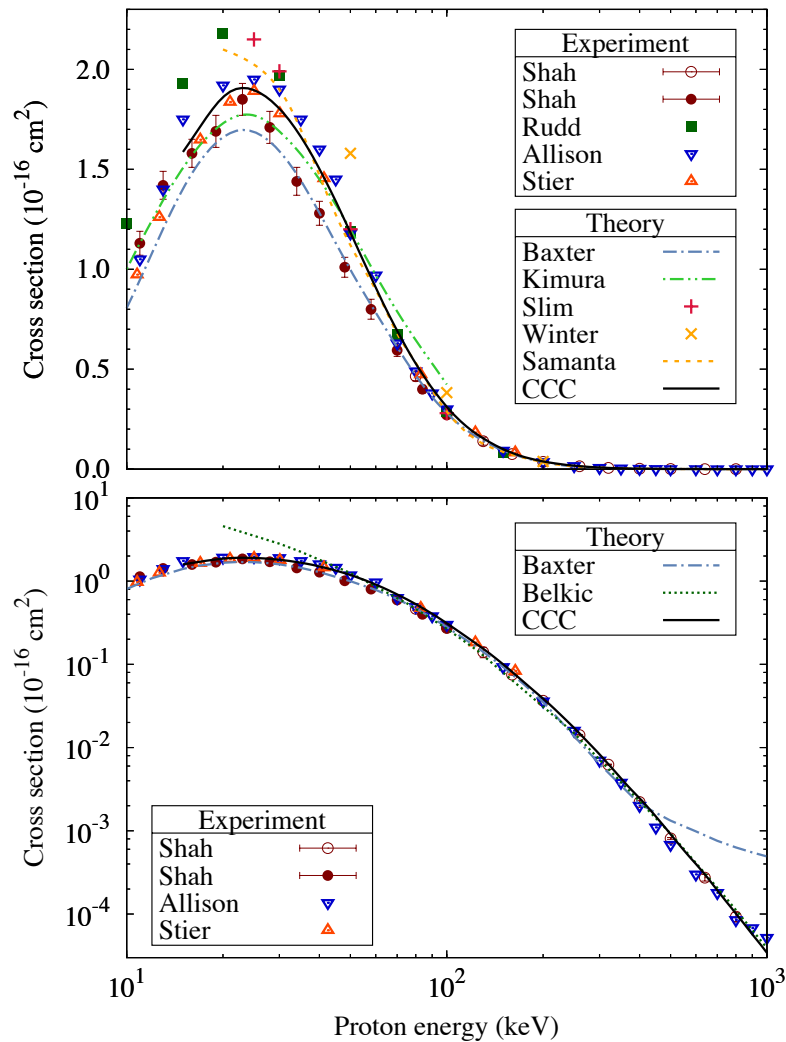


Figure 9.3: Total cross section for electron capture in $p\text{-He}(1s^2)$ collisions as a function of the incident proton energy (top and bottom panels linear and log y scales respectively). The present results are compared with the experimental data [59–63], and the other theoretical results [38, 39, 45–48].

the total electron-capture cross section is the sum of the cross sections for the transitions into all included negative-energy states of hydrogen. Capture into the $1s$ state provides the dominant contribution. It can be seen from the figure that the total electron-capture cross section reaches its peak around 25 keV. The present results are in good agreement with the experimental data of Shah and Gilbody [60] and Shah *et al.* [61], except for the energy range of 30-100 keV, where our calculated cross section exceeds the data by about 15%. In this energy range only the results of Baxter and Kirchner [38] agree with the measurements of Shah *et al.* [61], while the results of all other calculations are slightly higher, most likely due to the frozen-core approximation used to treat the target structure. It is also interesting to compare our results with the close-coupling calculations of Winter [48] and Slim *et al.* [47]. Winter neglected electron exchange in the final transfer channel and the calculations included only 50 Sturmian basis functions. The result of Winter [48] exceeds ours by about 30% at 50 keV but agrees at 200 keV, the largest incident energy considered by him. Slim *et al.* [47] succeeded to include electron exchange between H and He^+ in the transfer channel, even though they used only 51 basis functions. Their electron-capture results exceed the CCC predictions by about 15% near the peak, but agree for the higher energies. Measurements by Stier and Barnett [63], Allison [59] and Rudd *et al.* [62] are also shown, however these include the transfer-ionisation cross section in addition to electron capture with the second electron staying bound.

In the lower panel of Fig. 9.3, the same results are given on a logarithmic y scale to highlight the higher energy region. In the energy range from 100 keV to 1 MeV, our calculations agree well with the experimental results of Shah and Gilbody [60]. The theoretical results of Baxter and Kirchner [38] are also in good agreement with the experimental data up to 400 keV, whereas they deviate from

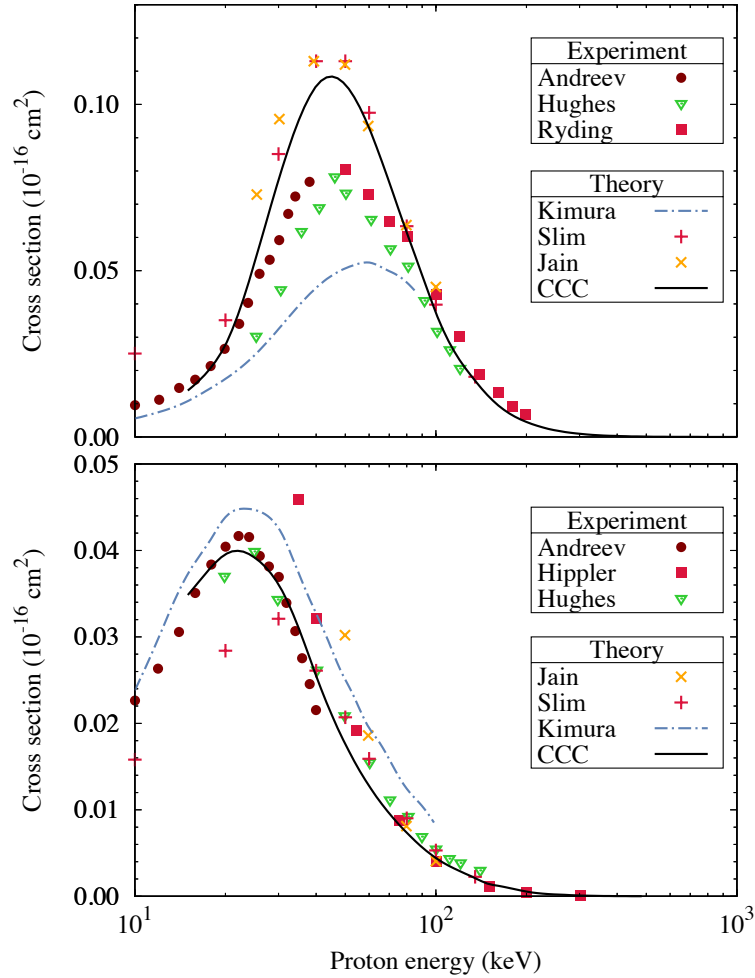


Figure 9.4: Cross sections for electron capture into the $2s$ (upper panel) and $2p$ (lower panel) states of hydrogen in $p\text{-He}(1s^2)$ collisions. The CCC results are represented by the black solid line. The experimental data are due to Hughes *et al.* [64], Hippler *et al.* [66], Ryding *et al.* [67], Andreev *et al.* [180]. The other theoretical results are from Kimura and Lin [45], Slim *et al.* [50], Jain *et al.* [51].

the data and other calculations at higher energies. In this energy range the B1B calculations of Belkić [39], using the Roothaan-Hartree-Fock wave functions, also yield excellent agreement with the experimental data.

Electron capture into the $1s$ state of hydrogen dominates the charge-transfer process, but capture into other specific states is also important for plasma modelling. In Fig. 9.4 we present the partial cross sections for electron capture into the $n = 2$ shell of hydrogen. At low and high energies the CCC results for elec-

tron capture into the $2s$ state agree with the experimental data. However, clear discrepancy between the experimental and theoretical results is seen in the intermediate energy range, where the CCC results are in good agreement with the calculations of Slim *et al.* [50] and Jain *et al.* [51], but exceed the experimental data. For electron capture into the $2p$ state we observe fairly good agreement with the cross sections obtained experimentally, except for the results of Hippler and Schartner [65], which exceed other results at the intermediate energy range.

In Fig. 9.5 we provide the cross sections for direct excitation of helium into the $2p$ state and the sum of the cross sections for excitation into the $2s$ and $2p$ states of helium. We obtained agreement with the experimental data of Park and Schowengerdt [68] for both cases in the low and intermediate energy regions. The CCC results for excitation of helium into the $2p$ state lie slightly below the experimental data and other theoretical results above 150 keV, the difference with experiment being within 10%. The sum of the calculated cross sections for excitation into the $2s$ and $2p$ states is in good agreement with the results of Begum *et al.* [53] in the intermediate energy range. At higher energies our results are below all the other theories, including the calculations by van den Bos [56] and Joachain and Vanderpoorten [55].

9.2.2 Ionisation

In Fig. 9.6 the total single-ionisation cross section is compared with the experimental data [60, 61] and other calculations [38, 42, 47, 48]. It can be seen that the ionisation cross section reaches its maximum around 100 keV and decreases almost linearly with increasing energy of the projectile. On the other hand, as we have observed in the previous section, the electron-capture cross section falls off exponentially after reaching its maximum near 25 keV. The CCC results for single ionisation exceed the experimental data of Shah and Gilbody [60] and

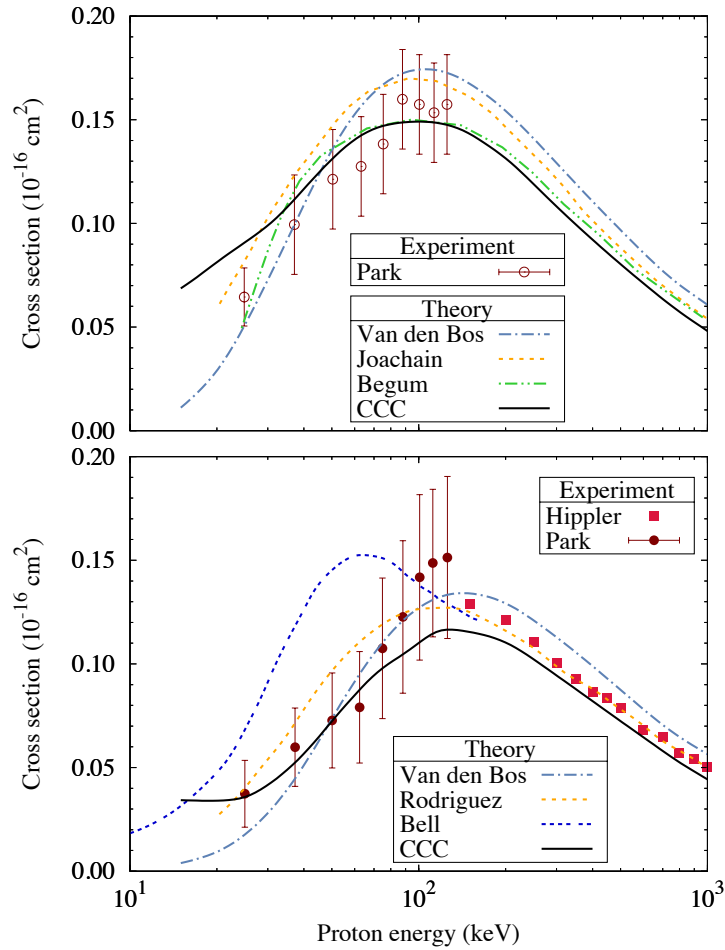


Figure 9.5: Sum of the cross sections for target excitation into the $2s$ and $2p$ states (upper panel), and the cross section for excitation into the $2p$ state (lower panel) of helium in $p\text{-He}(1s^2)$ collisions. The CCC results are represented by the black solid line. The experimental data are due to Hippler and Schartner [65], Park and Schowengerdt [68]. The other theoretical results are from Begum *et al.* [53], Joachain and Vanderpoorten [55], van den Bos [56].

Shah *et al.* [61] by about 10% below 200 keV. The calculations of Baxter and Kirchner [38] based on the time-dependent density-functional theory, where the Wilken-Bauer model is applied, agree with the experiments except for the lower energies. Below 60 keV their results lie slightly below the data. Experimental data of Rudd *et al.* [62] that include double ionisation in addition to single ionisation are also shown. As we will see later, the double ionisation cross section is very small and cannot explain the difference between the data of Shah and

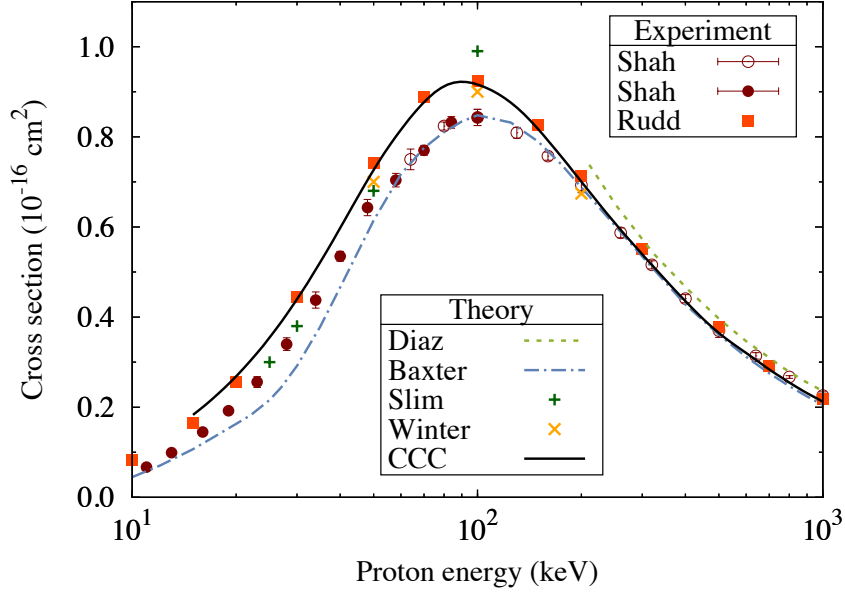


Figure 9.6: Cross section for single ionisation in $p\text{-He}(1s^2)$ collisions as a function of incident energy. The CCC results represented by the black solid line. The experimental data are due to Shah and Gilbody [60], Shah *et al.* [61], Rudd *et al.* [62]. The other theoretical results are from Baxter and Kirchner [38], Díaz *et al.* [42], Slim *et al.* [47], Winter [48].

Gilbody [60], Shah *et al.* [61] and Rudd *et al.* [62].

Our results are in fair agreement with the close-coupling calculations by Winter [48]. The results of Slim *et al.* [47], which take into account electron exchange in the final states, exceed the experimental data as well as the CCC calculations at 100 keV. Above 200 keV all theoretical predictions, including ours, and the experimental data agree very well with each other, with the exception of the results of Díaz *et al.* [42], which are moderately higher. Note that employing a more accurate multicore description of the helium target will likely result in a reduction of the theoretical cross sections [49].

In Fig. 9.7 we present our results for double ionisation, as obtained with the IEM model. Below 40 keV we observe good agreement with experiment, but for the higher energies our cross sections significantly exceed the measured data. Significantly larger double-ionisation cross sections were also obtained in IEM

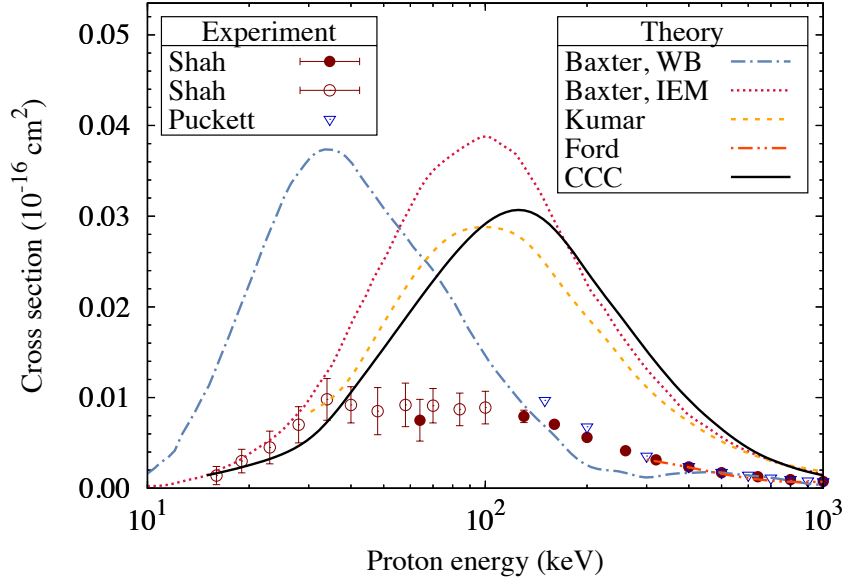


Figure 9.7: Cross section for double ionisation of helium in $p\text{-He}(1s^2)$ collisions as a function of incident energy. The CCC results are represented by the black solid line. The experimental data are due to Shah and Gilbody [60], Shah *et al.* [61], Puckett and Martin [69]. The other theoretical results are from Baxter and Kirchner [38], Ford and Reading [57], Kumar and Roy [58].

calculations by Baxter and Kirchner [38], Kumar and Roy [58], and Ford and Reading [57]. The present results and those of all displayed IEM calculations are overall in reasonable agreement with each other. The observed large discrepancy with experiment suggests that there exist a strong correlation between one- and two-electron processes as far as double ionisation of helium is concerned. In other words, the representation of double ionisation using the IEM does not seem appropriate.

9.3 Chapter summary

To summarise, we studied the convergence of the WP-CCC results in terms of the number of basis functions and the maximum allowed orbital angular momentum of the included states at several energies of the projectile. Having obtained satisfactory convergence, the total electron-capture and single-ionisation cross

sections were calculated in the energy range from 15 keV to 1 MeV.

There are many experiments and theoretical results available for these processes for comparison. We observed noticeable discrepancies among them below 150 keV. In this energy range agreement between our calculations and the experimental data of Shah and Gilbody [60] and Shah *et al.* [61] was found to be within 15% for both electron capture and single ionisation. Above 150 keV our results and all experiments agreed very well. It is worth mentioning that among the close-coupling calculations for electron capture, the CCC results were found to be in better agreement with experiment. This was likely due to the more accurate target description and a significantly larger size of the basis used in the CCC method. Apart from the total cross sections, we calculated the cross sections for capture into the $2s$ and $2p$ states of hydrogen, and excitation into the $2s$ and $2p$ states of helium. Fair agreement with other works was obtained in these particular cases as well. Furthermore, we used the independent-event model to study double ionisation of the target, where double ionisation is formulated as a combination of two independent processes: single ionisation of helium and sequential ionisation of the resulting helium ion by proton impact. However, except for lower energies, we failed to get agreement with the experimental data.

In this work we discretised the continuum using the wave-packet method. An advantage of this method is that it allows us to study electrons ejected with arbitrary energies without interpolation. This is achieved by including a bin state exactly matching the ejected-electron energy. Therefore, this approach can be applied to study differential ionisation. Specifically, the partial cross sections for transfer into all positive-energy pseudostates that we calculated can be used to obtain the differential cross sections for ionisation of helium.

Chapter 10

Conclusion and Outlook

In this thesis, we described the extension of the WP-CCC method to proton scattering on excited atomic hydrogen, collisions of multiply-charged bare ions (He^{2+} and C^{6+}) with hydrogen and proton collisions with the helium atom and the He^+ ion. We first discussed the background of ion-atom collisions and briefly described some theoretical methods, which have been applied to these collisions. We also stated the importance of these collisions in different fields of science and the practical application areas. The underlying theory of the WP-CCC method to three- and four-body problems was described including the details of the performed numerical calculations. We presented the results of our calculations for various processes in these collisional systems and compared with experiment and other theories when available. Together with the integrated cross sections, we also provided the differential cross sections for ionisation of the hydrogen and helium atoms.

In our approach, we employed a semiclassical treatment for both three- and four-body systems, where the projectile motion was treated classically and the target structure was treated fully quantum mechanically. The target nucleus was set at the origin and we assumed that the projectile moves along the classical straight-line trajectory. The z axis of the coordinate system was chosen to be

parallel to the projectile direction. We applied the impact-parameter method.

A collisional system was described by the time dependent Schrödinger equation. The corresponding total scattering wave function was expanded in terms of the target- and projectile-centred basis functions. The basis functions were formed by a number of negative-energy eigenstates and positive-energy pseudostates. The pseudostates were constructed using the wave-packet approach, where they were obtained by discretising the continuum and superposing the continuum eigenfunctions in a given energy range. For collisions of fully-stripped ions with atomic hydrogen and $p\text{-He}^+$ collisions, the basis functions were written analytically. The expansion of the scattering function was substituted into the exact three-body Schrödinger equation and we obtained a set of the differential equations for the time-dependent coefficients, the transition amplitudes. The matrix elements, present in the system of equations, were reduced to the forms ready for numerical calculations using spherical and spheroidal coordinates. The resulting system was solved numerically to obtain the transition amplitudes. The amplitudes were used to calculate the total and differential cross sections for the considered processes.

The WP-CCC method was also applied to the four-body problem of proton collisions with helium. The helium atom was treated as a three-body system. The electron-electron correlations were fully taken into account. We employed the frozen-core approximation, where one of the electrons remains in the ground state of He^+ throughout the collision. The wave functions of the active electron were obtained numerically by solving the Schrödinger equation for helium. Then, the scattering wave function was expanded in the target- and projectile-centred pseudostates, where the former are helium wave functions and the latter were written as products of the ground-state wave function of the He^+ ion and the hydrogen wave functions. Then we followed the same procedure as in the case

for the three-body problem.

For all the considered processes and collisional systems, we first investigated the dependence of the results on the basis size. The maximum principal and orbital angular-momentum numbers of the included states, as well as the number of the discretisation bins were carefully checked to obtain well-converged results. The convergence of the results was demonstrated for selected processes. Together with the two-centre calculation, we provided the single-centre calculations for some collisions. In the single-centre approach, the scattering wave function was expanded only in the target basis functions. The convergence studies have revealed that the single-centre results converge relatively slower with respect to the maximum allowed orbital number, l_{\max} . To obtain a sufficiently convergent integrated cross section, values of l_{\max} were set between 3 and 6, depending on a considered process. But for differential cross sections, the parameter had to be increased to $l_{\max} = 8$ in the two-centre approach, and to $l_{\max} = 10$ in the single-centre approach.

For proton collisions with the excited atomic hydrogen, the convergence of the results were studied for all processes in the entire incident energy range (from 10 keV to 1MeV). We observed the systematic convergence. The convergence rate was especially fast at higher energies. Having obtained the full convergence, we presented our final results and compared with the available experimental and theoretical results. We calculated the total cross section for elastic scattering, electron capture and ionisation in proton scattering on the excited $2s$, $2p_0$ and $2p_1$ states of hydrogen. The present results for excitation of the $n = 3$ -shell states in p -H($2s$) collisions were in noticeable disagreement with the existing AOCC and CTMC calculations. However, for electron capture into the selected states of the projectile, we obtained overall good agreement. Also, we presented the results for the cross section for super-elastic, elastic and quasi-elastic scattering

and electron capture in proton scattering on the excited $2p_0$ and $2p_1$ states of atomic hydrogen. Additionally, we provided the data for the density matrices for excitation of the $n = 2$ -shell states into the final $n = 1$ -4-shell states of the target.

Establishing the convergence of the results in collisions of bare ions (He^{2+} and C^{6+}) with hydrogen required including the states with larger l_{max} . The full convergence of the total cross sections was obtained with $l_{\text{max}} = 6$ and the differential cross sections with $l_{\text{max}} = 10$. For C^{6+} -H collisions, together with the two-centre WP-CCC approach, we also showed the results of the single-centre approach. We demonstrated the l -dependence of the single- and two-centre results for the singly differential cross sections for ionisation of hydrogen by 1 MeV C^{6+} ions. Outcomes of these two approaches were compared at a certain electron ejection angle. The results of both methods were convergent. The convergence rate of the single-centre results was a bit slower than the two-centre method. The results of these methods approached each other with increasing l_{max} , the difference between the final results was within a few percent.

For C^{6+} -H collisions, we compared the calculated results for the total cross section for electron capture and ionisation with the available experiments and other theoretical calculations. Overall, good agreement was observed. Also, we studied the dependence of the singly differential ionisation cross section on the angle of the ejected electron at 1 MeV and 2.5 MeV incident energies. Apart from these, the doubly differential cross section results for ionisation were presented for the same impact energies. The dependence of the DDCS on the electron ejection angle was shown for several fixed ejection energies (3 eV, 10 eV, 40 eV, 100 eV, respectively), as well as on the electron ejection energies for certain ejection angles (15° , 45° , 90° , 120° , respectively). The results were found to be in good agreement with the available experimental data.

We also provided the total cross sections for electron capture, excitation and ionisation in He^{2+} -H and p - He^+ collisions. For all underlying processes we obtained generally good agreement with the experimental data. However, our results for Balmer- α emission underestimated the data by a factor of two and agreed with the other close-coupling calculations. It should be pointed out that the present results for electron capture into the selected states of He^+ ion in He^{2+} -H($1s$) collisions were found to be in excellent agreement with the corresponding experimental measurements, as well as with the corresponding close-coupling and AOCC calculations.

The cross sections for electron capture and single ionisation in p - $\text{He}(1s)$ collisions were also investigated. We studied the dependence of the results on the maximum orbital quantum number of the included states and on the number of the discretisation bins. Once we obtained an acceptable level of convergence for all parameters, we provided the cross sections for total electron capture, single- and double-ionisation, as well as electron capture into the selected states of the projectile and excitation of the $n = 2$ -shell states of the target. We observed overall good agreement with the experimental results of Shah and Gilbody [60] and Shah *et al.* [61] for both total electron capture and single ionisation. Our results exceeded the data by 10 to 15% in intermediate energies and agreed very well at high energies for both processes. We emphasise that this difference is due to the frozen-core approximation we employed. To calculate the double-ionisation cross section, we applied the independent event model. The results agreed with other similar calculations, however in comparison with experiment, the present results significantly exceed the data except for the lowest energy region. The employed model was not directly applicable for the double-transfer processes. A proper treatment would be developing the multicore description of the helium atom. Our results for electron capture into $n = 2$ -shell states of the

projectile and excitation of the $n = 2$ -shell states of the target were also in good agreement with experiment.

Calculations for the fully differential cross sections for single ionisation of helium by 75 keV proton impact in both coplanar and perpendicular planes are underway. The FDCS will be studied in both planes for different scattering angles of the projectile. We will investigate the dependence of the FDCS on the ejection angle of the ionised electrons with the energy of 5.4 eV. Also, the dependence of the doubly differential cross section on the electron ejection angle will be calculated for several ejection energies for ionisation of helium by 50 keV, 75 keV, 100 keV, and 150 keV incident protons.

Summarising, the WP-CCC approach was shown to generally describe the considered collisional systems and the processes well, although we observed some disagreements with the experiment for certain processes. The results presented in this work and the previous successful applications of the WP-CCC method to various collisions give an optimistic outlook for further extension of the method to more complex collisional systems, involving many-electron atoms and molecules. In particular, one of the potential areas of the development of the method could be collisions of multiply-charged bare ions with helium. The approach employed for proton scattering on helium could be directly applied to these collisions. Another important step in the development of the approach would be to apply the method to collisions of heavy particles with water molecule. The data for these collisions are very valuable for hadron therapy.

Appendix A

Momentum-transfer vectors

In this appendix, we derive formulas for the momentum-transfer vectors used in Chapter 3. The position vectors of the projectile and the target nucleus ($\boldsymbol{\sigma}$ and $\boldsymbol{\rho}$, respectively) relative to the centres of mass of the target atom and the atom formed after the electron capture by the projectile are expressed as (see Fig. 3.2)

$$\boldsymbol{\sigma} = \gamma_1 \mathbf{r}_1 - \mathbf{r}_2, \quad \boldsymbol{\rho} = \mathbf{r}_1 - \gamma_2 \mathbf{r}_2, \quad (\text{A.1})$$

where γ_1 and γ_2 are the reduced masses of the target nucleus-electron and the projectile-electron systems

$$\gamma_1 = \frac{m_T - 1}{m_T}, \quad \gamma_2 = \frac{m_P}{m_P + 1}, \quad (\text{A.2})$$

with m_T and m_P being the masses of the target and the projectile, respectively (in atomic units electron mass is 1).

Let us introduce the following vectors

$$\mathbf{k} = \mathbf{k}_\alpha - \mathbf{k}_{\alpha'}, \quad \mathbf{q} = \gamma_1 \mathbf{k}_\alpha - \mathbf{k}_{\beta'}, \quad \mathbf{p} = \mathbf{k}_\alpha - \gamma_2 \mathbf{k}_{\beta'}. \quad (\text{A.3})$$

Using these notations, the exponential terms present in the direct matrix element (3.23) can be rewritten as

$$\mathbf{k}_\alpha \boldsymbol{\sigma} - \mathbf{k}_{\alpha'} \boldsymbol{\sigma} = \mathbf{k} \boldsymbol{\sigma} = \mathbf{k}(\gamma_1 \mathbf{r}_1 - \mathbf{r}_2) = \mathbf{k} \mathbf{R} + (\gamma_1 - 1) \mathbf{r}_1 \approx \mathbf{k} \mathbf{R}$$

and in the rearrangement matrix element (3.25) as

$$\begin{aligned}
\mathbf{k}_\alpha \boldsymbol{\sigma} - \mathbf{k}_{\beta'} \boldsymbol{\rho} &= \mathbf{k}_\alpha (\gamma_1 \mathbf{r}_1 - \mathbf{r}_2) - \mathbf{k}_{\beta'} (\mathbf{r}_1 - \gamma_2 \mathbf{r}_2) \\
&= (\gamma_1 \mathbf{k}_\alpha - \mathbf{k}_{\beta'}) \mathbf{r}_1 - (\mathbf{k}_\alpha - \gamma_2 \mathbf{k}_{\beta'}) \mathbf{r}_2 \\
&= \mathbf{q} \mathbf{r}_1 - \mathbf{p} \mathbf{r}_2 = \mathbf{q} (\mathbf{r}_1 - \mathbf{r}_2) - (\mathbf{q} - \mathbf{p}) \mathbf{r}_2.
\end{aligned} \tag{A.4}$$

For the term $\mathbf{q} - \mathbf{p}$ in Eq. (A.4), we have

$$\mathbf{q} - \mathbf{p} = (\gamma_1 \mathbf{k}_\alpha - \mathbf{k}_{\beta'}) - (\mathbf{k}_\alpha - \gamma_2 \mathbf{k}_{\beta'}) = -\frac{\mathbf{k}_\alpha}{m_T} - \frac{\mathbf{k}_{\beta'}}{m_P + 1}. \tag{A.5}$$

Absolute values of the vectors \mathbf{k}_α and $\mathbf{k}_{\beta'}$ are found as

$$k_\alpha = \mu_1 v = \frac{m_P m_T}{m_P + m_T} v, \tag{A.6}$$

$$k_{\beta'} = \mu_2 v = \frac{(m_T - 1)(m_P + 1)}{m_P + m_T} v, \tag{A.7}$$

where μ_1 and μ_2 are the reduced masses defined as

$$\mu_1 = \frac{m_P m_T}{m_P + m_T}, \quad \mu_2 = \frac{(m_T - 1)(m_P + 1)}{m_P + m_T}. \tag{A.8}$$

Therefore, taking into account the relation

$$\frac{k_\alpha}{m_T + 1} + \frac{k_{\beta'}}{m_P + 1} = - \left(\frac{m_P}{m_P + m_T + 1} - \frac{m_T}{m_P + m_T + 1} \right) v \approx -v \tag{A.9}$$

we get

$$\mathbf{q} - \mathbf{p} = \frac{\mathbf{k}_\alpha}{m_T + 1} + \frac{\mathbf{k}_{\beta'}}{m_P + 1} \approx \mathbf{v}. \tag{A.10}$$

Applying these and the relation $\mathbf{r}_1 - \mathbf{r}_2 = \mathbf{R}$, Eq. (A.4) is reduced to

$$\mathbf{k}_\alpha \boldsymbol{\sigma} - \mathbf{k}_{\beta'} \boldsymbol{\rho} = \mathbf{q} \mathbf{R} + \mathbf{v} \mathbf{r}_2. \tag{A.11}$$

We separate the parallel and perpendicular components of the vectors \mathbf{k} and \mathbf{q} using the relation $\mathbf{R} = \mathbf{b} + \mathbf{v}t$ (note that $\mathbf{b} \cdot \mathbf{v} = 0$) and write

$$\mathbf{k} \mathbf{R} = \mathbf{k}_{\parallel} \mathbf{v}t + \mathbf{k}_{\perp} \mathbf{b}, \quad \mathbf{q} \mathbf{R} = \mathbf{q}_{\parallel} \mathbf{v}t + \mathbf{q}_{\perp} \mathbf{b}.$$

Next, we describe the parallel and perpendicular components of the vectors \mathbf{k} and \mathbf{q} , starting from the first. The vector \mathbf{k}_α is directed along the z axis. Accordingly, $\mathbf{k}_\parallel = k_\alpha$ and $\mathbf{k}_\perp = 0$, therefore

$$\mathbf{k}_\parallel = k_\alpha - k_{\alpha'} \cos \theta, \quad (\text{A.12})$$

which can be written using the small angle approximations $\cos \theta \approx 1$ as

$$\mathbf{k}_\parallel \approx k_\alpha - k_{\alpha'}. \quad (\text{A.13})$$

On the other hand, from the conservation of the total energy we have

$$\frac{k_\alpha^2}{2\mu_1} + \epsilon_\alpha = \frac{k_{\alpha'}^2}{2\mu_1} + \epsilon_{\alpha'}. \quad (\text{A.14})$$

Using this, the momentum $k_{\alpha'}$ is found as

$$k_{\alpha'} = k_\alpha \sqrt{1 - \frac{2\mu_1 \Delta E}{k_\alpha^2}}, \quad (\text{A.15})$$

where $\Delta E = \epsilon_{\alpha'} - \epsilon_\alpha$. Now we consider the expansion series

$$(1 + x)^\eta = \sum_{\lambda=0}^{\infty} \binom{\eta}{\lambda} x^\lambda, \quad (\text{A.16})$$

where $\binom{\eta}{\lambda}$ is the binomial coefficient. By applying this, we can express the square root in Eq. (A.15) as

$$\left(1 - \frac{2\mu_1 \Delta E}{k_\alpha^2}\right)^{1/2} = 1 - \frac{1}{2} \left(\frac{2\mu_1 \Delta E}{k_\alpha^2}\right) - \frac{1}{8} \left(\frac{2\mu_1 \Delta E}{k_\alpha^2}\right)^2 - \frac{1}{16} \left(\frac{2\mu_1 \Delta E}{k_\alpha^2}\right)^3 - \dots \quad (\text{A.17})$$

Therefore,

$$k_\alpha \sqrt{1 - \frac{2\mu_1 \Delta E}{k_\alpha^2}} = k_\alpha - \frac{\mu_1 \Delta E}{k_\alpha} - \frac{1}{2} \frac{\mu_1^2 \Delta E^2}{k_\alpha^3} - \frac{1}{2} \frac{\mu_1^3 \Delta E^3}{k_\alpha^5} - \dots \quad (\text{A.18})$$

Finally, using the relation $k_\alpha = \mu_1 v$ we obtain

$$k_\alpha - k_{\alpha'} = k_\alpha - k_\alpha \sqrt{1 - \frac{2\mu_1 \Delta E}{k_\alpha^2}} = \frac{\Delta E}{v} + \frac{1}{2v^3} \frac{\Delta E^2}{\mu_1} + \frac{1}{2v^5} \frac{\Delta E^3}{\mu_1^2} - \dots \quad (\text{A.19})$$

If the energy difference ΔE is small enough and v is sufficiently large, we can neglect all terms in the expansion series except $\Delta E/v$ (because μ_1 is large) to get

$$k_\alpha - k_{\alpha'} \approx \frac{\Delta E}{v}. \quad (\text{A.20})$$

Next, we deal with the momentum-transfer vector \mathbf{q} . The parallel component \mathbf{q}_{\parallel} of the vector $\mathbf{q} = \gamma_1 \mathbf{k}_\alpha - \mathbf{k}_{\beta'}$ is expressed as

$$\mathbf{q}_{\parallel} = \gamma_1 k_\alpha - k_{\beta'} \cos \theta, \quad (\text{A.21})$$

which can be written in the form

$$\mathbf{q}_{\parallel} \approx \gamma_1 k_\alpha - k_{\beta'}, \quad (\text{A.22})$$

by applying the small angle approximation ($\cos \theta \approx 1$). From the conservation of the total energy

$$\frac{k_\alpha^2}{2\mu_1} + \epsilon_\alpha = \frac{k_{\beta'}^2}{2\mu_2} + \epsilon_{\beta'}, \quad (\text{A.23})$$

where μ_1 and μ_2 are the reduced masses defined above. Therefore, $k_{\beta'}$ can be found as

$$k_{\beta'} = k_\alpha \sqrt{\frac{\mu_2}{\mu_1} - \frac{2\mu_2 \Delta E}{k_\alpha^2}} = k_\alpha \sqrt{\frac{\mu_2}{\mu_1}} \sqrt{1 - \frac{2\mu_1 \Delta E}{k_\alpha^2}}, \quad (\text{A.24})$$

where now $\Delta E = \epsilon_{\beta'} - \epsilon_\alpha$. Applying the expansion series described in Eq. (A.16) yields

$$k_\alpha \sqrt{1 - \frac{2\mu_1 \Delta E}{k_\alpha^2}} = k_\alpha - \frac{\mu_1 \Delta E}{k_\alpha} - \frac{1}{2} \frac{\mu_1^2 \Delta E^2}{k_\alpha^3} - \frac{1}{2} \frac{\mu_1^3 \Delta E^3}{k_\alpha^5} - \dots$$

Also, we note that for the reduced mass μ_1 and μ_2 it holds

$$\frac{\mu_2}{\mu_1} = \frac{(m_T - 1)(m_P + 1)}{m_T m_P} = \left(1 - \frac{1}{m_T}\right) \left(1 + \frac{1}{m_P}\right) \quad (\text{A.25})$$

and therefore

$$\sqrt{\frac{\mu_2}{\mu_1}} \approx \sqrt{\left(1 - \frac{1}{m_T}\right) \left(1 + \frac{1}{m_P}\right)} \approx 1 - \frac{1}{2m_T} + \frac{1}{2m_P}. \quad (\text{A.26})$$

Taking into account this and the relation

$$\gamma_1 k_\alpha = \frac{m_T}{m_T + 1} k_\alpha = \left(1 - \frac{1}{m_T}\right) k_\alpha, \quad (\text{A.27})$$

the parallel component of the vector \mathbf{q} is written as

$$\begin{aligned} \mathbf{q}_\parallel &= \gamma_1 k_\alpha - k_\alpha \sqrt{\frac{\mu_2}{\mu_1}} \sqrt{1 - \frac{2\mu_1 \Delta E}{k_\alpha^2}} \\ &= \left(1 - \frac{1}{m_T}\right) k_\alpha - \left(1 - \frac{1}{2m_T} + \frac{1}{2m_P}\right) \left(k_\alpha - \frac{\mu_1 \Delta E}{k_\alpha} - \frac{1}{2} \frac{\mu_1^2 \Delta E^2}{k_\alpha^3} - \dots\right) \\ &= -k_\alpha \left(\frac{1}{2m_T} + \frac{1}{2m_P}\right) + \frac{\mu_1 \Delta E}{k_\alpha} + \frac{1}{2} \frac{\mu_1^2 \Delta E^2}{k_\alpha^3} + \dots \end{aligned} \quad (\text{A.28})$$

We also have

$$-k_\alpha \left(\frac{1}{m_T} + \frac{1}{m_P}\right) = v, \quad (\text{A.29})$$

which yields the final expression

$$\mathbf{q}_\parallel = -\frac{v}{2} + \frac{\Delta E}{v} + \frac{1}{2v^3} \frac{\Delta E^2}{\mu_1} + \dots \quad (\text{A.30})$$

As in the case of the direct scattering, if energy difference ΔE is small enough and v is sufficiently large we can neglect all terms except $\Delta E/v$ and obtain

$$\mathbf{q}_\parallel = -\frac{v}{2} + \frac{\Delta E}{v}. \quad (\text{A.31})$$

Using the derived expressions for the parallel components, we obtain

$$(\mathbf{k}_\alpha - \mathbf{k}_{\alpha'}) \boldsymbol{\sigma} \approx \mathbf{k} \mathbf{R} = (k_\alpha - k_{\alpha'}) vt + \mathbf{k}_\perp \mathbf{b} \approx (\epsilon_{\alpha'} - \epsilon_\alpha) t + \mathbf{k}_\perp \mathbf{b}, \quad (\text{A.32})$$

$$\mathbf{k}_\alpha \boldsymbol{\sigma} - \mathbf{k}_{\beta'} \boldsymbol{\rho} = \mathbf{q} \mathbf{R} + \mathbf{v} \mathbf{r}_2 = \mathbf{q}_\parallel vt + \mathbf{q}_\perp \mathbf{b} + \mathbf{v} \mathbf{r}_2 = -\frac{v^2}{2} t + (\epsilon_{\beta'} - \epsilon_\alpha) t + \mathbf{q}_\perp \mathbf{b} + \mathbf{v} \mathbf{r}_2. \quad (\text{A.33})$$

In a similar way, we have

$$(\mathbf{k}_\beta - \mathbf{k}_{\beta'}) \boldsymbol{\rho} \approx (\epsilon_{\beta'} - \epsilon_\beta) t + (\mathbf{k}_\beta - \mathbf{k}_{\beta'})_\perp \mathbf{b}, \quad (\text{A.34})$$

$$\mathbf{k}_\beta \boldsymbol{\rho} - \mathbf{k}_{\alpha'} \boldsymbol{\sigma} = \frac{v^2}{2} t + (\epsilon_{\alpha'} - \epsilon_\beta) t + \mathbf{q}_\perp \mathbf{b} - \mathbf{v} \mathbf{r}_2. \quad (\text{A.35})$$

Appendix B

Momentum-transfer vectors for proton-helium system

Here, we derive expressions for momentum transfer vectors used in Chapter 4 for proton-helium collisions. Taking into account the coordinates of the centres of mass both for p -H and H-He⁺ channels (see Fig. 4.2) the vector $\boldsymbol{\sigma}$ can be expressed as

$$\boldsymbol{\sigma} = \mathbf{R} - \gamma(\mathbf{r}_1 + \mathbf{r}_2) = (1 - \gamma)\mathbf{R} - \gamma(\mathbf{x}_1 + \mathbf{r}_2) = (1 - \gamma)\mathbf{R} - \gamma(\mathbf{r}_1 + \mathbf{x}_2) \quad (\text{B.1})$$

and the vectors $\boldsymbol{\rho}_1$ and $\boldsymbol{\rho}_2$ as

$$\boldsymbol{\rho}_1 = \mathbf{R} - \gamma_1\mathbf{r}_2 + \gamma_2\mathbf{x}_1 = (1 - \gamma_2)\mathbf{R} - \gamma_1\mathbf{r}_2 + \gamma_2\mathbf{r}_1, \quad (\text{B.2})$$

$$\boldsymbol{\rho}_2 = \mathbf{R} - \gamma_1\mathbf{r}_1 + \gamma_2\mathbf{x}_2 = (1 - \gamma_2)\mathbf{R} - \gamma_1\mathbf{r}_1 + \gamma_2\mathbf{r}_2, \quad (\text{B.3})$$

with $\gamma_1 = 1/(m_T - 1)$, $\gamma_2 = 1/(m_P + 1)$, $\gamma = 1/m_T$.

Using these expressions, the momentum-transfer vectors entering the direct

matrix elements (4.42)–(4.44) are approximated in the following forms

$$(\mathbf{k}_\alpha - \mathbf{k}_{\alpha'})\boldsymbol{\sigma} \approx (\mathbf{k}_\alpha - \mathbf{k}_{\alpha'})\mathbf{R} = (\mathbf{k}_\alpha - \mathbf{k}_{\alpha'})_{\parallel}\mathbf{R} + (\mathbf{k}_\alpha - \mathbf{k}_{\alpha'})_{\perp}\mathbf{b}, \quad (\text{B.4})$$

$$(\mathbf{k}_{1\beta} - \mathbf{k}_{1\beta'})\boldsymbol{\rho}_1 \approx (\mathbf{k}_{1\beta} - \mathbf{k}_{1\beta'})\mathbf{R} = (\mathbf{k}_{1\beta} - \mathbf{k}_{1\beta'})_{\parallel}\mathbf{R} + (\mathbf{k}_{1\beta} - \mathbf{k}_{1\beta'})_{\perp}\mathbf{b}, \quad (\text{B.5})$$

$$(\mathbf{k}_{2\beta} - \mathbf{k}_{2\beta'})\boldsymbol{\rho}_1 \approx (\mathbf{k}_{2\beta} - \mathbf{k}_{2\beta'})\mathbf{R} = (\mathbf{k}_{2\beta} - \mathbf{k}_{2\beta'})_{\parallel}\mathbf{R} + (\mathbf{k}_{2\beta} - \mathbf{k}_{2\beta'})_{\perp}\mathbf{b}, \quad (\text{B.6})$$

$$\mathbf{k}_{1\beta}\boldsymbol{\rho}_1 - \mathbf{k}_{2\beta'}\boldsymbol{\rho}_2 \approx (\mathbf{k}_{1\beta} - \mathbf{k}_{2\beta'})\mathbf{R} = (\mathbf{k}_{1\beta} - \mathbf{k}_{2\beta'})_{\parallel}\mathbf{R} + (\mathbf{k}_{1\beta} - \mathbf{k}_{2\beta'})_{\perp}\mathbf{b}, \quad (\text{B.7})$$

$$\mathbf{k}_{2\beta}\boldsymbol{\rho}_1 - \mathbf{k}_{1\beta'}\boldsymbol{\rho}_2 \approx (\mathbf{k}_{2\beta} - \mathbf{k}_{1\beta'})\mathbf{R} = (\mathbf{k}_{2\beta} - \mathbf{k}_{1\beta'})_{\parallel}\mathbf{R} + (\mathbf{k}_{2\beta} - \mathbf{k}_{1\beta'})_{\perp}\mathbf{b}. \quad (\text{B.8})$$

The terms appearing in the rearrangement matrix elements (4.45)–(4.48) can be written as

$$\begin{aligned} \mathbf{k}_\alpha\boldsymbol{\sigma} - \mathbf{k}_{1\beta'}\boldsymbol{\rho}_1 &= \mathbf{k}_\alpha(1 - \gamma)\mathbf{R} - \gamma(\mathbf{x}_1 + \mathbf{r}_2)) - \mathbf{k}_{1\beta'}(\mathbf{R} - \gamma_1\mathbf{r}_2 + \gamma_2\mathbf{x}_1) \\ &= ((1 - \gamma)\mathbf{k}_\alpha - \mathbf{k}_{1\beta'})\mathbf{R} + (\mathbf{k}_{1\beta'}\gamma_1 - \mathbf{k}_\alpha\gamma)\mathbf{r}_2 - (\mathbf{k}_\alpha\gamma + \mathbf{k}_{1\beta'}\gamma_2)\mathbf{x}_1, \end{aligned} \quad (\text{B.9})$$

where the term $(\mathbf{k}_{1\beta'}\gamma_1 - \mathbf{k}_\alpha\gamma)\mathbf{r}_2$ is very small and can be neglected. Following the procedure described in Appendix A, we obtain

$$\mathbf{k}_\alpha\boldsymbol{\sigma} - \mathbf{k}_{1\beta'}\boldsymbol{\rho}_1 = ((1 - \gamma)\mathbf{k}_\alpha - \mathbf{k}_{1\beta'})\mathbf{R} + \mathbf{v}\mathbf{x}_1, \quad (\text{B.10})$$

$$\mathbf{k}_\alpha\boldsymbol{\sigma} - \mathbf{k}_{2\beta'}\boldsymbol{\rho}_2 = ((1 - \gamma)\mathbf{k}_\alpha - \mathbf{k}_{2\beta'})\mathbf{R} + \mathbf{v}\mathbf{x}_2, \quad (\text{B.11})$$

$$\mathbf{k}_{1\beta}\boldsymbol{\rho}_1 - \mathbf{k}_{\alpha'}\boldsymbol{\sigma} = ((1 - \gamma_2)\mathbf{k}_{1\beta} - \mathbf{k}_{\alpha'})\mathbf{R} - \mathbf{v}\mathbf{x}_1, \quad (\text{B.12})$$

$$\mathbf{k}_{2\beta}\boldsymbol{\rho}_1 - \mathbf{k}_{\alpha'}\boldsymbol{\sigma} = ((1 - \gamma_2)\mathbf{k}_{2\beta} - \mathbf{k}_{\alpha'})\mathbf{R} - \mathbf{v}\mathbf{x}_2. \quad (\text{B.13})$$

By using the approximations for the parallel components of the momentum transfer vectors given in the previous appendix, we have

$$(\mathbf{k}_\alpha - \mathbf{k}_{\alpha'})\boldsymbol{\sigma} = \mathbf{q}_{\perp}\mathbf{b} + (\varepsilon_{\alpha'} - \varepsilon_{\alpha})t, \quad (\text{B.14})$$

$$(\mathbf{k}_{1\beta} - \mathbf{k}_{1\beta'})\boldsymbol{\rho}_1 = \mathbf{q}_{\perp}\mathbf{b} + (\varepsilon_{\beta'} - \varepsilon_{\beta})t, \quad (\text{B.15})$$

$$(\mathbf{k}_{2\beta} - \mathbf{k}_{2\beta'})\boldsymbol{\rho}_1 = \mathbf{q}_{\perp}\mathbf{b} + (\varepsilon_{\beta'} - \varepsilon_{\beta})t, \quad (\text{B.16})$$

$$\mathbf{k}_{1\beta}\boldsymbol{\rho}_1 - \mathbf{k}_{2\beta'}\boldsymbol{\rho}_2 = \mathbf{q}_{\perp}\mathbf{b} + (\varepsilon_{\beta'} - \varepsilon_{\beta})t, \quad (\text{B.17})$$

$$\mathbf{k}_{2\beta}\boldsymbol{\rho}_1 - \mathbf{k}_{1\beta'}\boldsymbol{\rho}_2 = \mathbf{q}_{\perp}\mathbf{b} + (\varepsilon_{\beta'} - \varepsilon_{\beta})t. \quad (\text{B.18})$$

The terms appearing in the rearrangement matrix elements (4.45)–(4.48) can be written as

$$\mathbf{k}_\alpha \boldsymbol{\sigma} - \mathbf{k}_{1\beta'} \boldsymbol{\rho}_1 = \mathbf{k}_\alpha \boldsymbol{\sigma} - \mathbf{k}_{2\beta'} \boldsymbol{\rho}_2 = \mathbf{q}_\perp \mathbf{b} + \mathbf{q}_{\alpha,\beta'\parallel} vt - \mathbf{v} \mathbf{r}_1, \quad (\text{B.19})$$

$$\mathbf{k}_{1\beta} \boldsymbol{\rho}_1 - \mathbf{k}_{\alpha'} \boldsymbol{\sigma} = \mathbf{k}_{2\beta} \boldsymbol{\rho}_1 - \mathbf{k}_{\alpha'} \boldsymbol{\sigma} = \mathbf{q}_\perp \mathbf{b} + \mathbf{q}_{\beta,\alpha'\parallel} vt + \mathbf{v} \mathbf{r}_1, \quad (\text{B.20})$$

where

$$\mathbf{q}_{\alpha,\beta'\parallel} = \frac{v}{2} + \frac{\varepsilon_{\beta'} - \varepsilon_\alpha}{v}, \quad \mathbf{q}_{\beta,\alpha'\parallel} = -\frac{v}{2} + \frac{\varepsilon_{\alpha'} - \varepsilon_\beta}{v}. \quad (\text{B.21})$$

The perpendicular component of the momentum transfers, \mathbf{q}_\perp are the same in all transitions.

Appendix C

Signed Statement of Coauthors

To Whom It May Concern I, Shukhrat Alladustov, contributed to the development of research ideas, methodology, underlying computer code and the preparation of the manuscript for the publication entitled **"Electron capture, excitation and ionization in He²⁺-H and H⁺-He⁺ collisions"**. Plasma Phys. Control. Fusion **61**, 095005 (2019).



I, as a Co-Author, endorse that this level of contribution by the candidate indicated above is appropriate.

Joshua Faulkner



Ilkhom Abdurakhmanov



Alisher Kadyrov



Igor Bray



To Whom It May Concern I, Shukhrat Alladustov, contributed to the development of research ideas, methodology, underlying computer code and the preparation of the manuscript for the publication entitled "**Wave-packet continuum-discretization approach to proton collisions with helium**". Phys. Rev. A **99**, 052706 (2019).



I, as a Co-Author, endorse that this level of contribution by the candidate indicated above is appropriate.

Ilkhom Abdurakhmanov



Alisher Kadyrov



Igor Bray



Klaus Bartschat



To Whom It May Concern I, Shukhrat Alladustov, contributed to the development of research ideas, methodology, underlying computer code and the preparation of the manuscript for the publication entitled **“Development of convergent close-coupling approach to hadron interactions with matter”**. J. Phys. Conf. Ser. **1154**, 012013 (2019).



I, as a Co-Author, endorse that this level of contribution by the candidate indicated above is appropriate.

Alisher Kadyrov



Ilkhom Abdurakhmanov



Jackson Bailey



Igor Bray



To Whom It May Concern I, Shukhrat Alladustov, contributed to the development of research ideas, methodology, underlying computer code and the preparation of the manuscript for the publication entitled "ionization and electron capture in collisions of bare carbon ions with hydrogen". Phys. Rev. A **98**, 062710 (2018).

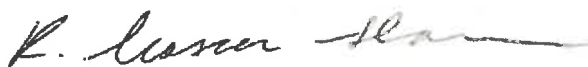


I, as a Co-Author, endorse that this level of contribution by the candidate indicated above is appropriate.

Ilkhom Abdurakhmanov



Kym Massen-Hane



Jackson Bailey



Alisher Kadyrov



Igor Bray



To Whom It May Concern I, Shukhrat Alladustov, contributed to the development of research ideas, methodology, underlying computer code and the preparation of the manuscript for the publication entitled "**Proton scattering from excited states of atomic hydrogen**". Plasma Phys. Control. Fusion **60**, 095009 (2018).



I, as a Co-Author, endorse that this level of contribution by the candidate indicated above is appropriate.

Ilkhom Abdurakhmanov



Jackson Bailey



Alisher Kadyrov



Igor Bray



Abbreviations

Abbreviation	Description
AO	Atomic Orbital
AOCC-PS	Atomic-Orbital Close-Coupling with Pseudostates
CCC	Convergent Close-Coupling
CDW-EIS	Continuum-Distorted-Wave Eikonal-Initial-State
CTMC	Classical-Trajectory Monte Carlo
DI	Double Ionisation
DS	Direct Scattering
DW	Distorted Wave
DWBA	Distorted-Wave Born Approximation
EC	Electron Capture
FBA	First Born Approximation
IEM	Independent event model
LTDSE	Lattice Time-Dependent Schrödinger equation
MO	Molecular Orbital
QM	Quantum Mechanical
SE	Schrödinger equation
SI	Single Ionisation
TDSE	Time-Dependent Schrödinger equation
WP	Wave Packet

List of Figures

1.1	Tokamak. Image courtesy of ITER.	2
1.2	Comparison of proton and traditional x-ray therapies [7].	3
3.1	An illustration of collisions of multiply-charged ions with hydrogen in the coordinate system, with the origin set at the target nucleus.	21
3.2	The Jacobi coordinates for the scattering system.	24
3.3	The Jacobi coordinates for the scattering system. The origin is set at the midpoint of the nuclei.	37
4.1	An illustration of the coordinate system, with the origin set at the target nucleus.	43
4.2	The Jacobi coordinates for the proton-helium system.	46
6.1	Cross sections for elastic scattering, electron capture and ionisation in p -H($2s$) collisions: convergence of the present WP-CCC results with respect to l_{\max}	72

6.2	Cross sections for elastic scattering, electron capture and ionisation in $p\text{-H}(2p_0)$ and $p\text{-H}(2p_1)$ collisions: convergence of the WP-CCC results with respect to l_{\max}	73
6.3	Cross sections for super-elastic ($2s \rightarrow 1s$), elastic ($2s \rightarrow 2s$) and quasi-elastic ($2s \rightarrow 2p_0$) scattering in $p\text{-H}(2s)$ collisions as functions of the incident proton energy.	74
6.4	Cross sections for excitation of the $n = 3$ shell ($3s, 3p, 3d$) states in $p\text{-H}(2s)$ collisions as a function of the incident proton energy. The CTCM and AOCC-PS results are due to Pindzola <i>et al.</i> [143]. The FBA results are also shown for comparison.	76
6.5	Cross sections for electron capture into the $1s, 2s, 2p, 3s, 3p$ and $3d$ states of hydrogen in $p\text{-H}(2s)$ collisions. The WP-CCC results are represented by the red solid line. The CTMC and AOCC-PS results are due to Pindzola <i>et al.</i> [143].	77
6.6	Cross sections for super-elastic, elastic and quasi-elastic scattering and electron capture for proton scattering on the excited $2p_0$ and $2p_1$ states of hydrogen as a function of the incident proton energy.	78
7.1	Total cross section for electron capture in $\text{C}^{6+}\text{-H}(1s)$ collisions: convergence of the present WP-CCC results with respect to l_{\max} (top and bottom panels are on linear and logarithmic y scales, respectively).	85
7.2	Total cross section for ionisation in $\text{C}^{6+}\text{-H}(1s)$ collisions: convergence of the present WP-CCC results with respect to l_{\max} (top and bottom panels are on linear and logarithmic y scales, respectively).	86

7.3	Singly differential cross section in the ejected-electron angle for 1 MeV/amu C^{6+} -impact ionisation of atomic hydrogen: convergence of the present two-centre WP-CCC results with respect to l_{\max}	87
7.4	The same as in Fig. 7.3, but for the single-centre WP-CCC approach.	88
7.5	Singly differential cross section for 1 MeV/amu C^{6+} -impact ionisation of atomic hydrogen. Dependence of the present single- and two-centre WP-CCC results on l_{\max} at $\theta = 0^\circ$	89
7.6	Total cross section for electron capture in C^{6+} -H(1s) collisions as a function of incident proton energy (top and bottom panels are on linear and logarithmic y scales, respectively). The present WP-CCC results are represented by the dark blue solid line. The experimental data are due to Goffe <i>et al.</i> [145] and Meyer <i>et al.</i> [144]. The other theoretical results are from Harel <i>et al.</i> [146], Toshima [148], Igenbergs <i>et al.</i> [147], Jorge <i>et al.</i> [37], and Belkic <i>et al.</i> [149]. The FBA results are also given.	91
7.7	Total cross section for ionisation in C^{6+} -H(1s) collisions as a function of incident proton energy (top and bottom panels linear and logarithmic y scales respectively). The present WP-CCC results are represented by the dark blue solid line. The experimental point is due to Shah and Gilbody [150]. The other theoretical results are from Igenbergs <i>et al.</i> [147], Toshima [148], Jorge <i>et al.</i> [37], and Rivarola <i>et al.</i> [151]. The FBA results are also given for comparison.	93

<i>List of Figures</i>	159
7.8 Singly differential cross section in the ejected-electron angle for 1 MeV/amu C^{6+} -impact ionisation of atomic hydrogen. The measurements and other calculations are due to Tribedi <i>et al.</i> [154, 155]. The FBA results are also shown for comparison. . . .	95
7.9 The same as in Fig. 7.8 but for 2.5 MeV/amu C^{6+} -H(1s) collisions.	96
7.10 Doubly differential cross sections in the ejected-electron energy at certain fixed ejection angles for 1 MeV/amu C^{6+} -impact ionisation of atomic hydrogen. The measurements and the CDW-EIS calculations are due to Tribedi <i>et al.</i> [154, 155]. The FBA results are also shown for comparison.	97
7.11 The same as in Fig. 7.10, but for 2.5 MeV/amu C^{6+} -H(1s) collisions.	99
7.12 Doubly differential cross sections in the ejected-electron angle at certain fixed ejection energies for 1 MeV/amu C^{6+} -impact ionisation of atomic hydrogen. The measurements and the CDW-EIS calculations are due to Tribedi <i>et al.</i> [154, 155]. The FBA results are also shown for comparison.	100
7.13 The same as in Fig. 7.12, but for 2.5 MeV/amu C^{6+} -H(1s) collisions	101
8.1 Total cross section for electron capture in H^{2+} -H(1s) collisions: convergence of the present WP-CCC results with respect to l_{\max}	105
8.2 Total cross section for ionisation in H^{2+} -H(1s) collisions: convergence of the present WP-CCC results with respect to l_{\max}	106

<i>List of Figures</i>	160
8.3 Total cross section for electron capture in $p\text{-He}^+$ collisions: convergence of the present WP-CCC results with respect to l_{max} .	107
8.4 Total cross section for ionisation in $p\text{-He}^+$ collisions: convergence of the present WP-CCC results with respect to l_{max} .	107
8.5 Fully differential cross section for He^{2+} -impact ionisation of atomic hydrogen as a function of the electron ejection angle: convergence of the WP-CCC results with respect to l_{max} . The arrow points in the momentum-transfer direction.	108
8.6 Doubly differential cross section for He^{2+} -impact ionisation of atomic hydrogen in the energy and the angle of the ejected electron: convergence of the WP-CCC results with respect to l_{max} .	109
8.7 Singly differential cross section for He^{2+} -impact ionisation of atomic hydrogen in the angle of the ejected electron: convergence of the WP-CCC results with respect to l_{max} .	109
8.8 Singly differential cross section in the angle of the scattered projectile for He^{2+} -impact ionisation of atomic hydrogen: convergence of the WP-CCC results with respect to l_{max} .	110
8.9 Singly differential cross section in the energy of the ejected electron for He^{2+} -impact ionisation of atomic hydrogen: convergence of the WP-CCC results with respect to l_{max} .	111
8.10 Total cross section for electron capture in $\text{H}^{2+}\text{-H}(1s)$ collisions: the WP-CCC results are compared with the experimental measurements [156–159] and the close-coupling calculations [160, 161]	112

8.11 Total cross section for ionisation in H^{2+} -H(1s) collisions: the present WP-CCC results are compared with the experimental measurements of Shah and Gilbody [163], Shah *et al.* [164] and the close-coupling calculations of Winter [161] and Toshima [160]. 113

8.12 Cross sections for excitation of the $n = 1, 2$ and 3 shell states in He^{2+} -H(1s) collisions: the present WP-CCC results are compared with the theoretical calculations of Winter [161]. The experimental data for 2s, 2p and 3p excitation are due to Hughes *et al.* [165] and Detleffsen *et al.* [166]. 114

8.13 Cross sections for electron capture into the $n = 1, 2$ and 3 shell states in He^{2+} -H(1s) collisions: the present WP-CCC results are compared with the theoretical calculations of Winter [161] and Minami *et al.* [162]. The experimental data are due to Shah and Gilbody [158] and Bayfield and Khayrallah [156]. . 116

8.14 Balmer- α emission cross section in He^{2+} -H collisions as a function of the impact energy: the present WP-CCC results are compared with the experimental measurements of Donnelly *et al.* [167] and the close-coupling calculations of Winter [161]. The WP-CCC results multiplied by a factor of 2 are also presented for comparison. 117

8.15 Total electron-capture cross section in p - He^+ collisions: the present WP-CCC results are compared with the experimental measurements of Peart *et al.* [169], Watts *et al.* [170] and Rinn *et al.* [171] and the close-coupling calculations of Reading *et al.* [172], Minami *et al.* [173] and Winter [174]. 118

8.16	Total ionisation cross section in $p\text{-He}^+$ collisions: the present WP-CCC results are compared with the experimental measurements of Watts <i>et al.</i> [170] and Rinn <i>et al.</i> [175] and the close-coupling calculations of Reading <i>et al.</i> [172], Minami <i>et al.</i> [173] and Winter [174].	119
8.17	Total cross section for electron loss by the target in $p\text{-He}^+$ collisions: the present WP-CCC results are compared with the experimental data of Peart <i>et al.</i> [169, 176], Mitchell <i>et al.</i> [177], Angel <i>et al.</i> [178], Rinn <i>et al.</i> [175], Watts <i>et al.</i> [170] and the single-centre calculations of Hall <i>et al.</i> [179].	120
8.18	Cross sections for excitation and electron capture into the $n = 1, 2$ and 3 shell states in $p\text{-He}^+$ collisions.	121
9.1	Total cross sections for electron capture (upper panel) and single ionisation (lower panel) in $p\text{-He}$ collisions: convergence of the present WP-CCC results with respect to the number of bin states N_c . The four lines represent the cross sections at the incident proton energies of 50 keV, 100 keV, 500 keV and 1 MeV, respectively.	125
9.2	The same as in Fig. 9.1, but with respect to l_{\max} . The number of bins was set to $N_c = 20$	126
9.3	Total cross section for electron capture in $p\text{-He}(1s^2)$ collisions as a function of the incident proton energy (top and bottom panels linear and log y scales respectively). The present results are compared with the experimental data [59–63], and the other theoretical results [38, 39, 45–48].	127

- 9.4 Cross sections for electron capture into the $2s$ (upper panel) and $2p$ (lower panel) states of hydrogen in $p\text{-He}(1s^2)$ collisions. The CCC results are represented by the black solid line. The experimental data are due to Hughes *et al.* [64], Hippler *et al.* [66], Ryding *et al.* [67], Andreev *et al.* [180]. The other theoretical results are from Kimura and Lin [45], Slim *et al.* [50], Jain *et al.* [51]. 129
- 9.5 Sum of the cross sections for target excitation into the $2s$ and $2p$ states (upper panel), and the cross section for excitation into the $2p$ state (lower panel) of helium in $p\text{-He}(1s^2)$ collisions. The CCC results are represented by the black solid line. The experimental data are due to Hippler and Schartner [65], Park and Schowengerdt [68]. The other theoretical results are from Begum *et al.* [53], Joachain and Vanderpoorten [55], van den Bos [56]. 131
- 9.6 Cross section for single ionisation in $p\text{-He}(1s^2)$ collisions as a function of incident energy. The CCC results represented by the black solid line. The experimental data are due to Shah and Gilbody [60], Shah *et al.* [61], Rudd *et al.* [62]. The other theoretical results are from Baxter and Kirchner [38], Díaz *et al.* [42], Slim *et al.* [47], Winter [48]. 132
- 9.7 Cross section for double ionisation of helium in $p\text{-He}(1s^2)$ collisions as a function of incident energy. The CCC results are represented by the black solid line. The experimental data are due to Shah and Gilbody [60], Shah *et al.* [61], Puckett and Martin [69]. The other theoretical results are from Baxter and Kirchner [38], Ford and Reading [57], Kumar and Roy [58]. 133

Bibliography

- [1] D. Tseliakhovich, C. M. Hirata, and K. Heng, [Mon. Not. R. Astron. Soc.](#) **422**, 2356 (2012).
- [2] D. E. Post, *The role of atomic collisions in fusion* (Presented at the NATO Advanced Study Institute on the Physics of Ion-Ion and Electron-Ion Collisions, 1981).
- [3] O. Marchuk, Y. Ralchenko, and D. R. Schultz, [Plasma Phys. Control. Fusion](#) **54**, 095010 (2012).
- [4] O. Marchuk, [Phys. Scr.](#) **89**, 114010 (2014).
- [5] D. Belkić, [J. Math. Chem.](#) **47**, 1366 (2010).
- [6] D. Belkić, *Theory of Heavy Ion Collision Physics in Hadron Therapy* (Elsevier, Amsterdam, 2013).
- [7] J. Hansen, “[Proton therapy: The new weapon of choice against cancer is coming to Australia](#),” *The Daily Telegraph* (20/9/2014), Accessed: May, 2019.
- [8] E. Rutherford, *Philos. Mag.* **6**, 21 (1911).
- [9] H. C. Brinkman and H. A. Kramers, *Proc. Acad. Sci. Amsterdam* **33**, 973 (1930).

- [10] J. B. Hasted and H. S. W. Massey, *Proc. R. Soc. Lond. A. Math. Phys. Sci.* **212**, 235 (1952).
- [11] D. R. Bates and A. Dalgarno, *Proc. Phys. Soc. A* **65**, 919 (1952).
- [12] D. R. Bates and G. Griffing, *Proc. Phys. Soc. A* **66**, 961 (1953).
- [13] J. B. H. Stedeford, J. B. Hasted, and H. S. W. Massey, *Proc. R. Soc. Lond. A* **227**, 466 (1955).
- [14] J. D. Jackson and H. Schiff, *Phys. Rev.* **89**, 359 (1953).
- [15] M. R. C. McDowell and J. P. Coleman, *Introduction to the Theory of Ion-Atom Collisions* (North-Holland publishing co.-Amsterdam, United Kingdom, 1970).
- [16] B. H. Bransden and M. R. C. McDowell, *Charge Exchange and the Theory of Ion-Atom Collisions* (Clarendon, Oxford, 1992).
- [17] B. Bransden and C. Joachain, *Physics of Atoms and Molecules*, 2nd ed. (Prentice Hall, 2003).
- [18] J. Eichler, *Lectures on Ion-Atom Collisions*, 1st ed. (Elsevier, 2005).
- [19] D. R. Bates, *Proc. R. Soc. Lond. A. Math. Phys. Sci.* **245**, 299 (1958).
- [20] D. R. Bates, *Proc. R. Soc. A* **247**, 294 (1958).
- [21] R. McCarroll and D. R. Bates, *Proc. R. Soc. Lond. A. Math. Phys. Sci.* **264**, 547 (1961).
- [22] R. Abrines and I. C. Percival, *Proc. Cambridge Philos. Soc.* **88**, 861 (1966).
- [23] I. M. Cheshire, D. F. Gallaher, and A. J. Taylor, *J. Phys. B: At. Mol. Phys.* **3**, 813 (1970).

- [24] T. G. Winter and C. C. Lin, [Phys. Rev. A **10**, 2141 \(1974\)](#).
- [25] R. E. Olson and A. Salop, [Phys. Rev. A **16**, 531 \(1977\)](#).
- [26] D. Belkic, R. Gayet, and A. Salin, [Phys. Rep. **56**, 279 \(1979\)](#).
- [27] R. E. Olson and D. R. Schultz, [Phys. Scr. **1989**, 71 \(1989\)](#).
- [28] N. Toshima, [Phys. Rev. A **59**, 1981 \(1999\)](#).
- [29] A. S. Kadyrov and I. Bray, [J. Phys. B: At. Mol. Opt. Phys. **33**, L635 \(2000\)](#).
- [30] J. Fiol and R. E. Olson, [J. Phys. B: At. Mol. Opt. Phys. **35**, 1759 \(2002\)](#).
- [31] A. S. Kadyrov and I. Bray, [Phys. Rev. A **66**, 012710 \(2002\)](#).
- [32] A. S. Kadyrov, I. Bray, and A. T. Stelbovics, [Phys. Rev. A **73**, 012710 \(2006\)](#).
- [33] A. S. Kadyrov, I. Bray, and A. T. Stelbovics, [Phys. Rev. Lett. **98**, 263202 \(2007\)](#).
- [34] T. G. Winter, [Phys. Rev. A **80**, 032701 \(2009\)](#).
- [35] A. S. Kadyrov, I. B. Abdurakhmanov, I. Bray, and A. T. Stelbovics, [Phys. Rev. A **80**, 022704 \(2009\)](#).
- [36] I. B. Abdurakhmanov, A. S. Kadyrov, I. Bray, and A. T. Stelbovics, [J. Phys. B: At. Mol. Opt. Phys. **44**, 075204 \(2011\)](#).
- [37] A. Jorge, L. F. Errea, C. Illescas, and L. Méndez, [Eur. Phys. J. D **68**, 227 \(2014\)](#).
- [38] M. Baxter and T. Kirchner, [Phys. Rev. A **93**, 012502 \(2016\)](#).

- [39] D. Belkić, *Phys. Rev. A* **37**, 55 (1988).
- [40] B. H. Bransden and L. T. S. F. Lam, *Proc. Phys. Soc.* **87**, 653 (1966).
- [41] G. R. Deco, J. M. Maidagan, and R. D. Rivarola, *J. Phys. B: At. Mol. Phys.* **17**, L707 (1984).
- [42] C. Díaz, F. Martín, and A. Salin, *J. Phys. B: At. Mol. Opt. Phys.* **33**, 4373 (2000).
- [43] T. A. Green, H. E. Stanley, and Y. C. Chiang, *Helv. Phys. Acta* **38**, 109 (1965).
- [44] S. Jana, C. R. Mandal, and M. Purkait, *J. Phys. B: At. Mol. Opt. Phys.* **48**, 045203 (2015).
- [45] M. Kimura and C. D. Lin, *Phys. Rev. A* **34**, 176 (1986).
- [46] R. Samanta and M. Purkait, *Phys. Scr.* **84**, 065301 (2011).
- [47] H. A. Slim, E. L. Heck, B. H. Bransden, and D. R. Flower, *J. Phys. B: At. Mol. Opt. Phys.* **24**, L421 (1991).
- [48] T. G. Winter, *Phys. Rev. A* **44**, 4353 (1991).
- [49] X. Guan and K. Bartschat, *Phys. Rev. Lett.* **103**, 213201 (2009).
- [50] H. A. Slim, E. L. Heck, B. H. Bransden, and D. R. Flower, *J. Phys. B: At. Mol. Opt. Phys.* **24**, 1683 (1991).
- [51] A. Jain, C. D. Lin, and W. Fritsch, *Phys. Rev. A* **36**, 2041 (1987).
- [52] R. J. Bell, *Proc. Phys. Soc.* **78**, 903 (1961).
- [53] S. Begum, B. H. Bransden, and J. Coleman, *J. Phys. B: At. Mol. Phys.* **6**, 837 (1973).

- [54] V. D. Rodríguez, C. A. Ramírez, R. D. Rivarola, and J. E. Miraglia, *Phys. Rev. A* **55**, 4201 (1997).
- [55] J. Joachain and R. Vanderpoorten, *J. Phys. B: At. Mol. Phys.* **7**, 817 (1974).
- [56] J. van den Bos, *Phys. Rev.* **181**, 191 (1969).
- [57] A. L. Ford and J. F. Reading, *J. Phys. B: At. Mol. Opt. Phys.* **27**, 4215 (1994).
- [58] A. Kumar and B. N. Roy, *J. Phys. B: At. Mol. Phys.* **10**, 3047 (1977).
- [59] S. K. Allison, *Rev. Mod. Phys.* **30**, 1137 (1958).
- [60] M. B. Shah and H. B. Gilbody, *J. Phys. B: At. Mol. Phys.* **18**, 899 (1985).
- [61] M. B. Shah, P. McCallion, and H. B. Gilbody, *J. Phys. B: At. Mol. Opt. Phys.* **22**, 3037 (1989).
- [62] M. E. Rudd, R. D. DuBois, L. H. Toburen, C. A. Ratcliffe, and T. V. Goffe, *Phys. Rev. A* **28**, 3244 (1983).
- [63] P. M. Stier and C. F. Barnett, *Phys. Rev.* **103**, 896 (1956).
- [64] R. H. Hughes, C. A. Stigers, B. M. Doughty, and E. D. Stokes, *Phys. Rev. A* **1**, 1424 (1970).
- [65] R. Hippler and K. H. Schartner, *J. Phys. B: At. Mol. Phys.* **7**, 618 (1974).
- [66] R. Hippler, W. Harbich, M. Faust, H. O. Lutz, and L. J. Dube, *J. Phys. B: At. Mol. Phys.* **19**, 1507 (1986).
- [67] G. Ryding, A. B. Wittkower, and H. B. Gilbody, *Proc. Phys. Soc.* **89**, 547 (1966).

- [68] J. T. Park and F. D. Schowengerdt, *Phys. Rev.* **185**, 152 (1969).
- [69] L. J. Puckett and D. W. Martin, *Phys. Rev. A* **1**, 1432 (1970).
- [70] H. Ehrhardt, M. Schulz, T. Tekaas, and K. Willmann, *Phys. Rev. Lett.* **22**, 89 (1969).
- [71] P. J. Marchalant, C. T. Whelan, and H. R. J. Walters, *J. Phys. B: At. Mol. Opt. Phys.* **31**, 1141 (1998).
- [72] T. N. Rescigno, M. Baertschy, W. A. Isaacs, and C. W. McCurdy, *Science* **286**, 2474 (1999).
- [73] R. Moshhammer, J. Ullrich, M. Unverzagt, W. Schmidt, P. Jardin, R. E. Olson, R. Mann, R. Dörner, V. Mergel, U. Buck, and H. Schmidt-Böcking, *Phys. Rev. Lett.* **73**, 3371 (1994).
- [74] J. McGuire, T. Reeves, N. Deb, and N. Sil, *Nuclear Instruments and Methods in Physics Research Section B: Beam Interactions with Materials and Atoms* **24-25**, 243 (1987).
- [75] T. Vajnai, A. D. Gaus, J. A. Brand, W. Htwe, D. H. Madison, R. E. Olson, J. L. Peacher, and M. Schulz, *Phys. Rev. Lett.* **74**, 3588 (1995).
- [76] M. Schulz, T. Vajnai, A. D. Gaus, W. Htwe, D. H. Madison, and R. E. Olson, *Phys. Rev. A* **54**, 2951 (1996).
- [77] A. L. Godunov, V. A. Schipakov, and M. Schulz, *J. Phys. B: At. Mol. Opt. Phys.* **31**, 4943 (1998).
- [78] M. Schulz, R. Moshhammer, D. H. Madison, R. E. Olson, P. Marchalant, C. T. Whelan, H. R. J. Walters, S. Jones, M. Foster, H. Kollmus, A. Cas-simi, and J. Ullrich, *J. Phys. B: At. Mol. Opt. Phys.* **34**, L305 (2001).

- [79] N. V. Maydanyuk, A. Hasan, M. Foster, B. Tooke, E. Nanni, D. H. Madison, and M. Schulz, *Phys. Rev. Lett.* **94**, 243201 (2005).
- [80] M. Schulz, A. Hasan, N. V. Maydanyuk, M. Foster, B. Tooke, and D. H. Madison, *Phys. Rev. A* **73**, 062704 (2006).
- [81] M. F. Ciappina, W. R. Cravero, and M. Schulz, *J. Phys. B: At. Mol. Opt. Phys.* **40**, 2577 (2007).
- [82] X. Y. Ma, X. Li, S. Y. Sun, and X. F. Jia, *EPL* **98**, 53001 (2012).
- [83] Y. H. Duan, S. Y. Sun, and X. F. Jia, *EPL* **110**, 13001 (2015).
- [84] X. Niu, S. Sun, F. Wang, and X. Jia, *Phys. Rev. A* **96**, 022703 (2017).
- [85] I. B. Abdurakhmanov, A. S. Kadyrov, I. Bray, and K. Bartschat, *Phys. Rev. A* **96**, 022702 (2017).
- [86] J. Hirschfelder, H. Eyring, and B. Topley, *J. Chem. Phys.* **4**, 170 (1936).
- [87] R. E. Olson, J. Ullrich, and H. Schmidt-Böcking, *Phys. Rev. A* **39**, 5572 (1989).
- [88] D. Zajfman and D. Maor, *Phys. Rev. Lett.* **56**, 320 (1986).
- [89] D. R. Schultz and R. E. Olson, *Phys. Rev. A* **38**, 1866 (1988).
- [90] C. E. Kuyatt and T. Jorgensen, *Phys. Rev.* **130**, 1444 (1963).
- [91] Y. V. Popov, A. Galstyan, O. Chuluunbaatar, S. Houamer, A. A. Bulychev, M. S. Schöffler, H.-K. Kim, J. N. Titze, T. Jahnke, L. P. H. Schmidt, H. Schmidt-Böcking, and R. Dörner, *J. Phys. Conf. Ser.* **601**, 012008 (2015).
- [92] N. Toshima, T. Ishihara, and J. Eichler, *Phys. Rev. A* **36**, 2659 (1987).

- [93] I. Mancev, V. Mergel, and L. Schmidt, *J. Phys. B: At. Mol. Opt. Phys.* **36**, 2733 (2003).
- [94] M. Rahmanian, F. Shojaei, and R. Fathi, *Eur. Phys. J. D* **70**, 241 (2016).
- [95] I. M. Cheshire, *Proc. Phys. Soc.* **84**, 89 (1964).
- [96] D. Belkic and R. Gayet, *J. Phys. B: At. Mol. Phys.* **10**, 1911 (1977).
- [97] D. Belkic, *J. Phys. B: At. Mol. Phys.* **11**, 3529 (1978).
- [98] D. Belkić, R. Gayet, J. Hanssen, I. Mančev, and A. Nuñez, *Phys. Rev. A* **56**, 3675 (1997).
- [99] D. S. F. Crothers and J. F. McCann, *J. Phys. B: At. Mol. Phys.* **16**, 3229 (1983).
- [100] P. D. Fainstein, V. H. Ponce, and R. D. Rivarola, *J. Phys. B: At. Mol. Opt. Phys.* **23**, 1481 (1990).
- [101] P. D. Fainstein, V. H. Ponce, and R. D. Rivarola, *J. Phys. B: At. Mol. Opt. Phys.* **21**, 287 (1988).
- [102] P. N. Abufager, A. E. Martínez, R. D. Rivarola, and P. D. Fainstein, *J. Phys. B: At. Mol. Opt. Phys.* **37**, 817 (2004).
- [103] H. A. Bethe and E. E. Salpeter, *Quantum Mechanics of One- and Two-Electron Atoms* (Plenum, New York, 1977).
- [104] D. F. Gallaher and L. Wilets, *Phys. Rev.* **169**, 139 (1968).
- [105] R. Shakeshaft, *J. Phys. B: At. Mol. Phys.* **8**, 1114 (1975).
- [106] M. Kimura and W. R. Thorson, *Phys. Rev. A* **24**, 1780 (1981).

- [107] A. L. Ford, J. F. Reading, and K. A. Hall, *J. Phys. B: At. Mol. Opt. Phys.* **26**, 4537 (1993).
- [108] G. V. Avakov, A. R. Ashurov, L. D. Blokhinstev, A. M. Mukhamedzhanov, and M. V. Poletayeva, *J. Phys. B: At. Mol. Opt. Phys.* **23**, 2309S (1990).
- [109] G. V. Avakov, A. R. Ashurov, L. D. Blokhintsev, A. S. Kadyrov, A. M. Mukhamedzhanov, and M. V. Poletayeva, *J. Phys. B: At. Mol. Opt. Phys.* **23**, 4151 (1990).
- [110] G. V. Avakov, L. D. Blokhintsev, A. S. Kadyrov, and A. M. Mukhamedzhanov, *J. Phys. B: At. Mol. Opt. Phys.* **25**, 213 (1992).
- [111] E. O. Alt, G. V. Avakov, L. D. Blokhintsev, A. S. Kadyrov, and A. M. Mukhamedzhanov, *J. Phys. B: At. Mol. Opt. Phys.* **27**, 4653 (1994).
- [112] E. O. Alt, A. S. Kadyrov, and A. M. Mukhamedzhanov, *Phys. Rev. A* **60**, 314 (1999).
- [113] V. Maruhn-Rezwani, N. Grün, and W. Scheid, *Phys. Rev. Lett.* **43**, 512 (1979).
- [114] C. Bottcher, *Phys. Rev. Lett.* **48**, 85 (1982).
- [115] A. Kołakowska, M. S. Pindzola, F. Robicheaux, D. R. Schultz, and J. C. Wells, *Phys. Rev. A* **58**, 2872 (1998).
- [116] A. S. Kadyrov, I. Bray, A. T. Stelbovics, and B. Saha, *J. Phys. B: At. Mol. Opt. Phys.* **38**, 509 (2005).
- [117] I. Bray and A. T. Stelbovics, *Phys. Rev. A* **46**, 6995 (1992).
- [118] I. Bray and A. T. Stelbovics, *Phys. Rev. Lett.* **70**, 746 (1993).
- [119] D. V. Fursa and I. Bray, *Phys. Rev. A* **52**, 1279 (1995).

- [120] I. Bray, [Phys. Rev. A **49**, 1066 \(1994\)](#).
- [121] D. V. Fursa and I. Bray, [J. Phys. B: At. Mol. Opt. Phys. **30**, 5895 \(1997\)](#).
- [122] M. C. Zammit, J. S. Savage, D. V. Fursa, and I. Bray, [Phys. Rev. Lett. **116**, 233201 \(2016\)](#).
- [123] A. S. Kadyrov, C. M. Rawlins, A. T. Stelbovics, I. Bray, and M. Charlton, [Phys. Rev. Lett. **114**, 183201 \(2015\)](#).
- [124] C. M. Rawlins, A. S. Kadyrov, A. T. Stelbovics, I. Bray, and M. Charlton, [Phys. Rev. A **93**, 012709 \(2016\)](#).
- [125] A. S. Kadyrov and I. Bray, [J. Phys. B: At. Mol. Opt. Phys. **49**, 222002 \(2016\)](#).
- [126] A. S. Kadyrov, I. Bray, M. Charlton, and I. I. Fabrikant, [Nat. Commun. **8**, 1544 \(2017\)](#).
- [127] I. B. Abdurakhmanov, A. S. Kadyrov, I. Bray, and A. T. Stelbovics, [J. Phys. B **44**, 075204 \(2011\)](#).
- [128] I. B. Abdurakhmanov, A. S. Kadyrov, I. Bray, and A. T. Stelbovics, [J. Phys. B **44**, 165203 \(2011\)](#).
- [129] I. B. Abdurakhmanov, A. S. Kadyrov, D. V. Fursa, and I. Bray, [Phys. Rev. Lett. **111**, 173201 \(2013\)](#).
- [130] I. B. Abdurakhmanov, A. S. Kadyrov, S. K. Avazbaev, and I. Bray, [J. Phys. Conf. Ser. **635**, 022100 \(2015\)](#).
- [131] I. B. Abdurakhmanov, A. S. Kadyrov, and I. Bray, [Phys. Rev. A **94**, 022703 \(2016\)](#).

- [132] I. B. Abdurakhmanov, J. J. Bailey, A. S. Kadyrov, and I. Bray, [Phys. Rev. A **97**, 032707 \(2018\)](#).
- [133] I. B. Abdurakhmanov, S. U. Alladustov, J. J. Bailey, A. S. Kadyrov, and I. Bray, [Plasma Phys. Control. Fusion **60**, 095009 \(2018\)](#).
- [134] I. B. Abdurakhmanov, K. Massen-Hane, S. U. Alladustov, J. J. Bailey, A. S. Kadyrov, and I. Bray, [Phys. Rev. A **98**, 062710 \(2018\)](#).
- [135] I. B. Abdurakhmanov, A. S. Kadyrov, D. V. Fursa, I. Bray, and A. T. Stelbovics, [Phys. Rev. A **84**, 062708 \(2011\)](#).
- [136] I. B. Abdurakhmanov, I. Bray, D. V. Fursa, A. S. Kadyrov, and A. T. Stelbovics, [Phys. Rev. A **86**, 034701 \(2012\)](#).
- [137] I. B. Abdurakhmanov, A. S. Kadyrov, I. Bray, and K. Bartschat, [Phys. Rev. A **96**, 022702 \(2017\)](#).
- [138] S. U. Alladustov, I. B. Abdurakhmanov, A. S. Kadyrov, I. Bray, and K. Bartschat, [Phys. Rev. A **99**, 052706 \(2019\)](#).
- [139] D. A. Varshalovich, A. N. Moskalev, and V. K. Khersonskii, *Quantum theory of angular momentum*, 1st ed. (World Scientific Pub., Philadelphia, 1988).
- [140] I. B. Abdurakhmanov, A. S. Kadyrov, I. Bray, and K. Bartschat, [Phys. Rev. A **96**, 022702 \(2017\)](#).
- [141] S. Bashkin and J. Stoner, *Atomic Energy Levels and Grotrian Diagrams*, Vol 1 (North-Holland Publishing Company, 1975).
- [142] I. B. Abdurakhmanov, J. J. Bailey, A. S. Kadyrov, and I. Bray, [Phys. Rev. A **97**, 032707 \(2018\)](#).

- [143] M. S. Pindzola, T. G. Lee, T. Minami, and D. R. Schultz, *Phys. Rev. A* **72**, 062703 (2005).
- [144] F. W. Meyer, A. M. Howald, C. C. Havener, and R. A. Phaneuf, *Phys. Rev. A* **32**, 3310 (1985).
- [145] T. V. Goffe, M. B. Shah, and H. B. Gilbody, *J. Phys. B: At. Mol. Phys.* **12**, 3763 (1979).
- [146] C. Harel, H. Jouin, and B. Pons, *Atomic Data and Nuclear Data Tables* **68**, 279 (1998).
- [147] K. Igenbergs, J. Schweinzer, A. Veiter, L. Perneczky, E. Frühwirth, M. Wallerberger, R. E. Olson, and F. Aumayr, *J. Phys. B: At. Mol. Opt. Phys.* **45**, 065203 (2012).
- [148] N. Toshima, *Phys. Rev. A* **50**, 3940 (1994).
- [149] D. Belkic, S. Saini, and H. S. Taylor, *Phys. Rev. A* **36**, 1601 (1987).
- [150] M. B. Shah and H. B. Gilbody, *J. Phys. B: At. Mol. Phys.* **16**, L449 (1983).
- [151] R. D. Rivarola, P. D. Fainstein, and V. H. Ponce, *Phys. Scr.* **1989**, 101 (1989).
- [152] I. B. Abdurakhmanov, A. S. Kadyrov, S. K. Avazbaev, and I. Bray, *J. Phys. B: At. Mol. Phys.* **49**, 115203 (2016).
- [153] I. B. Abdurakhmanov, J. J. Bailey, A. S. Kadyrov, and I. Bray, *Phys. Rev. A* **97**, 032707 (2018).
- [154] L. C. Tribedi, P. Richard, W. DeHaven, L. Gulyás, M. W. Gealy, and M. E. Rudd, *J. Phys. B: At. Mol. Opt. Phys.* **31**, L369 (1998).

- [155] L. C. Tribedi, P. Richard, L. Gulyás, and M. E. Rudd, [Phys. Scr. **1999**, 333 \(1999\)](#).
- [156] J. E. Bayfield and G. A. Khayrallah, [Phys. Rev. A **12**, 869 \(1975\)](#).
- [157] R. E. Olson, A. Salop, R. A. Phaneuf, and F. W. Meyer, [Phys. Rev. A **16**, 1867 \(1977\)](#).
- [158] M. B. Shah and H. B. Gilbody, [J. Phys. B: At. Mol. Phys. **11**, 121 \(1978\)](#).
- [159] P. Hvelplund and A. Andersen, [Phys. Scr. **26**, 375 \(1982\)](#).
- [160] N. Toshima, [Phys. Rev. A **50**, 3940 \(1994\)](#).
- [161] T. G. Winter, [Phys. Rev. A **76**, 062702 \(2007\)](#).
- [162] T. Minami, T.-G. Lee, M. S. Pindzola, and D. R. Schultz, [J. Phys. B: At. Mol. Opt. Phys. **41**, 135201 \(2008\)](#).
- [163] M. B. Shah and H. B. Gilbody, [J. Phys. B: At. Mol. Phys. **14**, 2361 \(1981\)](#).
- [164] M. B. Shah, D. S. Elliott, P. McCallion, and H. B. Gilbody, [J. Phys. B: At. Mol. Opt. Phys. **21**, 2455 \(1988\)](#).
- [165] M. P. Hughes, J. Geddes, and H. B. Gilbody, [J. Phys. B: At. Mol. Opt. Phys. **27**, 1143 \(1994\)](#).
- [166] D. Detleffsen, M. Anton, A. Werner, and K. H. Schartner, [J. Phys. B: At. Mol. Opt. Phys. **27**, 4195 \(1994\)](#).
- [167] A. Donnelly, J. Geddes, and H. B. Gilbody, [J. Phys. B: At. Mol. Opt. Phys. **24**, 165 \(1991\)](#).
- [168] I. B. Abdurakhmanov, O. Erkilic, A. S. Kadyrov, I. Bray, S. K. Avazbaev, and A. M. Mukhamedzhanov, [J. Phys. B: At. Mol. Opt. Phys. **52**, 105701 \(2019\)](#).

- [169] B. Peart, K. Rinn, and K. Dolder, *J. Phys. B: At. Mol. Phys.* **16**, 1461 (1983).
- [170] M. F. Watts, K. F. Dunn, and H. B. Gilbody, *J. Phys. B: At. Mol. Phys.* **19**, L355 (1986).
- [171] K. Rinn, F. Melchert, and E. Salzborn, *J. Phys. B: At. Mol. Phys.* **18**, 3783 (1985).
- [172] J. F. Reading, A. L. Ford, and R. L. Becker, *J. Phys. B: At. Mol. Phys.* **15**, 625 (1982).
- [173] T. Minami, M. S. Pindzola, T.-G. Lee, and D. R. Schultz, *J. Phys. B: At. Mol. Opt. Phys.* **40**, 3629 (2007).
- [174] T. G. Winter, *Phys. Rev. A* **87**, 032704 (2013).
- [175] K. Rinn, F. Melchert, K. Rink, and E. Salzborn, *J. Phys. B: At. Mol. Phys.* **19**, 3717 (1986).
- [176] B. Peart, R. Grey, and K. T. Dolder, *J. Phys. B: At. Mol. Phys.* **10**, 2675 (1977).
- [177] J. B. A. Mitchell, K. F. Dunn, G. C. Angel, R. Browning, and H. B. Gilbody, *J. Phys. B: At. Mol. Phys.* **10**, 1897 (1977).
- [178] G. C. Angel, K. F. Dunn, E. C. Sewell, and H. B. Gilbody, *J. Phys. B: At. Mol. Phys.* **11**, L49 (1978).
- [179] K. A. Hall, J. F. Reading, and A. L. Ford, *J. Phys. B: At. Mol. Opt. Phys.* **27**, 5257 (1994).
- [180] E. P. Andreev, V. A. Ankudinov, and S. V. Bobashev, *Sov. Phys. JETP* **23**, 375 (1966).

Every reasonable effort has been made to acknowledge the owners of copyright material. I would be pleased to hear from any copyright owner who has been omitted or incorrectly acknowledged.